



New ultrasensitive bimetallic substrates for surface enhanced Raman scattering

Mohammad Yehia Khaywah

► To cite this version:

Mohammad Yehia Khaywah. New ultrasensitive bimetallic substrates for surface enhanced Raman scattering. Micro and nanotechnologies/Microelectronics. Université de Technologie de Troyes; Université Libanaise, 2014. English. NNT : 2014TROY0041 . tel-03358871

HAL Id: tel-03358871

<https://theses.hal.science/tel-03358871>

Submitted on 29 Sep 2021

HAL is a multi-disciplinary open access archive for the deposit and dissemination of scientific research documents, whether they are published or not. The documents may come from teaching and research institutions in France or abroad, or from public or private research centers.

L'archive ouverte pluridisciplinaire **HAL**, est destinée au dépôt et à la diffusion de documents scientifiques de niveau recherche, publiés ou non, émanant des établissements d'enseignement et de recherche français ou étrangers, des laboratoires publics ou privés.

Thèse
de doctorat
de l'UTT

Mohammad Yehia KHAYWAH

New Ultrasensitive Bimetallic Substrates for Surface Enhanced Raman Scattering

Spécialité :
Optique et Nanotechnologies

2014TROY0041

Année 2014

Thèse en cotutelle avec l'Université Libanaise - Beyrouth - Liban

THESE

pour l'obtention du grade de

DOCTEUR de l'UNIVERSITE DE TECHNOLOGIE DE TROYES

Spécialité : OPTIQUE ET NANOTECHNOLOGIES

présentée et soutenue par

Mohammad Yehia KHAYWAH

le 19 décembre 2014

**New Ultrasensitive Bimetallic Substrates for
Surface Enhanced Raman Scattering**

JURY

M. T. HAMIEH	PROFESSEUR	Président
M. P.-M. ADAM	PROFESSEUR DES UNIVERSITES	Directeur de thèse
M. É. FINOT	PROFESSEUR DES UNIVERSITES	Rapporteur
M. S. JRADI	ENSEIGNANT CHERCHEUR UTT	Examinateur
M. G. LOUARN	PROFESSEUR DES UNIVERSITES	Examinateur
M. M. NAKHL	PROFESSEUR	Rapporteur
Mme J. TOUFAILY	PROFESSEUR	Directrice de thèse

“We live on an island surrounded by a sea of ignorance. As our island of knowledge grows, so does the shore of our ignorance.”

- John Archibald Wheeler (1911-2008)

Abstract

Driven by the interest in finding ultrasensitive sensors devices, reliable surface enhanced Raman scattering (SERS) based substrates are fabricated. Silver and gold nanoparticles are two of the best candidates for SERS substrates where Ag nanoparticles exhibit large enhancing ability in Raman intensity while Au nanostructures are stable in biological systems. Hence, combining the two metals in bimetallic nanostructures appeared to be a promising approach in order to sum the merits of Au surface properties and Ag enhancing ability. Thermal annealing of thin metallic films is used as a simple and relatively inexpensive technique to elaborate homogenous and reproducible Ag/Au bimetallic nanoparticles SERS substrates with high enhancing ability. The fabricated nanoparticles proved their enhancing stability even after one year of fabrication. Manipulating the composition of Ag/Au bimetallic NPs resulted in tuning the Localized Surface Plasmon Resonance (LSPR) over the whole visible spectrum, where the substrates are characterized with higher SERS enhancement when they exhibit LSPR closer to the Raman excitation wavelength. Additionally, bimetallic nanoparticles patterns with different size, composition and lattice constants have been conducted by electron beam lithography. The systematic study of their interesting plasmonic and SERS enhancing properties revealed maintenance in the LSPR-SERS relation by changing the nanoparticle size.

RESUMÉ

Afin de développer des capteurs ultrasensibles des substrats fiables pour la diffusion Raman exaltée de surface (SERS) ont été fabriqués. Les deux meilleurs candidats de matériaux constituant les nanoparticules pour des substrats SERS sont l'argent et l'or. L'argent présente un meilleur facteur d'exaltation de l'intensité Raman et l'or est stable dans les milieux biologiques. C'est pourquoi la combinaison de ces deux métaux dans des nanostructures bimétalliques semble être une approche prometteuse qui combine les propriétés de surface de l'or et d'exaltation de l'argent. Le recuit thermique des couches métalliques minces est utilisé comme une technique simple et peu coûteuse. Cette dernière permet d'élaborer des substrats homogènes et reproductibles de nanoparticules bimétalliques or-argent ayant un facteur d'exaltation importante. Ces nanoparticules gardent leurs propriétés d'exaltation même après une année de fabrication. En jouant sur la composition de nanoparticules bimétalliques il est possible d'avoir une résonance de plasmons de surface localisés (LSPR) sur tout le spectre visible. Ces substrats sont caractérisés par une exaltation SERS supérieure lorsque la résonance plasmon est plus proche de la longueur d'onde d'excitation Raman. En outre, les nanoparticules bimétalliques de différentes tailles, compositions ont été réalisés par lithographie électronique. L'étude systématique de leurs propriétés plasmoniques et de leur exaltation SERS a révélé une conservation du lien entre résonance plasmon et signal SERS.

Acknowledgements

The completion of my dissertation and subsequent Ph.D. has been a long three years journey. I could not have succeeded without the invaluable support of several. Without these people, especially the select few I am about to mention, this thesis would not have been possible.

I would like first to express my special appreciation and gratitude to my thesis advisors, Prof. Pierre-Michel Adam and Prof. Joumana Toufaily, you have been a tremendous mentor for me. Thank you for your continuous encouraging, your understanding, your sympathy and your precious help since the first day in my Ph.D. thesis.

Many thanks also to Dr. Safi Jradi for the continuous valuable discussions during my masters and Ph.D. thesis. These discussions resulted in more detailed and global understanding of my thesis subject.

I would like also to thank my committee members, Prof. Eric FINOT, Prof. Michel NAKHL, Prof. Tayssir HAMIEH, Prof. Guy LOUARN, and Dr. Safi JRADI, for accepting the task of evaluating my work. I also want to thank you for letting my defense be an enjoyable moment, and for your brilliant comments and suggestions, thanks to you.

I want also to express my sincere thanks to the “Institut des Materiaux Jean Rouxel, Nantes”, for having me as a guest and for the valuable TEM and XPS measurements.

I also want to thank Mr. Yvon Lacroute from the " Laboratoire de Physique, Optique Submicronique, Université de Bourgogne" for the SEM images.

I want also to thank Dr.Suzzana Jradi, a previous Post-doc at LNIO laboratory for her valuable help.

My gratitude goes to the LNIO members because it is their kindness that creates this agreeable working ambiance. Special thanks go to Roy, Joyce, Lina, Zeinab, Johnny, Maher, Abeer, Rana, Nancy and Lama.

Thanks to everyone who has participated either directly or indirectly in this accomplishment.

Of course no acknowledgements would be complete without giving thanks to my family. My deepest love goes to my father, my mother, my brothers, and my sisters who have always been supportive in every step. Especially for you dad, no words can express my thanks for the sacrifices you have made for me, my brothers, and my sisters.

Finally, but by no means least, my beloved wife Kholoud Al Saghir, I am incapable to express my thanks to you. You are my life partner in weal and woe, I will say thank you for everything and you know what is in my heart. To my beloved daughter Mira, your birth, nine days before my defense date, was and will always be the happiest moments of my life. Your birth overshadows all other happy moments, even obtaining my Ph.D. degree.

Table of contents

<i>List of Figures and tables.....</i>	<i>i</i>
General Introduction.....	1
Chapter I Background of Surface Enhanced Raman Scattering.....	7
I.1 Plasmonics in metallic nanoparticles	9
I.1.1 Surface plasmon oscillation in metal nanoparticles	9
I.1.2 Optical properties of isolated metal nanoparticles: the Mie theory	10
I.1.2.1 Introduction to Mie theory	10
I.1.2.2 Quasi-static response of a spherical metal nanoparticle to an electric field	10
I.1.2.3 Metal nanoparticles size effect on the optical response.....	11
I.1.2.4 Particle shape effect: deviation from sphericity.....	13
I.1.3 Non-isolated metallic nanoparticles: Maxwell Garnett Effective Medium theory.....	15
I.2 Raman scattering and surface enhanced Raman scattering	18
I.2.1 Raman scattering	18
I.2.1.1 Raman effect	18
I.2.1.2 Raman selection rules.....	19
I.2.1.3 Classical theory of light scattering	21
I.2.1.4 Raman intensities.....	22
I.2.2 Surface Enhanced Raman Scattering (SERS).....	24
I.2.2.1 SERS effect	24
I.2.2.2 Enhancement mechanisms	24
IV.2.2.2.a Electromagnetic enhancement (EM)	24
IV.2.2.2.b Chemical enhancement	26
I.3 SERS substrates: ultimate properties, progress and challenges.....	28
References.....	32

Chapter II Methods and experimental techniques.....	41
II.1 Fabrication of metal nanostructures	43
II.1.1 Thermal annealing of metallic films	43
II.1.1.1 Physical vapour deposition	43
II.1.1.2 PLASSYS MEB 400 evaporator.....	43
II.1.2 Electron Beam Lithography(EBL)	43
II.2 UV-Vis-NIR spectroscopy	47
II.3 X-Ray Photoelectron spectroscopy (XPS)	49
II.4 Scanning Electron Microscopy (SEM)	51
II.5 Transmission Electron Microscopy (SEM).....	52
II.6 Raman system.....	53
References.....	54
Chapter III Morphological and Optical studies on Au/Ag bimetallic nanoparticles	55
III.1 Introduction	57
III.1.1 Homogeneous and hybrid nanostructures.....	58
III.1.1.1 Silver and gold metals in the nanometric domain.....	59
III.1.1.2 Au/Ag bimetallic nanoparticles.....	60
III.1.1.2.a Au/Ag alloy bimetallic nanoparticles	60
III.1.1.2.b Au/Ag core/shell bimetallic nanoparticles.....	60
III.1.2 Metallic thin films	62
III.1.2.1 Growth and crystallization of metallic thin films.....	62
III.1.2.2 Annealing effects on metallic thin films.....	63
III.2 Double layer bimetallic nanoparticles	64
III.2.1 Fabrication of double layer Au/Ag bimetallic nanoparticles.....	64
III.2.2 X-ray photoelectron spectroscopy (XPS) measurements.....	65
III.2.3 Localized surface plasmon resonance tunability for the double layer bimetallic nanoparticles	67
III.2.4 Localized surface plasmon resonance effect on surface enhanced Raman scattering	70
III.3 Three layered Au/Ag bimetallic nanoparticles	74

III.3.1 Fabrication of triple layer Au/Ag bimetallic nanoparticles	74
III.3.2 XPS measurements	75
III.3.3 Localized surface plasmon resonance tunability for triple layered bimetallic nanoparticles	79
III.3.4 Localized surface plasmon resonance effect on surface enhanced Raman scattering	81
III.4 Double layered Au/Ag nanoparticles vs three layered nanoparticles in the surface enhanced Raman spectroscopy according to their enhancement ability.....	83
References.....	85

Chapter IV Improving the Sensitivity of Au/Ag Bimetallic Nanoparticles Substrates for SERS Application **91**

IV.1 Introduction.....	93
IV.2 Au-Ag/Au core/shell bimetallic nanoparticles.....	93
IV.2.1 Morphological study.....	93
IV.2.2 Silver presence effect in Au-Ag/Au core/shell nanoparticles on the optical and enhancing behavior	97
IV.2.3 Homogeneity, reproducibility and stability.....	99
IV.2.3.1 Homogeneity	99
IV.2.3.2 Reproducibility.....	101
IV.2.3.3 Stability	103
IV.2.4 Au-Ag/Au core/shell bimetallic nanoparticles: quantitative SERS sensors.	104
IV.3 Enhancing ability improvements of bimetallic nanoparticles.....	106
IV.3.1 Evaporated thickness variations.....	106
IV.3.2 Thermal annealing temperature effect (post-deposition treatment)	110
IV.3.3 SERS intensity improvements on Au-Ag/Au core/shell bimetallic nanoparticles by coupling with a gold mirror and a thin oxide spacer layer ...	115
IV.3.3.1 Surface plasmon polaritons at flat metal dielectric interface ..	115
IV.3.3.2 Nanoparticles on mirrors.....	121
IV.3.3.3 Au-Ag/Au core/shell nanoparticles coupling with Au film	122

IV.3.3.4 Results and discussion	123
References.....	128
<i>Chapter V Shape-controlled Ag/Au Monometallic and Bimetallic Nanoparticles.....</i>	131
V.1 Introduction.....	133
V.2 Monometallic and bimetallic nanocylinders arrays	133
V.3 Extinction measurements.....	137
V.3.1 The LSPR dependence on NCs size	137
V.3.2 Effect of interparticle spacing on the LSPR	139
V.3.3 Composition distributin and NCs nature effect on the LSPR	141
V.4 SERS measurements over monometallic and bimetallic NCs	144
References.....	152
<i>General Conclusion and Perspectives.....</i>	155
<i>Résumé de la Thèse en Français</i>	161

List of Figures and Tables

- Figure I.1.** Schematic view of the electron density oscillation inside a metal nanoparticle caused by incident electromagnetic radiation, so-called localized surface plasmons (LSP). The dipole is induced in the same direction as the incident polarization (blue arrow).....9
- Figure I.2.** Surface plasmon resonance of 9, 22, 48, and 99 nm spherical gold nanoparticles.....13
- Figure I.3.** Size-dependent surface plasmon absorption of gold nanorods. Optical absorption spectra of gold nanorods with mean aspect ratios of 2.7 (dot) and 3.3 (dash) are shown. The short-wavelength absorption band is due to the oscillation of the electrons perpendicular to the major axis of the nanorod while the long-wavelength band is caused by the oscillation along the major axis. The absorption bands are referred to as the transverse and longitudinal surface plasmon resonances respectively.....14
- Figure I.4.** Experimentally observed (a, c) and simulated (b, d) intensity distribution of the optical near-field above an ensemble of well-separated gold particles (a, b) and a chain of closely spaced gold nanoparticles (c, d).....16
- Figure I.5.** Schematic presentation of near-field coupling between nanoparticles for the two different polarizations.....17
- Figure I.6.** (a) Extinction spectra for square two-dimensional gratings of gold nanoparticles (height 14 nm, diameter 150 nm) with grating constant d situated on a glass substrate. (b) Plasmon decay time versus grating constant observed using a time-resolved measurement.....17
- Figure I.7.** Schematic representation of Raman and Rayleigh scattering: (a) an energy diagram of scattering process; (b) Raman and Rayleigh spectra.....19
- Figure I.8.** Schematic representation of symmetric C-o stretch and asymmetric C-o stretch, Infrared selection rules.....20

Figure I.9. Schematic representation of symmetric stretch in carbon dioxide for its equilibrium, extended, and compressed symmetric motions. Raman selection rules.....	20
Figure I.10. Simple schematic diagram for understanding the concept of electromagnetic SERS enhancement.....	25
Figure I.11. Schematic diagram of the four-step process of the photon-driven charge transfer model for a molecule adsorbed on an electrode.....	27
Figure I.12. (a) Transmission electron microscopy (TEM) image of Au nanospheres. (b) TEM image of Au nanorods and (c) Au nanoprisms. (d) SEM image of Au bipyramids. (e) TEM image of Au nanostars. (f) SEM image of Ag polyhedra.....	29
Figure II.1. The schematic of the electron beam lithography process: (1) Cover a thin layer of resist on the glass substrate by spin coating. (2) Deposit a conducting polymer layer. (3) Write the structure by electron beam. (4) Remove spacer 300Z polymer layer by water (5) Development with MIBK/IPA. (6) Evaporation of chromium adhesive layer. (7) Evaporate a metal (Au, Ag) layer. (8) Remove the remaining resist and the metal covering it ("lift off") leaving a small metal pattern behind. (9) After "lift-off": The metallic nano-patterns are on glass substrate.....	44
Figure II.2. Schematic illustration of an EBL system controlled by PC.....	46
Figure II.3. Diagram of electron beam exposure procedure.....	46
Figure II.4. Schematic illustration of the homemade UV-Vis-NIR spectroscopy.....	49
Figure II.5. Drawing of a scanning electron microscope.....	51
Figure III.1. Examples of hybrid nanoparticles: (a) dielectric@metal core-shell, (b) metal@dielectric core-shell, (c) metal@metal coreshell,(d) metal@metal@metal core-shell, (e) metallic nanotriangle with overcoat of second metal, (f) heterodimer composed of dielectric and metal parts, (g) heterodimer composed of two different metal parts,(h) semiconductor crystal with attached metal nanosphere, (i) crosssection through alloyed metal nanoparticle showing disordered nature of atomic occupancies, (j) cross section through nanoparticle composed of an intermetallic compound showing ordered atomic occupancy, (k) metal nanorods coated in a thick shell of	

dielectric, (l) dimer with incoherent crystalline interface between the parts, (m) dimer with coherent interface between the parts, (n) nanorods with overgrowth of another metal at the rod ends, (o) nanorods with a sparse overgrowth of a second metal, (p) segmented nanowires or nanowire composed of two or more elements, and (q) “nanotadpole”	59
Figure III.2. Plasmon bands of different silver–gold alloy nanodispersions at different Au mole fractions: (a) 0.1, (b) 0.3, (c) 0.5, (d) 0.7, and (e) 0.9.....	60
Figure III.3. UV/Vis absorption spectra of Ag/Au core/shell nanoparticles with varying gold shell thickness.....	61
Figure III.4. Basic modes of thin-film growth	63
Figure III.5. X-ray photoelectron spectra for Au 4f and Ag 3d regions of the (a) Ag-T-Au and the (b) Au-T-Ag substrates	66
Figure III.6. SEM images of the (a) Au-T-Ag and (b) Ag-T-Au nanoparticles ; size distribution correspondent to the SEM images for the (c) Au-T-Ag and (d) Ag-T-Au nanoparticles.....	68
Figure III.7. LSPR spectra for the double-layered nanoparticles : Ag-T-Ag, Ag-T-Au, Au-T-Ag, and Au-T-Au substrates	70
Figure III.8. Normal Raman spectra of 0.1 M BPE solution in ethanol-water 1:2 v/v and SERS spectrum of 10^{-5} M BPE solution measured over Au-T-Au substrate.....	71
Figure III.9. The SERS spectra of 10^{-5} M BPE solution over Ag-T-Ag, Ag-T-Au, Au-T-Ag, and Au-T-Au substrates.....	72
Figure III.10. The inversely proportional relation between SERS intensities of the benzene ring stretching (1605 cm^{-1}) and $\Delta\lambda$ (the difference between the Raman excitation wavelength, 632.8 nm, and the LSPR resonance) for Ag-T-Ag, Ag-T-Au, Au-T-Ag, and Au-T-Au substrates.....	73
Figure III.11. X-ray photoelectron spectra for Au 4f and Ag 3d regions of the (a) Au-T-Ag-T-Ag and the (b)Ag-T-Au-T-Ag substrates.....	76

Figure III.12. X-ray photoelectron spectra for Au 4f and Ag 3d regions of the (c) Ag-T-Au-T-Au and the (d)Au-T-Ag-T-Au substrates.....	77
Figure III.13. LSPR spectra for the three-layered bimetallic nanoparticles : Au-T-Ag-T-Ag, Ag-T-Au-T-Ag, Ag-T-Au-T-Au, and Au-T-Ag-T-Au substrates.....	80
Figure III.14. The SERS spectra of 10^{-5} M BPE solution over Au-T-Ag-T-Ag, Ag-T-Au-T-Ag, Ag-T-Au-T-Au, and Au-T-Ag-T-Au substrates.....	82
Figure III.15. The inversely proportional relation between SERS intensities of the benzene ring stretching (1605 cm^{-1}) and $\Delta\lambda$ (the absolute value for the difference between the Raman excitation wavelength, 632.8 nm, and the LSPR resonance) for Au-T-Ag-T-Ag, Ag-T-Au-T-Ag, Ag-T-Au-T-Au, and Au-T-Ag-T-Au substrates.....	82
Figure III.16. SEM image (a) and the size distribution (b) of the Au-T-Ag-Au nanoparticles.....	84
Figure IV.1. SEM images for the as-synthesized NPs (a) Au-T, (b) Au-T-Ag and (c) Au-T-Ag-T-Au NPs; the size distribution based on the SEM images for (d) Au-T, (e) Au-T-Ag, and (f) the Au-T-Ag-T-Au NPs.....	94
Figure IV.2. HRTEM image of a single Au-Ag/Au NP.....	96
Figure IV.3. Extinction spectra for Ag-T-Ag-T-Ag, Au-T-Ag-T-Au, and the Au-T-Au-T-Au NPs.....	97
Figure IV.4. SERS signals for BPE solution (10^{-5}M) over Ag-T-Ag-T-Ag, Au-T-Ag-T-Au, and the Au-T-Au-T-Au NPs.....	98
Figure IV.5. SEM image (a) and the SEM based size distribution (b) for the Au-T-Au-T-Au NPs.....	99
Figure IV.6. Extinction spectra for five different positions on the Au-Ag/Au core/shell NPs	100
Figure IV.7. SERS signals for ten BPE drops (10^{-5} M) placed on different spots over the Au-Ag/Au core/shell NPs substrate.....	100
Figure IV.8. Extinction spectra for five different Au-Ag/Au core/shell NPs substrates.....	102

Figure IV.9. SERS signals for BPE solution (10^{-5} M) over five different Au-Ag/Au core/shell NPs substrates.....	103
Figure IV.10. SERS response of BPE solution (10^{-5} M) over the Au-Ag/Au NPs (line a), Au-Ag NPs (line b) and Au NPs (line c) freshly prepared (A); after 1 year from preparation (B)	104
Figure IV.11. SERS spectra for BPE solutions of different concentrations ranging from 10^{-5} to 10^{-15} M over Au-Ag/Au core/shell NPs substrate.....	105
Figure IV.12. SERS intensity of the 1605 cm^{-1} band as a function of the BPE concentration obtained over Au-Ag/Au core/shell NPs substrate, the error bars represent the standard deviation of the average Raman intensity obtained for ten SERS measurements.....	106
Figure IV.13. SEM images of (a) 2nmAu-T-2nmAg-T-2nm Au, (b) 3nmAu-T-3nmAg-T-2nmAu and (c) 4nmAu-T-4nmAg-T-2nmAu NPs.	108
Figure IV.14. Extinction spectra for the 2nmAu-T-2nmAg-T-2nmAu, 3nmAu-T-3nmAg-T-2nmAu, and 4nmAu-T-4nmAg-T-2nmAu substrates.....	109
Figure IV.15. SERS signals of BPE solution (10^{-5} M) over the 2nmAu-T-2nmAg-T-2nmAu, 3nmAu-T-3nmAg-T-2nmAu and 4nmAu-T-4nmAg-T-2nmAu substrates.....	110
Figure IV.16. The inversely proportional relation between SERS intensities of the benzene ring stretching (1605 cm^{-1}) and $\Delta\lambda$ (the absolute value for the difference between the Raman excitation wavelength, 632.8 nm, and the LSPR resonance) for 2nmAu-T-2nmAg-T-2nmAu, 3nmAu-T-3nmAg-T-2nmAu, and 4nmAu-T-4nmAg-T-2nmAu substrates.....	110
Figure IV.17. Extinction spectra for the five Au-Ag/Au NPs different substrates with thermal annealing temperatures ranging from $150\text{ }^{\circ}\text{C}$ to $350\text{ }^{\circ}\text{C}$	112
Figure IV.18. SEM images of 2nmAu-T-2nmAg-T-2nm Au NPs thermally annealed at (a) $T=150\text{ }^{\circ}\text{C}$ and (b) $T=350\text{ }^{\circ}\text{C}$	113

Figure IV.19. SERS response for BPE solution (10^{-5} M) over the five Au-Ag/Au NPs different substrates with thermal annealing temperatures ranging from 150 °C to 350 °C.....	114
Figure IV.20. The proportional relation between SERS intensities of the benzene ring stretching (1605 cm^{-1}) and $\Delta\lambda$ (the absolute value for the difference between the Raman excitation wavelength, 632.8 nm, and the LSPR resonance) for five Au-Ag/Au NPs different substrates with thermal annealing temperatures ranging from 150 °C to 350 °C.....	114
Figure IV.21. The inversely proportional relation between SERS intensities of the benzene ring stretching (1605 cm^{-1}) and FWHM for the five Au-Ag/Au NPs different substrates with thermal annealing temperatures ranging from 150 °C to 350 °C.....	115
Figure IV.22. Scheme of surface plasmon polariton propagation.	117
Figure IV.23. (a) Composed character of SPPs at the interface between dielectric and metal.(b) Evanescent fields in the two half spaces.....	118
Figure IV.24. Dispersion relation for surface plasmon at the flat interface between a Drude metal and dielectric (air) with $\epsilon_d = 1$ and $\text{Im}_{\epsilon_{\text{em}}} = 0$	120
Figure IV.25. SEM image (a) and the SEM based size distribution (b) for the 30nm Au-10nm SiO ₂ -(Au-Ag/Au NPs) substrate.....	123
Figure IV.26. SERS signals for BPE solution (10^{-5} M) over the five 30 nm Au film-xSiO ₂ -Au-Ag/Au NPs substrates (x=10, 20, 30, 40 and 50 nm) and the reference Au-Ag/Au NPs substrate.....	123
Figure IV.27. SERS intensities of the benzene ring stretching (1605 cm^{-1}) versus the SiO ₂ thickness.....	125
Figure IV.28. The relative enhancement factor of the benzene ring stretching peak (1605 cm^{-1}) versus the SiO ₂ thickness.....	126
Figure V.1. Schematic presentation of the five different fabricated NCs types.....	134

Figure V.2. SEM images for the eight different Au NCs patterns where “d” represent the diameter size and “a” the lattice constant.....	136
Figure V.3. The extinction spectra of (A) Au, (B) Ag, (C) Au-Ag, (D) Ag-Au and(E) Au-Ag-Au NCs patterns having different diameter sizes 110, 145, 175 and 210 nm with 300 nm as lattice constant.	138
Figure V.4. The maxima wavelength λ_{LSPR} (F) and the FWHM (G) of the LSPR peak as a function of the diameter size for the Au, Ag, Au-Ag, Ag-Au and Au-Ag-Au NCs.	139
Figure V.5. The extinction spectra of Au NCs patterns of diameter sizes (A) 110, (B) 145, (C) 175 and (D) 210 nm with 300 and 450 nm lattice constant; (E) the red-shift value $ \lambda_{LSPR}^{a=300nm} - \lambda_{LSPR}^{a=450nm} $ as a function of the diameter size for the five different substrates Au, Ag, Au-Ag, Ag-Au and Au-Ag-Au NCs.....	141
Figure V.6. The LSPR spectra for Au, Ag, Au-Ag, Ag-Au and Au-Ag-Au arrays having lattice constants of 300 nm for the (A) 110, (B) 145, (C) 175 and (D) 210 nm diameter sizes.	142
Figure V.7. The LSPR spectra for Au, Ag, Au-Ag, Ag-Au and Au-Ag-Au arrays having lattice constants of 450 nm for the (A) 110, (B) 145, (C) 175 and (D) 210 nm diameter sizes.	143
Figure V.8. SERS spectra of BPE ($10^{-5}M$) over the four different diameter sizes arrays (110, 145, 175 and 210 nm) with 300nm lattice constant for the (A) Au, (B) Ag, (C) Au-Ag, (D) Ag-Au and (E) Au-Ag-Au NCS.	145
Figure V.9. Plot of the SERS intensity of the benzene ring stretching (1605 cm^{-1}) versus the diameter size of the NCs arrays (Au, Ag, Au-Ag, Ag-Au and Au-Ag-Au NCs)	146
Figure V.10. The inversely proportional relation between SERS intensities of the benzene ring stretching (1605 cm^{-1}) and $\Delta\lambda$ (the absolute value for the difference between the Raman excitation wavelength, 632.8 nm, and the LSPR resonance) as a function of diameter sizes for the (A) Au, (B) Ag and (C) Ag-Au NCs patterns....	148

Figure V.11. The SERS intensities of the benzene ring stretching (1605 cm^{-1}) and $\Delta\lambda$ (the absolute value for the difference between the Raman excitation wavelength, 632.8 nm, and the LSPR resonance) as a function of diameter sizes for the Au-Ag NCs patterns.....	149
Figure V.12. The relation between SERS intensities of the benzene ring stretching (1605 cm^{-1}) and (A) $\Delta\lambda$ (the absolute value for the difference between the Raman excitation wavelength, 632.8 nm, and the LSPR resonance); (B) $\Delta\lambda_{L-LSPR}$ (the absolute value of the difference between the $\lambda_L = (\lambda_{ext} + \lambda_R)/2$ and the LSPR resonance) as a function of diameter sizes for the Au-Ag-Au NCs patterns.....	151
Table III.1. Experimental details for fabricating the two layered bimetallic nanoparticles.....	65
Table III.2. The Ag 3d and Au 4f peaks positions, FWHM, area, and the percentage of Au and Ag in the Ag-T-Au and Au-T-Ag substrates.....	67
Table III.3. Experimental details for fabricating the three layered bimetallic nanoparticles.....	75
Table III.4. The Ag 3d and Au 4f peaks positions, FWHM, area, and the percentage of Au and Ag in the Au-T-Ag-T-Ag, Ag-T-Au-T-Ag, Ag-T-Au-T-Au, and Au-T-Ag-T-Au substrates.....	78
Table IV.1. Average diameter size and the surface coverage for the Au-T, Au-T-Ag, and Au-T-Ag-T-Au NPs.....	95
Table IV.2. HRTEM image analysis of a single Au-Ag/Au core/shell NP.....	96
Table IV.3. Statistical study on SERS signals for ten BPE drops (10^{-5} M) placed on different spots over the Au-Ag/Au core/shell NPs substrate.....	101
Table IV.4. Statistical study on extinction spectra for five different Au-Ag/Au core/shell NPs substrates.....	102

Table IV.5. Statistical study on SERS signals for BPE solution (10^{-5} M) over five different Au-Ag/Au core/shell NPs substrates.....	103
Table IV.6. Experimental details for fabricating the 2nmAu-T-2nmAg-T-2nmAu, 3nmAu-T-3nmAg-T-2nmAu and 4nmAu-T-4nmAg-T-2nmAu substrates.....	107
Table IV.7. Experimental details for fabricating the five Au-Ag/Au NPs different substrates with thermal annealing temperatures ranging from 150 °C to 350 °C....	111
Table IV.8. Experimental details for fabricating the five 30 nm Au film-xSiO ₂ -Au-Ag/Au NPs substrates (x=10, 20, 30, 40 and 50 nm) and the reference Au-Ag/Au NPs substrate.....	122
Table IV.9. The SERS intensity of the benzene ring stretching (1605 cm^{-1}) and the relative enhancement factor for different SiO ₂ thicknesses in the Au film-xSiO ₂ -(Au-Ag/Au NPs) substrates.....	126

General Introduction

Nanotechnology is the art and science of manipulating matter at the nanoscale, thus presenting potential opportunities to create new materials with interesting and unique properties. Due to the substantial changes in the physical chemistry of nanoscale material compared to their bulk or individual atoms, the research field concerning nanoparticles has grown abundantly in the last three decades.

The interest in studying the nanoparticles is owed to their distinct optical, electronic, catalytic and magnetic properties. In particular, the adoption of semiconductor nanostructures in electronic field results in decreasing the computer ship size, increasing the power density in lithium ion batteries and converting sunlight into electricity by solar cells. Moreover, quantum dots, iron oxide particles and other nanoparticles have proven to be highly effective agents for imaging, sensing and therapeutic intervention in the biomedical domain. Additionally, nanoscale materials proved their potential to improve the environment, both through direct application of those materials in order to detect, prevent and remove pollutants, as well as indirectly by using nanotechnology to design cleaner industrial process and create environmentally products.

The molecular finger printing capability of Raman spectroscopy makes it an attractive tool in sensing applications. However two drawbacks prevent Raman from being a prominent sensing technique; the low cross-section (less than 10^{-29} $\text{cm}^2.\text{sr}^{-1}$) where one in every $10^6\text{-}10^8$ incident photons is actually Raman scattered and the competing phenomena namely fluorescence which is 13 times of magnitude in cross-section higher than a typical Raman scattering. For the last three decades Raman techniques have been experiencing increasing application in many fields. The interest in Raman spectroscopy has re-emerged due to the high enhancement in Raman signals observed for molecules in a close proximity to special metallic surfaces. This enhancement in Raman signal, so called surface enhanced Raman scattering (SERS) opens a wide range of application of Raman technique for trace analysis, chemical analysis, environmental monitoring and biomedical treatments.

SERS originates from coupled optical responses of metallic nanostructures such as gold, silver or copper and of molecules located on their surfaces. Such kind of nanoparticles differs strongly from the respective bulk material in their optical response, exhibiting localized surface Plasmon resonance (LSPR). These collective electron charge oscillations upon excitation by light lead to a strong extinction band in the visible or near-infrared spectral

range. The spectral properties of this resonance behavior are highly dependent on the metal's size, shape and dielectric surrounding of the particles.

Driven by the research for reliable SERS substrates for sensing applications, the aim of our study is to engineer versatile SERS-active substrates which could meet the following requirements: large enhancement factor, good stability, reproducibility, homogeneity, easy fabrication and large scale production. Thermal annealing of thin metallic films nano-fabrication method fulfills the majority of the requirements. Concurrently, silver nanoparticles exhibit significantly larger electric field enhancement compared to gold nanoparticles, imposing silver as the ultimate material for SERS substrates characterized with high enhancement factors. However, silver nanoparticles fabricated by the previous mentioned strategy have LSPR lying in the spectral range 400-470 nm, thus limiting the high enhancements for Raman excitation wavelengths lying within or near this spectral domain, whereas the majority of Raman spectrometers have excitation wavelength of 633 nm. Moreover, silver nanoparticles are unstable due to sulfuration and surface oxidation. Contrarily, gold nanoparticles show high stability under physiological conditions and have LSPR position within the spectral range of 550 – 650 nm following the same fabrication strategy. Therefore combining the two metals in a bimetallic nanostructure appears to be a promising approach in order to sum the merits of both, silver optical enhancing properties and gold surface properties.

This manuscript is divided into five chapters.

In the first chapter, we describe the optical characteristics of noble nanostructures. A special accentuation is placed on the tunability of such properties by change in size, shape and inter-particle separation of the nanoparticles. A background of Raman scattering, SERS features, the widely reported enhancement mechanisms and the recent achievements in the SERS domain are narrated.

Throughout chapter II we introduce the experimental set-up used for nanoparticles fabrication (thermal annealing of thin metallic films and electron beam lithography). Additionally, we present the different characterization techniques employed along this study which aided in a complementary manner in the understanding of the nanoparticles composition, morphology and optical properties. These include X-Ray photoelectron spectroscopy (XPS), electron microscopy (scanning electron microscopy (SEM) and

transmission electron microscopy (TEM)), UV-Vis-Near IR spectroscopy, and Raman spectroscopy.

In chapter III, the fabrication of Au/Ag bimetallic nanoparticles SERS-active substrates (bi- and tri-layered) realized through thermal annealing of thin metallic films is presented. The chemical composition of the prepared SERS substrates is verified using XPS. Then the morphological and optical characterizations of the obtained nanoparticles are studied using SEM and UV-Vis-near IR spectroscopy. Moreover, the enhancement SERS ability of the double layered nanoparticles is compared to that of the triple layered Au/Ag nanoparticles.

In Chapter IV, first we study the homogeneity, reproducibility and stability of the Au/Ag bimetallic nanoparticles SERS substrate which exhibit the most intense Raman enhancement signal. Second we report the possibility of optimization on this substrate for a further efficient SERS enhancement. The evaporation thickness, thermal annealing temperature effects and the coupling of the Au/Ag bimetallic nanoparticles with the Au film are morphologically and optically studied in order to better understand their effect on the SERS activity.

In the last Chapter of this manuscript, a systematic study of the Au/Ag bimetallic features using Electron Beam Lithography (EBL) fabrication strategy is considered in order to improve our understanding of their plasmonic and SERS enhancing properties. First, the size and periodicity effects of bimetallic nanoparticles on the LSPR and SERS enhancement ability are studied in details. Secondly, different metallic types and compositions of nanocylinders having unified morphological parameters are fabricated in order to follow the effect of nanocylinders metallic nature and composition on the LSPR and SERS properties.

At the end of the manuscript, we present a general conclusion of this work in light of the results obtained. We also present our future outlooks and perspectives concerning this subject.

Chapter I

Background of Surface Enhanced Raman Scattering

I.1 Plasmonics in metallic nanoparticles

I.1.1 Surface plasmon oscillation in metal nanoparticles

Plasmons, mainly exist in noble metals, can be described as a collective oscillation of free electrons with respect to the fixed positively charged atom cores. Plasmons in bulk metals, called volume plasmons, cannot be excited by direct photoexcitation, that is, by coupling to light.¹ Surface plasmons (SP) are a distinct type of plasmons that propagate along an interface between a metal and dielectric medium. The SP can be excited by appropriate energy and momentum giving rise to surface plasmons resonance (SPR). In metallic nanoparticles, the electric field of an incident electromagnetic wave induces a polarization of the quasi-free conduction electrons, displacing them from the positive charges in the particle, resulting in a net charge difference at the nanoparticle boundaries, *Figure I.1*. The induced dipole in its turn emerges a linear restoring force to the system. Collective electron oscillations with a particular time period also exist in metallic nanoparticles and are referred as localized surface plasmon (LSP). If the energy of the electromagnetic radiation matches the LSP energy, localized surface plasmon resonance (LSPR) is induced and leads to a strong enhancement in the electromagnetic near-field in the vicinity of the particle surface. For noble metal nanoparticles such as gold, silver and copper, their LSPR peaks lie in the visible and near-infrared spectral range. The LSPR frequency is dependent on the particle shape, size, material dielectric function and surrounding dielectric medium.

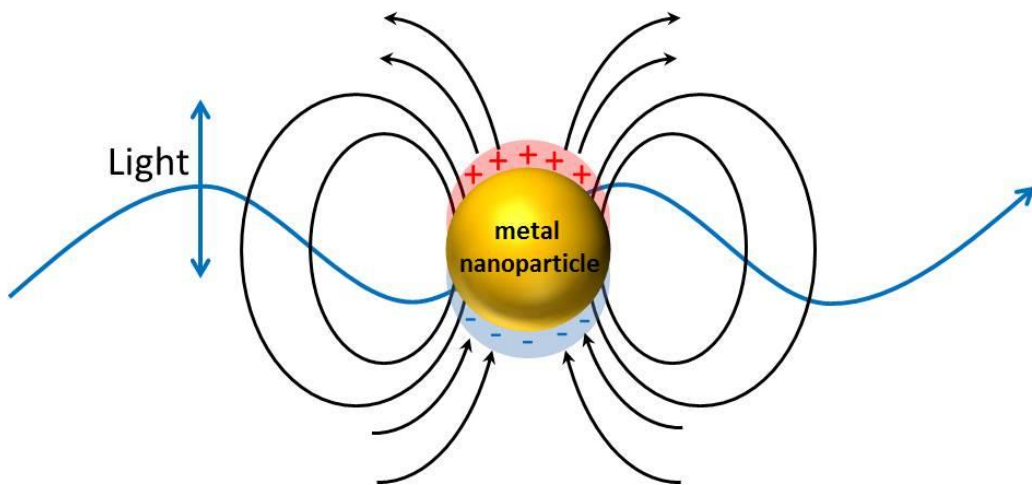


Figure I.1 Schematic view of the electron density oscillation inside a metal nanoparticle caused by incident electromagnetic radiation, so-called localized surface plasmons (LSP). The dipole is induced in the same direction as the incident polarization (blue arrow).

I.1.2 Optical properties of isolated metal nanoparticles: the Mie theory

I.1.2.1 Introduction to Mie theory

In 1908, Gustav Mie developed his well-known theory of light scattering by spherical particles.² It was the color variation of colloidal gold with particle size that motivated Mie to apply the general theory of light extinction to small particles. He applied Maxwell's equations with appropriate boundary conditions in spherical coordinates using multipole expansions of the incoming electric and magnetic fields. His theory offered an exact electrodynamic calculation of the interaction of light with spherical metallic nanoparticles.^{3,4} It provides an exact analytical solution in calculating the extinction (absorption and scattering) of spherical particles of arbitrary sizes.

In the case of metallic nanoparticles that are much smaller than the wavelength of light, the driven oscillating polarization of the dielectric sphere can be approximated as uniform throughout the sphere reducing the problem to that of the classic problem of a dielectric sphere in a uniform field. Thus, the electric field of light is anticipated as constant and the interaction between the particle and the field is managed as electrostatically rather than electromagnetically.

This is often referred to as quasi-static approximation, since the wavelength-dependent dielectric constant of the metallic nanoparticle, E, and of the surrounding medium Em, is used in a similar manner to those of other electrostatic theories.

I.1.2.2 Quasi-static response of a spherical metal nanoparticle to an electric field

The quasi-static approximation provides the explanation of the optical response of metallic nanoparticles to an electric field. This approximation considers the influence of the electric field of the incident electromagnetic field without taking the magnetic field effect into consideration. Under the influence of externally applied electric field (E_0) of the incident electromagnetic field, the electric field inside the particle (E_i) is given by:

$$E_i = E_0 \frac{3\epsilon_m}{\epsilon + 2\epsilon_m}$$

Where ϵ_m is the dielectric constant of the surrounding medium, and ϵ is the dielectric function of the metallic sphere.

The electromagnetic field interacting with particle can be obtained by solving Laplace's equation, $\nabla^2\varphi = 0$, where φ is the electric potential which is related to the electric field E_0 by $E_0 = -\nabla\varphi$.

The electric field of an incoming electromagnetic field induces a polarization of the free conduction electrons, and using the two boundary conditions; i) φ is continuous at the surface of the sphere and ii) the normal component of the electric displacement (D) is also continuous where $D=E_mE_0$, one can calculate the sphere polarization. The static polarizability of the sphere (α) is obtained by solving the Laplace's equation where it is given by:

$$\alpha = 4\pi\epsilon_0R^3 \frac{\epsilon - \epsilon_m}{\epsilon + 2\epsilon_m}$$

Where R is the radius of the metallic sphere.

Then, the induced dipole moment resulting from the polarization of the conduction free electron is given by $P = \epsilon_m\alpha E_0$.

The materials dielectric function affects the position and the shape of the plasmon resonance, i.e. it determines the width and height of these resonances. Moreover, the spectral properties of the plasmon peak are also related to the dielectric constant of the surrounding medium.⁵⁻⁷ The increasing in the dielectric function of the surrounding environment leads to a red shift in the plasmon resonance position.^{8,9} Thus, the optical material properties of the particles and the medium specify the plasmon resonance properties.

I.1.2.3 Metal nanoparticles size effect on the optical response

The particle size effect on the optical properties of isolated nanoparticles have been intensively investigated using Mie scattering theory.^{5,8-10} The Mie theory is a mathematical-physical explanation theory for the electromagnetic field scattering by spherical objects found in a homogeneous surrounding medium.¹¹⁻¹⁵ The Mie scattering solution starts with macroscopic Maxwell equations. The solution of the electrodynamic calculation with appropriate bounding conditions for a spherical particle emerges a series of multiple oscillations for the excitation cross-section of the particle.¹⁶⁻¹⁹ After expanding the involved fields into particle waves, extinction cross-section σ_{ext} and scattering cross-section σ_{scat} becomes as following.¹⁷

$$\sigma_{ext} = \frac{2\pi}{|K|^2} \sum_{L=1}^{\infty} (2L+1) R_e (a_L + b_L)$$

$$\sigma_{scat} = \frac{2\pi}{|K|^2} \sum_{L=1}^{\infty} (2L+1) (|a_L|^2 + |b_L|^2)$$

Where $\sigma_{abs} = \sigma_{ext} - \sigma_{scat}$,

$$a_L = \frac{m\psi_L(mx)\psi_L'(x) - \psi_L'(mx)\psi_L(x)}{m\psi_L(mx)\eta_L'(x) - \psi_L'(mx)\eta_L(x)}$$

$$b_L = \frac{\psi_L(mx)\psi_L'(x) - m\psi_L'(mx)\psi_L(x)}{\psi_L(mx)\eta_L'(x) - m\psi_L'(mx)\eta_L(x)}$$

and $m=n/n_m$, where n is the particle's complex refractive index and n_m is the real refractive index of the surrounding medium. K is the wave-vector and $x = |K|r$, with r the radius of the nanoparticle. ψ_L and η_L are the Riccati-Bessel cylindrical functions, where the prime indicates differentiation with respect to the argument in parenthesis. In these expansions, L is the summation index of the particle waves. $L=1$ refers to the dipole oscillation and so on.

For nanoparticles much smaller than the excitation wavelength (in the limit $2r < \lambda_{max}/10$), only the electric dipole term contributes to the extinction cross-section.¹⁶⁻²⁰ The Mie theory then is reduced, due to dipole approximation, to the following relation:

$$\sigma_{ext} = 9 \frac{\omega}{c} \varepsilon_m^{3/2} V \frac{\varepsilon_2(\omega)}{[\varepsilon_1(\omega) + 2\varepsilon_m(\omega)^2]}$$

Where V is the particle volume, c the velocity of light, ω the angular frequency of the exciting light, ε_m the dielectric function of the surrounding medium, which is assumed to be frequency independent, and $\varepsilon(\omega) = \varepsilon_1(\omega) + i\varepsilon_2(\omega)$ the dielectric function of the particle, which is complex and function of energy. The resonance condition is achieved when $\varepsilon_1(\omega) = -2\varepsilon_m(\omega)$ if ε_2 is small or weakly dependent on ω .¹⁷

Optical properties of small metallic nanoparticles and their absorption spectra have been widely investigated through the above equation.^{17,21} For relatively large nanoparticles, greater than 20 nm in the case of gold nanoparticles, the dipole approximation is no longer valid. The quadrupole mode and higher order modes become more important with the increasing of the particle size, because the light can no longer polarize the nanoparticles

homogeneously. This retardation effects of the electromagnetic field across the nanoparticles lead to huge shifts and broadening of the surface plasmon resonances. Furthermore, the higher order modes peak at lower energies causing red shifts of the plasmon band with increasing of the particle size,^{20–23} *Figure I.2*.

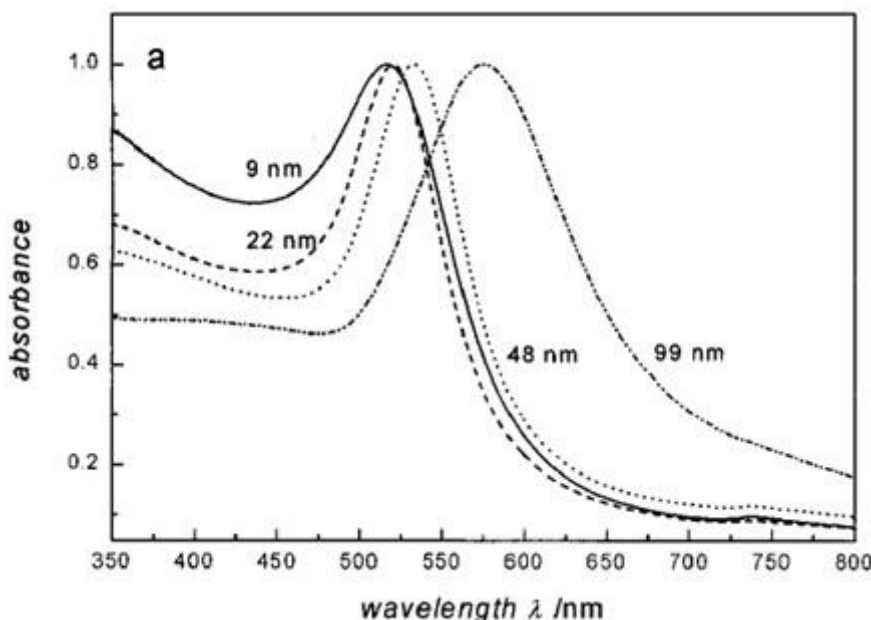


Figure I.2 Surface plasmon resonance of 9, 22, 48, and 99 nm spherical gold nanoparticles.²⁴

The size of the metallic nanoparticles also affects the band width of surface plasmon resonance, resulting in broadening of the SPR band for very small and relatively large nanoparticles.²⁵ The size confinement of the conduction electrons on the surface of the particle causes an increasing in band width with decreasing the nanoparticle size. As for relatively large nanoparticles, due to the radiation damping, the SPR band width broadens again with increasing the nanoparticle size.^{26–29}

I.1.2.4 Particle shape effect: deviation from sphericity

While particle size and the surrounding medium affects the surface plasmon oscillation, shape deviation from sphericity seems to be even more influential on the optical absorption spectrum of nanoparticles.^{30–39} The shape-dependent radiative properties of metallic particles can be treated by the Gans modification of Mie theory.⁴⁰ The theory

anticipates a split in the surface plasmon resonance when the particle deviates from spherical geometry.^{16,18,19} This split in the surface plasmon band is a consequence of the differences in resonances between the longitudinal and transverse dipole polarizability, where two plasmon resonances appear; a broadened red-shifted longitudinal plasmon resonance and a transverse plasmon resonance. The aspect ratio is the value of the long axis divided by the short one of a cylindrical or rod-shaped particle. As, this aspect ratio increases the energy separation between the resonance frequencies of the longitudinal and transversal plasmon bands increases.^{16,18,19}

Figure I.3 illustrates the size-dependent surface plasmon absorption of gold nanorods. The high-energy mode (transverse mode), shows a resonance band at around 520 nm, which co-insides spectrally with surface plasmon oscillation of the spherical particle.³⁷ The other absorption mode (longitudinal mode), shows a red-shifted resonance band with strong dependence on the aspect ratio, *Figure I.3*.²⁴

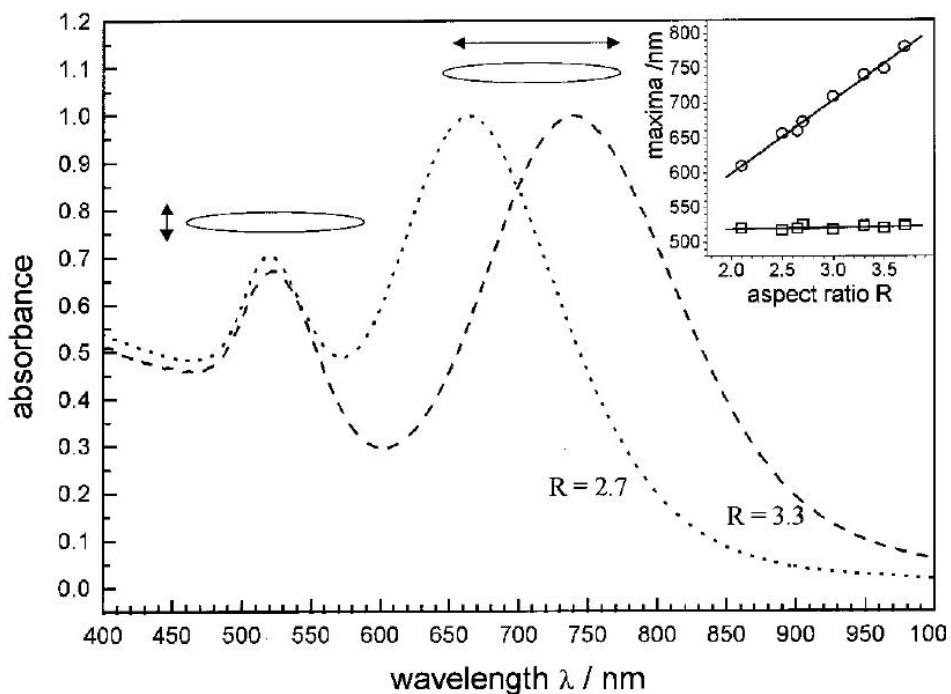


Figure I.3 Size-dependent surface plasmon absorption of gold nanorods. Optical absorption spectra of gold nanorods with mean aspect ratios of 2.7 (dot) and 3.3 (dash) are shown. The short-wavelength absorption band is due to the oscillation of the electrons perpendicular to the major axis of the nanorod while the long-wavelength band is caused by the oscillation along the major axis. The absorption bands are referred to as the transverse and longitudinal surface plasmon resonances respectively.²⁴

The optical plasmon spectrum of a collection of randomly oriented gold nanorods with aspect ratio R, can be modeled using Gans extension of the Mie theory. The extinction cross-section is given by:

$$\sigma_{ext} = \frac{\omega}{3c} \varepsilon_m^{3/2} V \sum_j \frac{(1/P_j^2)\varepsilon_2}{\{\varepsilon_1 + [(1 - P_j)/P_j]\varepsilon_m\}^2 + \varepsilon_2^2}$$

Where P_j are the depolarization factors along the three axes A, B and C of the nanorod with A>B=C defined as:

$$P_A = \frac{1 - e^2}{e^2} \left[\frac{1}{2e} \ln \left(\frac{1 + e}{1 - e} \right) - 1 \right]$$

$$P_B = P_C = \frac{1 - P_A}{2}$$

And the aspect-ratio R is included in e as follows:

$$e = \left[1 - \left(\frac{B}{A} \right)^2 \right]^{1/2} = \left(1 - \frac{1}{R^2} \right)^{1/2}$$

I.1.3 Non-isolated metallic nanoparticles: Maxwell Garnett Effective Medium theory

As mentioned before, the localized plasmon oscillation of isolated metallic nanoparticle can be shifted in frequency due to the alterations in particle size and shape. In particle ensembles, the surface plasmon resonance is drastically changed due to the electromagnetic interactions between the localized fields. If the interparticle distances are small in comparison to the particle dimension, the plasmon resonance is red-shifted and often a second absorption band at lower energy is observed.^{17,21,41,42} For small particles, under the quasistatic approximation, the particle ensemble can be treated as an ensemble of interacting dipoles.

Taking into consideration the magnitude of the interparticle spacing d , one can differentiate two regimes. For low particle separation, closely spaced ($d \ll \lambda$), near-field interactions with a distance dependency of d^{-3} dominates, and the system can be described as an array of near-field interacting dipole points. Consequently, strong field localization

emerges in the nano-sized gaps between the adjacent nanoparticles.⁴³ This strong field localization results from the response of the far-field scattering, supplanted by the near-field excitation of plasmon modes in neighbor particles. *Figure I.4* illustrates the experimentally observed (a,c) and simulated (b,d) distribution of electric field above well-separated gold nanoparticles and a chain of closely spaced gold nanoparticles.⁴⁴ These interparticle junctions, having highly localized fields, can serve as hot spots for field enhancement. Such hot spots have been claimed to provide extraordinary enhancements to the surface enhanced Raman scattering (SERS).

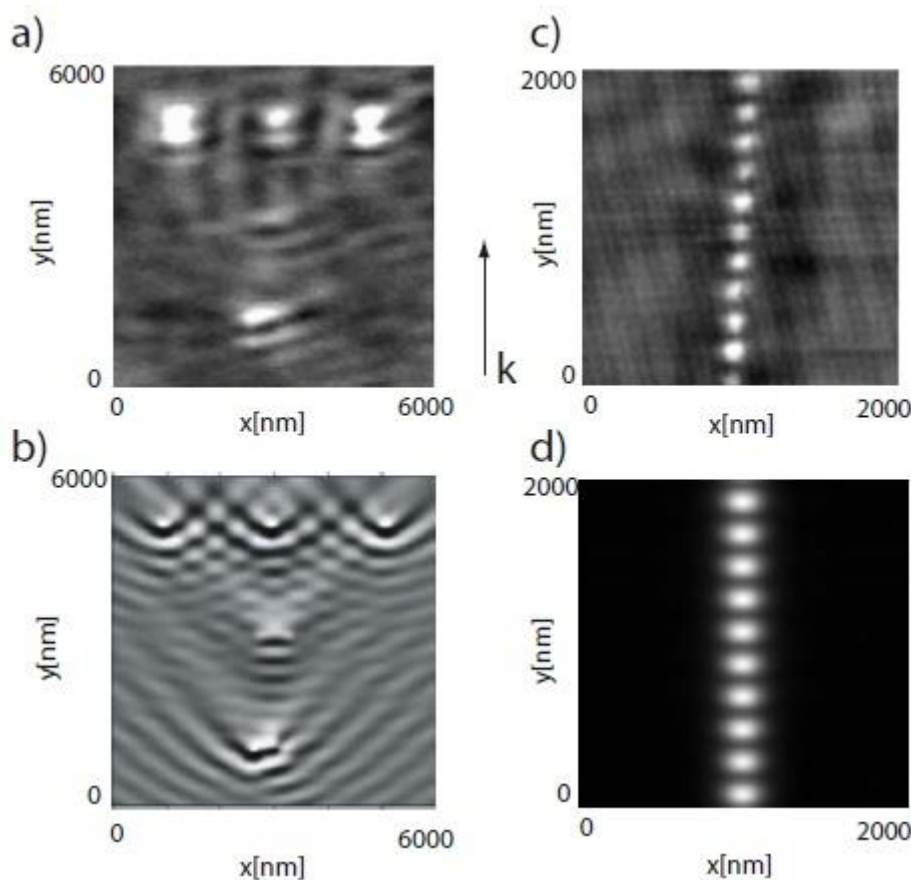


Figure I.4 Experimentally observed (a, c) and simulated (b, d) intensity distribution of the optical near-field above an ensemble of well-separated gold particles (a, b) and a chain of closely spaced gold nanoparticles (c, d).⁴⁴

The interparticular coupling between the nanoparticles will cause a shift in the plasmon resonance spectral position. As sketched in *Figure I.5*, the restoring force acting on the oscillating electrons of each particle in the array is either increased or decreased by the

charge distribution of neighboring particles. Generally, the interparticle coupling causes a blue shift of the transverse-plasmon resonance and red-shift for the longitudinal modes.

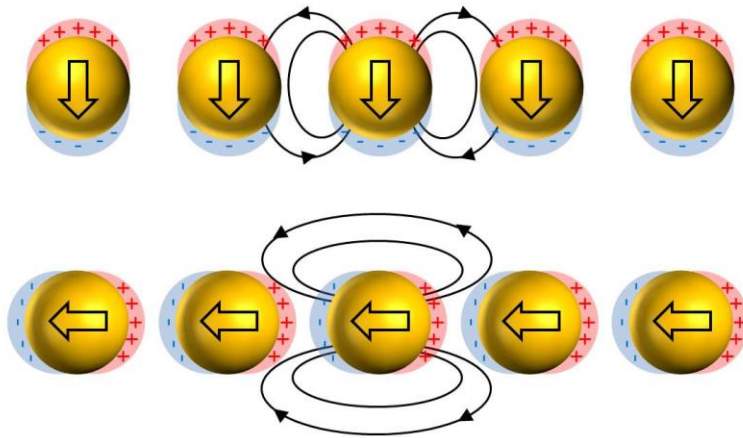


Figure I.5 Schematic presentation of near-field coupling between nanoparticles for the two different polarizations.

For the second regime, relatively large particle separations, far-field interactions occur, with d^{-1} dependence. Figure I.6 illustrates the effect of far-field coupling on the plasmon band shape for gold nanoparticles, in terms of resonance wavelength as well as spectral band-width.⁴⁵ The change in band-width is related to the strong dependence of the decay time T_2 on the grating constant which affect the amount of radiative damping as successive grating orders change in character from evanescent to radiative.

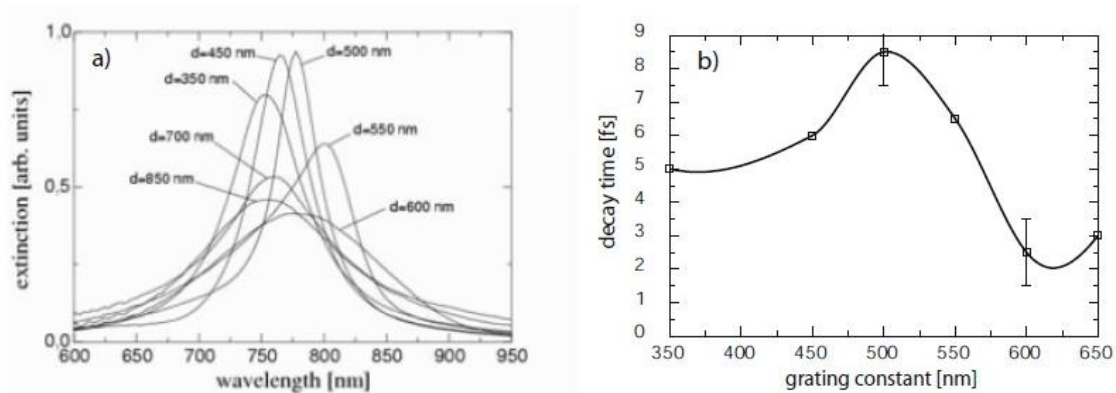


Figure I.6 (a) Extinction spectra for square two-dimensional gratings of gold nanoparticles (height 14 nm, diameter 150 nm) with grating constant d situated on a glass substrate. (b) Plasmon decay time versus grating constant observed using a time-resolved measurement.⁴⁵

I.2 Raman scattering and surface enhanced Raman scattering

I.2.1 Raman scattering

I.2.1.1 Raman Effect

Inelastic scattering of light phenomena was first experimentally observed in 1928 by Indian physicists C. V. Raman and K. S. Krishnan,⁴⁶ and by G. Landsberg and L. I. Mandelstam in crystals, after being first assumed by Smekal in 1923.⁴⁷ When molecules with internal vibration modes having frequency $\Delta\nu$ are illuminated by a monochromatic light with frequency ν_0 , a fraction of the incident light is scattered from the molecules being blue or red shifted from ν_0 to ν_0' . The difference in frequency between the incident light and the scattered light is equal to the molecular vibrational frequency. This phenomenon is known as Raman Effect.

$$\nu_0 - \nu_0' = \pm\Delta\nu$$

When photons interact with molecules, a transition between the energy states occurs. Most photons are elastically scattered; Rayleigh scattering, having the same frequency as the incident photons ν_0 . Nevertheless, a small portion of photons are scattered inelastically; Raman scattering, having frequency different from the frequency of the incident photons. The energy of the incident photon is $h\nu_0$ and the difference between the two energy states $V=0$ and $V=1$ is equal to $h\Delta\nu$.

Stokes scattering and anti-stokes scattering are the two types of Raman scattering. Stokes scattering are Raman scattering which occurs from the ground vibrational state ($V=0$) to a higher excited vibrational state ($V=1$) due to the energy absorption ($h\Delta\nu$) from the incident photon by the molecule. However, some molecules may exist in an excited state $V=1$, *Figure I.7(a)*. Anti-stokes scattering are Raman scattering which occurs from the excited states ($V=1$) to the ground state ($V=0$), in this case, $h\Delta\nu$ energy is transferred to the scattered photons.

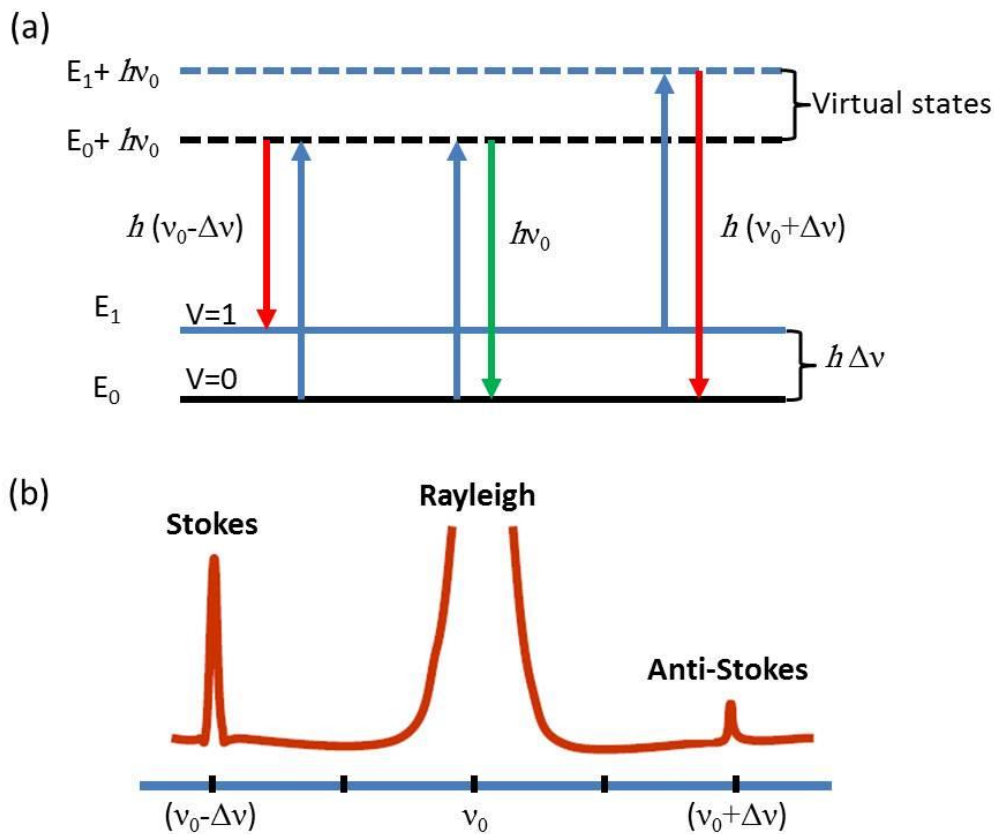


Figure I.7 Schematic representation of Raman and Rayleigh scattering: (a) energy diagram of scattering process; (b) Raman and Rayleigh spectra.

In Raman scattering only one vibrational quantum energy is gained or lost, this explains why stokes and anti-stokes lines are symmetrically shifted from the Rayleigh line, *Figure I.7(b)*. Since more molecules exist in the ground state than those in the excited state, the anti-stokes line is much less intense than the stokes line.⁴⁸

I.2.1.2 Raman selection rules

Raman spectroscopy and infrared IR spectroscopy are two main spectroscopies based on molecular vibrations. Not all molecular vibrations can be detected by Raman or IR spectroscopy, i.e., being Raman-active or IR-active modes, therefore selection rules were introduced. Molecular vibrations are IR-active when at least one of the components of the dipole moment vector has a non-zero gradient at the equilibrium position, e.g., the asymmetric stretch in carbon dioxide is IR-active since a net change occurs in the dipole

moment. Contrarily, the symmetric stretch is not IR-active since no change in the dipole moment occurs, *Figure I.8*.

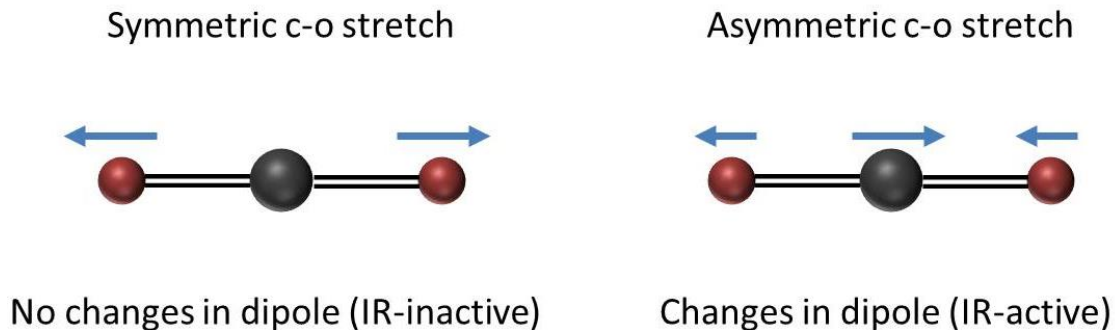


Figure I.8 Schematic representation of symmetric c-o stretch and asymmetric c-o stretch, Infrared selection rules.

For a vibration to be Raman active, the condition is that, for at least one component of the polarizability tensor must have a non-zero gradient at the equilibrium position, e.g., the symmetric stretch in carbon dioxide is Raman-active, since the polarizability of the molecule changes, *Figure I.9*. For the carbon dioxide molecule, the Raman intensities come from the symmetric vibrations where IR intensities arises from the asymmetric vibrations. The selection rules for IR-spectroscopy and Raman spectroscopy makes the two spectroscopies as complementary to each other.

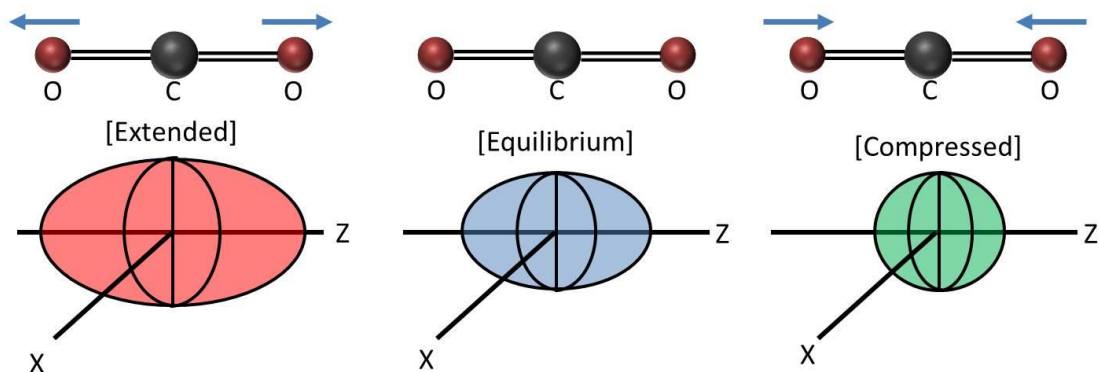


Figure I.9 Schematic representation of symmetric stretch in carbon dioxide for its equilibrium, extended, and compressed symmetric motions. Raman selection rules.

I.2.1.3 Classical theory of light scattering

Considering the relationship between the induced electric dipole moment of a molecule and the dynamic electric field characterized by E, the total time-dependent induced electric dipole moment vector of a molecule may be written as the sum of a series of time-dependent induced electric dipole moment vectors $\rho^{(1)}, \rho^{(2)}, \rho^{(3)} \dots$ as follows:⁴⁹

$$\rho = \rho^{(1)} + \rho^{(2)} + \rho^{(3)} + \dots$$

As $\rho^{(1)} \gg \rho^{(2)} \gg \rho^{(3)}$ this is a rapidly converging series.

The relationship between $\rho^{(1)}, \rho^{(2)}, \rho^{(3)}$ and E are given by:

$$\rho^{(1)} = \alpha \cdot E$$

$$\rho^{(2)} = \frac{1}{2} \beta : EE$$

$$\rho^{(3)} = \frac{1}{6} \gamma : EEE$$

From the equations $\rho^{(1)}$ is linear in E, $\rho^{(2)}$ is quadratic in E, and $\rho^{(3)}$ is cubic in E.

α is the polarizability tensor, β is the hyper polarizability tensor and γ is the second hyper polarizability tensor.

- For $\rho^{(1)}$, there can be three frequency components; the Rayleigh scattering component with frequency ν_0 , the two Raman scattering at frequencies $\nu_0 \pm \nu$. Therefore, equation $\rho^{(1)}$ can be suited to equations:

$$\begin{aligned}\rho_0(\nu_0) &= \alpha^{Ray} \cdot E_0(\nu_0) \\ \rho_0(\nu_0 \pm \nu) &= \alpha^{Ram} \cdot E_0(\nu_0)\end{aligned}$$

Where α^{Ray} is an equilibrium polar tensor and α^{Ram} is a polarizability tensor associated with ν .

- For $\rho^{(2)}$, there can be one hyper-Rayleigh scattering component with frequency $2\nu_0$ and the two hyper-Raman scattering with frequencies $2\nu_0 \pm \nu$. Hence, equation $\rho^{(2)} = \frac{1}{2} \beta : EE$ can be suited to equations:

$$\rho_0(2\nu_0) = \frac{1}{2}\beta^{HRay} : E_0(\nu_0) E_0(\nu_0)$$

$$\rho_0(2\nu_0 \pm \nu) = \frac{1}{2}\beta^{HRam} : E_0(\nu_0) E_0(\nu_0)$$

Where β^{HRay} is an equilibrium hyper-polarizability tensor and β^{HRam} is a hyper-polarizability tensor associated with ν .

- For $\rho^{(3)}$, the frequency component includes one second hyper-Rayleigh scattering with frequency $3\nu_0$, and two second hyper-Raman scattering with frequencies $(3\nu_0 \pm \nu)$. Thus equation $\rho^{(3)} = \frac{1}{6}\gamma : EEE$ can be suited to equations:

$$\rho_0(3\nu_0) = \frac{1}{6}\gamma^{HRam} : E_0(\nu_0) E_0(\nu_0) E_0(\nu_0)$$

$$\rho_0(3\nu_0 \pm \nu) = \frac{1}{6}\gamma^{HRam} : E_0(\nu_0) E_0(\nu_0) E_0(\nu_0)$$

Where γ^{HRay} is an equilibrium second hyper-polarizability tensor and γ^{HRam} is a second hyper-polarizability tensor associated with ν .

I.2.1.4 Raman intensities

The classical theory of light can be used to explain many of the important features of Raman band intensities.⁵⁰⁻⁵² Making use of the relationship,

$$\rho^{(1)} = \alpha \cdot E$$

Where E is the external electric field, $E = E_0 \cos 2\pi\nu_0 t$, (E_0 is the amplitude and t is the time)

$$\rho^{(1)} = \alpha E_0 \cos 2\pi\nu_0 t$$

The proportionality constant α is the polarizability of the molecule. The polarizability tensor is a function of the nuclear coordinates and hence of the molecular vibrational frequencies. Considering the scattering system to be one molecule vibrating at frequency ν without rotation, i.e., the molecule is space-fixed in its equilibrium configurations, but the nuclei may be displaced from the equilibrium positions, the normal coordinates of vibration can be

written as $Q = Q_0 \cos 2\pi\nu t$. Where Q_0 is the vibrational amplitude. Taking only one normal mode of vibration Q , α is a linear function of Q_0

$$\alpha = \alpha_0 + (\delta\alpha/\delta Q)_0 Q$$

Where α_0 is the polarizability at the equilibrium position, and $(\delta\alpha/\delta Q)_0$ is the change rate of α with respect to the normal coordinate Q .

From equation $\rho = \alpha \cdot E$ and $E = E_0 \cos 2\pi\nu_0 t$

$$\rho = \alpha E_0 \cos 2\pi\nu_0 t$$

where $\alpha = \alpha_0 + (\delta\alpha/\delta Q)_0 Q_0$, and $Q = Q_0 \cos 2\pi\nu t$

Therefore by substituting for α and Q in ρ , we obtain

$$\rho = \alpha_0 E_0 \cos 2\pi\nu_0 t + (\delta\alpha/\delta Q)_0 \times Q_0 E_0 \cos 2\pi\nu_0 t \cos 2\pi\nu t$$

And knowing that $\cos A \cos B = 1/2(\cos(A+B) + \cos(A-B))$

Therefore we obtain:

$$\rho = \alpha_0 E_0 \cos 2\pi\nu_0 t + 1/2 (\delta\alpha/\delta Q)_0 Q_0 E_0 \times \{\cos[2\pi(\nu_0 + \nu)t] + \cos[2\pi(\nu_0 - \nu)t]\}$$

The first term of this equation defines the Rayleigh scattering of frequency ν_0 and the second term accounts for Raman scattering of frequencies; $(\nu_0 - \nu)$ for stokes mode and $(\nu_0 + \nu)$ for anti-stokes mode.

Based on this equation, the significant condition for Rayleigh scattering is that α_0 should be non-zero. Since all molecules are polarizable, the equilibrium polarizability α_0 will always be non-zero. Hence all molecules display Rayleigh scattering.

The corresponding condition for Raman scattering is non-zero rate of change of α with respect to the change in a normal coordinate Q .

This equation also shows that Raman intensities increases with the molecular polarizability and with stronger electric field exerted on the molecules.

Two drawbacks prevent Raman from being a prominent analysis technique after its discovery. Raman scattering is a second-order process with a typical scattering cross sections less than $10^{-29} \text{ cm}^2 \cdot \text{Sr}^{-1}$ ⁵³. Another drawback derives from the competitive phenomenon, namely fluorescence, which is 13 times order of magnitude, in cross section, higher than a

typical Raman scattering. However, the usage of metallic nanoparticles to enhance Raman cross section of molecules, namely surface enhanced Raman scattering, upgrades the interest for Raman spectroscopy.

I.2.2 Surface Enhanced Raman Scattering (SERS)

I.2.2.1 SERS effect

Surface enhanced Raman scattering (SERS) was firstly observed by Fleischmann et al. (University of Southampton, UK) in 1974.^{54,55} After observing a huge enhancement of the Raman signal of pyridine molecules adsorbed on an electrochemically roughened silver electrode.⁵⁴ Formerly, the authors explained the enhancement of the Raman signal due to the increase in surface area of the roughened metal surface, which enables more pyridine molecules to adsorb on the surface. Latter studies revealed that the large enhancement could not be related to the increase in surface area only, since the estimated increase in Raman intensity from the roughened surface would be less than a factor of 10, whereas the obtained enhancement was of an order of 10^6 . Strong Raman signal must be related to the enhancement of Raman scattering efficiency. Following these studies, surface enhanced Raman spectroscopy has emerged.^{56,57}

I.2.2.2 Enhancement mechanisms

In spite of several SERS mechanisms that have been suggested to clarify the previously-mentioned SERS aspect, the two most widely accepted mechanisms are electromagnetic enhancement (EE) and chemical enhancement (CE).^{50,58–61} The EE is derived from the excitation of LSP maintained by the metallic nanoparticles⁶². However, the chemical enhancement effect is due to a charge-transfer between the metal surface and the Raman molecule.^{63,64}

I.2.2.2.a Electromagnetic Enhancement

SERS predominantly emanate from an electromagnetic enhancement mechanism (EE) associated to the excitation of localized surface plasmon (LSP) of metallic nanoparticles (NPs). Consequently, the electromagnetic mechanism has been the central approach for calculating the Raman enhancement and it has been intensely reviewed in the literature.^{50,58–61,65} Various electromagnetic models for explaining the SERS phenomenon have been

summarized and detailed by Moskovits⁶⁰ and Vo-dinh⁵⁰ in their reviews, of which the models for flat or rough surfaces, metallic non-spheres, concentric spheres, spheroidal particles, prolate spheroids and ellipsoids have been described.

The electromagnetic effect consists of two complementary processes where both depend on the surface plasmon field sustained by the metallic nanoparticles.^{66,67} First, the enhancement of the incident electromagnetic field caused by the superposition of the localized plasmon field and the incident laser light. Second, the enhancement of the Raman photons emitted by the molecule in the same aspect. Since the localized plasmon field has very short range, molecules adsorbed in the first surface layer display the largest Raman enhancement factors. However, some recent studies indicate relatively large-range interactions, around 30 nm.⁶⁸ To illustrate the electromagnetic enhancement mechanism, we assume a Raman-molecule in the vicinity of nanoparticle, *Figure I.10*. The metallic nanoparticle is represented as a small sphere with a complex dielectric constant $\epsilon(V)$ in a surrounding medium of dielectric constant ϵ_0 . The diameter of the sphere ($2r$) is small in comparison to the wavelength of light to sustain the Rayleigh limit.⁵⁸

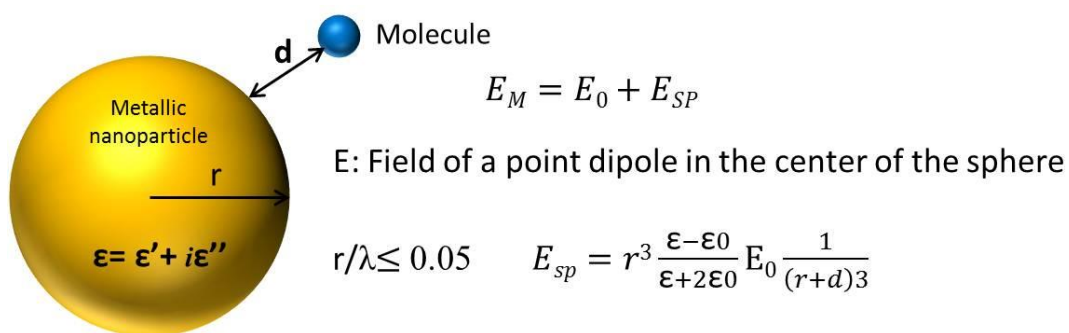


Figure I.10 Simple schematic diagram for understanding the concept of electromagnetic SERS enhancement.

A molecule separated by a distance d from the sphere, is subjected to two electromagnetic fields. The first is the incoming field E_0 and the second is the induced dipole E_{sp} from the metal sphere. The two fields are combined in one field E_M .

The field enhancement factor $A(v)$ is the ratio of the field at the molecule position and the incident field.

$$A(v) = \frac{E_M(v)}{E_0(v)} \sim \frac{\epsilon(v) - \epsilon_0}{\epsilon(v) + 2\epsilon_0} \left(\frac{v}{v + d} \right)^3$$

$A(v)$ increases strongly when the real part of $\varepsilon(v)$ tends to $(-2\varepsilon_0)$. Furthermore, small imaginary part of the dielectric constant leads to strong electromagnetic enhancement. This conduction is realized in the resonant excitation of surface plasmons of a metal sphere.

In addition to the laser field enhancement, the scattered stokes or anti-stokes fields will be enhanced in the same manner, i.e., in resonance with the surface plasmons of the metal sphere. Considering the enhancements for the laser and for the stokes field, the electromagnetic enhancement factor for the stokes signal power $G_{em}(\gamma_s)$ is written as:

$$G_{em}(\gamma_s) = |A(\nu_L)|^2 |A(\nu_s)|^2 \sim \left| \frac{\varepsilon(\nu_L) - \varepsilon_0}{\varepsilon(\nu_L) + 2\varepsilon_0} \right|^2 \left| \frac{\varepsilon(\nu_s) - \varepsilon_0}{\varepsilon(\nu_s) + 2\varepsilon_0} \right|^2 \left(\frac{\nu}{\nu + d} \right)^{12}$$

Where $A(\nu_L)$ and $A(\nu_s)$ are the enhancement factors for laser field and stokes field, respectively. This equation shows that the enhancement factor is in order of fourth power of the local field of the metallic nanosphere. It also shows that the Raman enhancement strongly decreases with the growing distance from the surface, even though the molecules do not require direct contact with the surface.

I.2.2.2.b Chemical enhancement

Several experimental studies reveal a debate about a second enhancement mechanism which takes place independently of the electromagnetic mechanism. This second mechanism named chemical enhancement (CE) or charge transfer (CT), originates from the charge-transfer between the metal surface and the Raman molecule.^{63,64} Unlike electromagnetic enhancement, chemical enhancement is still not fully understood.^{61,69} The early clue for the existence of chemical enhancements was the different SERS intensities of the molecules CO and N₂ operated at the same experimental conditions.⁷⁰ The difference in the SERS intensities was by a factor of 200, this result could not be explained by only considering the electromagnetic enhancement for two reasons. Firstly, the polarizabilities of both molecules are nearly identical and even the most substantial differences in orientation upon adsorption could not display such a large difference. Secondly, the dependence of the enhancement factor on the electrode potential emerges from the potential-dependent electrochemical experiments.^{69,71}

Resonance Raman mechanism can resolve this chemical effect. Chemical enhancement theory considers two discrete hypotheses; either the electronic states of the

adsorbate are shifted and broadened by their interaction with the surface or new electronic states, which emerge from chemisorption, serve as resonant intermediate states in Raman scattering. Since the large energy gap between the highest occupied molecular orbitals (HOMO) and the lowest un-occupied molecular orbitals (LUMO), the resonance Raman process rarely occurs in spite of the perturbed redistribution of the energy levels for a molecule adsorbed on a rough surface. However, the resonance Raman scattering might occur due to a charge-transfer mechanism because of the electronic coupling between the molecule and the metal,^{72–74} *Figure I.11*. The wavefunctions of the electron in the metal and adsorbate overlap, resulting in electrons tunneling between the metal and the molecule. The charge –transfer process can be identified by four steps:^{50,69,71} i) an electron-hole pair of the metal is created by the incident photon with energy $h\nu_0$, and the electron is excited as a hot-electron; ii) the hot-electron tunnels into the accessible vacant levels (LUMO of the adsorbate) generating a charge-transfer excited state; iii) the electron from the excited level of the adsorbate is transferred back to the metal; iv) the electron will recombine with the hole generated in step 1, which initiates the emission of a Raman-shifted photon with energy $h\nu$.

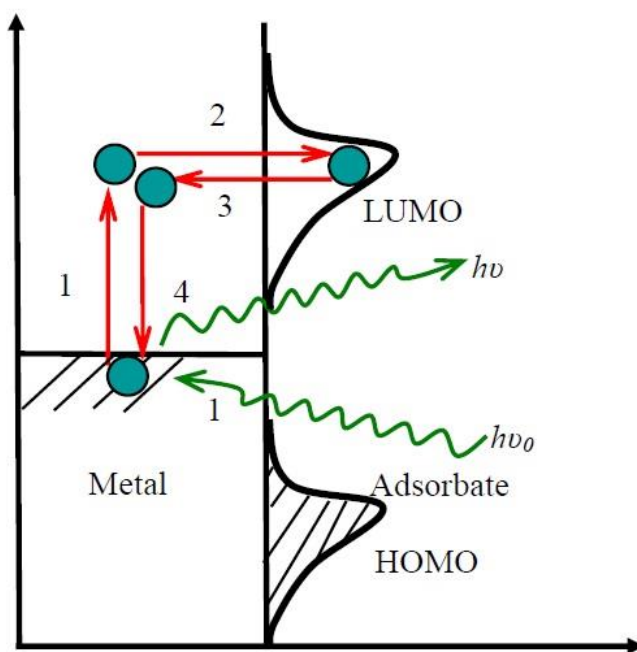


Figure I.11 Schematic diagram of the four-step process of the photon-driven charge transfer model for a molecule adsorbed on an electrode.

Generally, chemical mechanism contributes to Raman enhancement on the molecular level. This effect is influenced by the adsorption surface, the bonding geometry and the

energy level of the adsorbed molecules. Regardless of being a specific mechanism due to its chemical specificity, CE mechanism can provide useful information on chemisorptive interactions between metals and adsorbates.

I.3 SERS substrates: ultimate properties, progress and challenges

The most prominent research topic in the SERS field is the development of powerful plasmonic substrates for SERS applications. Historically, the first SERS effect was obtained over a roughened silver electrode.⁵⁴ Overtime, different concepts of bottom-up and top-down approaches have been developed and improved for better SERS substrate fabrication.

Comparison of various SERS substrates is challenging, because rigorous characterization of substrates is frequently overlooked for reasons of complexity. This hinders the evaluation of analytical parameters such as sensitivity and reproducibility. In order to classify a material as a reliable, high enhancing SERS substrate, several factors need to be taken into consideration:

- The fabricated SERS substrates must be reproducible from sample to sample and from batch to batch.
- The SERS enhancement signal has to be homogenous across the substrate.
- The substrate needs to have long-term stability.
- The metallic surface should be insensitive to environmental effects such as oxygen, humidity and light.
- The substrate has to show large enhancement ability in Raman signals.
- The biocompatibility of the metallic surface plays an important role in the application of SERS in biomedical sensing.
- SERS spectra should be collected for non-resonant molecules to exclude the resonance Raman effect which can increase the overall enhancement by 10^3 - 10^6 .⁷⁵
- The SERS substrates should be cost-efficient and provide large enhancement factors combined with an easy preparation protocol.

The most popular method for SERS substrate fabrication is colloidal nanofabrication. Colloidal nanoparticles have been employed as SERS substrates for several decades.⁷⁶ *Figure I.12* shows representative electron microscopy images of diverse colloidal nanoparticles types. The nanoparticle size, shape and material play a key role in the resulting plasmonic resonance characteristics, allowing plasmonic resonance tunability over wide spectrum.⁷⁷ Accordingly, different colloidal nanofabrication methods have been recently

adopted for controlling the nanoparticles morphology. One of the most popular methods for controlling nanoparticles morphology originates from the polyol synthesis of silver nanocubes by Sun and Xia.⁷⁸ Etchants and surfactants can be introduced into the reaction which aid in altering the growth speed of different crystalline faces. During the last few years, different additives ions have been used in preparing nanoparticles with diverse shapes, including tetrahedral,⁷⁹ bipyramids,^{80,81} decahedra,⁸² prisms,^{83,84} nanorods, nanowires,^{85,86} nanoshells,⁸⁷ stars,^{88,89} laces⁹⁰ and other polyhedral shapes.^{81,91–93}

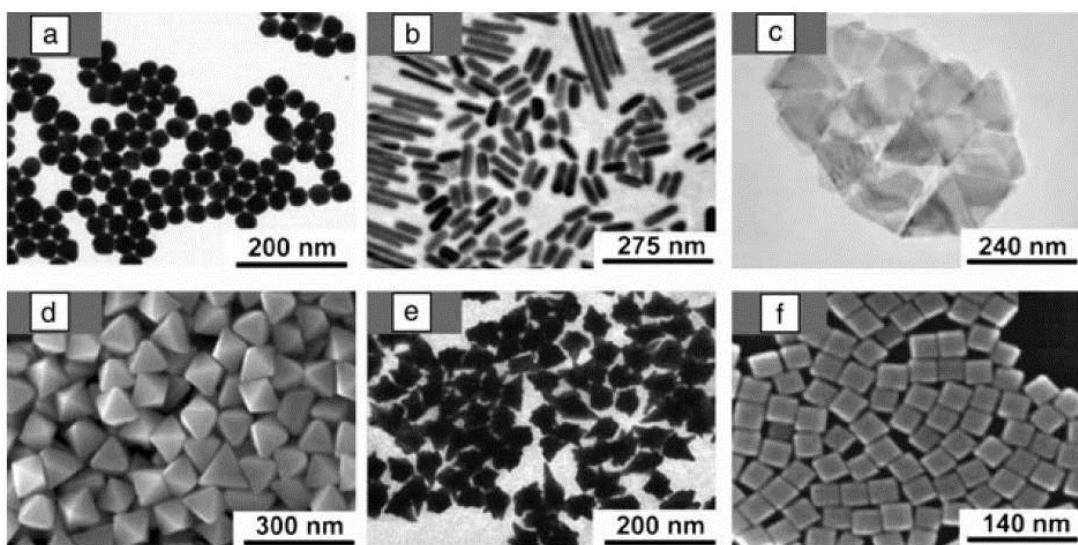


Figure 1.12 (a) Transmission electron microscopy (TEM) image of Au nanospheres.⁹⁴ (b) TEM image of Au nanorods and (c) Au nanoprisms.⁸⁴ (d) SEM image of Au bipyramids.⁹² (e) TEM image of Au nanostars.⁸⁸ (f) SEM image of Ag polyhedra.⁹⁵

In SERS domain, the enhancement is much greater in closely packed nanoparticles than in individual nanoparticles. This increase in enhancement results from the presence of hotspots at the intersection or close interaction of two or more nanoparticles. For colloidal solutions, nanoparticles aggregation can be induced by the addition of aggregating agents such as chlorides, bromides, nitrates and other ionic species to alter the zeta potential. However, the pure aggregated colloids in some cases show specific Raman modes which can be assigned to citrate or nitrate. Thus, the detection of molecules of interest might be prevented by the strong SERS contribution of the aggregated metal colloids itself.⁹⁶ Additionally, the colloidal nanoparticles lose their surface plasmons resonance tunability after being aggregated.

Lithographic-based techniques have also attracted considerable research efforts. The Electron Beam Lithography (EBL) is an ideal method for fabricating highly uniform and reproducible SERS substrates. This technique has the advantage of allowing accurate control over the size, shape and spacing of nanoparticles, making it one of the best fabrication methods for optical characterization studies. Disadvantages related to this technique include high cost, low throughput, complexity and low areal density. Recently, diverse nanostructures have been achieved by changing the EBL fabrication conditions such as gold nanorhomb arrays,^{97,98} rectangle structures,^{99,100} elliptical disks,^{101,102} nanohole arrays,¹⁰⁰ metal nanocrescents,¹⁰³ nanowells,¹⁰⁴ fisher patterns,^{105,106} nanotriangle arrays,¹⁰⁷ and moreover aperiodic arrays.^{108,109} Van Duyne and coworkers have pioneered lithography-based technique, namely nanosphere lithography (NSL), which is more efficient and less expensive than EBL.^{110–113} NSL involves evaporating Ag or Au onto performed arrays of nanopore masks by colloidal particles, followed by the mask removal, leaving the metal deposited in the interstices to form a regular nanoparticles array. Although not lithography but similar technique, so called film on nanosphere (FON) coating, is based on deposition of thick metallic layer over the top of periodically arranged spheres.^{111,114} the key-process in NSL and FON techniques is the micro-sphere arrangement in a monolayer. While there are several methods available for controlling these arrangements, gaps in the monolayer or multi-layer arrangements can still occur. Additionally, large areas formation of these surfaces is difficult, limiting the potential for these techniques for large scale manufacturing.

Optical fiber SERS sensors have been also extensively studied in recent years. Here, the excitation laser couples into an optical fiber and is guided towards the sample of interest. The fiber facet is modified with metallic nanostructure, where the enhanced Raman scattered light couples back into the fiber and is guided to the spectrometer. Various configurations of fibers such as flat,¹¹⁵ angled,¹¹⁶ tapered, side-polished^{117,118} and photonic crystal fibers^{119,120} have been employed as optical fiber-based SERS sensors. However, the fiber material contributes as background to the recorded spectrum, which is an issue in fiber Raman applications.

More recently, SERS research has greatly increased for diverse applications, branching out into explosive detection,^{121–123} food safety,^{124–126} and live cell imaging and bio-analysis.^{127,128} Advances in portable spectrometers, diode laser, and even collection optics¹²⁹ are making portable on-site Raman detection analysis a reality. Accordingly, searching for accompanying reliable SERS substrates for on-site Raman detection is mandatory for ultra-

sensitive detection in the mentioned fields these substrates should, besides combining the majority of the discussed properties, characterize with small foot print, simple operation, robusticity and durability. From here lies our major concern and objective of this thesis which is fabrication of satisfying SERS substrates.

References

1. Xia, C., Yin, C. & Kresin, V. V. Photoabsorption by Volume Plasmons in Metal Nanoclusters. *Phys. Rev. Lett.* **102**, 156802 (2009).
2. Mie, G. Der physik. 1. *Ann. Phys.* **25**, 337 (1908).
3. Paule Pileni, M. Optical properties of nanosized particles dispersed in colloidal solutions or arranged in 2D or 3D superlattices. *New J. Chem.* **22**, 693–702 (1998).
4. Bonacic-Koutecky, V., Fantucci, P. & Koutecky, J. Quantum chemistry of small clusters of elements of groups Ia, Ib, and IIA: fundamental concepts, predictions, and interpretation of experiments. *Chem. Rev.* **91**, 1035–1108 (1991).
5. Chumanov, G., Sokolov, K., Gregory, B. W. & Cotton, T. M. Colloidal metal films as a substrate for surface-enhanced spectroscopy. *J. Phys. Chem.* **99**, 9466–9471 (1995).
6. Persson, B. N. J. Polarizability of small spherical metal particles: influence of the matrix environment. *Surf. Sci.* **281**, 153–162 (1993).
7. Hövel, H., Fritz, S., Hilger, A., Kreibig, U. & Vollmer, M. Width of cluster plasmon resonances: Bulk dielectric functions and chemical interface damping. *Phys. Rev. B* **48**, 18178–18188 (1993).
8. Jensen, T. R. *et al.* Nanosphere Lithography: Effect of the External Dielectric Medium on the Surface Plasmon Resonance Spectrum of a Periodic Array of Silver Nanoparticles. *J. Phys. Chem. B* **103**, 9846–9853 (1999).
9. Mochizuki, S and Ruppin, R. Optical spectra of free silver clusters and microcrystal produced by the gas evaporation technique: transition from atom to microcrystal. *J. Phys. Condens. Matter* **5**, 135 (1993).
10. Fletcher, P. D. I., Howe, A. M. & Robinson, B. H. The kinetics of solubilisate exchange between water droplets of a water-in-oil microemulsion. *J. Chem. Soc. Faraday Trans. 1 Phys. Chem. Condens. Phases* **83**, 985–1006 (1987).
11. Novotny, L. & Hecht, B. *Principles of Nano-Optics*; (2006).
12. I. Roldughin, V. Quantum-size colloid metal systems. *Russ. Chem. Rev.* **69**, 821–843 (2000).
13. Wilcoxon, J. P., Williamson, R. L. & Baughman, R. Optical properties of gold colloids formed in inverse micelles. *J. Chem. Phys.* **98**, (1993).
14. Schmitt, J., Mächtle, P., Eck, D., Möhwald, H. & Helm, C. A. Preparation and Optical Properties of Colloidal Gold Monolayers. *Langmuir* **15**, 3256–3266 (1999).
15. Lin, J., Zhou, W. & O'Connor, C. J. Formation of ordered arrays of gold nanoparticles from CTAB reverse micelles. *Mater. Lett.* **49**, 282–286 (2001).

16. Papavassiliou, G. C. Optical properties of small inorganic and organic metal particles. *Prog. Solid State Chem.* **12**, 185–271 (1979).
17. Kreibig, U. & Vollmer, M. *Optical Properties of Metal Clusters*. (1995).
18. Kerker, M. The Scattering of Light and Other Electromagnetic Radiation (New York: Academic Press). (1969).
19. Bohren, C. F. & Huffman, D. R. *Absorption and Scattering of Light by Small Particles*. Wiley (1998).
20. Mulvaney, P. Surface Plasmon Spectroscopy of Nanosized Metal Particles. *Langmuir* **12**, 788–800 (1996).
21. Kreibig, U. & Genzel, L. Optical absorption of small metallic particles. *Surf. Sci.* **156**, Part , 678–700 (1985).
22. Kreibig, U. & Fragstein, C. V. No Title. *Z. Phys.* **224**, 307 (1969).
23. Devaty, R. P. & Sievers, A. J. Possibility of observing quantum size effects in the electromagnetic absorption spectrum of small metal particles. *Phys. Rev. B* **32**, 1951–1954 (1985).
24. Link, S. & El-Sayed, M. A. Shape and size dependence of radiative, non-radiative and photothermal properties of gold nanocrystals. *Int. Rev. Phys. Chem.* **19**, 409–453 (2000).
25. Pinchuk, A. & Kreibig, U. Interface decay channel of particle surface plasmon resonance. *New J. Phys.* **5**, 151 (2003).
26. Yeshchenko, O. A. et al. Size-dependent surface-plasmon-enhanced photoluminescence from silver nanoparticles embedded in silica. *Phys. Rev. B* **79**, 235438 (2009).
27. Dahmen, C., Schmidt, B. & von Plessen, G. Radiation Damping in Metal Nanoparticle Pairs. *Nano Lett.* **7**, 318–322 (2007).
28. Grechko, L. G., Blank, A. Y., Panchenko, O. A. & Pinchuk, A. A. Resonant Absorption of Electromagnetic Radiation in Matrix Disperse Systems with Metallic Inclusions. *Telecommun. Radio Eng.* **51**, 160 (1997).
29. Novo, C. et al. Contributions from radiation damping and surface scattering to the linewidth of the longitudinal plasmon band of gold nanorods: a single particle study. *Phys. Chem. Chem. Phys.* **8**, 3540–3546 (2006).
30. Perenboom, J. A. A. J., Wyder, P. & Meier, F. Electronic properties of small metallic particles. *Phys. Rep.* **78**, 173–292 (1981).
31. Nozik, A. J. & Memming, R. Physical Chemistry of Semiconductor–Liquid Interfaces. *J. Phys. Chem.* **100**, 13061–13078 (1996).

32. Schaaff, T. G., Knight, G., Shafiqullin, M. N., Borkman, R. F. & Whetten, R. L. Isolation and Selected Properties of a 10.4 kDa Gold:Glutathione Cluster Compound. *J. Phys. Chem. B* **102**, 10643–10646 (1998).
33. Van der Zande, B. M. I., Böhmer, M. R., Fokkink, L. G. J. & Schönenberger, C. Aqueous Gold Sols of Rod-Shaped Particles. *J. Phys. Chem. B* **101**, 852–854 (1997).
34. Van der Zande, B. M. I., Koper, G. J. M. & Lekkerkerker, H. N. W. Alignment of Rod-Shaped Gold Particles by Electric Fields. *J. Phys. Chem. B* **103**, 5754–5760 (1999).
35. Van der Zande, B. M. I., Pagès, L., Hikmet, R. A. M. & van Blaaderen, A. Optical Properties of Aligned Rod-Shaped Gold Particles Dispersed in Poly(vinyl alcohol) Films. *J. Phys. Chem. B* **103**, 5761–5767 (1999).
36. Link, S., Mohamed, M. B. & El-Sayed, M. A. Simulation of the Optical Absorption Spectra of Gold Nanorods as a Function of Their Aspect Ratio and the Effect of the Medium Dielectric Constant. *J. Phys. Chem. B* **103**, 3073–3077 (1999).
37. Yu, Chang, S.-S., Lee, C.-L. & Wang, C. R. C. Gold Nanorods: Electrochemical Synthesis and Optical Properties. *J. Phys. Chem. B* **101**, 6661–6664 (1997).
38. Draine, B. T. & Flatau, P. J. Discrete-Dipole Approximation For Scattering Calculations. *J. Opt. Soc. Am. A* **11**, 1491–1499 (1994).
39. Kelly, K. L., Coronado, E., Zhao, L. L. & Schatz, G. C. The Optical Properties of Metal Nanoparticles: The Influence of Size, Shape, and Dielectric Environment. *J. Phys. Chem. B* **107**, 668–677 (2002).
40. Gans, R. Form of ultramicroscopic particles of silver. *Ann. Phys.* 270–284 (1915).
41. Kreibig, U., Althoff, A. & Pressmann, H. Veiling of optical single particle properties in many particle systems by effective medium and clustering effects. *Surf. Sci.* **106**, 308–317 (1981).
42. Quinten, M. & Kreibig, U. Optical properties of aggregates of small metal particles. *Surf. Sci.* **172**, 557–577 (1986).
43. Krenn, J. R. *et al.* Squeezing the Optical Near-Field Zone by Plasmon Coupling of Metallic Nanoparticles. *Phys. Rev. Lett.* **82**, 2590–2593 (1999).
44. Krenn, J. R. *et al.* Light field propagation by metal micro- and nanostructures. *J. Microsc.* **202**, 122–128 (2001).
45. Lamprecht, B. *et al.* Metal Nanoparticle Gratings: Influence of Dipolar Particle Interaction on the Plasmon Resonance. *Phys. Rev. Lett.* **84**, 4721–4724 (2000).
46. Raman, C. V. & Krishnan, K. S. No Title. *Nature* **121**, 169 (1928).
47. Smekal, A. Zur Quantentheorie der Dispersion. *Naturwissenschaften* **11**, 873–875 (1923).

48. Smith, E. & Dent, G. *Modern Raman Spectroscopy - A Practical Approach*. (Wiley & Sons, 2005).
49. Long, D. A. *The Raman Effect: A Unified Treatment of the Theory of Raman Scattering by Molecules*. (John Wiley & Sons Ltd, 2002).
50. Vo-Dinh, T. Surface-enhanced Raman spectroscopy using metallic nanostructures. *TrAC Trends Anal. Chem.* **17**, 557–582 (1998).
51. Lewis, I. R. & Edwards, H. G. M. *Handbook of Raman Spectroscopy*. 1 (Marcel Dekker, Inc., 2001).
52. Ball, D. W. Theory of Raman Spectroscopy. *Spectroscopy* **16**, 32 (2001).
53. Skinner, J. G. & Nilsen, W. G. Absolute Raman Scattering Cross-Section Measurement of the 992 cm⁻¹ Line of Benzene. *J. Opt. Soc. Am.* **58**, 113–118 (1968).
54. Fleischmann, M., Hendra, P. J. & McQuillan, A. J. Raman spectra of pyridine adsorbed at a silver electrode. *Chem. Phys. Lett.* **26**, 163–166 (1974).
55. McQuillan, A. J. The discovery of surface-enhanced Raman scattering. *Notes Rec. R. Soc.* **63**, 105–109 (2009).
56. Jeanmaire, D. L. & Van Duyne, R. P. Surface raman spectroelectrochemistry: Part I. Heterocyclic, aromatic, and aliphatic amines adsorbed on the anodized silver electrode. *J. Electroanal. Chem. Interfacial Electrochem.* **84**, 1–20 (1977).
57. Albrecht, M. G. & Creighton, J. A. Anomalously intense Raman spectra of pyridine at a silver electrode. *J. Am. Chem. Soc.* **99**, 5215–5217 (1977).
58. Kneipp, K., Kneipp, H., Itzkan, I., Dasari, R. R. & Feld, M. S. Surface-enhanced Raman scattering and biophysics. *J. Phys. Condens. Matter* **14**, R597 (2002).
59. Etchegoin, P. *et al.* Electromagnetic contribution to surface enhanced Raman scattering revisited. *J. Chem. Phys.* **119**, 5281 (2003).
60. Moskovits, M. Surface-enhanced spectroscopy. *Rev. Mod. Phys.* **57**, 783–826 (1985).
61. Otto, A and Mrozek, I and Grabhorn, H and Akemann, W. Surface-enhanced Raman scattering. *J. Phys. Condens. Matter* **4**, 1143 (1992).
62. Kerker, M., Wang, D.-S. & Chew, H. Surface enhanced Raman scattering (SERS) by molecules adsorbed at spherical particles: errata. *Appl. Opt.* **19**, 4159–4174 (1980).
63. Smith, E. & Rodger, C. *Surface-enhanced Raman scattering*. In John M. Chalmers and Peter R. Griffiths, editors, *Handbook of Vibrational Spectroscopy*, volume 1. 775–784 (2002).
64. Otto, A. The “chemical” (electronic) contribution to surface-enhanced Raman scattering. *J. Raman Spectrosc.* **36**, 497–509 (2005).

65. Aroca, R. *Surface-enhanced Vibrational Spectroscopy*. 101 (John Wiley & Sons, Ltd, 2006).
66. Baker, A. P. & Moore, D. S. P. Progress in plasmonic engineering of surface-enhanced Raman-scattering substrates toward ultra-trace analysis. *Anal. Bioanal. Chem.* **382**, 1751–1770 (2005).
67. Moskovits, M. Surface-enhanced Raman spectroscopy: a brief retrospective. *J. Raman Spectrosc.* **36**, 485–496 (2005).
68. Liu, F. M., Köllensperger, P. A., Green, M., Cass, A. E. G. & Cohen, L. F. A note on distance dependence in surface enhanced Raman spectroscopy. *Chem. Phys. Lett.* **430**, 173–176 (2006).
69. Campion, A. & Kambhampati, P. Surface-enhanced Raman scattering. *Chem. Soc. Rev.* **27**, 241–250 (1998).
70. Moskovits, M. Surface selection rules. *J. Chem. Phys.* **77**, (1982).
71. Tian, Z. Q. & Ren, B. Raman Spectroscopy of Electrode Surfaces. *Encycl. Electrochem. Wiley VCH* **3**, 575 (2003).
72. Otto, A. Surface-enhanced Raman scattering of adsorbates. *J. Raman Spectrosc.* **22**, 743–752 (1991).
73. Ausseregg, F. R. & Lippitsch, M. E. On raman scattering in molecular complexes involving charge transfer. *Chem. Phys. Lett.* **59**, 214–216 (1978).
74. Furtak, T. E. & Macomber, S. H. Voltage-induced shifting of charge-transfer excitations and their role in surface-enhanced Raman scattering. *Chem. Phys. Lett.* **95**, 328–332 (1983).
75. Shim, S., Stuart, C. M. & Mathies, R. A. Resonance Raman Cross-Sections and Vibronic Analysis of Rhodamine 6G from Broadband Stimulated Raman Spectroscopy. *ChemPhysChem* **9**, 697–699 (2008).
76. Lee, P. C. & Meisel, D. Adsorption and surface-enhanced Raman of dyes on silver and gold sols. *J. Phys. Chem.* **86**, 3391–3395 (1982).
77. Huang, T. & Xu, X.-H. N. Synthesis and characterization of tunable rainbow colored colloidal silver nanoparticles using single-nanoparticle plasmonic microscopy and spectroscopy. *J. Mater. Chem.* **20**, 9867–9876 (2010).
78. Sun, Y. G. & Xia, Y. N. Shape-controlled synthesis of gold and silver nanoparticles. *Science (80-.).* **298**, 2176–2179 (2002).
79. Kim, F., Connor, S., Song, H., Kuykendall, T. & Yang, P. Platonic Gold Nanocrystals. *Angew. Chemie Int. Ed.* **43**, 3673–3677 (2004).

80. Langille, M. R., Personick, M. L., Zhang, J. & Mirkin, C. A. Defining Rules for the Shape Evolution of Gold Nanoparticles. *J. Am. Chem. Soc.* **134**, 14542–14554 (2012).
81. Lu, X., Rycenga, M., Skrabalak, S. E., Wiley, B. & Xia, Y. Chemical Synthesis of Novel Plasmonic Nanoparticles. *Annu. Rev. Phys. Chem.* **60**, 167–192 (2009).
82. Sánchez-Iglesias, A. *et al.* Synthesis and Optical Properties of Gold Nanodecahedra with Size Control. *Adv. Mater.* **18**, 2529–2534 (2006).
83. Ha, T. H., Koo, H.-J. & Chung, B. H. Shape-Controlled Syntheses of Gold Nanoprisms and Nanorods Influenced by Specific Adsorption of Halide Ions. *J. Phys. Chem. C* **111**, 1123–1130 (2006).
84. Millstone, J. E., Wei, W., Jones, M. R., Yoo, H. & Mirkin, C. A. Iodide Ions Control Seed-Mediated Growth of Anisotropic Gold Nanoparticles. *Nano Lett.* **8**, 2526–2529 (2008).
85. Ye, X. *et al.* Seeded Growth of Monodisperse Gold Nanorods Using Bromide-Free Surfactant Mixtures. *Nano Lett.* **13**, 2163–2171 (2013).
86. Murphy, C. J. *et al.* Anisotropic Metal Nanoparticles: Synthesis, Assembly, and Optical Applications. *J. Phys. Chem. B* **109**, 13857–13870 (2005).
87. Brinson, B. E. *et al.* Nanoshells Made Easy: Improving Au Layer Growth on Nanoparticle Surfaces. *Langmuir* **24**, 14166–14171 (2008).
88. Sau, T. K., Rogach, A. L., Döblinger, M. & Feldmann, J. One-Step High-Yield Aqueous Synthesis of Size-Tunable Multispiked Gold Nanoparticles. *Small* **7**, 2188–2194 (2011).
89. Rodríguez-Lorenzo, L., Álvarez-Puebla, R. A., de Abajo, F. J. G. & Liz-Marzán, L. M. Surface Enhanced Raman Scattering Using Star-Shaped Gold Colloidal Nanoparticles†. *J. Phys. Chem. C* **114**, 7336–7340 (2009).
90. Yang, M. *et al.* SERS-Active Gold Lace Nanoshells with Built-in Hotspots. *Nano Lett.* **10**, 4013–4019 (2010).
91. Grzelczak, M., Perez-Juste, J., Mulvaney, P. & Liz-Marzan, L. M. Shape control in gold nanoparticle synthesis. *Chem. Soc. Rev.* **37**, 1783–1791 (2008).
92. Niu, W. *et al.* Selective Synthesis of Single-Crystalline Rhombic Dodecahedral, Octahedral, and Cubic Gold Nanocrystals. *J. Am. Chem. Soc.* **131**, 697–703 (2008).
93. Xiong, Z., Liu, Y. & Sun, H. Electrostatic and Covalent Contributions in the Coordination Bonds of Transition Metal Complexes. *J. Phys. Chem. A* **112**, 2469–2476 (2008).
94. Bastús, N. G., Comenge, J. & Puntes, V. Kinetically Controlled Seeded Growth Synthesis of Citrate-Stabilized Gold Nanoparticles of up to 200 nm: Size Focusing versus Ostwald Ripening. *Langmuir* **27**, 11098–11105 (2011).

95. Xia, X., Zeng, J., Zhang, Q., Moran, C. H. & Xia, Y. Recent Developments in Shape-Controlled Synthesis of Silver Nanocrystals. *J. Phys. Chem. C* **116**, 21647–21656 (2012).
96. Yaffe, N. R. & Blanch, E. W. Effects and anomalies that can occur in SERS spectra of biological molecules when using a wide range of aggregating agents for hydroxylamine-reduced and citrate-reduced silver colloids. *Vib. Spectrosc.* **48**, 196 (2008).
97. Huebner, U. *et al.* Fabrication and characterization of silver deposited micro fabricated quartz arrays for surface enhanced Raman spectroscopy (SERS). *Microelectron. Eng.* **88**, 1761–1763 (2011).
98. Cialla, D., Hübner, U., Schneidewind, H., Möller, R. & Popp, J. Probing Innovative Microfabricated Substrates for their Reproducible SERS Activity. *ChemPhysChem* **9**, 758 (2008).
99. Yokota, Y. *et al.* Nano-textured metallic surfaces for optical sensing and detection applications. *J. Photochem. Photobiol. A Chem.* **207**, 126–134 (2009).
100. Yu, Y. H. and J. X. and X. Z. and D. SERS on periodic arrays of coupled quadrate-holes and squares. *Nanotechnology* **21**, 195203 (2010).
101. Oran, J. M., Hinde, R. J., Abu Hatab, N., Retterer, S. T. & Sepaniak, M. J. Nanofabricated periodic arrays of silver elliptical discs as SERS substrates. *J. Raman Spectrosc.* **39**, 1811–1820 (2008).
102. Yu, Q., Guan, P., Qin, D., Golden, G. & Wallace, P. M. Inverted Size-Dependence of Surface-Enhanced Raman Scattering on Gold Nanohole and Nanodisk Arrays. *Nano Lett.* **8**, 1923–1928 (2008).
103. Li, K., Clime, L., Cui, B. & Veres, T. Surface enhanced Raman scattering on long-range ordered noble-metal nanocrescent arrays. *Nanotechnology* **19**, 145305 (2008).
104. Li, K. *et al.* Multiple Surface Plasmon Resonances and Near-Infrared Field Enhancement of Gold Nanowells. *Anal. Chem.* **80**, 4945–4950 (2008).
105. Marquestaut, N. *et al.* Raman Enhancement of Azobenzene Monolayers on Substrates Prepared by Langmuir–Blodgett Deposition and Electron-Beam Lithography Techniques. *Langmuir* **24**, 11313–11321 (2008).
106. Galarreta, B. C., Harté, E., Marquestaut, N., Nortona, P. R. & Lagugné-Labarthet, F. Plasmonic properties of Fischer's patterns: polarization effects. *Phys. Chem. Chem. Phys.* **12**, 6810 (2010).
107. Stosch, R. *et al.* Lithographical gap-size engineered nanoarrays for surface-enhanced Raman probing of biomarkers. *Nanotechnology* **22**, 105303 (2011).

108. Wells, S. M., Retterer, S. D., Oran, J. M. & Sepaniak, M. J. Controllable Nanofabrication of Aggregate-like Nanoparticle Substrates and Evaluation for Surface-Enhanced Raman Spectroscopy. *ACS Nano* **3**, 3845–3853 (2009).
109. Beermann, J., Novikov, S. M., Albrektsen, O., Nielsen, M. G. & Bozhevolnyi, S. I. Surface-enhanced Raman imaging of fractal shaped periodic metal nanostructures. *J. Opt. Soc. Am. B* **26**, 2370 (2009).
110. Ormonde, A. D., Hicks, E. C. M., Castillo, J. & Van Duyne, R. P. Nanosphere Lithography: Fabrication of Large-Area Ag Nanoparticle Arrays by Convective Self-Assembly and Their Characterization by Scanning UV–Visible Extinction Spectroscopy. *Langmuir* **20**, 6927–6931 (2004).
111. Haynes, C. L. & Van Duyne, R. P. Nanosphere Lithography: A Versatile Nanofabrication Tool for Studies of Size-Dependent Nanoparticle Optics. *J. Phys. Chem. B* **105**, 5599–5611 (2001).
112. Jensen, T. R., Malinsky, M. D., Haynes, C. L. & Van Duyne, R. P. Nanosphere Lithography: Tunable Localized Surface Plasmon Resonance Spectra of Silver Nanoparticles. *J. Phys. Chem. B* **104**, 10549–10556 (2000).
113. Hulteen, J. C. *et al.* Nanosphere Lithography: Size-Tunable Silver Nanoparticle and Surface Cluster Arrays. *J. Phys. Chem. B* **103**, 3854–3863 (1999).
114. Dieringer, J. A. *et al.* Introductory Lecture Surface enhanced Raman spectroscopy: new materials, concepts, characterization tools, and applications. *Faraday Discuss.* **132**, 9–26 (2006).
115. Stokes, D. L. & Vo-Dinh, T. Development of an integrated single-fiber SERS sensor. *Sensors Actuators B Chem.* **69**, 28–36 (2000).
116. Stokes, D. L., Chi, Z. & Vo-Dinh, T. Surface-Enhanced-Raman-Scattering-Inducing Nanoprobe for Spectrochemical Analysis. *Appl. Spectrosc.* **58**, 292–298 (2004).
117. Zhang, Y., Gu, C., Schwartzberg, A. M. & Zhang, J. Z. Surface-enhanced Raman scattering sensor based on D-shaped fiber. *Appl. Phys. Lett.* **87**, 123105 (2005).
118. Gu, C., Zhang, Y., Schwartzberg, A. M. & Zhang, J. Z. Ultra-sensitive compact fiber sensor based on nanoparticle surface enhanced Raman scattering. *Proc. SPIE* **5911**, 591108–591166 (2005).
119. Zhang, Y., Shi, C., Gu, C., Seballos, L. & Zhang, J. Z. Liquid core photonic crystal fiber sensor based on surface enhanced Raman scattering. *Appl. Phys. Lett.* **90**, 193504 (2007).
120. Yan, H. *et al.* Hollow core photonic crystal fiber surface-enhanced Raman probe. *Appl. Phys. Lett.* **89**, 204101 (2006).

121. Xu, Z. *et al.* Surface-Enhanced Raman Scattering Spectroscopy of Explosive 2,4-Dinitroanisole using Modified Silver Nanoparticles. *Langmuir* **27**, 13773–13779 (2011).
122. Demeritte, T. *et al.* Highly efficient SERS substrate for direct detection of explosive TNT using popcorn-shaped gold nanoparticle-functionalized SWCNT hybrid. *Analyst* **137**, 5041–5045 (2012).
123. Hatab, N. A. *et al.* An integrated portable Raman sensor with nanofabricated gold bowtie array substrates for energetics detection. *Analyst* **136**, 1697–1702 (2011).
124. Li, J. F. *et al.* Shell-isolated nanoparticle-enhanced Raman spectroscopy. *Nature* **464**, 392–395 (2010).
125. Lin, M. , He, L. , Awika, J. , Yang, L. , Ledoux, D.R. , Li, H. and Mustapha, A. Detection of Melamine in Gluten, Chicken Feed, and Processed Foods Using Surface Enhanced Raman Spectroscopy and HPLC. *J. Food Sci.* (2008). at <<http://dx.doi.org/10.1111/j.1750-3841.2008.00901.x>>
126. Wu, X., Xu, C., Tripp, R. A., Huang, Y. & Zhao, Y. Detection and differentiation of foodborne pathogenic bacteria in mung bean sprouts using field deployable label-free SERS devices. *Analyst* **138**, 3005–3012 (2013).
127. Eliasson, C. *et al.* Surface-enhanced Raman scattering imaging of single living lymphocytes with multivariate evaluation. *Spectrochim. Acta Part A Mol. Biomol. Spectrosc.* **61**, 755–760 (2005).
128. Lee, S. *et al.* Biological Imaging of HEK293 Cells Expressing PLC γ 1 Using Surface-Enhanced Raman Microscopy. *Anal. Chem.* **79**, 916–922 (2007).
129. Kong, C.-R. *et al.* A novel non-imaging optics based Raman spectroscopy device for transdermal blood analyte measurement. *AIP Adv.* **1**, - (2011).

Chapter II



Methods and Experimental Techniques

II.1 Fabrication of metal nanostructures

II.1.1 Thermal annealing of metallic films

II.1.1.1 Physical vapour deposition

Physical vapour deposition (PVD) is a collective set of processes employed to deposit thin films of material, typically from the range of few nanometers to several micrometers.¹ The process starts by supplying thermal energy to the source material either by electrical current or direct electron beam. As the source material approaches its boiling temperature, individual atoms start to evaporate in a uniform and isotropic manner from the source. The process is carried out in vacuum environment, allowing the evaporated atoms to reach the substrate without collision with atmospheric gases. The residual pressure in the system, the source temperature, the distance from substrate to the source and the deposition duration are key parameters in PVD.

II.1.1.2 PLASSYS MEB 400 evaporator

The MEB 400 evaporator was used in this study to deposit gold and silver island films over glass substrates. In this system a tungsten boat is used to heat the metal till its melting point. MEB 400 is provided with a primary vane pump and secondary turbo molecular pump to achieve pressures of 10^{-7} torr. A quartz crystal oscillator is integrated in the evaporation unit to enable the monitoring of evaporation thickness. The monitor functions by measuring the change in oscillation frequency as the amount of material deposited onto the crystal face increases.

II.1.2 Electron Beam Lithography (EBL)

Electron beam lithography is a specialized technique for fabricating extremely fine patterns down to the nanometer scale.² Derived from the early scanning electron microscopes, this technique is based on scanning a focused beam of electrons across substrate covered with electron-sensitive resist layer. The resist exposure to the electron beam within specific parameters leads to well-defined patterns. The main features of EBL technique are: i) the high resolution and homogeneous output, ii) the technique flexibility allowing large range of materials and almost infinite number of patterns and iii) slow, expensive and complicated.

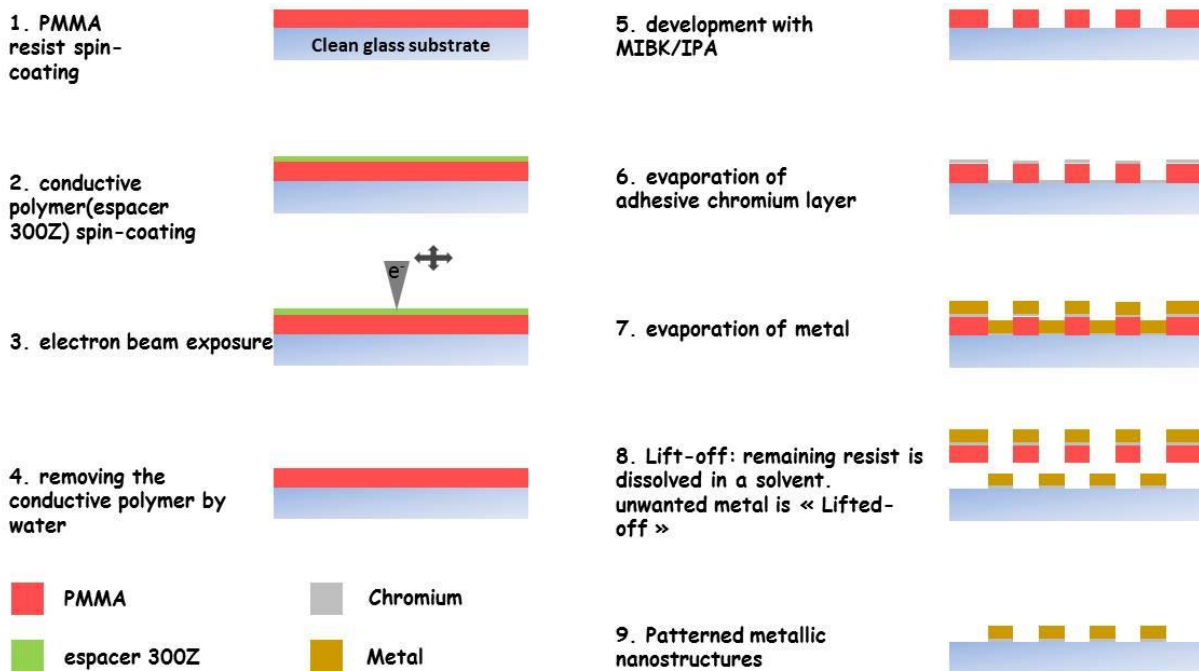


Figure II.1 The schematic of the electron beam lithography process: (1) Cover a thin layer of resist on the glass substrate by spin coating. (2) Deposit a conducting polymer layer. (3) Write the structure by electron beam. (4) Remove spacer 300Z polymer layer by water (5) Development with MIBK/IPA. (6) Evaporation of chromium adhesive layer. (7) Evaporate a metal (Au, Ag) layer. (8) Remove the remaining resist and the metal covering it ("lift off") leaving a small metal pattern behind. (9) After "lift-off": The metallic nano-patterns are on glass substrate.

Figure II.1 displays the fabrication steps of metallic nanoparticles with the use of EBL. The steps had been developed by engineers and researchers in the LNIO, UTT laboratory and were adapted in a manner compatible for preparing nanostructures. These steps are represented as follows:

• Positive e-beam resist deposition

A positive e-beam resist poly(methyl methacrylate) (PMMA), which is a long chain polymer that is broken into smaller and more soluble fragments after electron exposure, has been deposited on the substrate by spin coating. The used PMMA solution is of 30 g/l concentration with methyl isobutyl ketone (MIBK) as solvent. The spin coating parameters were set as 4000 round. $\text{min}^{-1} \cdot \text{s}^{-1}$ accelerating, 3000 round. s^{-1} speed and 30 seconds spinning time. Consequently, a PMMA polymer layer of approximately 150 nm thickness is formed

over the substrate. Thanks to previous studies in our lab, we know that the ratio of 3:1 to PMMA thickness over the metallic nanostructures height is recommended. Accordingly, in our work the PMMA layer thickness were carefully chosen for fabricating nanostructures of 50 nm height. The PMMA resist is then baked at 170°C for 15 minutes to achieve its homogeneous distribution over the substrate.

- ***Conductive layer deposition***

In order to avoid the accumulation of charges on the glass substrate (charging effect), a conductive layer is deposited over it. In this study we used a thin layer of conductive polymer- spacer 300Z to be deposited over the PMMA layer. The spacer 300Z deposition was realized by spin coating with an acceleration of 3000 round. $\text{min}^{-1} \cdot \text{s}^{-1}$, a speed of 2000 round. s^{-1} and a spinning time of 30 seconds.

- ***Electron beam exposure***

SEM is the most common type of microscopy used for lithography after combined to lithographic capability attachments. *Figure II.2* illustrates a schematic diagram of the typical EBL configuration. The basic components of lithography system are:

- XY controller.
- Picometer, used to measure the current at the sample's surface.
- Beam blanker.
- Digital SEM control for automatic setting of the magnification, focus, etc..
- Farady cage for automated beam current measuring and compensation.

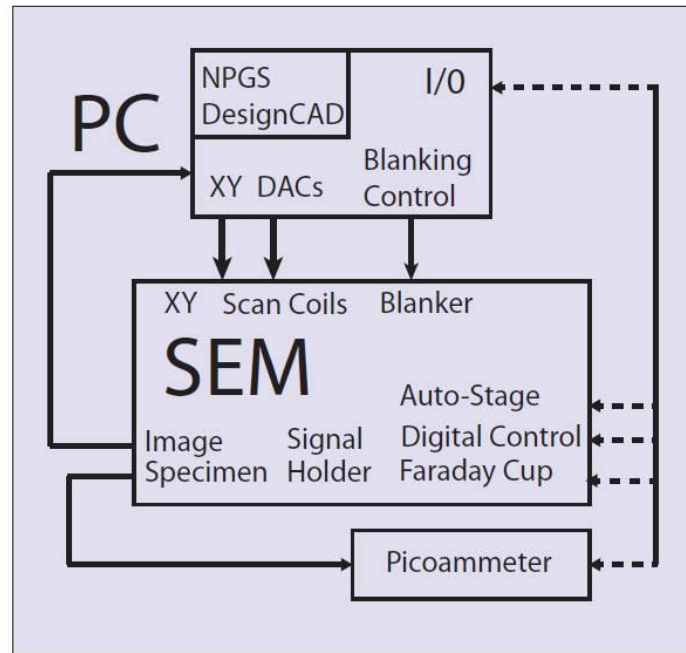


Figure II.2 Schematic illustration of an EBL system controlled by PC.³

The procedure for exposure comprises several steps: designing the patterns, determination of exposure coordinates, calibration of working field (writing field), definition of reference system for positioning and alignment, determination of actual beam current to establish the exposure conditions, optimization of focus. *Figure II.3* illustrates all the EBL operational steps using a Hitachi S-3500 N Scanning Electron Microscope connected to nano pattern generation system (NPGS).

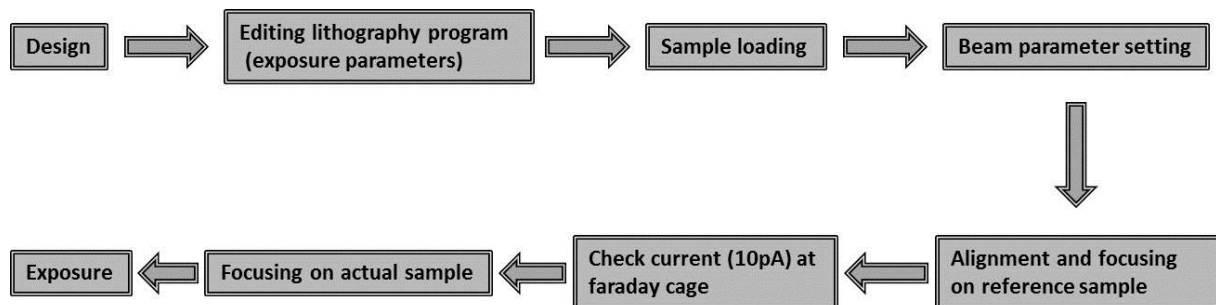


Figure II.3 Diagram of electron beam exposure procedure

- ***Chemical development***

After electron beam exposing, the AZ 3000 conductive layer is removed by immersing the sample in water for one minute. Then, the resist exposed areas are subsequently removed by a chemical development process. Firstly, the substrate is immersed in a solvent of methyl-isobutyl ketone (MIBK)/isopropyl alcohol (IPA) with the following volume proportion 1MIKBR:3IPA for exactly one minute. Secondly, the substrate is immersed in IPA for 10 seconds; as a result we obtain a pattern lithographed sample.

- ***Metallization***

For gold and silver deposition, PLASSYS MEB 400 evaporator has been also employed.

- ***“Lift-off”***

The last step in EBL fabrication is lift-off. The substrate is immersed in acetone for two hours in order to remove the remaining PMMA and the metal at the non-exposed areas. Consequently, patterned metallic nanostructures are only obtained on the sample.

II.2 UV-Vis-NIR spectroscopy

Absorption spectroscopy in the different regions of electromagnetic spectrum is an important characterization tool used to investigate how electromagnetic waves (light) interact with a sample.⁴ Knowing that nanoparticles optical properties are highly dependent on their size, shape and other features, and that they interact with specific wavelengths of light which consists the foundation for the field of plasmonics, this renders the UV-Vis-NIR spectroscopy as a valuable investigating technique for their identification and characterization.

The absorption of energy leads to the transition of electrons from the ground state to higher excited state. The energy absorbed (ΔE) can be expressed as:

$$E = h\nu = hc/\lambda = h\bar{\nu}$$

Where h is the Planck's constant, c the velocity of light, λ the wavelength of light and $\bar{\nu}$ the wavenumber.

The absorption band is characterized by two important features, first the position of the band which is in its turn dependent on the energy difference between the electronic levels and second the intensity which is also affected by the interaction between the radiation and the electronic system and the energy difference between the ground state and the excited state.

The absorbance is related to the path length that a radiation travels within the system and the concentration of the species given by the following expression derived from the Lambert-Beer law which is expressed as follows $A = a \cdot b \cdot c = \log I/I_0$ where A is the measured absorbance, a is the absorptivity, b is the path length, c the analyte concentration, I_0 the incident beam intensity and I the transmitted beam intensity.

UV-Vis-NIR spectroscopy has several measurement approaches. The most employed is extinction measurement. In this later, the quantity of light scattered and absorbed by the sample is quantified, this quantity is known as extinction (which is defined as the sum of absorbed and scattered light). Furthermore extinction measurements are carried out when the sample and the detector are enough separated, so that the scattered light is not detected.

In the present work, a home-made UV-Vis-NIR spectrometer (*Figure II.4*) had been used to study the optical properties of the prepared nanoparticles. The spectrometer consists of white light source focused on the sample by means of an optical fiber and two inverse objective lenses (20x, 0.28 N.A). The collected light is connected to the detector (Ocean optics QE65000) by an objective lens (20x, 0.28 N.A) and optical fiber. The spectrometer is provided with a high definition camera in order to precisely detect the measured zone, in addition to adjustable sample holder along the directions x, y and z. It should be noted that due to the optical fiber and lens combination used in the confocal setup, the incident light beam with a spatial resolution of 10 um is focused perpendicularly on the substrates during all the measurements.

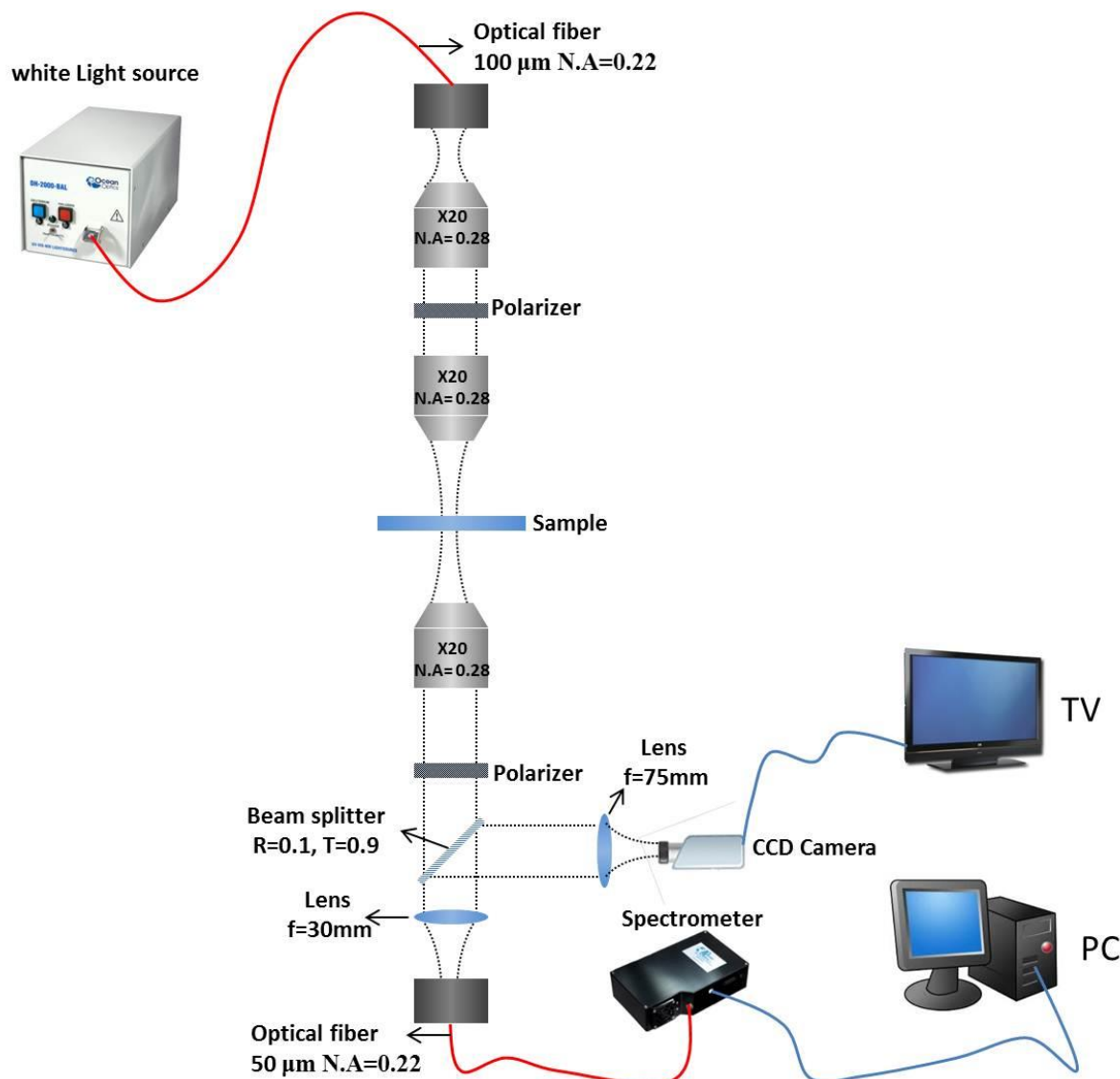


Figure II.4 Schematic illustration of the homemade UV-Vis-NIR spectroscopy.

II.3 X-Ray Photoelectron Spectroscopy (XPS)

X-Ray photoelectron spectroscopy is a surface sensitive technique. It is widely used for the chemical composition and oxidation state analysis of solids, thin films and nanostructures. XPS is also known as Electron Spectroscopy for Chemical Analysis (ESCA) due to the fact that it gives highly precise quantitative elemental and chemical state information of the samples surface.⁵

The basic principle of XPS is that when a sample is subjected to X-rays, also called photons, having energy greater than or equal to the binding energy of an electron in the atom, photoelectrons at the extreme outer surface of the sample are emitted. The binding energy (B_E) of these electrons is given by the following equation:

$$B_E = h\nu - E_k + \varphi$$

Where E_k is the kinetic energy of the emitted photoelectron and φ is the work function dependent on the spectrometer. The kinetic energy of the emitted photoelectrons is characteristic of the element from which the photoelectron is originated. The kinetic energy of the emitted photoelectron can be calculated using proper electrostatic or electromagnetic detector. The binding energy can then be obtained from the above equation and thus allowing the extraction of the sample's XPS spectrum i.e. number of electrons of specific energy emitted per unit time. Ultra high vacuum environment (10^{-8} torr) is essential for proper detection since photoelectrons interact with the environments atoms because of their negative charge. Photoelectrons originating from more than 50-100 Å in depth undergo inelastic collisions within the sample's atomic structure. The surface sensitivity of the material to photoelectrons can be determined by the term so called inelastic mean free path (IMPF). IMPF is the average distance measured along the trajectories that an electron beam can travel before its intensity decays to $\frac{1}{2}$ its initial value. Therefore photoelectrons emitted from atoms close to surface (< 10 nm) can only reach the detector.^{5,6}

In our study, XPS has been used to confirm the composition of the fabricated Au/Ag bimetallic nanoparticles. The obtained XPS data has been analyzed in order to assure the evaporated metal percentage of each substrate by calculating the area under Ag3d and Au4f peaks.

XPS measurements were carried out in the laboratory “Institut des materiaux Jean Rouxel (IMN), CNRS-Université de Nantes, NANTES (France)”⁷ through collaboration with Prof. Guy Louarn. An Axis Nova instrument has been used from Kratos Analytical spectrometer with a monochromatic Al K α line (1486.6 eV) source operated at 300 W. Survey spectra were acquired at pass energies of 80 eV. The core level spectra (C1s, Au4f and Ag3d) were acquired with an energy step of 0.1 eV and using a constant pass energy mode of 20 eV to obtain data in a reasonable experimental time (energy resolution of 0.48 eV). XPS data were acquired for a minimum of three areas per sample. Data analysis was performed using Casa XPS software.

II.4 Scanning Electron Microscopy (SEM)

Scanning electron microscopy is used to obtain information about the sample surface morphology, chemical homogeneity, qualitative and quantitative chemical composition at the micrometer or nanometer scale. In this manuscript, SEM was mainly used for visualizing the morphological properties of the fabricated monometallic and bimetallic nanoparticles.

In SEM, the incident electrons emitted by an electron gun are thermoelectrically generated by passing an electrical current through a tungsten filament (*Figure II.5*). These electrons are accelerated by applying a sufficient potential (1-30 KV), then a set of different electromagnetic lenses is used to control their flow and generate an electron beam which can be focused and scanned on a definite spot on the sample's surface. The incident electrons with sufficient kinetic energy give different signals depending on the electron-sample interaction. The signals notably include secondary electrons (SE), and backscattered electrons (BSE).

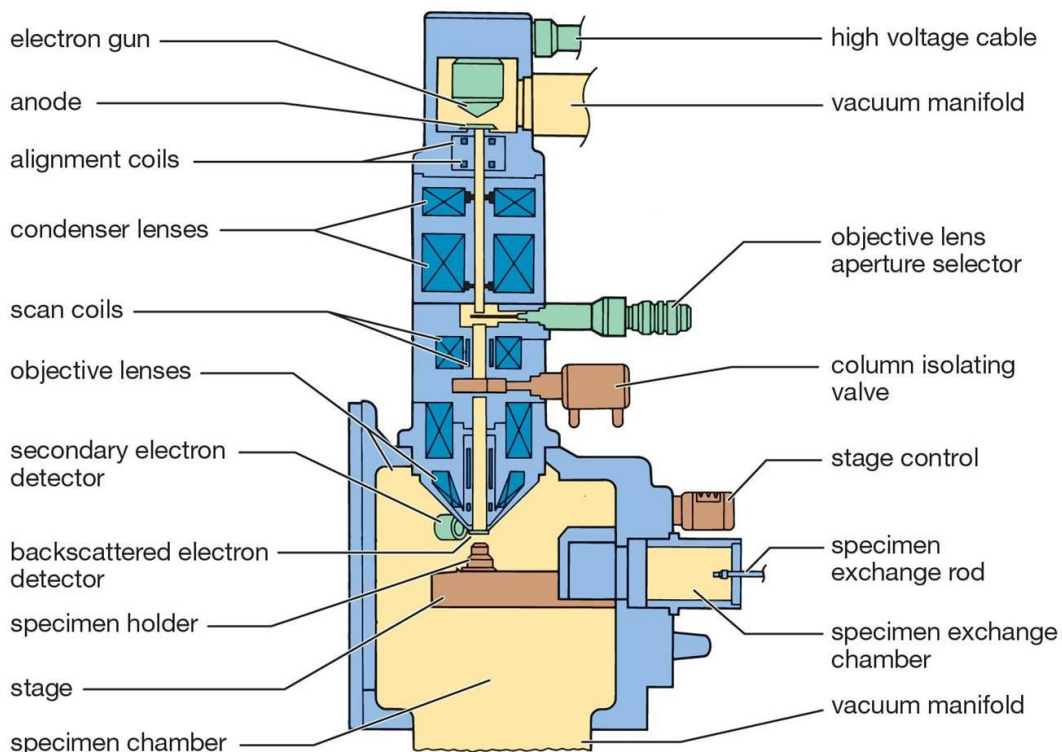


Figure II.5 Drawing of a scanning electron microscope

- **Secondary electrons (SE) imaging**

The incident electrons, with high kinetic energy, collide with the sample valence electrons, causing them to be ejected from their electronic level with lower energy (50 eV). The ejected electrons are called secondary electrons. Since the incident electron beam possesses high energy, each single electron from the beam leads to the emission of thousands of SE. The low-energy ejected SE are collected by a detector having a positive potential on its face in order to attract them.

The contrast of the obtained image is highly dependent on the angle between the incident beam and the sample's surface where a local inclination in the sample leads to a variation in the incident beam angle, therefore providing information about the sample's surface morphology and topography.

- **Backscattered electrons (BSE) imaging**

When the incident electrons collide elastically with the samples nucleus and bounce back, they are called backscattered electrons. The quantity of these high-energy backscattered electrons is directly dependent on the atomic number Z of the atoms (high atomic number regions appear bright relative to regions with low atomic number). So the backscattered imaging mode gives information about the sample's chemical homogeneity and contrast between areas with different chemical compositions.

In this manuscript three different scanning electron microscopes have been used. These are Jeol JSM 6500F field emission gun (FEG), carried out in the Laboratory “Laboratoire de Physique, Optique Submicronique, Université de Bourgogne, Dijon (France)” through collaboration with Mr. Yvon Lacroix),⁸ Hitachi SU 8030 and Hitachi S3500 N in LNIO.

II.5 Transmission Electron Microscopy (TEM)

Transmission electron microscopy through three different operating modes (imaging, diffraction and energy dispersive spectroscopy analysis (EDS)), gives information concerning the crystalline structure and the chemical composition of the studied material. The employed

imaging mode in this manuscript is the bright field imaging mode. In this mode, thick regions of the specimen or regions with a higher atomic number give dark contrast.

High resolution transmission electron microscopy (HRTEM) is an imaging mode of the transmission electron microscope (TEM) that allows materials imaging at the atomic scale. HRTEM is used to examine the size, structure and composition distribution of the fabricated nanoparticles. These were realized using Hitachi H9000 NAR operating at an acceleration voltage of 300KV and using LaB₆ single crystal as an electron source. The images were conducted through collaboration with Prof. Guy Louarn in the laboratory “Institut des matériaux Jean Rouxel (IMN), CNRS-Université de Nantes, NANTES (France)⁷.

II.6 Raman system

All Raman and SERS spectra presented in this manuscript were collected using the high resolution Raman microscope Jobin-Yvon Horiba (LABRAM). The operation principle of the Raman system is listed below:

1. A laser light is coupled into the microscope.
2. The light is filtered by a band-pass filter in order to remove undesired wavelengths.
3. The collimated beam is reflected off the Raman filter and directed to the objective.
4. Beam splitters and video camera can be inserted between the Raman filter and the objective as needed for sample inspection.
5. An infinity corrected lens focuses the laser onto the sample and collects the backscattered Raman signal.
6. A Raman filter removes the undesired Rayleigh scatter from the returning light, while passing the Raman signal.
7. The signal is reached to the spectrometer and it is dispersed by a holographic gating and then imaged by a peltier cooled CDD detector.

LABRAM microscope is equipped with an Olympus optical microscope of different objectives (10x NA 0.3, 50x NA 0.8, 100X NA 0.9), a helium Neon excitation laser of 632.8 nm wavelength, a 600 lines/mm dispersion grating, a 800 mm path monochromator and a peltier CD detector (1024x256 pixels) of 16 bits dynamic range.

References

1. Powell, C. F., Oxley, J. H. & Blocher, J. M. *Vapor Deposition*. (John Wiley & Sons, 1966).
2. Levinson, H. J. *Principles of Lithography*. (SPIE, 2011).
3. Nguyen, T. N. Second harmonic generation of three-fold symmetry gold nanoparticles : measurements and modelling. (2013).
4. Denney, R. C. & Sinclair, R. *Visible and Ultraviolet Spectroscopy*. (John Wiley & Sons, 1988).
5. Briggs, D. & Seah, P. *Practical Surface Analysis, Auger and X-ray Photoelectron Spectroscopy*. (Wiley, 1990). at <<http://books.google.fr/books?id=D9pTAAAAMAAJ>>
6. Heath, J. R., Knobler, C. M. & Leff, D. V. Pressure/Temperature Phase Diagrams and Superlattices of Organically Functionalized Metal Nanocrystal Monolayers: The Influence of Particle Size, Size Distribution, and Surface Passivant. *J. Phys. Chem. B* **101**, 189–197 (1997).
7. Institut des Matériaux Jean Rouxel. at <<http://www.cnrs-imn.fr>>
8. Laboratoire de Physique, Optique Submicronique, Université de Bourgogne, Dijon(France). at <<http://icb.u-bourgogne.fr>>

Chapter III

*Morphological and Optical Studies
on Au/Ag Bimetallic Nanoparticles*

III.1 Introduction

As mentioned before, SERS-active substrates should meet several requirements. These requirements can be achieved by engineering SERS substrates of specific materials following the appropriate fabrication method, where the most evident property is to have large enhancing ability. Silver nanoparticles exhibit significantly larger electric field enhancement compared to gold nanoparticles, imposing silver as the ultimate material for SERS substrates characterized with high enhancement factors. Thermal annealing of thin metallic films fabrication strategy fulfills other requirements for reliable SERS substrates, providing homogenous, reproducible, simple, and large-scale SERS substrates. Moreover, this fabrication method produces inert and mechanically stable substrates, since no chemicals are used in the fabrication process. The inert nature of the SERS substrates is crucial in Raman spectroscopy, where new peak formation related to the substrates will interfere to the fingerprint of the molecule under study. However, silver nanoparticles fabricated by the mentioned strategy have two limitations. First, silver nanoparticles fabricated by thermal annealing of thin metallic films have LSPR lying in the spectral range 400-470nm. This specification limits the Ag NPs high enhancements for Raman excitation wavelength lying within or near its LSPR spectral domain, since SERS performance was proved to be LSPR-dependent.¹ Meanwhile the majority of Raman spectroscopies are provided with excitation laser of 633 nm wavelength, we need SERS substrates having LSPR in the red region. Secondly, silver nanoparticles suffer from instability defect due to sulfuration and surface oxidation.^{2,3} The LSPR spectral range limitation can be overcome by colloidal or lithographic fabrication of silver nanorods, having LSPR peak in the red spectral range. Nonetheless, colloidal nanorods have random orientation, causing a decrease in SERS enhancement since Raman excitation is polarized. On the other hand, ordered arrays of silver nanorods fabricated by electron beam lithography are subjected to oxidation or sulfuration, decreasing its enhancing ability. The silver nanoparticles can be protected against oxidation and sulfuration by a protective dielectric layer. Nevertheless, this dielectric layer, SiO₂ for example, will reduce the SERS enhancement in its electromagnetic and chemical forms. For this reason, gold nanoparticles can be in contribution to the silver nanoparticles in order to overcome the two limitations, considering its chemical stability, biocompatibility, as well as having LSPR within the spectral domain 550-650 nm following the same fabrication strategy.

Therefore, combining the two metals in a bimetallic nanostructure appear to be a promising approach in order to sum the merits of both the silver optical enhancing properties and gold surface properties.

After introducing the Au/Ag bimetallic nanoparticles and the fabrication strategy we followed, we will investigate combining silver and gold metals in double-layered and triple-layered bimetallic nanoparticles searching for tunable SERS substrates and how can this tunability would affect the SERS enhancement ability of the substrates. In particular, we will study the compositional and morphological effect on the localized surface plasmon resonance position in addition to the relation between the later and the SERS enhancing ability.

III.1.1 Homogeneous and hybrid nanostructures

Monometallic noble nanoparticles have been extensively studied for decades due to their high potential optical,^{4–7} electronic,^{8–10} catalytic,^{11–17} and magnetic properties.^{16,17} Within the last few years, the focus was drawn to shape anisotropic or complex structured nanoparticles of gold and silver.¹⁸ Hybrid or multifunctional nanoparticles have also been attracting increasing interest due to their additional functionalities.^{19–24} The geometry of the hybrid nanostructures can vary from simple spherical core-shell to nanorods, cubes or even more complex shapes, *Figure III.1*.²⁵ Core-shell nanoparticles are of great interest in numerous application fields, for example in surface enhanced Raman scattering (SERS) or localized surface plasmon resonance (LSPR)-based bio sensing technique, in addition to the catalysis domain where bimetallic nanoparticles provide a higher catalytic activity compared to their monometallic analogous.^{3,26–29}

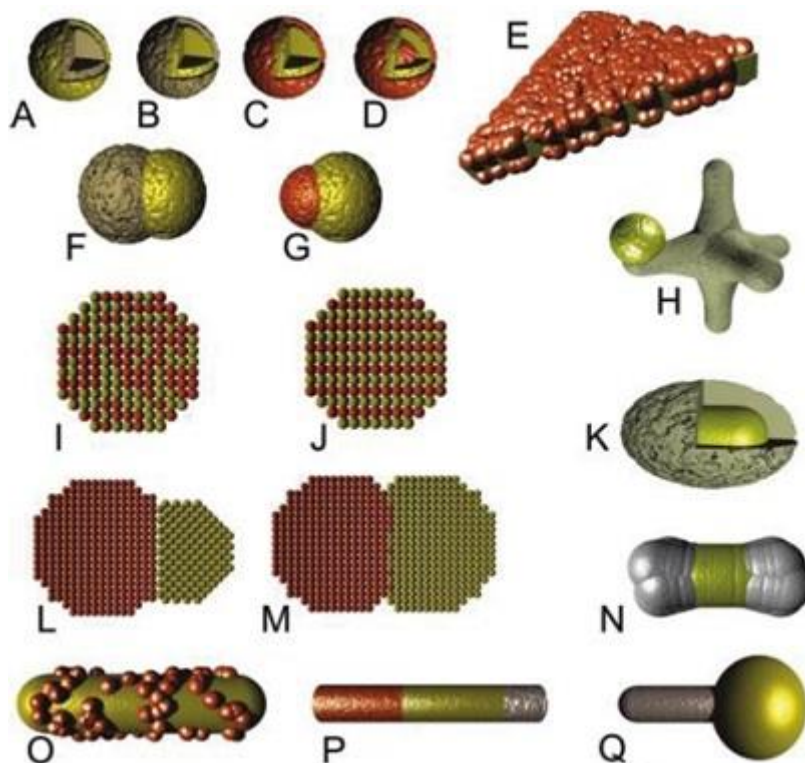


Figure III.1 Examples of hybrid nanoparticles: (a) dielectric@metal core-shell, (b) metal@dielectric core-shell, (c) metal@metal coreshell, (d) metal@metal@metal core-shell, (e) metallic nanotriangle with overcoat of second metal, (f) heterodimer composed of dielectric and metal parts, (g) heterodimer composed of two different metal parts, (h) semiconductor crystal with attached metal nanosphere, (i) cross section through alloyed metal nanoparticle showing disordered nature of atomic occupancies, (j) cross section through nanoparticle composed of an intermetallic compound showing ordered atomic occupancy, (k) metal nanorods coated in a thick shell of dielectric, (l) dimer with incoherent crystalline interface between the parts, (m) dimer with coherent interface between the parts, (n) nanorods with overgrowth of another metal at the rod ends, (o) nanorods with a sparse overgrowth of a second metal, (p) segmented nanowires or nanowire composed of two or more elements, and (q) “nanotadpole”.²⁵

III.1.1.1 Silver and gold metals in the nanometric domain

As it is known, silver nanoparticles provide significantly stronger electric field enhancements in comparison to gold nanoparticles resulting from their sharper localized plasmonic peak and higher inter-particle coupling effect.³⁰⁻³² On the other hand, gold nanoparticles show a higher chemical stability and better biocompatibility.^{26,33}

Silver and gold nanoparticles have intense and well-defined LSPR bands in the visible range.³⁴ Both metals form fcc crystals with very similar lattice constants (4.078 Å for Au and 4.086 Å for Ag). This characteristic provides stable Ag/Au bimetallic nanoparticles, in

addition to a strong tendency towards alloy formation. Knowing that LSPR position is shape-size dependent, spherical silver nanoparticles absorption band lies in the range between 395 and 470 nm, whereas for gold nanoparticles, the absorption band lies in a red shifted range between 550 and 650 nm. There are two main geometries for Au-Ag bimetallic nanoparticles designated by alloy and core-shell nanoparticles.

III.1.1.2 Au/Ag bimetallic nanoparticles

III.1.1.2.a Au/Ag alloy bimetallic nanoparticles

Several studies reported for Au-Ag alloy nanoparticles fabricated by simultaneous reduction of metal salts showed a linear relationship between the alloy ratio and the LSPR spectral position which lies between those for pure silver and pure gold nanoparticles.^{4,35-37} Their LSPR position is red shifted as the Au content of alloy is increased, *Figure III.2*. These shifts were modeled, assuming a linear combination of the dielectric data for pure gold and silver as input in calculations based on Mie theory.

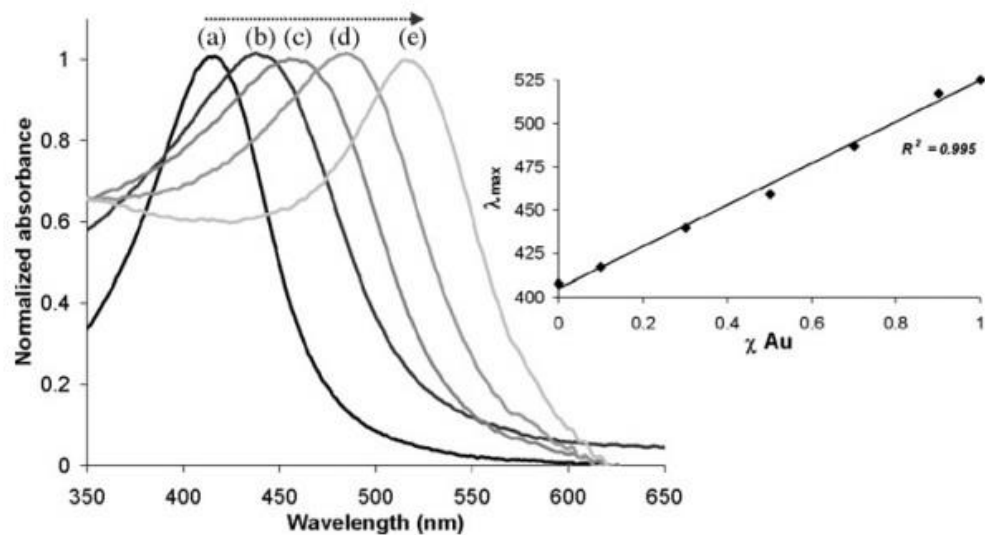


Figure III.2 Plasmon bands of different silver–gold alloy nanodispersions at different Au mole fractions: (a) 0.1, (b) 0.3, (c) 0.5, (d) 0.7, and (e) 0.9.³⁶

III.1.1.2.b Au/Ag core/shell bimetallic nanoparticles

Core-shell nanoparticles fabrication has also been widely reported in the literature. Generally, the core-shell nanoparticles are prepared either by sequential reduction of different metals or segregation during co-reduction. A previous review by Mulvaney³⁸ summarized optical studies on colloidal bimetallic nanoparticles. As for core-shell consisting of gold and

silver, Morris and Collins³⁹ followed by Henglein et al.^{40,41} fabricated this type of particles by radiolysis. Srnova-Sloufava et al⁴² fabricated Au shell on Ag seeds using hydroxylamine, Lu et al⁴³ used ascorbic acid as reductant and cetyltrimethyl ammonium chloride (CTAC) as an additional stabilizer to deposit silver shells on citrate stabilized gold nanoparticles. Rivas et al.⁴⁴ reported Au@Ag and Ag@Au under citrate reduction.

As for the LSPR of core-shell particles, one should take into consideration two different cases. For relatively thick shell of thickness more than 5 nm, the plasmon absorption peak will be directly related to the shell characteristics and unaffected by the core metal. In the case of shell thickness below 4 nm, the core material will have a role in affecting the LSPR spectral position. The plasmonic influence of the core metal increases with decreasing the shell thickness, *Figure III.3*.^{32,45–47}

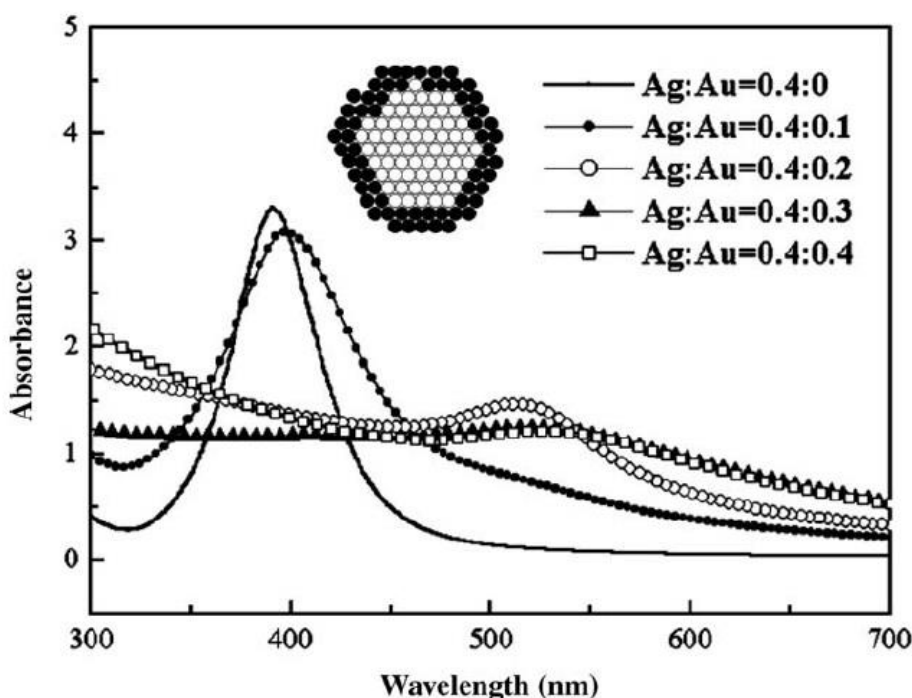


Figure III.3 UV/Vis absorption spectra of Ag/Au core/shell nanoparticles with varying gold shell thickness.

III.1.2 Metallic thin films

III.1.2.1 Growth and crystallization of metallic thin films

The thin-film formation dates back at least to 1920s.⁴⁸ The film formation starts to take place when a sufficient number of vapor atoms or molecules condense and establish a

permanent residence on the substrate. For most films formation, the starting stage is nucleation.

There are three main growth modes: i) island (Volmer-Weber) ii) layer-by-layer (or Frank-Vander Merwe) and iii) Stranski-Krastanov, *Figure III.4*.

i) Volmer-Weber or island growth: this type of growth take place when the smallest clusters nucleate on the substrate and grow forming three dimensional island features.⁴⁹ This growth behavior arises when the atoms or molecules being deposited are more strongly bonded to each other than to the substrate material. This is often the case when the materials of the film and the substrate are different.

ii) Frank-Vander Merwe or layer-by-layer growth: this growth type occurs when the extension of the smallest nucleus occurs in two dimensions resulting in planar sheets formation.⁵⁰ In layer-by-layer growth the depositing atoms or molecules are more strongly bonded to the substrate than to each other and each layer is progressively less strongly bonded than the previous one. The typical example of this growth type is the epitaxial growth of semiconductors and oxide materials.

iii) Stranski-krastanov mode: this type of growth is a combination of the layer-by-layer and islands growth.⁵¹ In this mode, the growth starts by layers formation until the growth becomes energetically unfavorable and instead islands begin to form. This sort of growth is fairly common and has been observed in a number of metal-metal and metal-semiconductor systems.

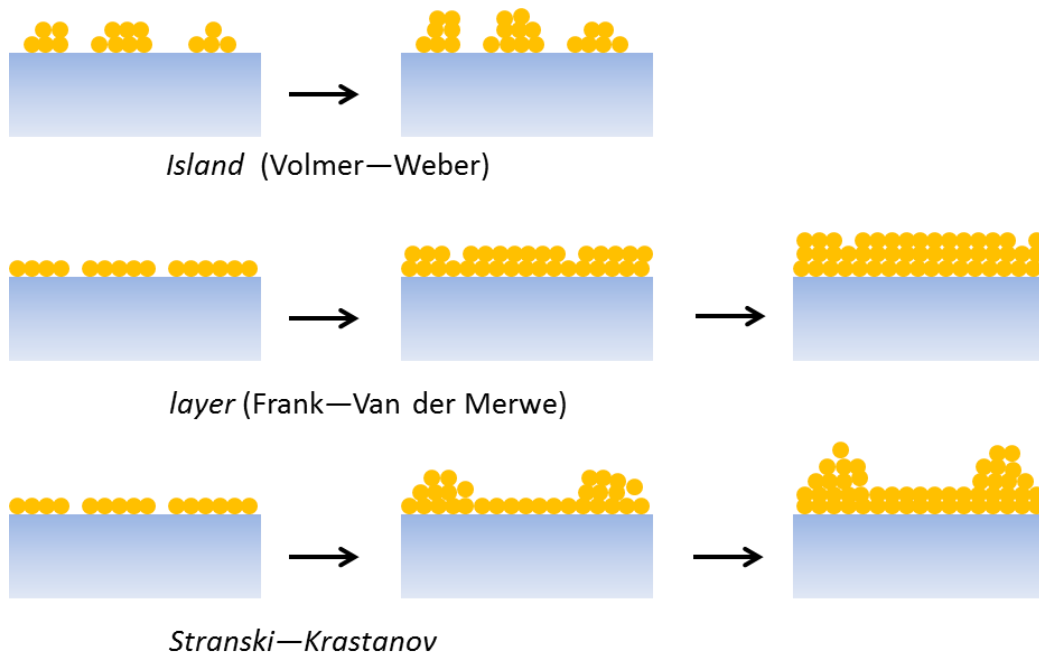


Figure III.4 Basic modes of thin-film growth.

For island Volmer-Weber growth, we have

$$\gamma_{SV} < \gamma_{FS} + \gamma_{FV}$$

Where γ_{SV} is the interface tension between the substrate and vapor, γ_{FS} is the interface tension between the film and the substrate and γ_{FV} is the interface tension between the film and the vapor.

If γ_{FS} is neglected, this relation introduce the idea that island growth takes place when the surface tension of the film exceeds that of the substrates. From here, it originates that the deposited metals tend to form clusters or islands on glass substrates.⁵²

III.1.2.2 Annealing effects on metallic thin films

Thermally evaporated thin metallic films have polycrystalline-granular structures. Thermal annealing treatment initiates recrystallization in the metallic film, causing modifications in all structural-sensitive physical properties of the film.⁵³ Additionally, thermal annealing contributes in reducing strain and decreasing in the number of intrinsic or extrinsic defects in crystal lattices. For thin metallic films, recrystallization takes place at lower temperatures than in bulk metals.⁵⁴⁻⁵⁷ It was shown that normal grain growth occurs at

temperature range from 200°C to 300°C, where a decrease in surface roughness also arise in this temperature range.^{58,59}

Thermal annealing treatment could be employed to change the metallic islands into metallic nanoparticles. Grain growth around the mentioned temperature is expected to occur mainly through grain boundary shifts towards the particle borders instead of direct adhesion of neighboring grains.

III.2 Double layer bimetallic nanoparticles

III.2.1 Fabrication of double layer Au/Ag bimetallic nanoparticles

The nanoparticles investigated in this part have been fabricated by thermal annealing of thin metallic film. Four different two layered nanoparticles have been produced which are represented by: Au-T-Au, Ag-T-Ag, Au-T-Ag and Ag-T-Au. All four substrates have been fabricated on thin commercial glass slides of thickness 0.13 mm and 20 mm × 20 mm dimension, purchased from Carl Roth. Prior to metal evaporation, the glass substrates have been washed with a mixture of detergent (Decon 90) and double-distilled water with a volume ratio of 1:9 in water bath at 50 °C for 20 min. This process has been repeated twice with double-distilled water ultrasonic only in order to ensure the removal of any detergent residues. After the cleaning process, the glass substrates have been dried using a N₂ stream. The metal evaporation process has been conducted in a vacuum evaporator (Plassys MEB 400, France) using the Joule effect mode with an evaporation rate of 3 Å.s⁻¹ monitored using a build-in quartz crystal sensor. All evaporation have been performed under vacuum of pressure 1.0×10^{-6} Torr. The evaporated thicknesses were chosen to be 2 nm to stay below the percolation threshold of the thin metallic films during successive evaporation.^{60,61} The thermal annealing operation has been realized using a hot plate at temperature of 250 °C for 20 seconds.

- The fabrication of the Au-T-Au substrate have started by evaporating thin gold film of 2 nm, followed by thermal annealing (250 °C for 20 seconds). A second evaporation of 2 nm gold was realized directly after the thermal annealing step.
- The Ag-T-Ag substrate fabrication firstly started by evaporating thin silver film of 2 nm pursued by thermal annealing. Immediately a second 2 nm thin silver film was evaporated after the thermal annealing.

- The Au-T-Ag substrate fabrication is similar to that of the previous substrate except that the first evaporation was of 2 nm thin film of gold and the second evaporation was of 2 nm thin film of silver separated by thermal annealing.
- The Ag-T-Au substrate was fabricated by the consecutive evaporation of 2 nm thin film of silver then 2 nm thin film of gold separated by thermal annealing. Full experimental details of the fabrication process are summarized in *Table III.1*.

Table III.1 Experimental details for fabricating the two layered bimetallic nanoparticles

	First evaporation		Thermal annealing		Second evaporation	
	Metal	Thickness (nm)	Temperature (°C)	Time (s)	Metal	Thickness (nm)
Au-T-Au	Au	2	250	20	Au	2
Ag-T-Ag	Ag	2	250	20	Ag	2
Au-T-Ag	Au	2	250	20	Ag	2
Ag-T-Au	Ag	2	250	20	Au	2

III.2.2 X-ray photoelectron spectroscopy (XPS) measurements

Diverse analytical techniques can be used to characterize bimetallic nanoparticles, among which XPS is the most vital due to the perfect match of its probe length (≈ 10 nm) to the thickness of the nanoparticles. Many reports have been published for using XPS characterization on various nanostructures.⁶²⁻⁷²

When XPS analysis is performed on nanoparticles, photoelectrons are attenuated throughout the particle before they escape into the vacuum for their kinetic energy analysis. The well-known attenuation can be modeled to extract structural and morphological information from the XPS data.

XPS has been used to verify the composition of the double layered bimetallic nanoparticles, shown in *Figure III.5*. Concerning the calibration, binding energy of the C1s hydrocarbons peak was set at 284.8 eV. We focus on the Ag3d and Au4f pairs for both Au-T-Ag and Ag-T-Au nanoparticles. The Ag3d pair of peaks Ag3d $/2$ and Ag3d $5/2$ are obtained at

374 eV and 368 eV respectively. The Au4f pair of peaks Au4f_{3/2} and Au4f_{7/2} are obtained at 87.9 eV and 84.2 eV respectively. In order to ensure the evaporated metal thickness on each substrate we calculate the percentage of gold and silver metals for the Au-T-Ag and Ag-T-Au substrates.

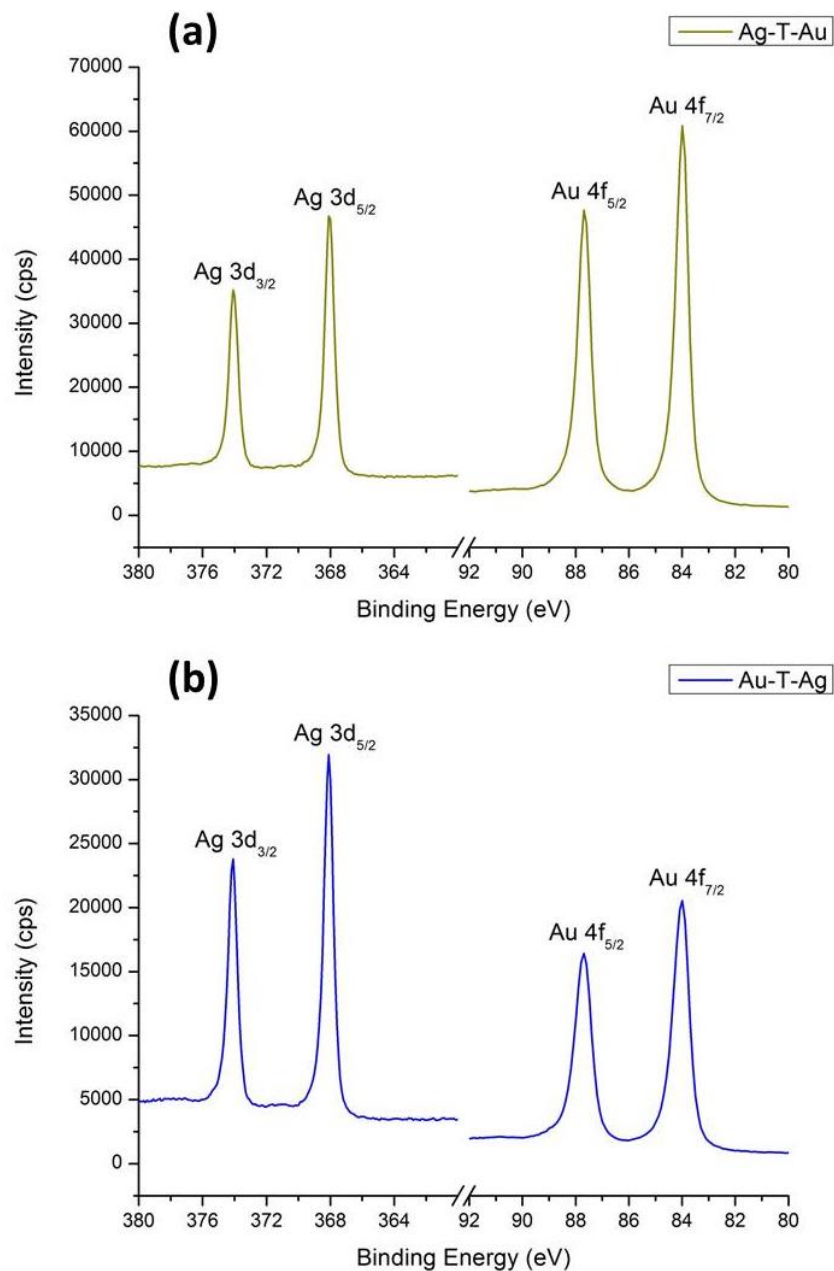


Figure III.5 X-ray photoelectron spectra for Au 4f and Ag 3d regions of the (a) Ag-T-Au and the (b) Au-T-Ag substrates.

The percentages are calculated by integrating the area under the Au4f peak and Ag3d peak *Table III.2*, illustrates the full width at half maximum and the area under each peak for the Au-T-Ag and Ag-T-Au samples with the calculated percentage of each metal.

Table III.2 The Ag 3d and Au 4f peaks positions, FWHM, area, and the percentage of Au and Ag in the Ag-T-Au and Au-T-Ag substrates.

	Name	Position	FWHM ^{a)}	Area	At% ^{b)}
Au-T-Ag	Ag 3d	368.2	2.435	58248.0	57.8
	Au4f	84.2	2.556	44299.6	42.2
Ag-T-Au	Ag 3d	368.2	2.492	85011.2	43.9
	Au 4f	84.2	2.584	113470.0	56.1

a) FWHM is the Full width at half maximum; b) At% is the metal percentage of Au and Ag

Au-T-Ag nanoparticles were fabricated by evaporating 2 nm gold followed by 2 nm silver separated by thermal annealing. The estimated metallic percentage would be 50% gold and 50% silver. The calculated percentage based on XPS measurements are 57.8 % silver and 42.2 % gold. The difference between the estimated and the calculated percentage arises from the fact that XPS is a surface effective technique.⁷³ Since the last evaporated metal is silver, this explains the higher silver percentage compared to gold percentage.

For Ag-T-Au nanoparticles, fabricated by the successive evaporation of 2 nm silver and gold metals, the calculated metallic percentages based on XPS peaks are 43.9 % for silver and 56.1 % for gold. The expected percentages would have been 50% for each metal. Similarly as described previously, the difference between the estimated and the calculated percentages results from the mentioned XPS characteristics (surface effective technique) where the last evaporated metal is gold.

Thanks to XPS measurements, one can verify the evaporated composition on each substrate. Even if it cannot provide the exact thickness of each metal, it can ensure that the evaporation thickness is reproducible regardless if it is exactly 2 nm or not.

III.2.3 Localized surface plasmon resonance tunability for the double layer bimetallic nanoparticles

LSPR measurements for all the substrates were conducted using UV-Vis-NIR spectroscopy ($200 \leq \lambda \leq 1100$ nm) consisting of white light source, two optical fibers; one for illumination and the second for collection; and an adjustable sample holder. It should be noted that due to the optical fiber and lens combination used in the confocal setup, the incident beam with a spatial resolution of 10 μm was focused perpendicularly on the substrates during all the measurements.

The SEM images of the Au-T-Ag and Ag-T-Au nanoparticles are presented in *Figure III.6 (a)* and *Figure III.6 (b)*, respectively.

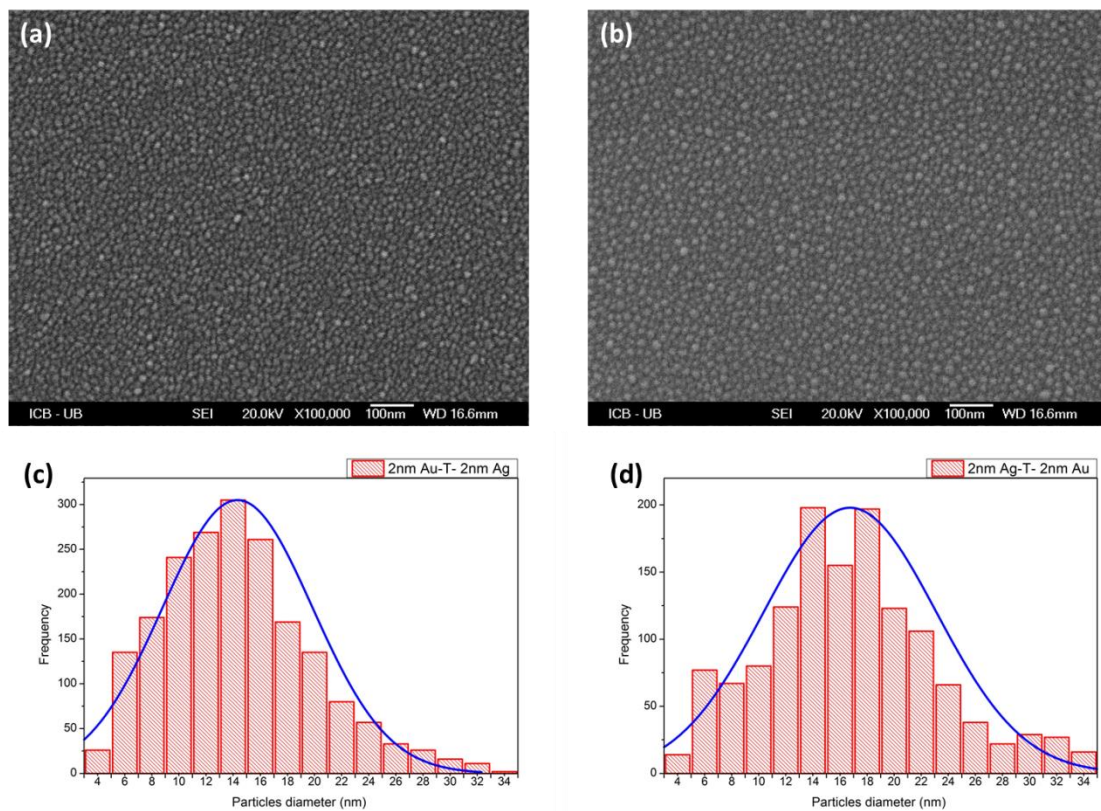


Figure III.6 SEM images of the (a) Au-T-Ag and (b) Ag-T-Au nanoparticles ; size distribution correspondent to the SEM images for the (c) Au-T-Ag and (d) Ag-T-Au nanoparticles

The nanoparticles size distribution presented in *Figure III.6 (c)* and *Figure III.6 (d)* were obtained by using the public software ImageJ developed at national institutes of health.⁷⁴

The Au-T-Ag and Ag-T-Au nanoparticles have average sizes of 14 nm and 16 nm in diameter, respectively. By assuming that all substrates exhibit similar sizes and surface coverage, we will focus on studying the LSPR spectral position for each substrate based on the metallic evaporation metal type and order.

Starting by doubled mono-metallic substrates, the Ag-T-Ag nanoparticles have a localized surface plasmon resonance at 469 nm in addition to a broad secondary resonance at 625 nm, *Figure III.7*. The Au-T-Au nanoparticles have an LSPR at 628 nm. As for hybrid doubled-bimetallic nanoparticles, Au-T-Ag and Ag-T-Au substrates have LSPR spectral positions at 599 nm and 710 nm respectively. For double evaporation system, the particles deposited from the first evaporation followed by thermal annealing can be referred as the as-synthesized core particles. As mentioned before, the metallic vapor have a higher tendency to bound to the metal than to the substrate,⁵² this leads to the formation of a shell over the core particles. For core/shell nanoparticles with shell thickness less than 4 nm, the plasmonic influence of the core material increases with decreasing the shell thickness.^{32,45-47} Knowing that the evaporated shell thickness in our substrates is 2 nm, this means that the shell thickness is small enough to allow the plasmonic influence of the core material to take place. The LSPR spectral position of the Au-T-Ag substrate lies between the LSPR of pure silver substrate (Ag-T-Ag) and that of pure gold substrate (Au-T-Au). This reveals the plasmonic effect of the core metal which is gold. For the Ag-T-Au NPs, the obtained LSPR position is red shifted in comparison to the Au-T-Ag NPs, which can be explained by the predominant plasmonic influence of the Au shell over the Ag core. The Ag-T-Au NPs have LSPR position even red shifted with respect to Au-T-Au NPs, which is not as expected since Ag-T-Au NPs should be blue shifted with respect to Au-T-Au NPs due to the presence of silver. This can be related to the slightly difference in the nanoparticles shape for the Ag-T-Au NPs in comparison to Au-T-Ag NPs. The Ag-T-Au NPs may have less height in its longitudinal axis causing expansion in the transverse plane. This transverse expansion will reduce the interparticle distance for the Ag-T-Au NPs, explaining the red shift in its LSPR. Additionally, we can notice that LSPR peak of bimetallic NPs are wider than those of monometallic NPs.

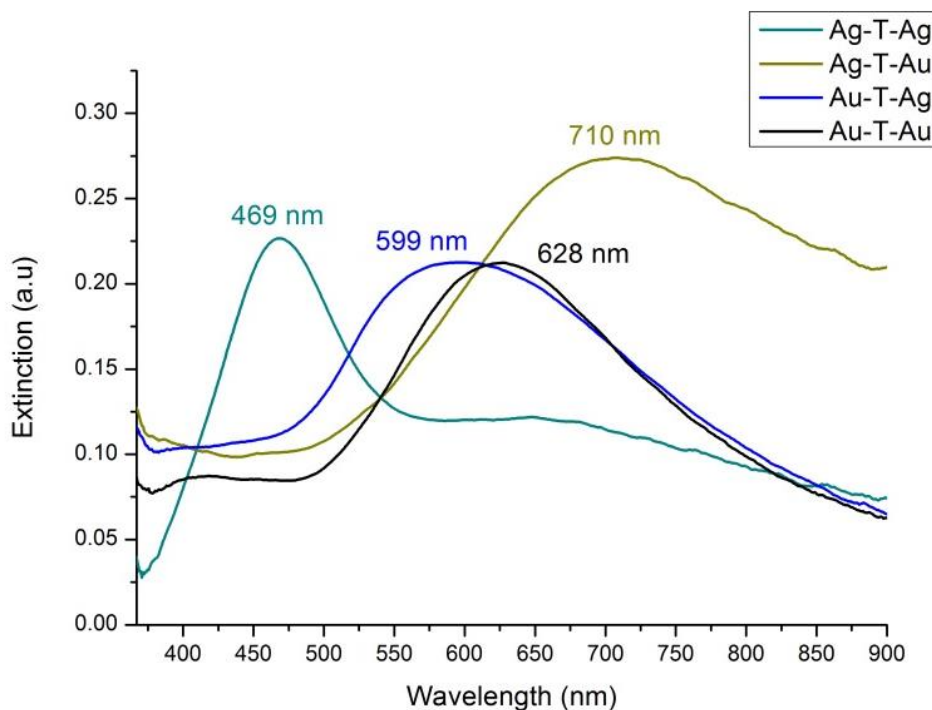


Figure III.7 LSPR spectra for the double-layered nanoparticles : Ag-T-Ag, Ag-T-Au, Au-T-Ag, and Au-T-Au substrates.

III.2.4 Localized surface plasmon resonance effect on surface enhanced Raman scattering

Surface enhanced Raman spectroscopy measurements were realized using the high-resolution Jobin Yvon-Horiba LABRAM. The Raman spectrometer is equipped with an Olympus optical microscope of objectives (10xNA 0.30, 50xNA 0.8, 100xNA 0.9), a red He-Ne laser (632.8 nm) with 20 mW power, a 600 lines/nm dispersive grating, an 800 mm path monochromator and a Peltier CDD detector (1024 x 256 pixels) of 16 bits dynamic range. The experimental parameters were adjusted as follows: the used objective was 10x, the pinhole was 1000 μm and the size of the slit was set at 100 μm with 10 seconds spectra acquisition time for a good S/N ratio. All SERS measurements were carried out after 1 minute of depositing the BPE drop (10 μl) on the substrate.

In order to determine the enhancement effect of the fabricated substrates, the normal Raman spectrum of BPE solution (0.1 M in ethanol-water 1:2 v/v) and the surface enhanced Raman spectrum of aqueous solution BPE (10^{-5} M) on the prepared substrates are presented in

Figure III.8. It should be noted that the Raman signal of BPE concentration used for the SERS measurements (10^{-5} M) could not be detected on pure glass in our experiments.

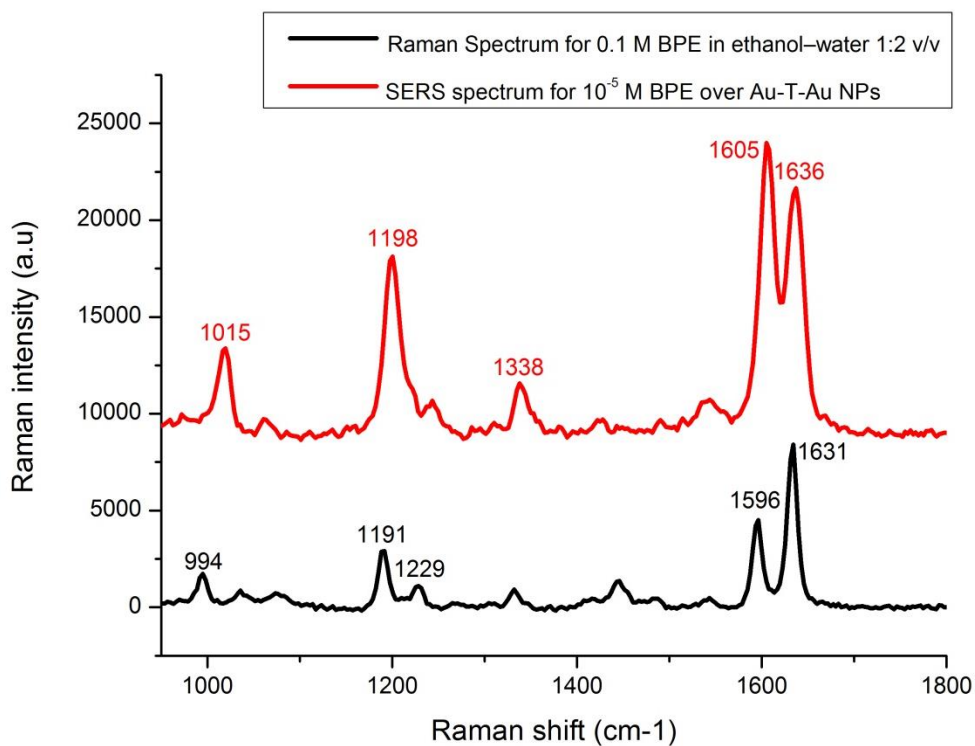


Figure III.8 Normal Raman spectra of 0.1 M BPE solution in ethanol-water 1:2 v/v and SERS spectrum of 10^{-5} M BPE solution measured over Au-T-Au substrate.

It is well known that frequency shifts, relative intensities and line widths of the Raman line characterize the Raman spectrum of a molecule.⁷⁵ *Figure III.8* shows the SERS spectrum of BPE (10^{-5} M) and the normal Raman spectrum of BPE (0.1 M). The detection of BPE signal adsorbed from the aqueous solution at such a low concentration ensures obtaining enhanced Raman spectrum. Both the Raman spectra of BPE and BPE adsorbed on the metallic nanoparticles are similar except for small shifts observed for the BPE SERS spectrum. This shifting in frequency or in the line width could be attributed to the interaction between the probe molecule and the metal nanoparticles.⁷⁵ The obtained SERS spectra of BPE are in good agreement with the reported spectra in the literature,⁷⁶⁻⁷⁸ where the characteristic BPE peaks; benzene ring breathing (1015 cm^{-1}), ring vibration (1198 cm^{-1}), in-plane CH bending of ethylene (1338 cm^{-1}), benzene ring stretching (1605 cm^{-1}) and C=C stretching mode (1636 cm^{-1}) are clearly present in all the spectra. After referring to the literature, the

most probable orientation of the adsorbed BPE molecule is assumed to be perpendicular to the surface.⁷⁹

Figure III.9 represents the SERS measurements for the BPE solution over the four prepared double layered bimetallic nanoparticle. Ag-T-Ag substrate shows the lowest enhancement between the four samples, whereas Au-T-Ag and Ag-T-Au nanoparticles provide moderate-similar enhancement. The highest SERS signal is obtained on the Au-T-Au substrate.

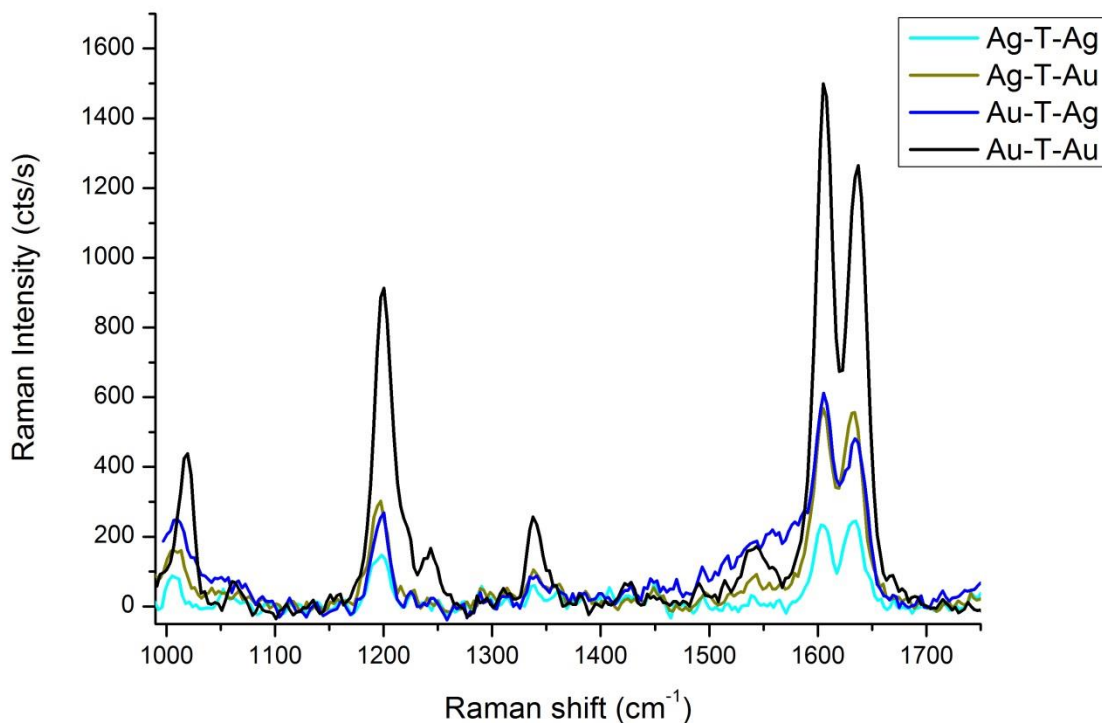


Figure III.9 The SERS spectra of 10^{-5} M BPE solution over Ag-T-Ag, Ag-T-Au, Au-T-Ag, and Au-T-Au substrates.

In order to evaluate the effect of the localized surface plasmon position on the Raman enhancements, the SERS intensities of the benzene ring stretching (1605 cm^{-1}) are plotted versus $\Delta\lambda$ (the absolute value of the difference between the Raman excitation wavelength (632.8 nm) and the LSPR resonance) for each of the four samples *Figure III.10*.

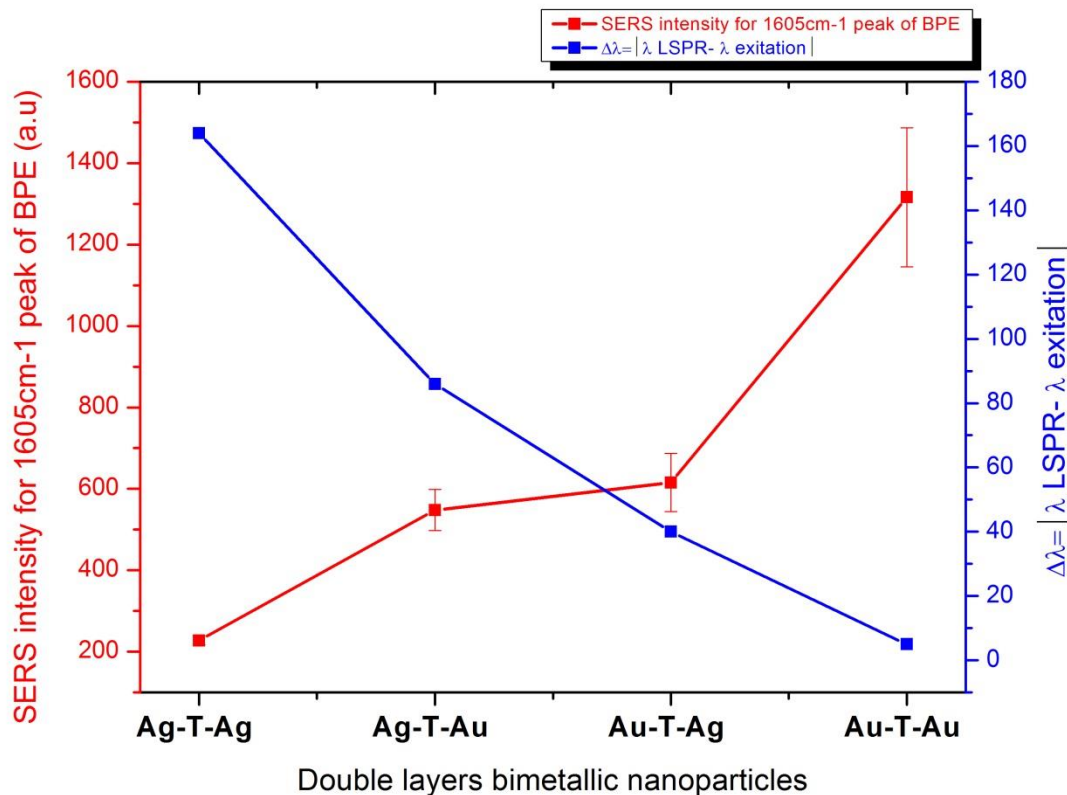


Figure III.10 The inversely proportional relation between SERS intensities of the benzene ring stretching (1605 cm^{-1}) and $\Delta\lambda$ (the difference between the Raman excitation wavelength, 632.8 nm , and the LSPR resonance) for Ag-T-Ag, Ag-T-Au, Au-T-Ag, and Au-T-Au substrates.

Clearly from the *Figure III.10*, we observe an inversely proportional relationship between the SERS intensity and $\Delta\lambda$. The substrate exhibiting the closest LSPR spectral position to the excitation wavelength provides the highest enhancement in Raman intensities which is the case for the Au-T-Au substrate. Even though silver nanoparticles are known to provide higher enhancements than their gold counterparts, however the Au-T-Au substrate which is constituted of pure gold only has showed the higher enhancement. This can be explained by two contributions. Firstly, the Au-T-Au NPs are characterized with LSPR spectral position closer to the excitation wave length. Secondly, the bimetallic NPs with the closest LSPR position (Au-T-Ag NPs) have broader peak than the Au-T-Au NPs which decrease its enhancing ability.

III.3 Three layered Au/Ag bimetallic nanoparticles

III.3.1 Fabrication of triple layer Au/Ag bimetallic nanoparticles

The nanoparticles studied in this part were fabricated following the same procedure described previously for the two layered bimetallic nanoparticles. However, three evaporation processes were conducted separated by two thermal annealing treatments. Four three layered nanoparticles have been fabricated which are represented as follows: Ag-T-Au-T-Au, Ag-T-Au-T-Ag, Au-T-Ag-T-Ag and Au-T-Ag-T-Au. All four samples have been fabricated according to the same experimental conditions of the two layered nanoparticles regarding the cleaning process, evaporation pressure, evaporation rate, thermal annealing temperature and time.

- The fabrication of Ag-T-Au-T-Au substrate started by evaporating thin silver film of 2 nm which is thermally annealed (250 °C for 20 seconds), followed by second evaporation of 2 nm thin gold film which was also thermally annealed (250 °C for 20 seconds) before the last evaporation step of 2 nm gold film.
- The Ag-T-Au-T-Ag substrate fabrication was carried out by a first evaporation of 2 nm of silver followed by 2 nm of gold separated by thermal annealing. Following this evaporation a second thermal annealing was realized. The third evaporation process consisted of evaporating thin silver film of 2 nm in thickness.
- The Au-T-Ag-T-Ag substrate fabrication is similar to that of the previous substrate, except for the type of the metal evaporated at each step, being separated by two thermal annealing after the deposition of the first (Au) and second (Ag) thin films, each with a thickness of 2 nm.
- The Au-T-Ag-T-Au substrate was also fabricated in the same manner with different order of evaporated metallic films (Au and Ag respectively). Similarly to the other substrates fabrication, the first and the second evaporation were followed by thermal annealing before the evaporation of the third layer (Au).

Full experimental details of the fabrication process are summarized in *Table III.3*.

Table III.3 Experimental details for fabricating the three layered bimetallic nanoparticles

		Ag-T-Au-T-	Ag-T-Au-T-	Au-T-Ag-T-	Au-T-Ag-T-
		Au	Ag	Ag	Au
First evaporation	Metal	Ag	Ag	Au	Au
	Thickness (nm)	2	2	2	2
First thermal annealing	Temperature (°C)	250	250	250	250
	Time (s)	20	20	20	20
Second evaporation	Metal	Au	Au	Ag	Ag
	Thickness (nm)	2	2	2	2
Second thermal annealing	Temperature (°C)	250	250	250	250
	Time (s)	20	20	20	20
Third evaporation	Metal	Au	Ag	Ag	Au
	Thickness (nm)	2	2	2	2

III.3.2 XPS measurements

Similarly to the double layered bimetallic nanoparticles, XPS technique was used to ensure the composition of the three layered bimetallic nanoparticles, shown in *Figure III.11* and *Figure III.12*. For calibration, the binding energy of the C1s hydrocarbons peak was set at 284.8 eV. The Ag3d pair peaks; Ag3d3/2 and Ag3d5/2; were obtained at 374 eV and 368 eV respectively. The Au4f pair peaks; Au4f3/2 and Au4f7/2; were obtained at 87.9 eV and 84.2 eV respectively.

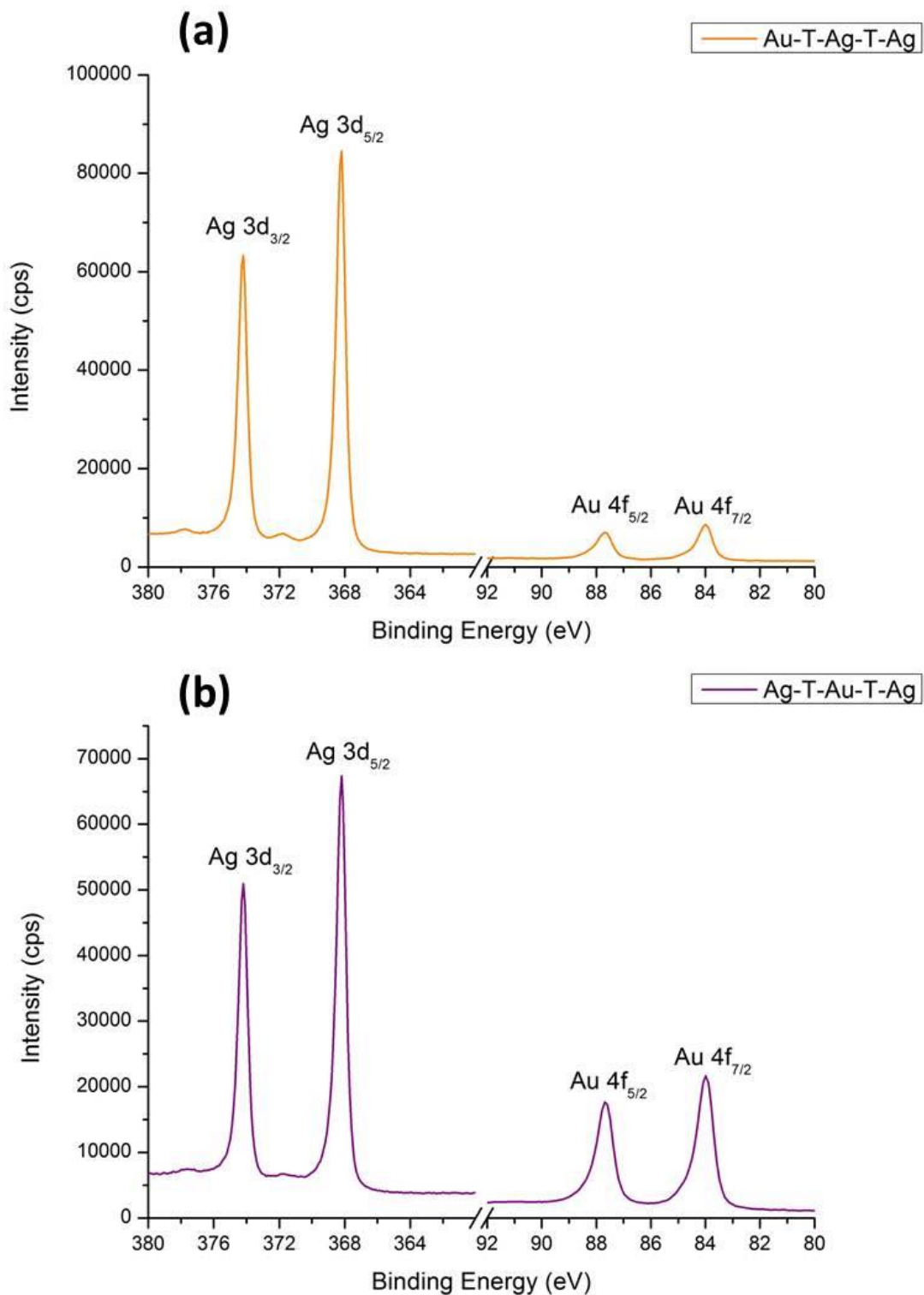


Figure III.11 X-ray photoelectron spectra for Au 4f and Ag 3d regions of the (a) Au-T-Ag-T-Ag and the (b) Ag-T-Au-T-Ag substrates.

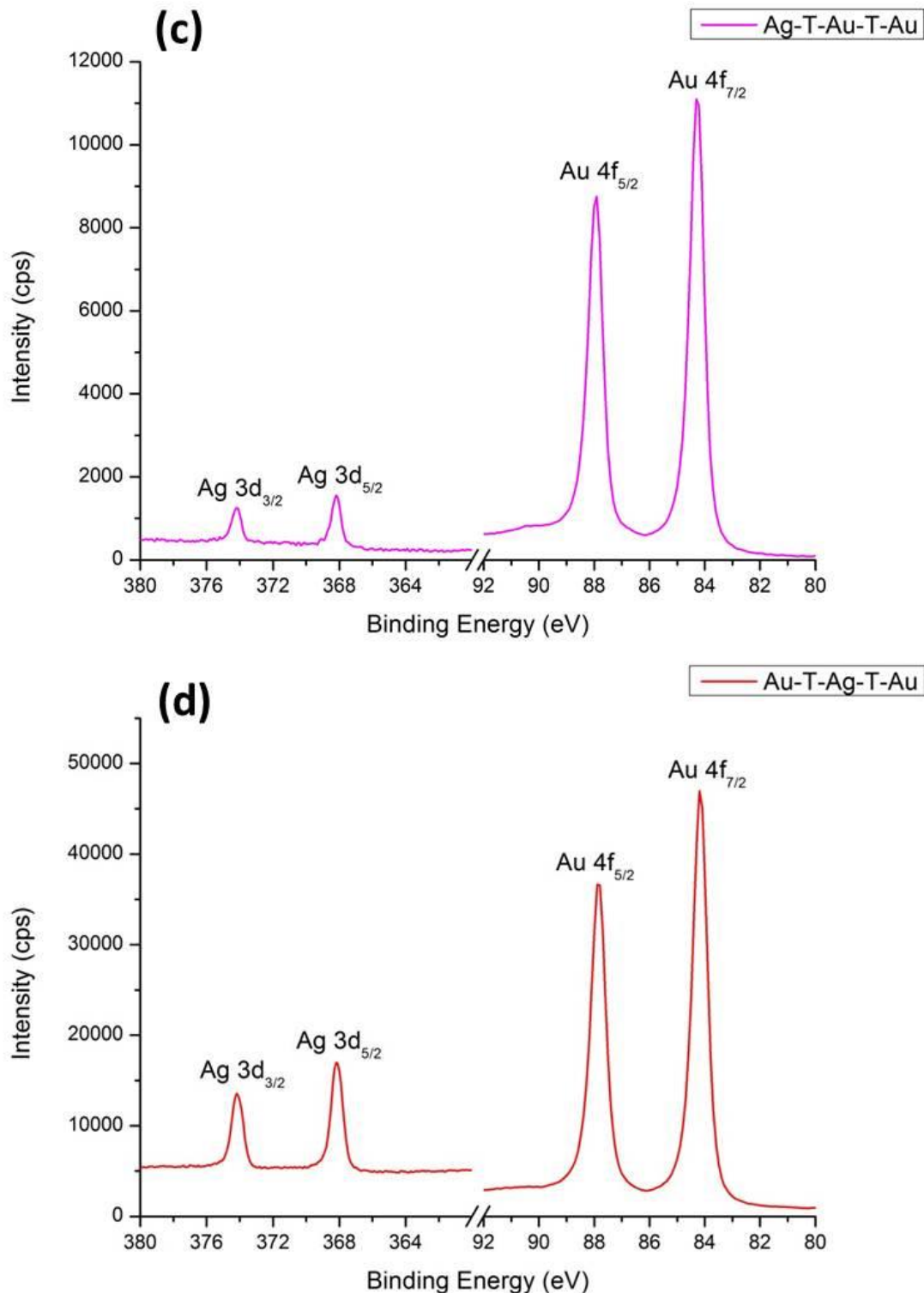


Figure III.12 X-ray photoelectron spectra for Au 4f and Ag 3d regions of the (c) Ag-T-Au-T-Au and the (d) Au-T-Ag-T-Au substrates.

The percentages of the silver and gold were calculated by integrating the area under the Ag3d and Au4f respectively. *Table III.4*, represents the full width at half maximum and the area under each peak for the Au-T-Ag-T-Ag, Ag-T-Au-T-Ag, Ag-T-Au-T-Au and Au-T-Ag-T-Au substrates with the relative atomic percentage of each metal.

Table III.4 The Ag 3d and Au 4f peaks positions, FWHM, area, and the percentage of Au and Ag in the Au-T-Ag-T-Ag, Ag-T-Au-T-Ag, Ag-T-Au-T-Au, and Au-T-Ag-T-Au substrates.

	Name	Position	FWHM ^{a)}	Area	At% ^{b)}
Au-T-Ag-T-	Ag 3d	368.8	2.522	168614	91.7
	Au4f	84.2	2.640	15797	8.3
Ag-T-Au-T-	Ag 3d	368.2	2.606	134050	74.5
	Au4f	84.2	3.013	47851	25.5
Ag-T-Au-T-	Ag 3d	368.2	2.674	2820	11.8
	Au4f	84.2	2.673	21090	88.2
Au-T-Ag-T-	Ag 3d	368.2	2.522	27754	23.8
	Au4f	84.2	2.687	92522	76.2

a) FWHM is the Full width at half maximum; b) At% is the metal percentage of Au and Ag

For the Au-T-Ag-T-Ag nanoparticles (fabricated by successive evaporation of 2nm gold, 2 nm silver and 2nm silver separated by thermal annealing), the estimated percentages of the metals for the Au-T-Ag-T-Ag is 33.33 % gold and 66.66% silver. Whereas the calculated percentages based on XPS analysis are 8.3% gold and 91.7 % silver. The over estimation of the silver percentage could be attributed to the fact that the last evaporated metal is silver and that XPS is a surface sensitive technique.

For the Ag-T-Au-T-Ag nanoparticles (fabricated by successive evaporation of 2nm gold, 2 nm silver and 2nm silver separated by thermal annealing), the calculated percentages of silver and gold are 74.5 % and 25.5 % respectively. Knowing that, based on the quantity of evaporated metals, estimated percentages of 66.66% silver and 33.33% gold were expected. The smaller difference between the expected and calculated percentages obtained for the Ag-T-Au-T-Ag substrate when compared with that of Au-T-Ag-T-Ag substrate could be explained by the order of metals evaporation. Where, for the Ag-T-Au-T-Ag substrate gold is

presented in a position closer to the surface and encapsulated with one silver layer rather than two silver layers (the case of gold in Au-T-Ag-T-Ag substrate).

Ag-T-Au-T-Au nanoparticles were prepared by evaporating 2 nm silver followed by two successive evaporation of 2 nm gold. The metallic percentages expected based on the sample's composition are 33.33 % silver and 66.66 % gold. Meanwhile, the calculated metallic percentages are 11.8 % silver and 88.2 % gold. According to the same effect that explain the over estimation of silver versus gold for the Au-T-Ag-T-Ag substrate, we can explain the difference observed for the Ag-T-Au-T-Au substrate.

Similarly to the Ag-T-Au-T-Ag substrate, Ag-T-Au-T-Ag nanoparticles have a slight difference between the expected and calculated percentages. However, the calculated percentages of the metals are 23.8% silver and 76.2 % gold. Based on XPS characteristics, one can claim that the presence of silver as the last evaporated metal is the reason for this difference.

III.3.3 Localized surface plasmon resonance tunability for triple-layered bimetallic nanoparticles

The LSPR measurements for the triple-layer bimetallic nanoparticles were realized using the transmission UV-Vis-NIR spectroscopy under the same experimental conditions described before for the double layer substrates. Assuming that all the four substrates have the same size and surface coverage, the LSPR spectral position were then studied based on the nature of the evaporated metals and their order.

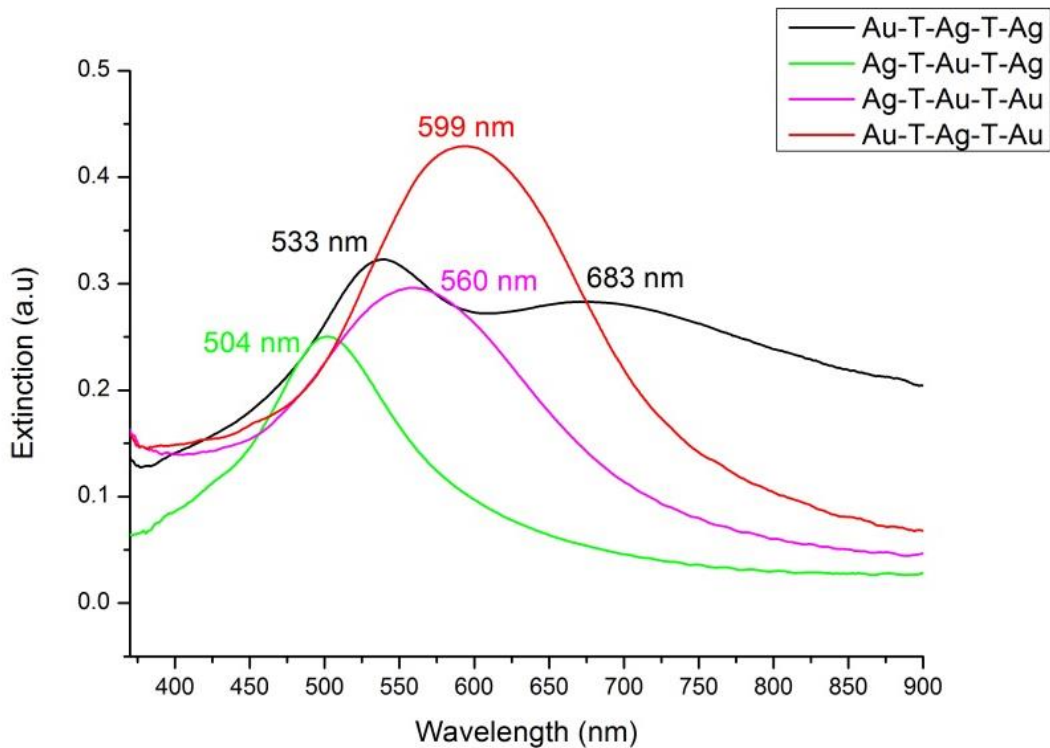


Figure III.13 LSPR spectra for the three-layered bimetallic nanoparticles : Au-T-Ag-T-Ag, Ag-T-Au-T-Ag, Ag-T-Au-T-Au, and Au-T-Ag-T-Au substrates.

Figure III.13 shows the LSPR spectral positions for each of the four substrates. For studying the effect of the evaporated percentage of each metal on the LSPR position, we compare the substrates having different metallic percentages of gold and silver. For Ag-T-Au-T-Ag and Ag-T-Au-T-Au substrates, they have metallic ratios of 2/3Ag:1/3Au and 1/3Ag:2/3Au respectively, with an LSPR position at 504 nm for the Ag-T-Au-T-Ag nanoparticles and 560 nm for Ag-T-Au-T-Au nanoparticles. This shows that with increasing gold percentage within the nanoparticle, a red shift in LSPR is obtained.

Similarly, Au-T-Ag-T-Ag NPs and Au-T-Ag-T-Au NPs exhibit metallic ratios of 2/3Ag:1/3Au and 1/3Ag :2/3Au respectively. The red shift observed for the Au-T-Ag-T-Au NPs at LSPR of 599 nm compared to Au-T-Ag-T-Ag NPs at LSPR of 533 nm could be attributed to the increase in its gold content.

Now we take into consideration the effect of the metal evaporation order on the LSPR position. Ag-T-Au-T-Ag and Au-T-Ag-T-Ag have the same metallic ratio of 2/3Ag and 1/3Au, but with different evaporation order. The Ag-T-Au-T-Ag have LSPR position at 504

nm while that of Au-T-Ag-T-Ag NPs is at 533 nm. This red shift observed for the Au-T-Ag-T-Ag reveals a higher plasmonic effect of the first layer than the second layer. In other words, the presence of gold in the first layer affects the plasmonic resonance more than its presence in the second layer. Similarly by comparing Ag-T-Au-T-Au and Au-T-Ag-T-Au NPs having LSPR positions at 560 nm and 599 nm, higher plasmonic effect is observed when silver is present in the first layer than in the second layer (blue shift). More importantly, the stronger effect of the third evaporated layer can be revealed after comparing Au-T-Ag-T-Ag NPs with Au-T-Ag-T-Au NPs or Ag-T-Au-T-Ag NPs with Ag-T-Au-T-Au NPs, having LSPR differences of 66 nm and 56 nm, respectively. Thus, the layer composition effect on the LSPR spectral position follows this ascending order, middle, first then the third layer.

III.3.4 Localized surface plasmon resonance effect on surface enhanced Raman scattering

The question arises if the triple layered system succeeded in providing bimetallic substrate containing silver and having LSPR position in the range of the excitation wavelength for high enhancement ability in SERS. To answer this question, SERS measurements have been carried out on the four triple-layered bimetallic substrates following the same experimental parameters of the double-layer substrates. The acquisition time was set to 10 seconds for all the samples except the Au-T-Ag-T-Au substrate which was set to 5 seconds due to the saturation in Raman intensity observed for an acquisition time of 10 seconds.

Figure III.14 represents the SERS measurements for the BPE solution (10^{-5} M) over the four fabricated triple-layered bimetallic nanoparticles. The Au-T-Ag-T-Ag substrate shows the lowest SERS signal, whereas Ag-T-Au-T-Ag provides slightly higher enhancement signal. Ag-T-Au-T-Au nanoparticles have moderate signal, meanwhile the highest SERS signal is obtained over the Au-T-Ag-T-Au substrate.

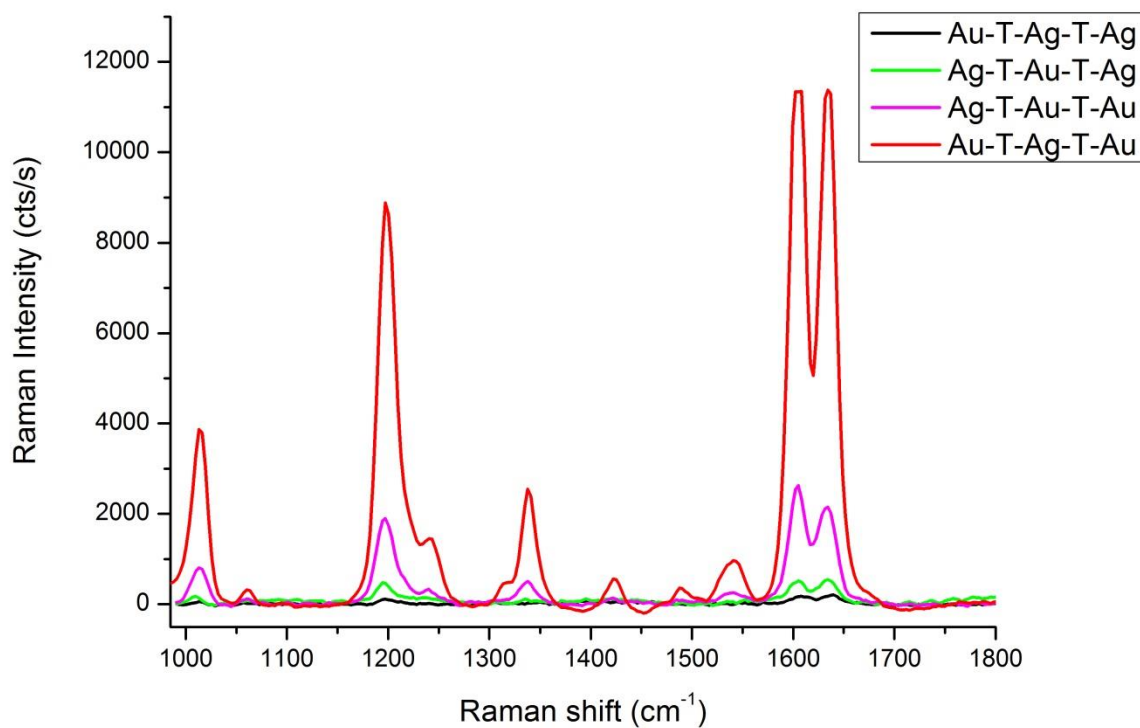


Figure III.14 The SERS spectra of 10^{-5} M BPE solution over Au-T-Ag-T-Ag, Ag-T-Au-T-Ag, Ag-T-Au-T-Au, and Au-T-Ag-T-Au substrates.

In order to monitor the relation between the enhancing ability of the substrates in comparison with their LSPR positions, the SERS intensity of the benzene ring stretching (1605 cm^{-1}) are plotted versus $\Delta\lambda$ (the difference between the LSPR and the excitation wavelengths) for each of the four substrates *Figure III.15*

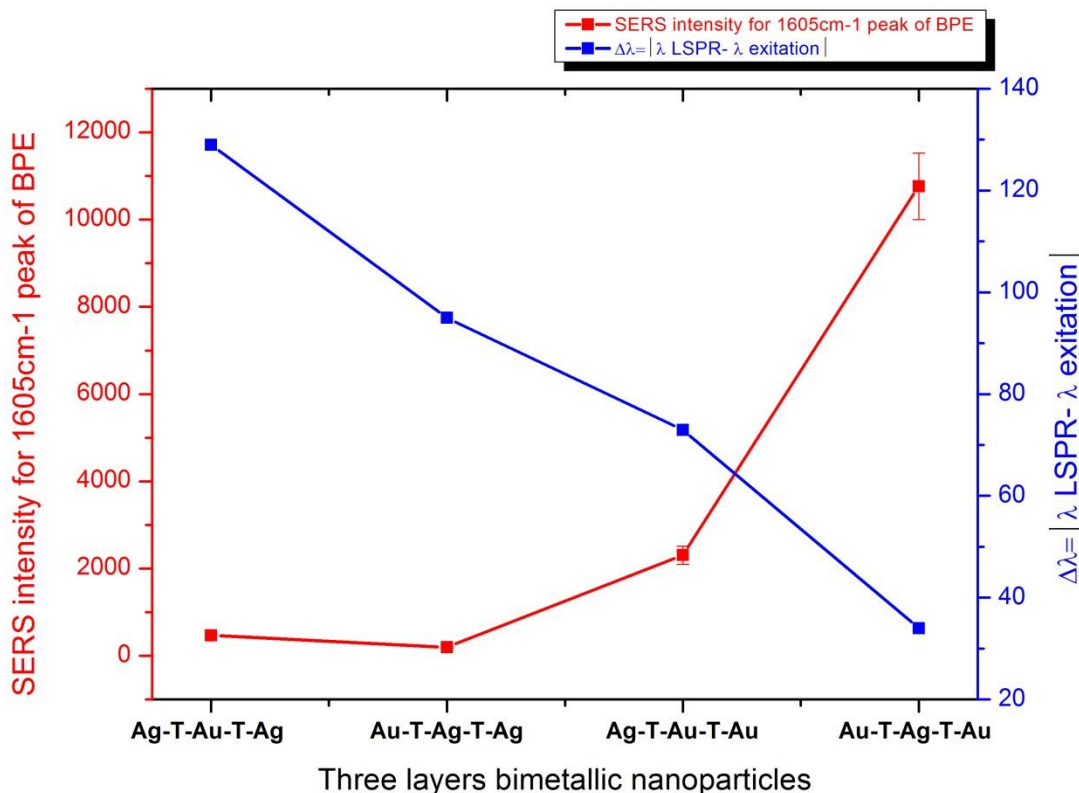


Figure III.15 The inversely proportional relation between SERS intensities of the benzene ring stretching (1605 cm^{-1}) and $\Delta\lambda$ (the absolute value for the difference between the Raman excitation wavelength, 632.8 nm , and the LSPR resonance) for Au-T-Ag-T-Ag, Ag-T-Au-T-Ag, Ag-T-Au-T-Au, and Au-T-Ag-T-Au substrates.

Similarly to double layered system, an inversely proportional relation between the SERS intensity and $\Delta\lambda$ was obtained also for the three layered system. The Au-T-Ag-T-Au system exhibit the smallest $\Delta\lambda$ with an LSPR spectral position at 599 nm , with an optical density of 0.47 provides the highest SERS signal.

III.4 Two layered Ag/Au nanoparticles vs three layered nanoparticles in the surface enhanced Raman spectroscopy according to their enhancing ability

By comparing the substrates within the two-layered and three-layered systems separately, we observe that the SERS enhancement ability is directly related to their LSPR positions and it degree of closeness to the excitation wavelength. However, regarding the two systems together, we observe that the inversely proportional relationship between the SERS signal intensity and $\Delta\lambda$ becomes no more valid. By comparing the best substrates obtained within each system we observe that, Au-T-Au substrate have lower SERS signal intensity

than that of Au-T-Ag-T-Au, despite having an LSPR at 628 nm which is in perfect resonance with the excitation wavelength (632.8 nm), whereas an LSPR of 599 nm was obtained for the Au-T-Ag-T-Au nanoparticles.

In addition, the comparison of the Au-T-Ag-T-Au and Au-T-Ag substrates where both have an LSPR of 599 nm, we observe that Au-T-Ag-T-Au substrate shows much more enhancing ability.

The superiority of the triple-layer system over the double layered-system originates from the difference in the interparticle coupling effect for each system. Based on the SEM imaging, the double layer system have nanoparticles with average diameter size of 16 nm with 41% surface coverage, while an average size of 22 nm and surface coverage of 49 % were obtained for the triple layer system, *Figure III.16*. The increase in particle size and surface coverage results in higher interparticle coupling effect due to the decrease in the interparticle distances. Accordingly, the substrates of the triple layer system have more efficient “hot-spots” than the substrates of the double layer system, explaining the higher SERS enhancement over the triple layer system than over the double layer one.

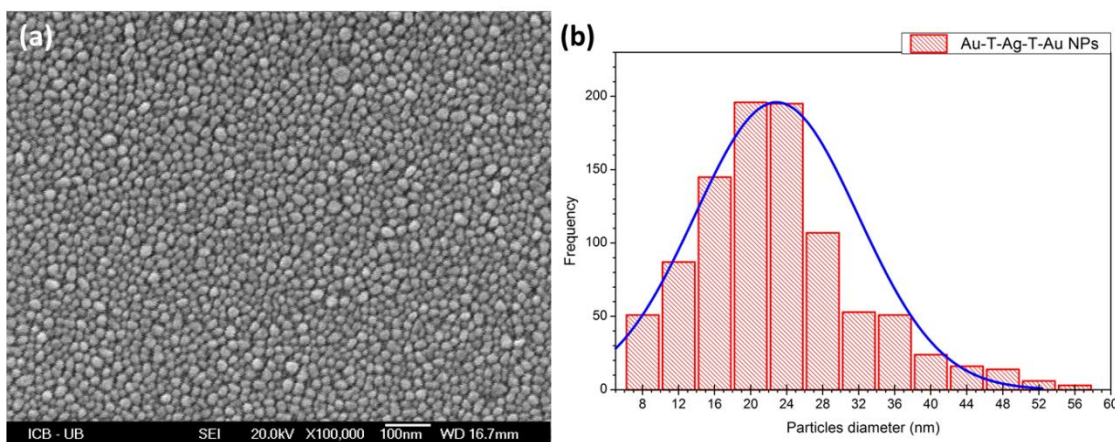


Figure III.16 SEM image (a) and the size distribution (b) of the Au-T-Ag-Au nanoparticles

References

1. Tan, T. *et al.* LSPR-dependent SERS performance of silver nanoplates with highly stable and broad tunable LSPRs prepared through an improved seed-mediated strategy. *Phys. Chem. Chem. Phys.* **15**, 21034–21042 (2013).
2. Srnová-Šloufová, I., Vlčková, B., Bastl, Z. & Hasslett, T. L. Bimetallic (Ag)Au Nanoparticles Prepared by the Seed Growth Method: Two-Dimensional Assembling, Characterization by Energy Dispersive X-ray Analysis, X-ray Photoelectron Spectroscopy, and Surface Enhanced Raman Spectroscopy, and Proposed Mechanism of Gro. *Langmuir* **20**, 3407–3415 (2004).
3. Yang, Y., Shi, J., Kawamura, G. & Nogami, M. Preparation of Au–Ag, Ag–Au core–shell bimetallic nanoparticles for surface-enhanced Raman scattering. *Scr. Mater.* **58**, 862–865 (2008).
4. Link, S., Wang, Z. L. & El-Sayed, M. A. Alloy Formation of Gold–Silver Nanoparticles and the Dependence of the Plasmon Absorption on Their Composition. *J. Phys. Chem. B* **103**, 3529–3533 (1999).
5. Rodriguez-Gonzalez, B., Sanchez-Iglesias, A., Giersig, M. & Liz-Marzan, L. M. AuAg bimetallic nanoparticles: formation, silica-coating and selective etching. *Faraday Discuss.* **125**, 133–144 (2004).
6. Rycenga, M. *et al.* Probing the surface-enhanced Raman scattering properties of Au–Ag nanocages at two different excitation wavelengths. *Phys. Chem. Chem. Phys.* **11**, 5903–5908 (2009).
7. Pellegrini, G., Bello, V., Mattei, G. & Mazzoldi, P. Local-field enhancement and plasmon tuning in bimetallic nanoplanets. *Opt. Express* **15**, 10097–10102 (2007).
8. Henglein, A. Physicochemical properties of small metal particles in solution: “microelectrode” reactions, chemisorption, composite metal particles, and the atom-to-metal transition. *J. Phys. Chem.* **97**, 5457–5471 (1993).
9. Henglein, A. Small-particle research: physicochemical properties of extremely small colloidal metal and semiconductor particles. *Chem. Rev.* **89**, 1861–1873 (1989).
10. Alivisatos, A. P. Perspectives on the Physical Chemistry of Semiconductor Nanocrystals. *J. Phys. Chem.* **100**, 13226–13239 (1996).
11. Stamenkovic, V. R. *et al.* Improved Oxygen Reduction Activity on Pt₃Ni(111) via Increased Surface Site Availability. *Sci.* **315**, 493–497 (2007).
12. Maksimuk, S., Yang, S., Peng, Z. & Yang, H. Synthesis and Characterization of Ordered Intermetallic PtPb Nanorods. *J. Am. Chem. Soc.* **129**, 8684–8685 (2007).

13. Yang, S., Peng, Z. & Yang, H. Platinum Lead Nanostructures: Formation, Phase Behavior, and Electrocatalytic Properties. *Adv. Funct. Mater.* **18**, 2745–2753 (2008).
14. Yen, C.-W. *et al.* CO Oxidation Catalyzed by Au–Ag Bimetallic Nanoparticles Supported in Mesoporous Silica. *J. Phys. Chem. C* **113**, 17831–17839 (2009).
15. Liu, J.-H., Wang, A.-Q., Chi, Y.-S., Lin, H.-P. & Mou, C.-Y. Synergistic Effect in an Au–Ag Alloy Nanocatalyst: CO Oxidation. *J. Phys. Chem. B* **109**, 40–43 (2004).
16. Wang, C., Daimon, H., Onodera, T., Koda, T. & Sun, S. A General Approach to the Size- and Shape-Controlled Synthesis of Platinum Nanoparticles and Their Catalytic Reduction of Oxygen. *Angew. Chemie Int. Ed.* **47**, 3588–3591 (2008).
17. Yano, K. *et al.* Synthesis and Characterization of Magnetic FePt/Au Core/Shell Nanoparticles. *J. Phys. Chem. C* **113**, 13088–13091 (2009).
18. Xia, Y., Xiong, Y., Lim, B. & Skrabalak, S. E. Shape-Controlled Synthesis of Metal Nanocrystals: Simple Chemistry Meets Complex Physics? *Angew. Chemie Int. Ed.* **48**, 60–103 (2009).
19. Costi, R., Saunders, A. E. & Banin, U. Colloidal Hybrid Nanostructures: A New Type of Functional Materials. *Angew. Chemie Int. Ed.* **49**, 4878–4897 (2010).
20. Katz, E. & Willner, I. Integrated Nanoparticle–Biomolecule Hybrid Systems: Synthesis, Properties, and Applications. *Angew. Chemie Int. Ed.* **43**, 6042–6108 (2004).
21. Cozzoli, P. D., Pellegrino, T. & Manna, L. Synthesis, properties and perspectives of hybrid nanocrystal structures. *Chem. Soc. Rev.* **35**, 1195–1208 (2006).
22. Sanvicens, N. & Marco, M. P. Multifunctional nanoparticles – properties and prospects for their use in human medicine. *Trends Biotechnol.* **26**, 425–433 (2008).
23. Zeng, H. & Sun, S. Syntheses, Properties, and Potential Applications of Multicomponent Magnetic Nanoparticles. *Adv. Funct. Mater.* **18**, 391–400 (2008).
24. Wang, C., Xu, C., Zeng, H. & Sun, S. Recent Progress in Syntheses and Applications of Dumbbell-like Nanoparticles. *Adv. Mater.* **21**, 3045–3052 (2009).
25. Cortie, M. B. & McDonagh, A. M. Synthesis and Optical Properties of Hybrid and Alloy Plasmonic Nanoparticles. *Chem. Rev.* **111**, 3713–3735 (2011).
26. Wu, L. *et al.* A SERS-based immunoassay with highly increased sensitivity using gold/silver core-shell nanorods. *Biosens. Bioelectron.* **38**, 94–99 (2012).
27. Ji, X. *et al.* Immunoassay using the probe-labeled Au/Ag core-shell nanoparticles based on surface-enhanced Raman scattering. *Colloids Surfaces A Physicochem. Eng. Asp.* **257–258**, 171–175 (2005).
28. Xiong, B. *et al.* Highly sensitive sulphide mapping in live cells by kinetic spectral analysis of single Au–Ag core-shell nanoparticles. *Nat Commun* **4**, 1708 (2013).

29. Wang, H., Liu, J., Wu, X., Tong, Z. & Deng, Z. Tailor-made Au@Ag core–shell nanoparticle 2D arrays on protein-coated graphene oxide with assembly enhanced antibacterial activity. *Nanotechnology* **24**, 205102 (2013).
30. Quinten, M. The color of finely dispersed nanoparticles. *Appl. Phys. B* **73**, 317–326 (2001).
31. Pustovalov, V. & Fritzsche, W. Nonlinear Dependences of Optical Properties of Spherical Core–Shell Silver–Gold and Gold–Silver Nanoparticles on Their Parameters. *Plasmonics* **8**, 983–993 (2013).
32. Pustovalov, V. K., Astafyeva, L. G. & Fritzsche, W. Optical Properties of Core–Shell Gold–Silver and Silver–Gold Nanoparticles for Near UV and Visible Radiation Wavelengths. *Plasmonics* **7**, 469–474 (2012).
33. Zheng, X. *et al.* High performance Au/Ag core/shell bipyramids for determination of thiram based on surface-enhanced Raman scattering. *J. Raman Spectrosc.* **43**, 1374–1380 (2012).
34. Kreibig, U. & Zacharias, P. Surface plasma resonances in small spherical silver and gold particles. *Zeitschrift für Phys.* **231**, 128–143 (1970).
35. Rodriguez-Gonzalez, B., Burrows, A., Watanabe, M., Kiely, C. J. & Liz Marzan, L. M. Multishell bimetallic AuAg nanoparticles: synthesis, structure and optical properties. *J. Mater. Chem.* **15**, 1755–1759 (2005).
36. Csapó, E. *et al.* Synthesis and characterization of Ag/Au alloy and core(Ag)–shell(Au) nanoparticles. *Colloids Surfaces A Physicochem. Eng. Asp.* **415**, 281–287 (2012).
37. Sanyal, U., Davis, D. T. & Jagirdar, B. R. Bimetallic core-shell nanocomposites using weak reducing agent and their transformation to alloy nanostructures. *Dalt. Trans.* **42**, 7147–7157 (2013).
38. Mulvaney, P. Surface Plasmon Spectroscopy of Nanosized Metal Particles. *Langmuir* **12**, 788–800 (1996).
39. Morriss, R. H. & Collins, L. F. Optical Properties of Multilayer Colloids. *J. Chem. Phys.* **41**, (1964).
40. Mulvaney, P., Giersig, M. & Henglein, A. Surface chemistry of colloidal gold: deposition of lead and accompanying optical effects. *J. Phys. Chem.* **96**, 10419–10424 (1992).
41. Mulvaney, P., Giersig, M. & Henglein, A. Electrochemistry of multilayer colloids: preparation and absorption spectrum of gold-coated silver particles. *J. Phys. Chem.* **97**, 7061–7064 (1993).
42. Srnová-Šloufová, I., Lednický, F., Gemperle, A. & Gemperlová, J. Core–Shell (Ag)Au Bimetallic Nanoparticles: Analysis of Transmission Electron Microscopy Images. *Langmuir* **16**, 9928–9935 (2000).

43. Lu, L. *et al.* Seed-mediated growth of large, monodisperse core-shell gold-silver nanoparticles with Ag-like optical properties. *Chem. Commun.* 144–145 (2002). doi:10.1039/B108473A
44. Rivas, L., Sanchez-Cortes, S., García-Ramos, J. V & Morcillo, G. Mixed Silver/Gold Colloids: A Study of Their Formation, Morphology, and Surface-Enhanced Raman Activity. *Langmuir* **16**, 9722–9728 (2000).
45. Bruzzone, S., Arrighini, G. P. & Guidotti, C. Theoretical study of the optical absorption behavior of Au/Ag core–shell nanoparticles. *Mater. Sci. Eng. C* **23**, 965–970 (2003).
46. Chen, Y. *et al.* The Study of Surface Plasmon in Au/Ag Core/Shell Compound Nanoparticles. *Plasmonics* **7**, 509–513 (2012).
47. Jiang, R., Chen, H., Shao, L., Li, Q. & Wang, J. Unraveling the Evolution and Nature of the Plasmons in (Au Core)-(Ag Shell) Nanorods. *Adv. Mater.* **24**, OP200–OP207 (2012).
48. Lewis, B. & Anderson, J. C. *Nucleation and Growth of Thin Films*. (Academic Press, London, 1978).
49. Oura, K., Lifshits, V. G., Saranin, A., Zotov, A. V. & Katayama, M. *Surface Science*. (Springer-Verlag, 2003).
50. Pimpinelli, A. & Villain, J. *Physics of Crystal Growth*. (Cambridge: Cambridge University Press, 1998).
51. Venables, J. A. *Introduction to Surface and Thin Film Processes*. (Cambridge: Cambridge University Press, 2000).
52. Ohring, M. *Materials Science of Thin Films Deposition and Structure*. (Academic Press, London, 2002).
53. Romanyuk, V. R., Kondratenko, O. S., Kondratenko, S. V, Kotko, A. V & Dmitruk, N. L. Transformation of thin gold films morphology and tuning of surface plasmon resonance by post-growth thermal processing. *Eur. Phys. J. - Appl. Phys.* **56**, null–null (2011).
54. Thompson, C. V. Grain Growth in Thin Films. *Annu. Rev. Mater. Sci.* **20**, 245–268 (1990).
55. Kennefick, C. M. & Raj, R. Copper on sapphire: Stability of thin films at 0.7 Tm. *Acta Metall.* **37**, 2947–2952 (1989).
56. Semin, D. J., Lo, A., Roark, S. E., Skodje, R. T. & Rowlen, K. L. Time- dependent morphology changes in thin silver films on mica: A scaling analysis of atomic force microscopy results. *J. Chem. Phys.* **105**, (1996).

57. Presland, A. E. B., Price, G. L. & Trimm, D. L. The role of microstructure and surface energy in hole growth and island formation in thin silver films. *Surf. Sci.* **29**, 435–446 (1972).
58. Rost, M. J., Quist, D. A. & Frenken, J. W. M. Grains, Growth, and Grooving. *Phys. Rev. Lett.* **91**, 26101 (2003).
59. Stranahan, S. M. & Willets, K. A. Super-resolution Optical Imaging of Single-Molecule SERS Hot Spots. *NANO Lett.* **10**, 3777–3784 (2010).
60. Hövel, M., Gompf, B. & Dressel, M. Dielectric properties of ultrathin metal films around the percolation threshold. *Phys. Rev. B* **81**, 35402 (2010).
61. Yagil, Y. & Deutscher, G. Transmittance of thin metal films near the percolation threshold. *Thin Solid Films* **152**, 465–471 (1987).
62. Boyen, H.-G. *et al.* Oxidation-Resistant Gold-55 Clusters. *Sci.* **297**, 1533–1536 (2002).
63. Cao, Y. W., Din, R. C. & Mirkin, C. A. Ag/Au coreshell nanocrystal as a biological marker. *Abstr. Pap. Am. Chem. Soc.* **222**, (2001).
64. Dabbousi, B. O. *et al.* (CdSe)ZnS core-shell quantum dots: Synthesis and characterization of a size series of highly luminescent nanocrystallites. *J. Phys. Chem. B* **101**, 9463–9475 (1997).
65. Katari, J. E. B., Colvin, V. L. & Alivisatos, A. P. X-ray Photoelectron Spectroscopy of CdSe Nanocrystals with Applications to Studies of the Nanocrystal Surface. *J. Phys. Chem.* **98**, 4109–4117 (1994).
66. Koktysh, D. S. *et al.* Biomaterials by design: Layer-by-layer assembled ion-selective and biocompatible films of TiO₂ nanoshells for neurochemical monitoring. *Adv. Funct. Mater.* **12**, 255–265 (2002).
67. Liu, S. Y., Ma, Y. H. & Armes, S. P. Direct verification of the core-shell structure of shell cross-linked micelles in the solid state using X-ray photoelectron spectroscopy. *LANGMUIR* **18**, 7780–7784 (2002).
68. Liu, Y. C. & Chuang, T. C. Synthesis and characterization of Gold/Polyppyrrole core-shell nanocomposites and elemental gold nanoparticles based on the gold-containing nanocomplexes prepared by electrochemical methods in aqueous solutions. *J. Phys. Chem. B* **107**, 12383–12386 (2003).
69. Piyakis, K. N., Yang, D. Q. & Sacher, E. The applicability of angle-resolved XPS to the characterization of clusters on surfaces. *Surf. Sci.* **536**, 139–144 (2003).
70. Wertheim, G. K. & Dicenzo, S. B. Cluster growth and core-electron binding energies in supported metal clusters. *Phys. Rev. B* **37**, 844–847 (1988).

71. Yang, D. Q., Gillet, J. N., Meunier, M. & Sacher, E. Room temperature oxidation kinetics of Si nanoparticles in air, determined by x-ray photoelectron spectroscopy. *J. Appl. Phys.* **97**, (2005).
72. Yang, D. Q., Meunier, M. & Sacher, E. The surface modification of nanoporous SiO_x thin films with a monofunctional organosilane. *Appl. Surf. Sci.* **252**, 1197–1201 (2005).
73. Hajati, S. & Tougaard, S. XPS for non-destructive depth profiling and 3D imaging of surface nanostructures. *Anal. Bioanal. Chem.* **396**, 2741–2755 (2010).
74. ImageJ. . at <<http://imagej.nih.gov/ij/>>
75. Kneipp, K., Kneipp, H., Itzkan, I., Dasari, R. R. & Feld, M. S. Surface-enhanced Raman scattering and biophysics. *J. Phys. Condens. Matter* **14**, R597 (2002).
76. Félidj, N. *et al.* Gold particle interaction in regular arrays probed by surface enhanced Raman scattering. *J. Chem. Phys.* **120**, (2004).
77. Félidj, N. *et al.* Optimized surface-enhanced Raman scattering on gold nanoparticle arrays. *Appl. Phys. Lett.* **82**, (2003).
78. Suzuki, M. *et al.* A study on the adsorption structure of an adhesive monomer for precious metals by surface-enhanced Raman scattering spectroscopy. *Biomaterials* **20**, 839–845 (1999).
79. Yang, W., Hulteen, J., Schatz, G. C. & Van Duyne, R. P. A surface-enhanced hyper-Raman and surface-enhanced Raman scattering study of trans-1,2-bis(4-pyridyl)ethylene adsorbed onto silver film over nanosphere electrodes. Vibrational assignments: Experiment and theory. *J. Chem. Phys.* **104**, (1996).

Chapter IV

*Improving the Sensitivity of Au/Ag
Bimetallic Nanoparticles Substrates
for SERS Application*

IV.1 Introduction

Following the work realized in the previous chapter and knowing that the highest SERS enhancement has been obtained over the Au-T-Ag-T-Au substrate, we aim in this chapter to study this substrate in more details, willing to understand the reason for such an enhancement, in addition for studying the improvements of its SERS sensitivity.

Firstly we will study the effect of each fabrication step on the SERS enhancement using morphological characterization and extinction spectroscopy. Secondly we will follow the effect of evaporated thickness, thermal annealing temperature and coupling with metallic film in improving the Au-T-Ag-T-Au substrate.

IV.2 Au-Ag/Au core/shell bimetallic nanoparticles

IV.2.1 Morphological study

For a better understanding of the Au-T-Ag-T-Au nanoparticles behavior in SERS enhancement, we monitor the morphological changes during the fabrication steps. The Au-T-Ag-T-Au where fabricated by the successive evaporation of Au, Ag and Au layers separated by thermal annealing, these are presented by Au-T NPs, Au-T-Ag NPs and Au-T-Ag-T-Au NPs. The SEM images following each fabrication step are illustrated in *Figure IV.1 (a), 1(b) and 1(c)*, respectively representing Au-T NPs, Au-T-Ag NPs and Au-T-Ag-T-Au NPs.

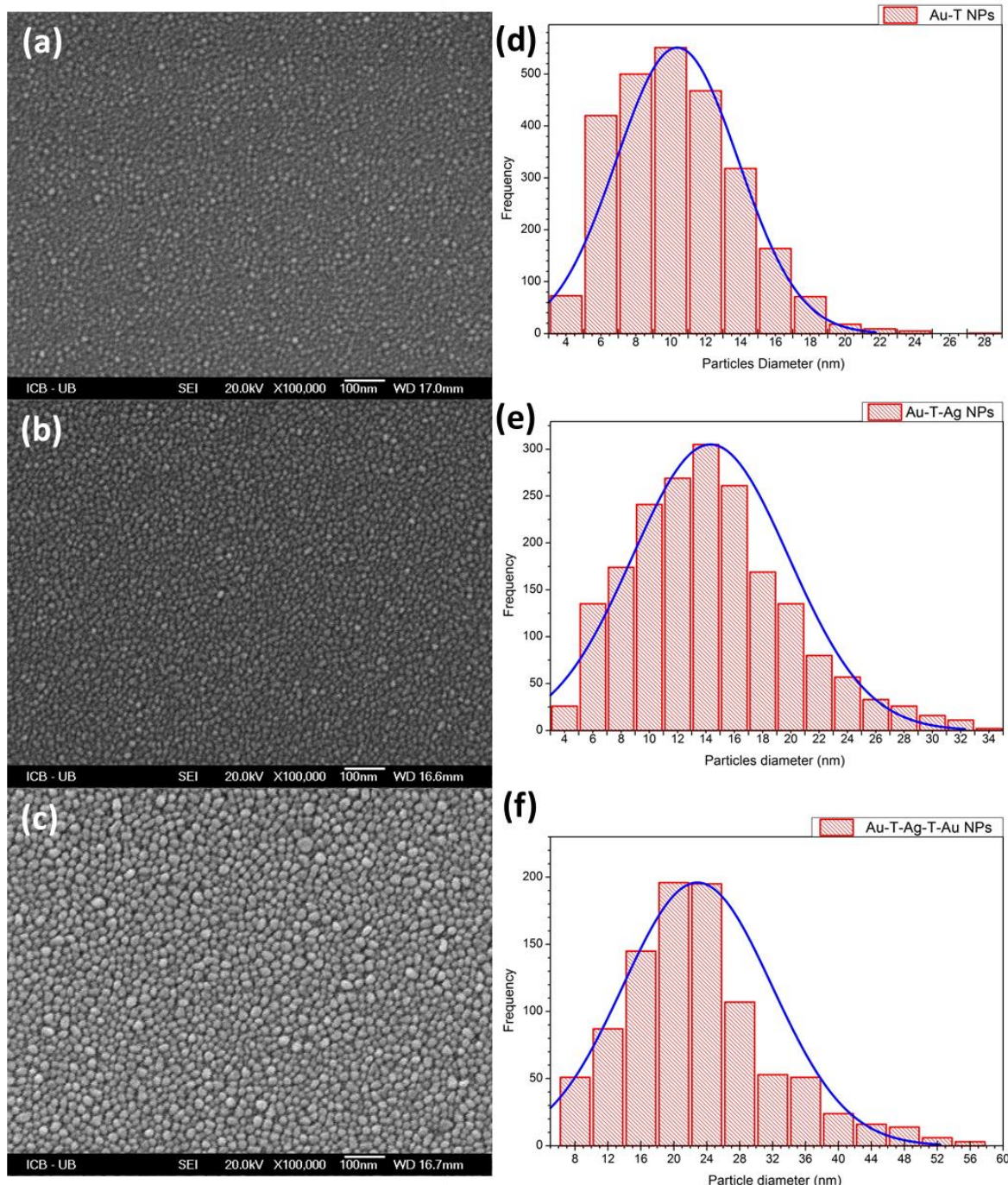


Figure IV.1 SEM images for the as-synthesized NPs (a) Au-T, (b) Au-T-Ag and (c) Au-T-Ag-T-Au NPs; the size distribution based on the SEM images for (d) Au-T, (e) Au-T-Ag, and (f) the Au-T-Ag-T-Au NPs

The size distributions obtained from SEM images analysis are illustrated in Figure IV.1 (d), 1(e) and 1(f) respectively representing Au-T NPs, Au-T-Ag NPs and Au-T-

Ag-T-Au NPs, in addition to the average diameter size and the surface coverage which are presented in *Table IV.1*.

Table IV.1 Average diameter size and the surface coverage for the Au-T, Au-T-Ag, and Au-T-Ag-T-Au NPs

Substrate	Average diameter size	Surface coverage
Au-T	11 nm	29 %
Au-T-Ag	15 nm	41 %
Au-T-Ag-T-Au	22 nm	49 %

The Au-T, Au-T-Ag and Au-T-Ag-T-Au NPs have approximately an average diameter size of 11 nm, 15 nm and 22 nm respectively. They also present a surface coverage of 29 %, 41 % and 49 % respectively. By comparing the average diameter size of the three NPs, we can notice an increase of approximately 4 nm between Au-T NPs and Au-T-Ag NPs, in addition to an increase of about 6 nm between Au-T-Ag NPs and Au-T-Ag-T-Au NPs. The estimated increase in nanoparticles diameter after each evaporation step is 4 nm, which is in good harmony with the average diameter size obtained (within the evaporation and size distribution calculation errors).

Figure IV.1 shows the HRTEM image of a single Au-T-Ag-T-Au nanoparticle showing a 15.6 nm/2.3 nm core/shell structure. The observed core size is in good agreement with the average size of Au-T-Ag NPs shown in *Figure IV.1* (b) and *Table IV.1*. Furthermore, the observed shell thickness is approximately 2.3 nm which corresponds to the final evaporated thickness of gold. As shown in the HRTEM image, the Au-Ag core is a bimetallic structure with neither core/shell nor alloy nature. However, the structure includes mixture zones of both gold and silver metals. The obtained metallic distribution in the core based on the HRTEM is in good agreement with the expected one, as the obtained Au and Ag percentages are 48.8% and 51.2 % respectively (knowing that the core is composed of 2 nm gold and 2 nm silver) *Table IV.2*. The dark zones in the core correspond to gold, as gold have higher atomic number than Ag and thus will appear darker in TEM imaging.¹ However, the Au shell has brighter contrast, this could be related to the low thickness of the shell, where the contrast in TEM imaging is also dependent on the sample's thickness.¹

Based on the HRTEM, we can refer now to the Au-T-Ag-T-Au NPs as Au-Ag/Au core/shell bimetallic NPs.

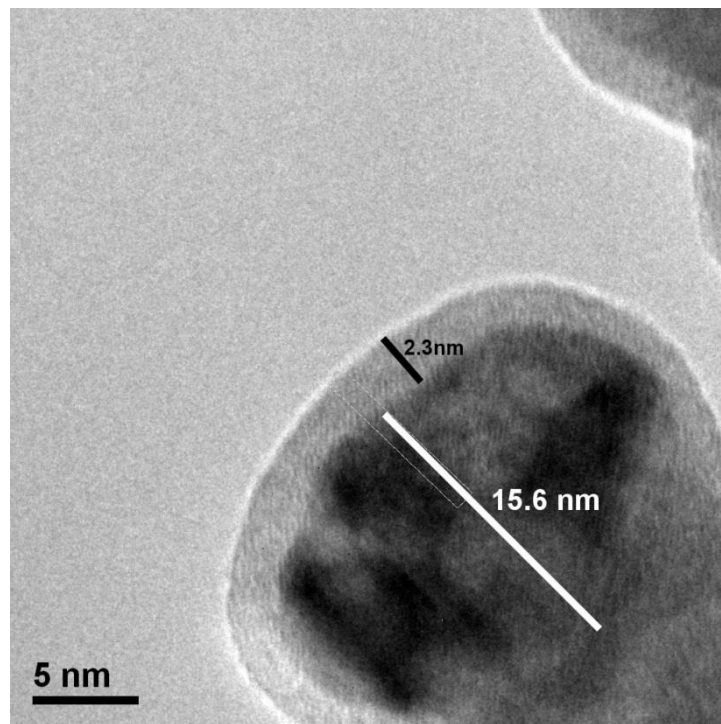


Figure IV.2 HRTEM image of a single Au-Ag/Au NP

Table IV.2 HRTEM image analysis of a single Au-Ag/Au core/shell NP

	Area (nm ²)	Percentage with respect to the core (%)	Percentage with respect to the core/shell (%)	Calculated Diameter (nm) ^{b)}
Au zones ^{a)}	34.65+67.07	48.10	28.32	-----
Au-Ag core	211.45	100	58.87	16.40
Au-Ag/Au core/shell	359.15	169.85	100	21.38

a) Au zones inside the core (dark zones); b) calculated diameter based on the HRTEM image

IV.2.2 Silver presence effect in Au-Ag/Au core/shell nanoparticles on the extinction and SERS behaviors

We have already succeeded in fabricating bimetallic nanoparticles containing silver and having an LSPR position close to the Raman excitation wavelength. The question which arises here is does the obtained SERS enhancement ability for the Au-Ag/Au NPs originates from the presence of silver, morphology or LSPR spectral position?

Answering the question would be possible by comparing the Au-Ag/Au bimetallic NPs with pure triple monometallic silver NPs, Ag-T-Ag-T-Ag and triple monometallic gold nanoparticles Au-T-Au-T-Au. *Table IV.3* shows the LSPR positions for the three mentioned substrates.

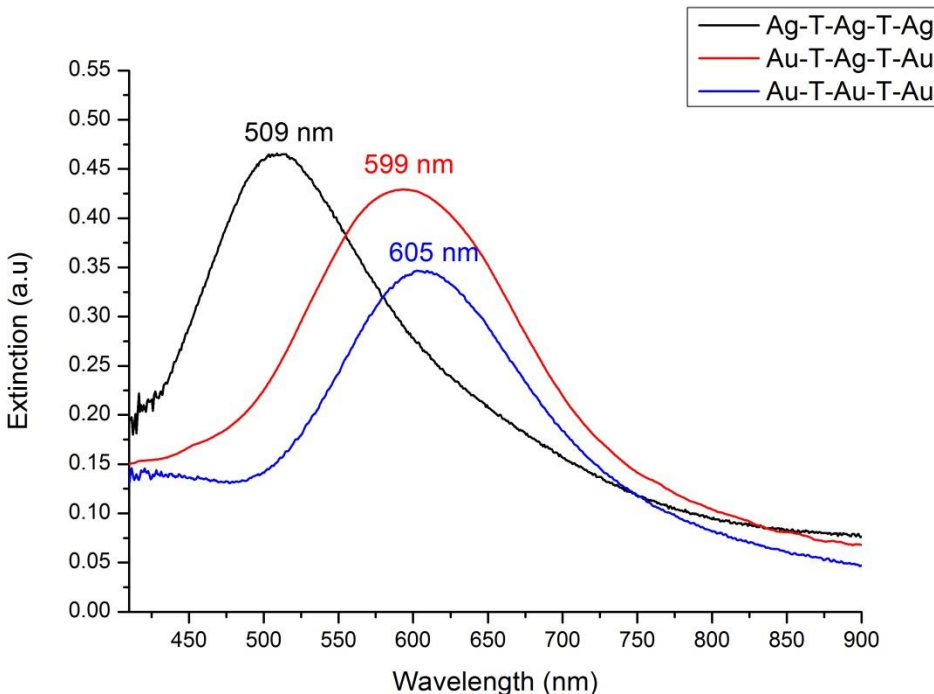


Figure IV.3 Extinction spectra for Ag-T-Ag-T-Ag, Au-T-Ag-T-Au, and the Au-T-Au-T-Au NPs

By comparing the Au-T-Ag-T-Au NPs with the Au-T-Au-T-Au NPs, we can observe a slight blue shift of 6 nm for the Au-T-Ag-T-Au NPs, which confirms the hypothesis we mentioned earlier that the second layer have the lowest effect on the LSPR position. Therefore by substituting the second evaporated metal in Au-T-Au-T-Au by silver nearly did

not largely affect the LSPR position. However, higher enhancement is obtained over the Au-T-Ag-T-Au in comparison with the Au-T-Au-T-Au substrate, *Figure IV.4*. This higher enhancement can be attributed to the presence of silver in system having LSPR spectral position in resonance with the Raman excitation wavelength. The size distribution of the nanoparticles in the two substrates based on their SEM images shows an average diameter of ≈ 19 nm and ≈ 22 nm for the Au-T-Au-T-Au and Au-T-Ag-T-Au substrates respectively. The two NPs types are comparable in size; meanwhile, the Au-T-Ag-T-Au NPs provide much higher SERS enhancement in comparison to the Au-T-Au-T-Au NPs, *Figure IV.5*.

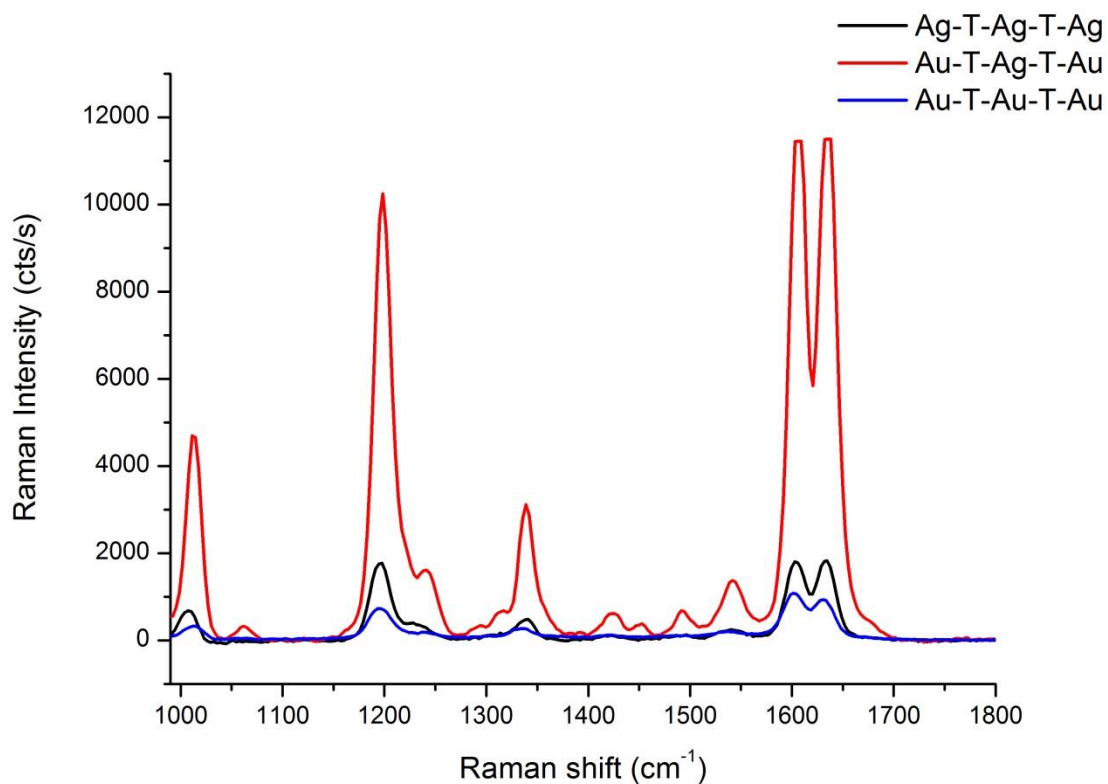


Figure IV.4 SERS signals for BPE solution ($10^{-5}M$) over Ag-T-Ag-T-Ag, Au-T-Ag-T-Au, and the Au-T-Au-T-Au NPs

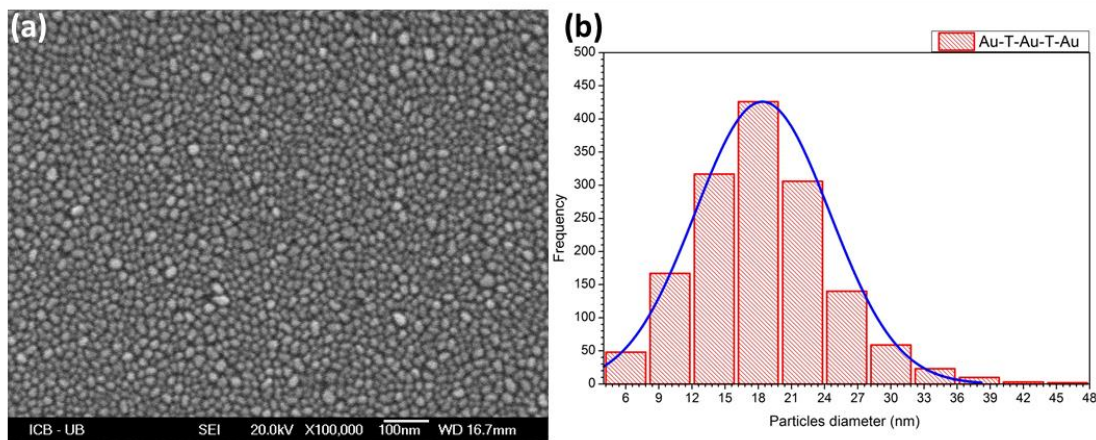


Figure IV.5 SEM image (a) and the SEM based size distribution (b) for the Au-T-Au-T-Au NPs

Secondly, comparing the Au-T-Ag-T-Au NPs with the Ag-T-Ag-T-Ag NPs confirms further the effect of LSPR position on the SERS enhancement ability, where pure silver system have lower SERS signal than Au-T-Ag-T-Au substrate (*Figure IV.4*), because its spectral position lies at 509 nm which is far from Raman excitation wavelength.

The highest enhancement obtained over the Au-Ag/Au NPs (Au-T-Ag-T-Au) is hence related to the presence of silver in a bimetallic structure having LSPR position in resonance with the Raman excitation wavelength.

IV.2.3 Homogeneity, reproducibility and stability

As mentioned before, the aim of our work is to fabricate SERS substrates characterized by high enhancement ability associated with homogeneity, reproducibility and high stability under physiological conditions. Thus, we tested the mentioned properties for the substrate having the highest SERS enhancement; Au-Ag/Au core/shell nanoparticles.

IV.2.3.1 Homogeneity

Figure IV.6 illustrates the LSPR for five different positions on the substrates distributed over 1cm² area. The measurements were conducted following the same parameters, mentioning that the collection spot for the LSPR measurements was 10 µm. From the LSPR measurements, one can conclude that the substrate is homogenous in the micro scale level over a large scale.

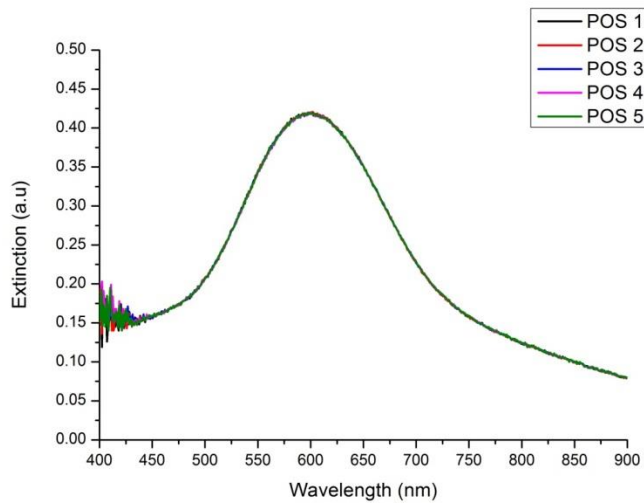


Figure IV.6 Extinction spectra for five different positions on the Au-Ag/Au core/shell NPs

For monitoring the SERS signal homogeneity all over the substrate, SERS measurements were made for 10 drops of BPE solution(10^{-5} M) placed on 10 different positions. The measurements were taken after 1 minute from depositing each drop and the acquisition time was fixed for 5 seconds, *Figure IV.7*. After comparing the SERS intensity of the benzene ring stretching (1605 cm^{-1}) one can calculate the relative standard deviation of the measurements which is 2% for Au-Ag/Au core/shell NPs, *Table IV.3*. Thus, the Au-Ag/Au core/shell NPs provide homogenous SERS measurements all over the substrate.

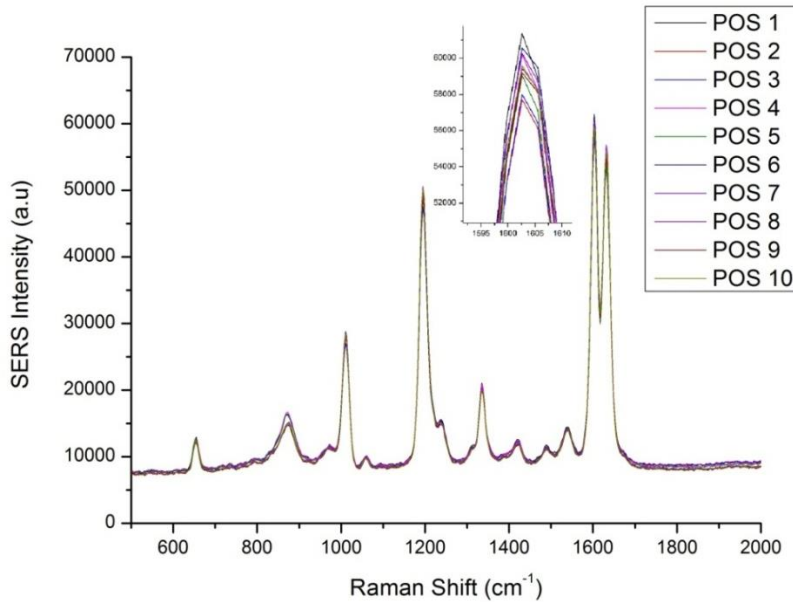


Figure IV.7 SERS signals for ten BPE drops (10^{-5} M) placed on different spots over the Au-Ag/Au core/shell NPs substrate

Table IV.3 Statistical study on SERS signals for ten BPE drops ($10^{-5} M$) placed on different spots over the Au-Ag/Au core/shell NPs substrate

Position	SERS intensity a.u (1605 cm ⁻¹)	Mean value	Standard deviation	% Relative standard deviation
1	57713			
2	58001			
3	59055			
4	59193			
5	59459			
6	59607			
7	60193			
8	60270			
9	60560			
10	61369			

IV.2.3.2 Reproducibility

To study the reproducibility of the Au-Ag/Au core/shell NPs, we compared five different substrates fabricated separately. *Figure IV.8* shows the LSPR spectra for the five substrates. *Table IV.4* illustrates the Gaussian peak fit for the LSPR spectra, in addition to the relative standard deviation (RSD) of the LSPR position and width. The obtained RSD are 1.3% and 6.2% for the LSPR peak and width, respectively.

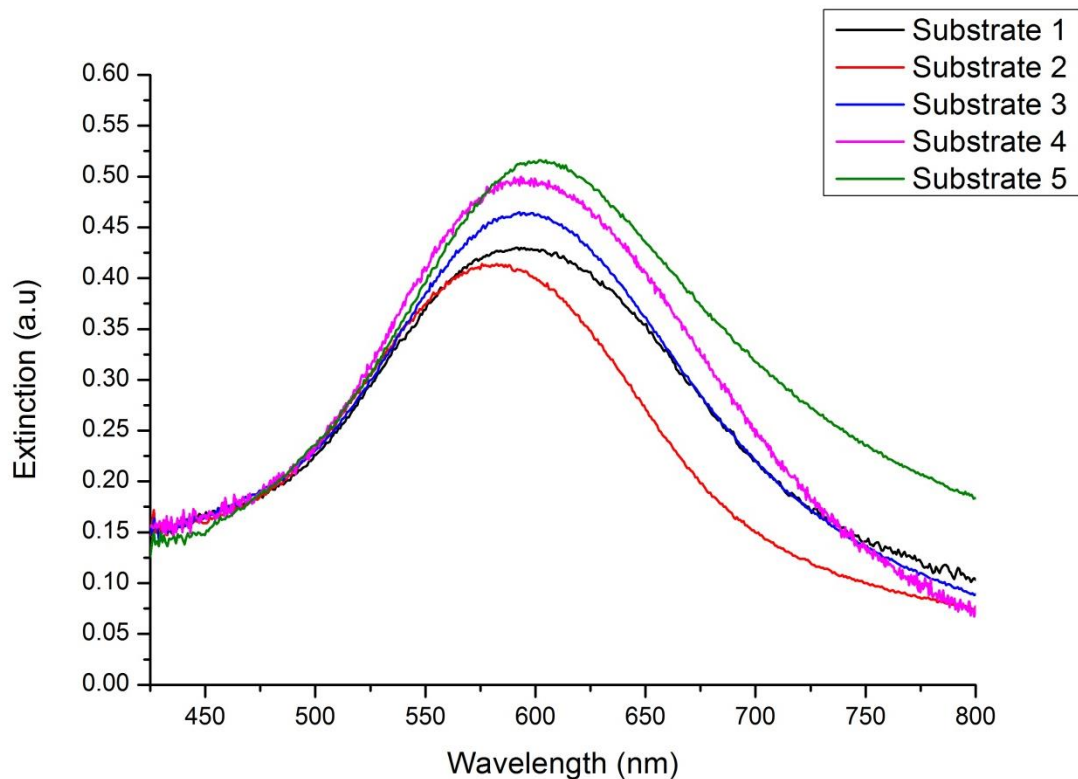


Figure IV.8 Extinction spectra for five different Au-Ag/Au core/shell NPs substrates

Table IV.4 Statistical study on extinction spectra for five different Au-Ag/Au core/shell NPs substrates

Substrate	1	2	3	4	5	Mean	SD	%RSD
LSPR position(nm)	597	580	596	599	596	594	7.7	1.3
FWHM	142	134	140	154	132	140.4	8.7	6.2

The SERS signals obtained over the five substrates were compared to follow the enhancing reproducibility of the Au-Ag/Au core/shell NPs. The SERS signals of the BPE solution (10^{-5} M) with acquisition time of 5 seconds are illustrated in *Figure IV.9*. *Table IV.5* shows the SERS intensity for the benzene ring stretching (1605 cm^{-1}) in addition to the calculated relative standard deviation which is 8%. Based on the above results, thermal-annealing of thin film strategy provides us with highly reproducible substrates for SERS measurements.

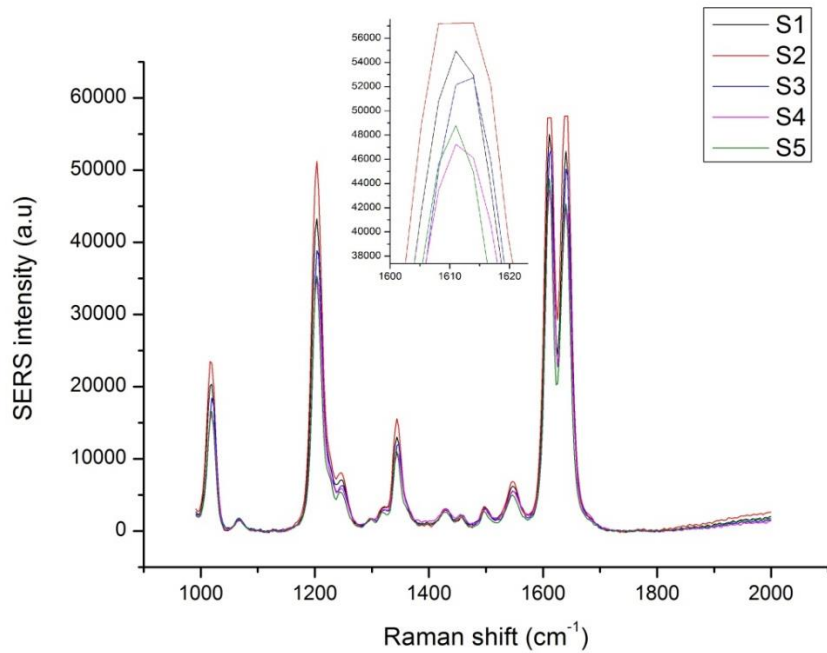


Figure IV.9 SERS signals for BPE solution (10^{-5} M) over five different Au-Ag/Au core/shell NPs substrates

Table IV.5 Statistical study on SERS signals for BPE solution (10^{-5} M) over five different Au-Ag/Au core/shell NPs substrates

Substrate	1	2	3	4	5	Mean	SD	%RSD
SERS intensity a.u (1605 cm^{-1})	47252	48802	52148	54939	57227	52072	4144	8

IV.2.3.3 Stability

In order to evaluate the role of the Au shell in providing stability to the Au-Ag/Au core/shell NPs, a SERS study was made for freshly prepared Au-Ag/Au core/shell NPs and its as-synthesized Au-T and Au-T-Ag NPs. Then, the SERS measurements were repeated over the three substrates after one year using the same probe molecule and following the same experimental conditions. *Figure IV.10* shows nearly the same SERS signal over the Au-Ag/Au NPs after one year whereas that over Au-T-Ag NPs appeared to fade almost totally. The reason for such results can be attributed to the sulfuration or oxidation of silver in the Au-T-Ag NPs, meanwhile this problem is avoided in the Au-Ag/Au NPs since the silver is encapsulated and protected by the Au shell. Thus, Au-Ag/Au core shell NPs represents the

advantage of combining the silver and gold metals in a stable bimetallic system in order to sum the merits of both the silver optical enhancing properties and gold surface properties.

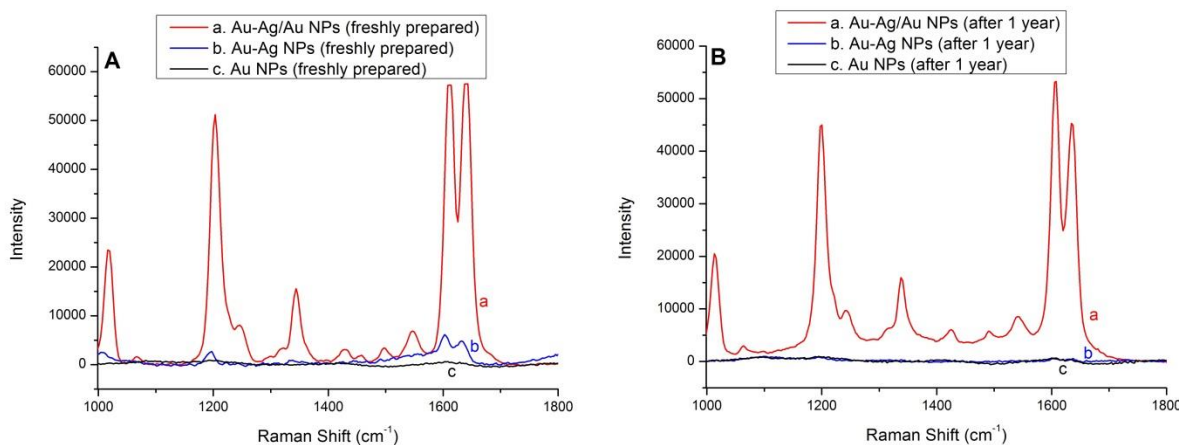


Figure IV.10 SERS response of BPE solution (10^{-5} M) over the Au-Ag/Au NPs (line a), Au-Ag NPs (line b) and Au NPs (line c) freshly prepared (A); after 1 year from preparation (B)

IV.2.4 Au-Ag/Au core/shell bimetallic nanoparticles : quantitative SERS sensors

In sensing applications, SERS substrates must have the capability for low analyte concentration detection. Additionally, these substrates can serve as quantitative analytical tools. Thus, SERS substrates having the ability for quantitative analysis even for low concentrations serve essentially for tend towards an application as quantitative SERS sensors for the environmental analysis.

In order to evaluate the sensitivity of the Au-Ag/Au core/shell bimetallic NPs for low concentration detection, the SERS responses for BPE solutions at different concentrations ranging from 10^{-15} to 10^{-5} M are recorded. All measurements have been carried out after one minute of depositing $10\mu\text{L}$ BPE drop of different concentration. The acquisition time has been set as 5 seconds. *Figure IV.11*, shows that the SERS signals decrease in intensity with decreasing the BPE concentration. The lowest concentration of BPE that can be detected over the Au-Ag/Au core/shell NPs for the mentioned experimental parameters is 10^{-12} M. Thus, we can estimate our detection threshold to a concentration equal to 10^{-12} M of BPE solution.

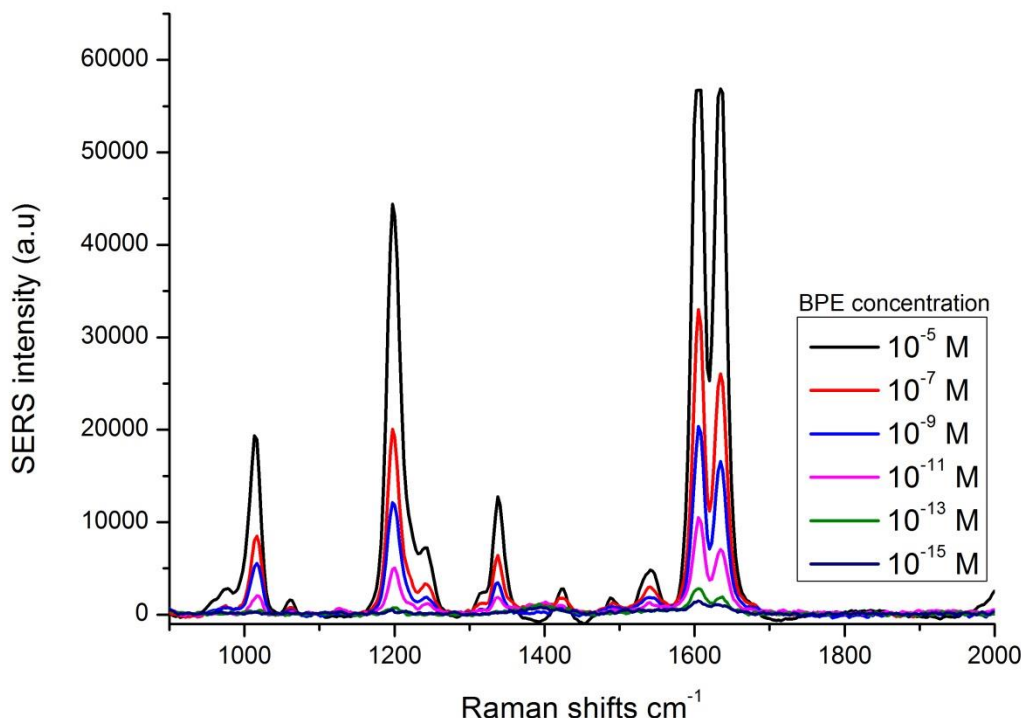


Figure IV.11 SERS spectra for BPE solutions of different concentrations ranging from 10^{-5} to 10^{-15} M over Au-Ag/Au core/shell NPs substrate.

For a further investigation of the quantitative analytical detection potentials for the Au-Ag/Au core/shell NPs, the evolution of the SERS intensity for the 1605 cm^{-1} band are plotted vs. the BPE concentration, *Figure IV.12*. The error bars represent the standard deviation of the average Raman intensity obtained for ten SERS measurements. From the linear fit, it can be observed that the Au-Ag/Au core/shell NPs substrate exhibits a linear detection range from 10^{-5} to 10^{-12} M with a correlation coefficient $R^2= 0.9602$. Thus, Au-Ag/Au core/shell bimetallic NPs have considerable potential as quantitative SERS sensors.

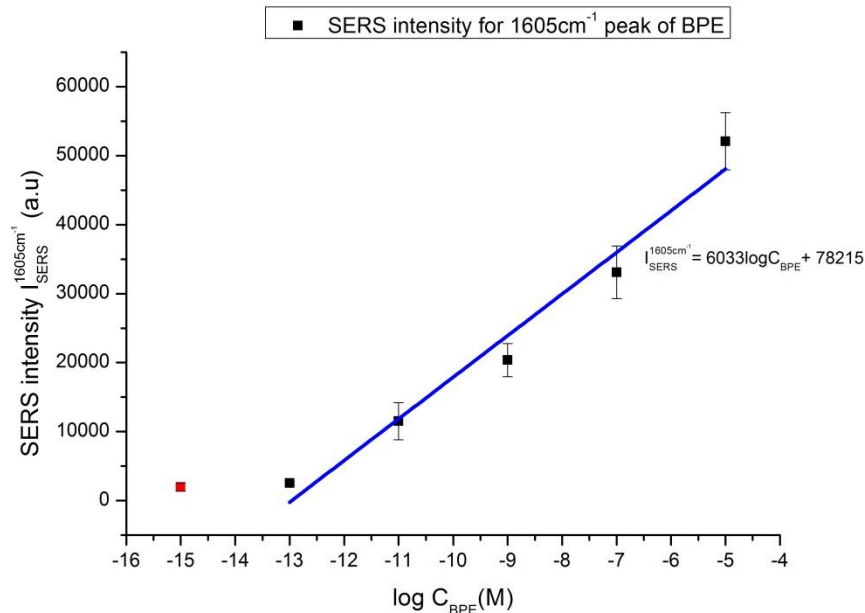


Figure IV.12 SERS intensity of the 1605 cm^{-1} band as a function of the BPE concentration obtained over Au-Ag/Au core/shell NPs substrate, the error bars represent the standard deviation of the average Raman intensity obtained for ten SERS measurements.

IV.3 Improvements of the sensitivity

IV.3.1 Evaporated thickness variations

The nanoparticles size have direct effect on the localized surface plasmon resonance spectral position,² where increasing the size will lead to a red shift in the LSPR position.³ Hence, by increasing the evaporated metal thickness, it is expected that the size of the nanoparticles will increase while keeping the thermal annealing parameters fixed (temperature and time). Therefore we have worked on changing the evaporated metallic thickness for the Au-Ag/Au bimetallic core/shell nanoparticles in an aim to shift their LSPR position more towards the Raman excitation wavelength (632.8 nm) and thus improve their enhancing properties.

Following the same experimental preparations used for the fabrication of Au-Ag/Au core/shell nanoparticles (2nmAu-T-2nmAg-T-2nmAu), three substrates were fabricated following the same strategy but with different evaporation thicknesses of 2 nm-2 nm, 3 nm-3 nm and 4 nm-4 nm for the first two evaporated metals. The last evaporated thickness was kept at 2 nm due to the fact that the plasmonic influence of the core material decreases with increasing the shell thickness.⁴⁻⁷ Additionally, increasing the thickness of the last layer will

prevent the LSPR tunability, since LSPR spectral position will be dominantly affected by the material of the last layer.

Table IV.6 presents the fabrication steps for the three substrates, 2nmAu-T-2nmAg-T-2nm Au, 3nmAu-T-3nmAg-T-2nmAu and 4nmAu-T-4nmAg-T-2nmAu. The SEM images for the three fabricated substrates presented in *Figure IV.13* confirm the increasing in nanoparticle size with increasing the evaporated thickness.

Table IV.6 Experimental details for fabricating the 2nmAu-T-2nmAg-T-2nmAu, 3nmAu-T-3nmAg-T-2nmAu and 4nmAu-T-4nmAg-T-2nmAu substrates

		2nmAu-T- 2nmAg-T- 2nmAu	3nmAu-T- 3nmAg-T- 2nmAu	4nmAu-T- 4nmAg-T- 2nmAu
First evaporation	Metal	Au	Au	Au
	Thickness (nm)	2	3	4
First thermal annealing	Temperature (°C)	250	250	250
	Time (s)	20	20	20
Second evaporation	Metal	Ag	Ag	Ag
	Thickness (nm)	2	3	4
Second thermal annealing	Temperature (°C)	250	250	250
	Time (s)	20	20	20
Third evaporation	Metal	Au	Au	Au
	Thickness (nm)	2	2	2

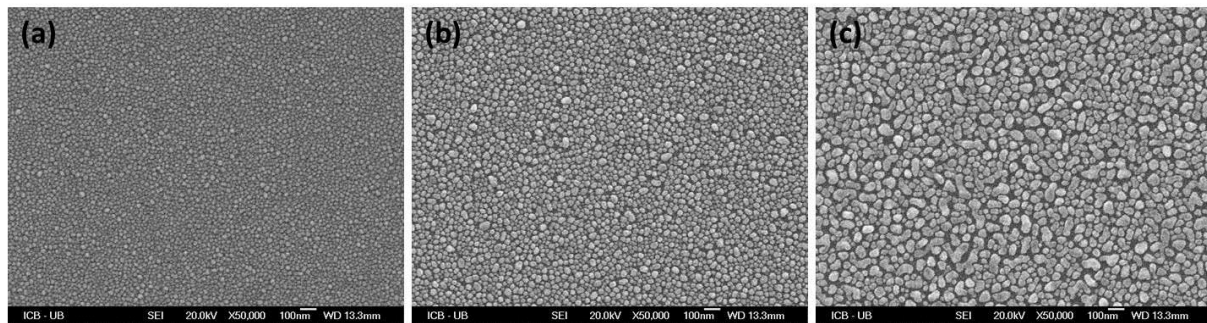


Figure IV.13 SEM images of (a) 2nmAu-T-2nmAg-T-2nm Au, (b) 3nmAu-T-3nmAg-T-2nmAu and (c) 4nmAu-T-4nmAg-T-2nmAu NPs.

Using UV-Vis-NIR spectroscopy, LSPR measurements for the three substrates were conducted (*Figure IV.14*). The 2nmAu-T-2nmAg-T-2nmAu, 3nmAu-T-3nmAg-T-2nmAu and 4nmAu-T-4nmAg-T-2nmAu substrates show LSPR positions at 598 nm, 619 nm and 546 nm respectively. By comparing the 3nmAu-T-3nmAg-T-2nm Au and the 2nmAu-T-2nmAg-T-2nmAu substrates, a red shift of 21 nm is obtained. In order to understand this change in LSPR position, two different approaches should be considered, i) the size effect and ii) the gold/silver metallic ratio present. The increase in NPs size for the 3nmAu-T-3nmAg-T-2nmAu over that of 2nmAu-T-2nmAg-T-2nmAu should result in red-shifting the LSPR position. Meanwhile, the increase in the silver ratio from 1/3 in the 2nmAu-T-2nmAg-T-2nmAu substrate to 3/8 in the 3nmAu-T-3nmAg-T-2nmAu substrate should have resulted in blue-shifting the LSPR position. From the obtained results we can conclude that the size effect overcomes the composition one in the 3nmAu-T-3nmAg-T-2nm Au substrate. Increasing the evaporated thickness to 4 nm in the 4nmAu-T-4nmAg-T-2nmAu substrate has blue shifted the LSPR position to 546 nm. The increasing in the NPs size should have caused a red shift in the LSPR position by comparing it to the other two substrates, and the increase in the silver content (4/10) should have resulted in a blue shift for LSPR position. Therefore the obtained blue shift for the 4nmAu-T-4nmAg-T-2nmAu substrate could be explained by the predomination of the composition effect over the size effect.

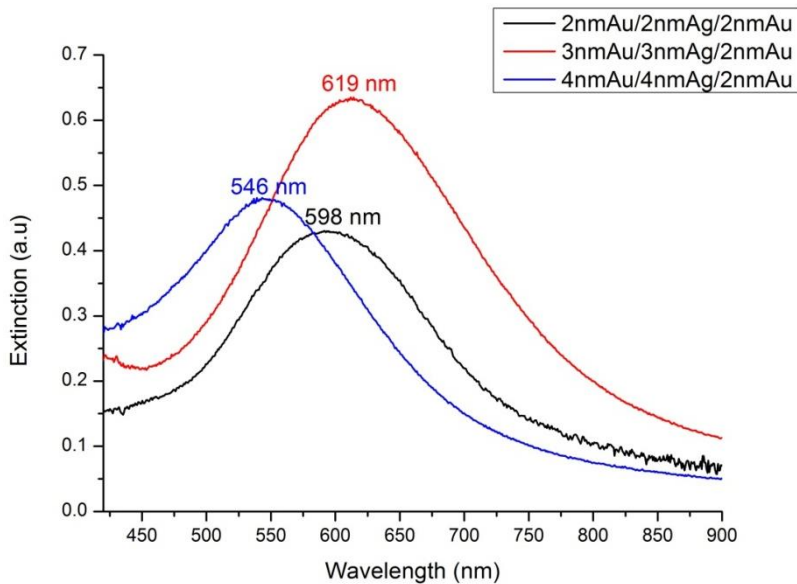


Figure IV.14 Extinction spectra for the 2nmAu-T-2nmAg-T-2nmAu, 3nmAu-T-3nmAg-T-2nmAu, and 4nmAu-T-4nmAg-T-2nmAu substrates

Based on the LSPR position, it is estimated that a better enhancement in the Raman scattering should be obtained over the 3nmAu-T-3nmAg-T-2nmAu substrate since its LSPR position is the closer to the Raman excitation wavelength than the 2nmAu-T-2nmAg-T-2nmAu substrate. In order to test this assumption, SERS measurements of BPE (10^{-5} M) have been carried out over the three substrates, *Figure IV.15*. The acquisition time was set at 3 seconds. The 3nmAu-T-3nmAg-T-2nmAu substrate leads to a higher SERS signal intensity than that over the 2nmAu-T-2nmAg-T-2nmAu substrate (nearly two orders of magnitude higher), whereas the 4nmAu-T-4nmAg-T-2nmAu substrate provides a lower SERS signal intensity than that of the 2nmAu-T-2nmAg-T-2nmAu substrate. *Figure IV.16* illustrates the relation between the enhancing ability of the three substrates in comparison with their LSPR positions. The inversely proportional relation between the SERS intensity and $\Delta\lambda$ is sustained in this study, allowing us to optimize the Au-Ag/Au bimetallic core/shell nanoparticles for a better enhancing ability by using the structure of 3nmAu-T-3nmAg-T-2nmAu substrate.

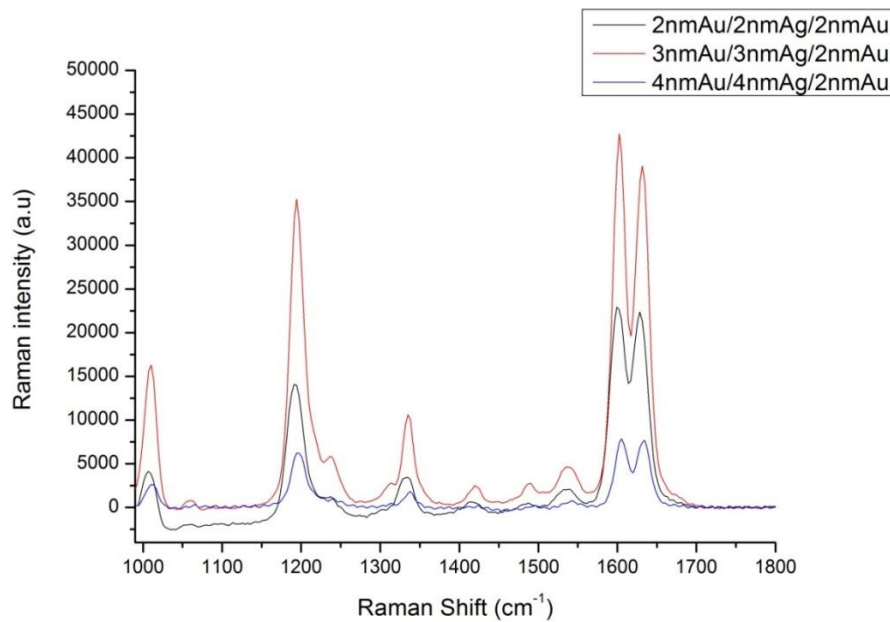


Figure IV.15 SERS signals of BPE solution (10^{-5} M) over the 2nmAu-T-2nmAg-T-2nmAu, 3nmAu-T-3nmAg-T-2nmAu and 4nmAu-T-4nmAg-T-2nmAu substrates

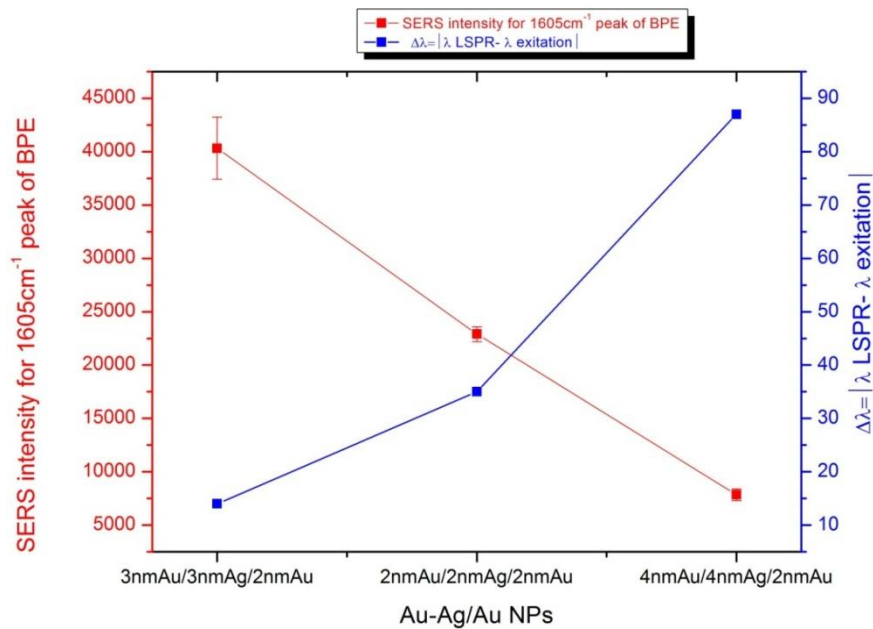


Figure IV.16 The inversely proportional relation between SERS intensities of the benzene ring stretching (1605 cm^{-1}) and $\Delta\lambda$ (the absolute value for the difference between the Raman excitation wavelength, 632.8 nm, and the LSPR resonance) for 2nmAu-T-2nmAg-T-2nmAu, 3nmAu-T-3nmAg-T-2nmAu, and 4nmAu-T-4nmAg-T-2nmAu substrates

IV.3.2 Thermal annealing temperature effect (post-deposition treatment)

Besides studying the evaporation thickness effect on the LSPR spectral position and its influence on the enhancing ability in Raman scattering, the parameter of thermal annealing temperature is also investigated. This parameter effect is studied because in the metal

evaporation annealing protocol, the evaporation thickness and the annealing temperature are the two most considerable parameters in determining the morphology of the obtained nanoparticles.⁸⁻¹⁰ Therefore in this part we investigate the effect of annealing temperature on the nanoparticles morphology and its repercussions on the LSPR properties and SERS ability. Au-Ag/Au bimetallic core/shell nanoparticles were fabricated following the same strategy with different thermal annealing temperatures ranging from 150 °C to 350 °C (50 °C intervals). Five different substrates were fabricated having thermal annealing temperatures as 150, 200, 250, 300 and 350 °C respectively. The treatment time was kept constant at 20 seconds, *Table IV.7*

Table IV.7 Experimental details for fabricating the five Au-Ag/Au NPs different substrates with thermal annealing temperatures ranging from 150 °C to 350 °C

Au-Ag/Au core/shell NPs		T=150°C	T=200°C	T=250°C	T=300°C	T=350°C
First evaporation	Metal	Au	Au	Au	Au	Au
	Thickness (nm)	2	2	2	2	2
First thermal annealing	Temperature (°C)	150	200	250	300	350
	Time (s)	20	20	20	20	20
Second evaporation	Metal	Ag	Ag	Ag	Ag	Ag
	Thickness (nm)	2	2	2	2	2
Second thermal annealing	Temperature (°C)	150	200	250	300	350
	Time (s)	20	20	20	20	20
Third evaporation	Metal	Au	Au	Au	Au	Au
	Thickness (nm)	2	2	2	2	2

Figure IV.17 illustrates the LSPR spectra of the five substrates. The increasing in thermal annealing temperature affects the plasmonic properties by two aspects, the LSPR position and broadness. For LSPR position, the gradual rise in temperature from 150 °C to 350 °C results in blue shift pattern in the LSPR position starting at 650 nm for the lowest temperature reaching 588 nm for the highest one. The blue-shifts obtained with increasing the temperature can be related to morphology modifications which take place with temperature changes. The obtained blue shift can be largely viewed as originating from the increase in interparticle separation in order to reduce the surface tension energy between the nanoparticle and the glass substrate¹¹. As for the LSPR peak broadness, the FWHM of the plasmonic peaks decreases with increasing temperature. This could be attributed to morphology changes induced by thermal annealing variations,^{9,10} where thermal annealing at higher temperatures provides more homogeneous metallic nanoparticles with higher circularity ratio, *Figure IV.18*. Such morphological characteristics demonstrate the sharper LSPR spectra with increasing the thermal annealing temperature, where uniform nanoparticles have sharper LSPR spectra than inhomogeneous ones.¹²

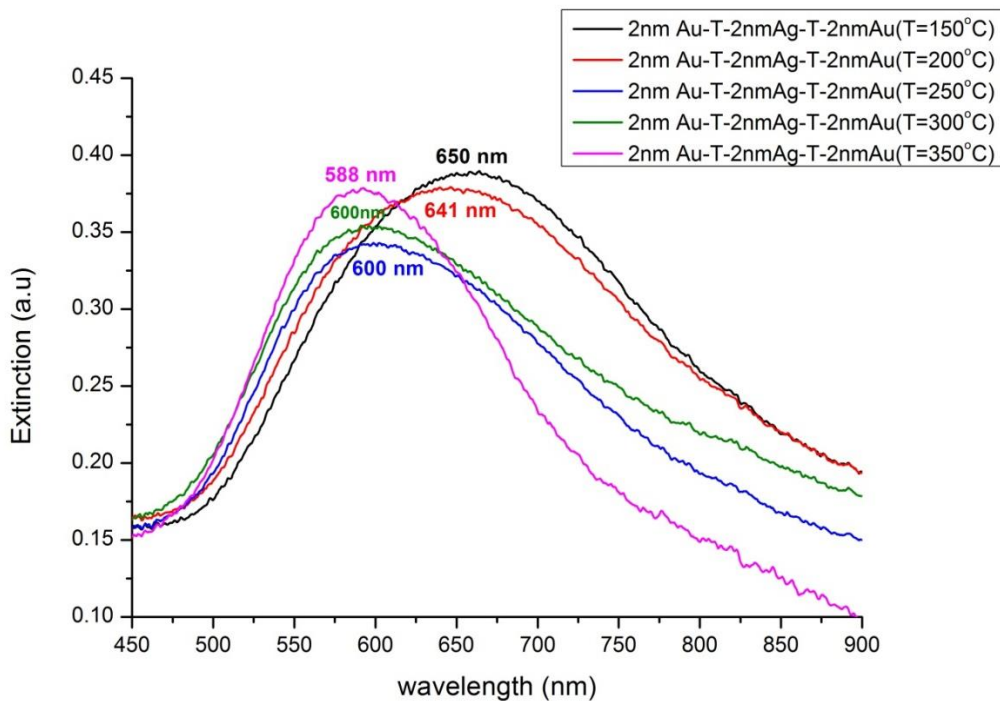


Figure IV.17 Extinction spectra for the five Au-Ag/Au NPs different substrates with thermal annealing temperatures ranging from 150 °C to 350 °C

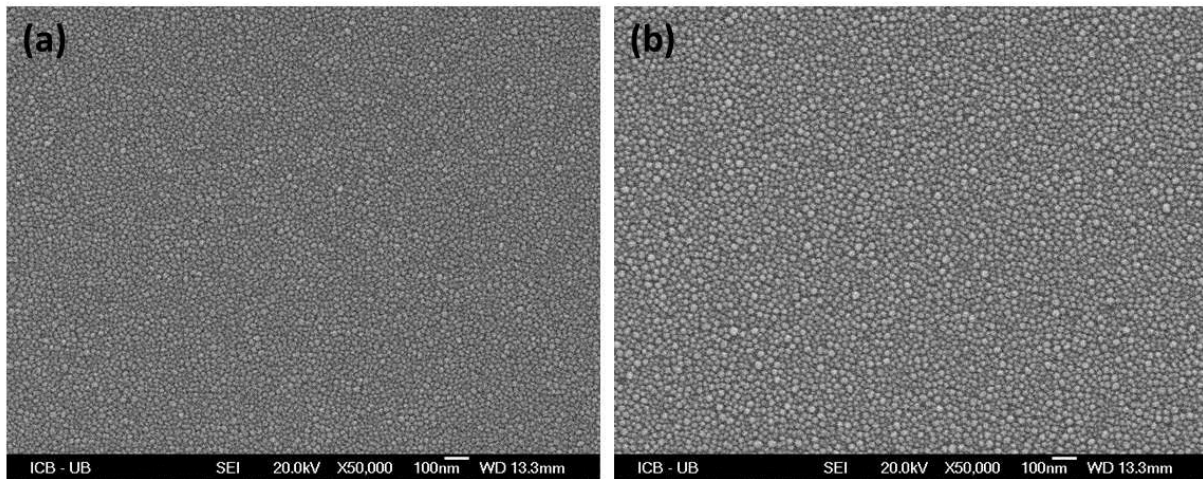


Figure IV.18 SEM images of 2nmAu-T-2nmAg-T-2nm Au NPs thermally annealed at (a) $T=150^{\circ}\text{C}$ and (b) $T=350^{\circ}\text{C}$.

In order to show the effect of thermal annealing temperature changes on the SERS enhancing ability, SERS measurements have been carried out on the five samples with different thermal annealing treatments. The acquisition time was set at 3 seconds for all the samples. *Figure IV.19* illustrates the SERS measurements for the BPE solution (10^{-5} M) over the five fabricated substrates. The Au-Ag/Au core/shell structure exhibits better enhancing ability with increasing the thermal annealing T, with the highest SERS signal obtained over the substrate thermally treated at 350°C . The SERS intensity of the benzene ring stretching (1605 cm^{-1}) is plotted versus $\Delta\lambda$ for each of the fabricated substrates in order to follow the enhancing ability versus the LSPR position, *Figure IV.20*. A proportional relation between the SERS intensity and $\Delta\lambda$ is obtained. Thus, the improvements in SERS enhancements could not be correlated with the LSPR spectral position. This proposes another competitive effect for explaining such obtained improvements. Changing temperature leads to shifts in LSPR positions in addition to changes in the LSPR peak shapes. Therefore, we focused our attention on the peak broadness effect on the SERS enhancing ability. *Figure IV.21* represents the relation between the enhancing ability of the substrates versus FWHM, where an inversely proportional relationship is observed. This obtained relationship is in good agreement with the inversely proportional relationship obtained between the near-field enhancement factor f and the LSPR width, where a narrower LSPR indicates a higher local field enhancement.^{13,14} Thus, the observed decrease of the LSPR line width, derived from increasing the thermal annealing temperature, has a clear influence on the near field enhancement. Hence, the LSPR

spectral position effect is overcome by the LSPR broadness one in determining the SERS performance.

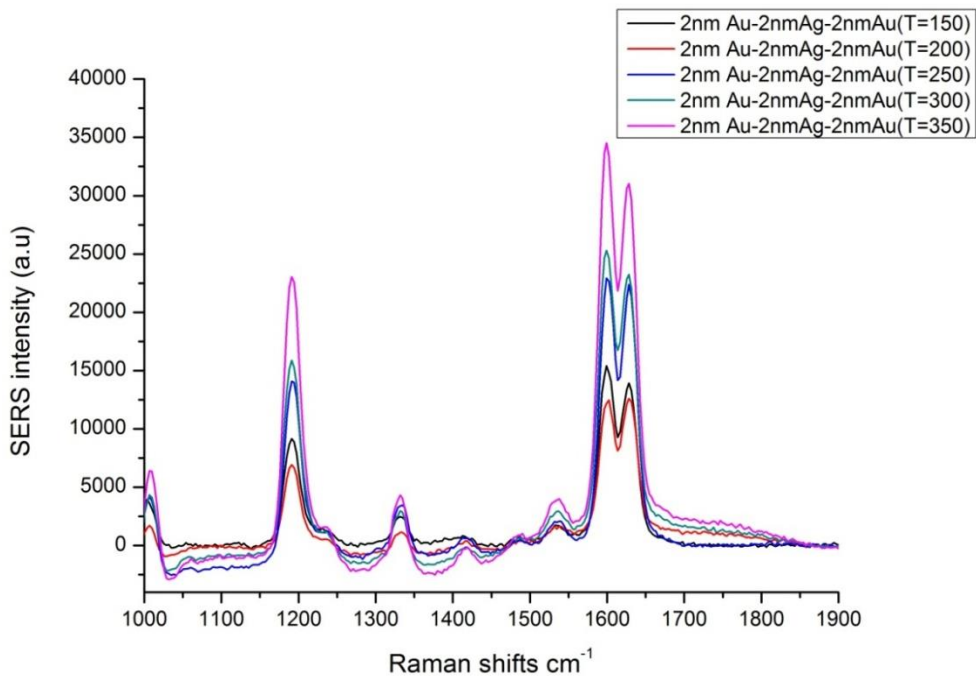


Figure IV.19 SERS response for BPE solution (10^{-5} M) over the five Au-Ag/Au NPs different substrates with thermal annealing temperatures ranging from 150 °C to 350 °C

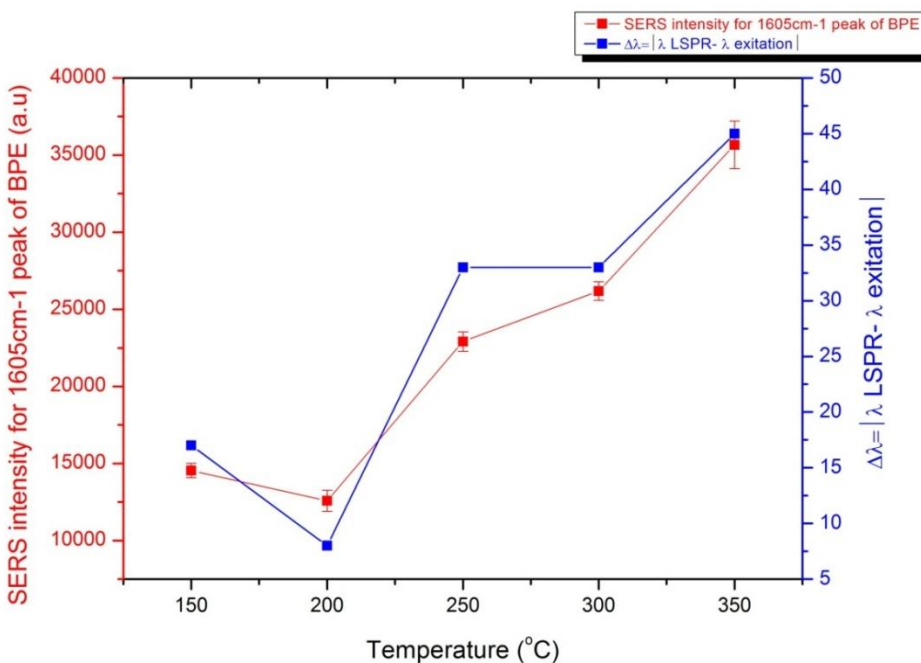


Figure IV.20 The proportional relation between SERS intensities of the benzene ring stretching (1605 cm^{-1}) and $\Delta\lambda$ (the absolute value for the difference between the Raman excitation wavelength, 632.8 nm, and the LSPR resonance) for five Au-Ag/Au NPs different substrates with thermal annealing temperatures ranging from 150 °C to 350 °C

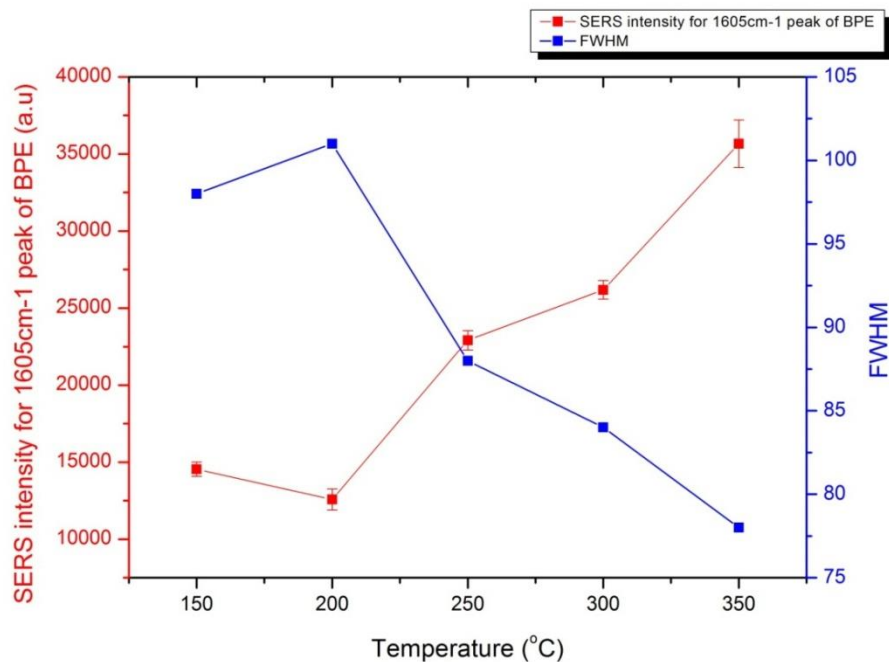


Figure IV.21 The inversely proportional relation between SERS intensities of the benzene ring stretching (1605 cm^{-1}) and FWHM for the five Au-Ag/Au NPs different substrates with thermal annealing temperatures ranging from $150\text{ }^{\circ}\text{C}$ to $350\text{ }^{\circ}\text{C}$

In the present study we have presented the amelioration attempts on the Au-Ag/Au core/shell NPs in order to improve their SERS activities by increasing the thermal annealing treatment temperature, with $350\text{ }^{\circ}\text{C}$ appearing as the optimum temperature.

IV.3.3 SERS intensity improvements on Au-Ag/Au core/shell bimetallic nanoparticles by coupling with a gold mirror and a thin oxide spacer layer

IV.3.3.1 Surface plasmon polaritons at flat metal dielectric interface

The classical description of surface plasmon polaritons (SPP) derives from the assumption that surface plasmons SP are coherent charge oscillations propagating on both parts of the semi-infinite metal-dielectric interface, having ϵ_m and ϵ_d as frequency-dependent dielectric functions for metal and dielectric mediums respectively, *Figure IV.22*.¹⁵ Moreover, for sake of simplicity, we will describe the SPP dispersion for an interface between two semi-infinite media. Maxwell equations are used to understand the physical properties of SPPs. The solution of these equations applied to the flat interface between a conductor and a dielectric

reveals two polarization types. The first is transverse magnetic mode (TM or p), with the magnetic field H^i being parallel to the interface and the second is the transverse electric mode (TE or s), with the electric field E^i being parallel to the interface. Surface plasmon polaritons can only be excited by TM polarization, since for SP wave propagates along the surface (x-axis) an E_{\perp}^i must exist. Accordingly, the TE polarized wave electric field doesn't allow SPP propagation where $E_{\perp}^i = 0$.¹⁶

Maxwell equations are presented by:

$$\nabla \cdot D = 0$$

$$\nabla \cdot B = 0$$

$$\nabla \times E = -\frac{\partial B}{\partial t}$$

$$\nabla \times H = \frac{\partial D}{\partial t}$$

Where D, B, E and H represent the dielectric displacement, the magnetic induction, the electric field and the magnetic field respectively.

Taking the x-axis along the propagating direction, the electric field and the magnetic field equation are expressed by:

$$E^i = (E_x^i, 0, E_z^i) e^{Zk_z^i} e^{i(k_x^i x - \omega t)}$$

And

$$H^i = (0, H_y^i, 0) e^{Zk_z^i} e^{i(k_x^i x - \omega t)}$$

Where i is the metal or dielectric component, having $Z < 0$ for metal and $Z > 0$ for dielectric. k_x^i is a wave number of a vector parallel to the surface, describing the propagation of electromagnetic wave along the interface. k_z^i vector is the damping of the wave along the direction normal to the surface, explaining the localization of the electromagnetic wave near the interface. The continuity of the in-plane electromagnetic field components reveals the relation $E_x^d = E_x^m, H_y^d = H_y^m$

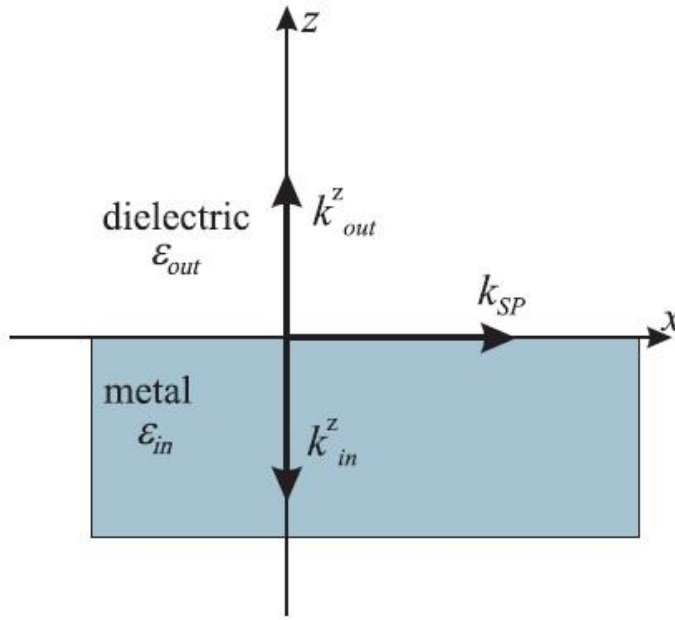


Figure IV.22 Scheme of surface plasmon polariton propagation.

Combining Maxwell's equations with E^i and H^i equations one finds:

$$k_z^d H_y^d + \frac{\omega}{c} \varepsilon_d E_x^d = 0$$

$$k_z^m H_y^m - \frac{\omega}{c} \varepsilon_m E_x^m = 0$$

Where ε_m and ε_d are the dielectric functions of the metal and the dielectric respectively. $c = 1/\sqrt{\varepsilon_0 \mu_0}$ is the speed of light in vacuum.

Knowing that $E_x^d = E_x^m$ and $H_y^d = H_y^m$, we obtain the SP dispersion relation:

$$\frac{k_z^d}{\varepsilon_d} + \frac{k_z^m}{\varepsilon_m} = 0$$

The equation above reveals that surface waves exist only at interfaces between materials with opposite signs of the real part of their dielectric permittivities, i.e. between a conductor and an insulator where both modes have an exponentially decaying evanescent character, *Figure IV.23*. Combining the homogeneous wave equation $(k_z^i)^2 + (k_x^i)^2 = \varepsilon_i \frac{\omega^2}{c^2}$ with the continuity condition for the in-plane wavenumber ($k_x^d = k_x^m = k_{SP}$), one obtains the total wavenumber in medium i as:

$$(k^i)^2 = (k_{SP})^2 - (k_z^i)^2 = \varepsilon_i \frac{\omega^2}{c^2}$$

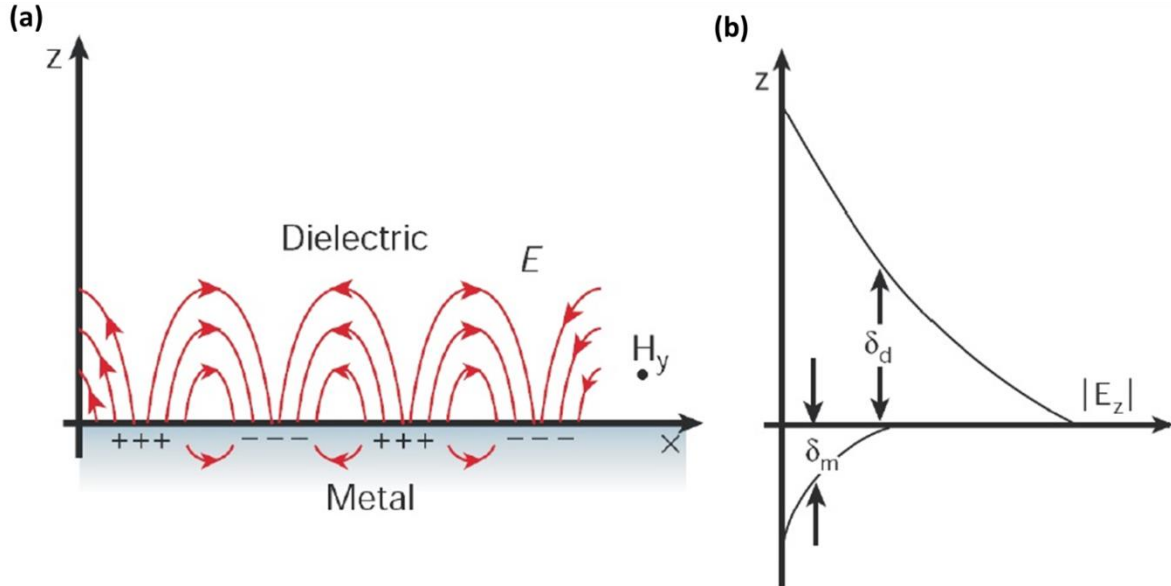


Figure IV.23 (a) Composed character of SPPs at the interface between dielectric and metal.(b) Evanscent fields in the two half spaces.¹⁷

Arriving to the dispersion relation of SPPs propagating at the interface between the two half spaces

$$k_{SP}(\omega) = \frac{\omega}{c} \sqrt{\frac{\varepsilon_m \varepsilon_d}{\varepsilon_m + \varepsilon_d}}$$

Considering that dielectric permittivity is real for the dielectric ($\varepsilon_d > 0$) and complex for the metal ($\varepsilon_m = \varepsilon'_m + i\varepsilon''_m$), with $\varepsilon''_m < |\varepsilon'_m|$. The dispersion relation can be expressed in terms of its real and imaginary components as $k_{SP} = k'_{SP} + ik''_{SP}$ with,

$$k'_{SP}(\omega) = \frac{\omega}{c} \left(\frac{\varepsilon_m \varepsilon_d}{\varepsilon_m + \varepsilon_d} \right)^{1/2}$$

$$k''_{SP} = \frac{\omega}{c} \left(\frac{\varepsilon''_m}{2\varepsilon'^2_m} \right) \left(\frac{\varepsilon_m \varepsilon_d}{\varepsilon_m + \varepsilon_d} \right)^{1/2}$$

The SPP wavelength is defined as $\lambda_{SP} = \frac{2\pi}{k'_{SP}}$, therefore we get:

$$\lambda_{SP} = \frac{2\pi c}{\omega} \sqrt{\frac{\epsilon'_m + \epsilon_d}{\epsilon'_m \epsilon_d}}$$

For metal with negative permittivity ($|\epsilon_m| > \epsilon_d$) we have:

$\lambda_{SP} < \lambda_0$ where $\lambda_0 = \frac{2\pi c \omega}{\sqrt{\epsilon_d}}$ is the excitation wavelength of SPP which is incident from the dielectric part of the interface. Having the ratio $\frac{\lambda_{SP}}{\lambda_0} < 1$, where its value depends on the metal, the dielectric and the excitation wavelength.

Together with the information of the frequency dependence of $\epsilon_i(\omega)$, one can express the dispersion relation in the form of $\omega = \omega(k_{SP})$

$$\omega^2(k_{SP}) = \frac{\omega_p^2}{2} + k_{SP}^2 c^2 - \sqrt{\left(\frac{\omega_p^4}{4} + k_{SP}^4 c^4\right)}$$

Assuming the metal as an ideal conductor with $Im\epsilon_m = 0$, having simplified dielectric function $\epsilon_m = 1 - \frac{\omega_p^2}{\omega^2}$

The dependence $\omega(k_{SP})$ of $k_{SP}(\omega) = \frac{\omega}{c} \sqrt{\frac{\epsilon_m \epsilon_d}{\epsilon_m + \epsilon_d}}$ has a slope $\frac{c}{\sqrt{\epsilon_d}}$ when $k_{SP} > 0$ having monotonic increasing function of k_{SP} with $\frac{CK_{SP}}{\sqrt{\epsilon_d}}$ as a limit. For large k_{SP} , it is asymptotic to the value $\omega_{SP} = \frac{\omega_p}{\sqrt{2}}$, *Figure IV.24*.

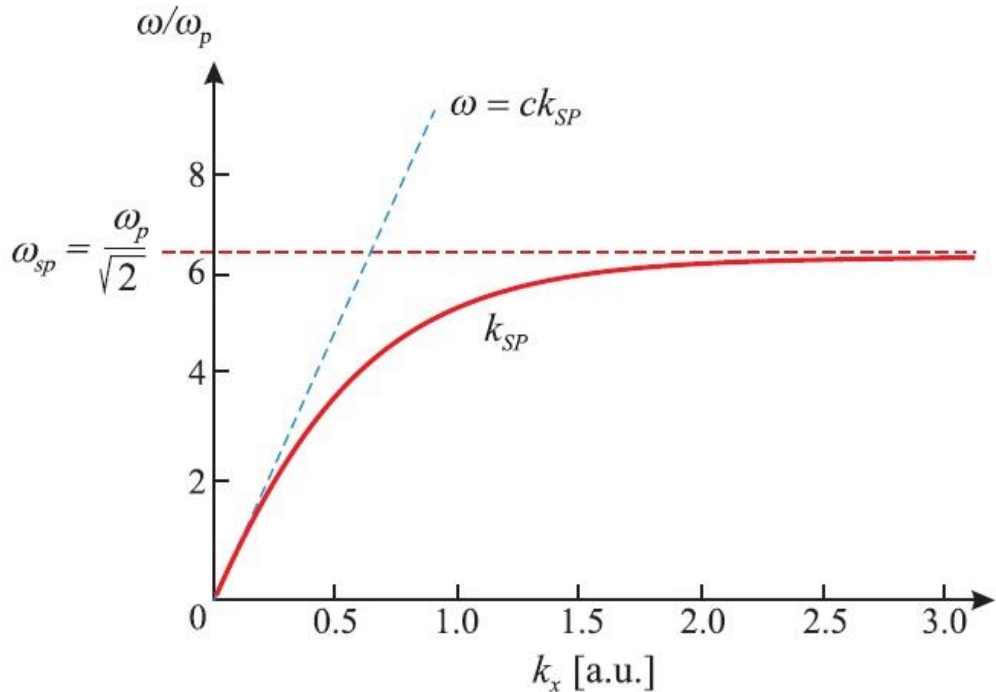


Figure IV.24 Dispersion relation for surface plasmon at the flat interface between a Drude metal and dielectric (air) with $\epsilon_d = 1$ and $\text{Im}\epsilon_m = 0$.

This is the case for non-retarded surface plasmon condition, with $k_x^m = k_x^d = k_{SP}$, applicable when the phase velocity $\frac{\omega}{k_{SP}}$ is much smaller than the speed of light c. Accordingly, the SPP wavelength is smaller than excitation wavelength $\lambda_{SP} \leq \lambda_0$, where the SPP wavevector is greater than the that of photon in the free medium.

However, in real metals the influence of both the free-electron and inter-band damping on the excitations of the conduction electrons reveals complex nature of ϵ_m and k_{SP} . The SPP are damped with a propagation length $L = \frac{1}{2I_m k_{SP}}$. The penetration depth through the dielectric, at which the amplitude of the evanescent SPP field is equal half the amplitude at the metal surface, is $\delta_{ppd}(\omega) = \left| \frac{1}{k_z^d} \right|$. Therefore, the general equation of the penetration depth of the SPP into the dielectric surrounding is written as $\delta_{ppd}(\omega) = \frac{c}{\omega} \sqrt{\left| \frac{\epsilon'_m + \epsilon_d}{\epsilon_d^2} \right|}$

IV.3.3.2 Nanoparticles on mirrors

It has been shown that coupling between localized surface plasmons of closely packed nanoparticles form the building blocks for effective SERS substrates. This results in very huge electric field enhancement occurring within the gap between two NPs (so-called a hot-spot regime).^{18–21} Additionally, nanoparticles residing above metallic film also show promising enhancements in Raman signals.^{22,23}

Nanoparticle-film or nanoparticle-on-mirror (NPOM) configuration was first theoretically reported by Metiu,^{24,25} illustrating nanoparticles separated by small distances from a bulk metal surface.^{26–38} When the separation distance is in the range between 1-50 nm, an electromagnetic concentration is induced within the gap, between the NPs and the film. The concentration intensity decreases rapidly with distance. However, distances around 20 nm can still provide high Raman gains (10^3 - 10^4), as calculated by R. Hell *et al.*³⁶ The mentioned electromagnetic concentration emerges from the interaction between the localized surface plasmon of the nanoparticles and the delocalized surface plasmon polariton of the metallic film.²¹

Several studies were realized to fabricate SERS substrates based on the coupling concept between metallic nanoparticles and metallic films. Using various separator types such as polymer,^{31,36,39} thiol groups^{30,33,35} and SiO₂^{23,40}, one can manage the separation distances between the nanoparticles and the film. Ye *et al.*⁴⁰ had reported the plasmonic interaction effect between gold nano-rings and a gold film on surface enhanced Raman scattering using Au nanorings-SiO₂-Au film structures. These Au rings were fabricated by nanosphere lithography with SiO₂ spacer. They have found that an SiO₂ thickness of 50 nm leads to the highest enhancement factor. This result was attributed to the closer structural resonance wavelength to the laser excitation wavelength obtained with this spacer thickness. Later, Mubeen *et al.*²³ studied the effect of SiO₂ spacer on the SERS enhancing ability of Au NPs-SiO₂-Au film structure. They obtained the maximum SERS activity for SiO₂ thickness of 2 nm with an angle of incidence of 60°.

It is worth to mention that most of the studies done following the nanoparticles on mirror strategy were realized to obtain SERS ability which did not exist for pure nanoparticles. In our work, we focus on the coupling of our Au-Ag/Au core/shell NPs; which already have high SERS enhancement ability; to Au film with variable SiO₂ spacer thicknesses. We investigate the effect of the spacer thickness in an aim to optimize the SERS

enhancing performance of our already existing substrates. SiO₂ spacer was chosen due to the ability to control its uniform thickness and to provide a fabrication platform for our nanoparticles similar to the glass substrates used in the fabrication of pure Au-Ag/Au core/shell nanoparticles.

IV.3.3.3 Au-Ag/Au core/shell nanoparticles coupling with Au film

In this part we describe the fabrication of the substrates combining the Au-Ag/Au core/shell nanoparticles with Au film separated by silica layer of variable thickness. The fabrication process consisted of thermally evaporating 30 nm gold film on cleaned glass substrates using an evaporation rate of 3 Å.s⁻¹. The Au film was then coated with SiO₂ layer of various thicknesses using electron-beam evaporator with an evaporation rate of 2 Å.s⁻¹. Au-Ag/Au core/shell NPs were then produced over the SiO₂ layer following the same fabrication strategy described before, where successive gold-silver-gold evaporation of 2 nm thickness each were performed with thermal annealing treatment following the first two evaporation.

For this study, five substrates represented by the following notation 30 nm Au film-xSiO₂-Au-Ag/Au NPs, where x=10, 20, 30, 40 and 50 nm were fabricated. In addition to the Au-Ag/Au NPs substrate which serves as a reference for our study was also prepared, *Figure IV.8*. *Figure IV.25* illustrates the SEM image and the SEM-based size distribution for the 30 nm Au-10nm SiO₂-(Au-Ag/Au NPs) substrate. The Au-Ag/Au NPs fabricated over the SiO₂ layer have average size of 20 nm in diameter, which proves the same morphology of the Au-Ag/Au core/shell NPs fabricated over the SiO₂ layer as over the glass substrate.

Table IV.8 Experimental details for fabricating the five 30 nm Au film-xSiO₂-Au-Ag/Au NPs substrates (x=10, 20, 30, 40 and 50 nm) and the reference Au-Ag/Au NPs substrate

	Au film (nm)	SiO ₂ film (nm)	Au-Ag/Au NPs Thickness = 2nm Temperature = 250°C
Au-10nmSiO₂-(Au-Ag/Au NPs)	30	10	Au-T-Ag-T-Au
Au-20nmSiO₂-(Au-Ag/Au NPs)	30	20	Au-T-Ag-T-Au
Au-30nmSiO₂-(Au-Ag/Au NPs)	30	30	Au-T-Ag-T-Au
Au-40nmSiO₂-(Au-Ag/Au NPs)	30	40	Au-T-Ag-T-Au
Au-50nmSiO₂-(Au-Ag/Au NPs)	30	50	Au-T-Ag-T-Au
Au-Ag/Au NPs	-	-	Au-T-Ag-T-Au

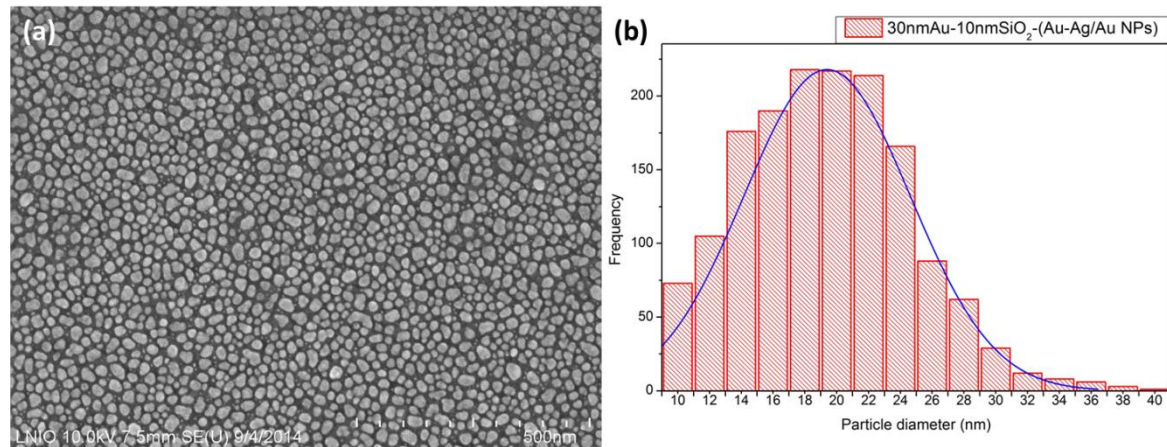


Figure IV.25 SEM image (a) and the SEM based size distribution (b) for the 30nm Au-10nm SiO₂-(Au-Ag/Au NPs) substrate

IV.3.3.4 Results and discussion

In order to investigate the enhancing ability in Raman intensities of the Au film-SiO₂-Au-Ag/Au NPs structures, SERS measurements have been carried out on the six different substrates using the same experimental parameters mentioned in Chapter III. The acquisition time was set at 3 seconds for all the substrates.

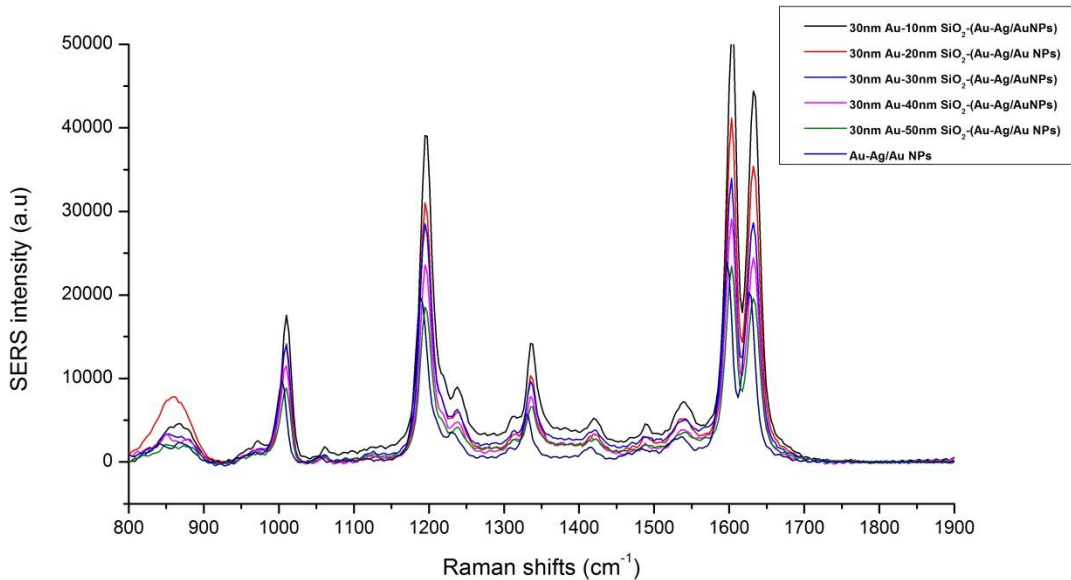


Figure IV.26 SERS signals for BPE solution (10^{-5} M) over the five 30 nm Au film- x SiO₂-Au-Ag/Au NPs substrates ($x=10, 20, 30, 40$ and 50 nm) and the reference Au-Ag/Au NPs substrate

Figure IV.26 shows the SERS measurements for the BPE solution (10^{-5} M) over the six substrates. The Au film-10 nm SiO₂-Au-Ag/Au substrate provides the highest SERS signal, then the SERS signals intensity decreases with increasing the SiO₂ spacer thickness. The Au film-50 nm SiO₂-Au-Ag/Au substrate almost provides a SERS signal whose intensity is equal to that obtained using pure Au-Ag/Au NPs substrate.

In order to study the relation between the enhancing ability of the Au film-xSiO₂-Au-Ag/Au NPs structure and the spacer thickness, the SERS intensity of the benzene ring stretching (1605 cm^{-1}) is plotted versus SiO₂ thickness, *Figure IV.27*. Not unexpectedly, the SERS intensity drops significantly on increasing the silica film thickness from 10 to 50 nm. The observed trend in the signal enhancement versus oxide layer thickness can be attributed to the exponentially decaying evanescent character for the surface plasmon polariton in gold film, where the obtained decay length is 23 nm. The penetration depth of the SPP into the dielectric surrounding is given by $\delta_{ppd}(\omega) = \frac{c}{\omega} \sqrt{\left| \frac{\varepsilon'_m + \varepsilon_d}{\varepsilon_d^2} \right|}$. The SERS enhancement of the electromagnetic field is expressed by $G_{em}(\gamma_s) = |A(\nu_L)|^2 |A(\nu_s)|^2$, where $A(\nu_L)$ and $A(\nu_s)$ are the enhancement factors for laser field and stokes field, respectively. Assuming that $\nu_L \approx \nu_s$, therefore the electromagnetic field enhancement expression can be simplified to $G_{em}(\gamma_s) = |A|^4$. It is important to note that the profile of the electromagnetic field amplitude inside the dielectric medium decays exponentially $E = E_0 e^{\frac{-z}{\delta_{ppd}}}$. Thus, the enhancement factor variation as a function of the spacer thickness can be described as:

$$G_{em}(\gamma_s) = \left(E_0 e^{\frac{-z}{\delta_{ppd}}} \right)^4 = E_0^4 e^{\frac{-4z}{\delta_{ppd}}} = E_0^4 e^{\frac{-z}{\delta_{ppd}'}} \text{, where } \delta_{ppd}' = \frac{\delta_{ppd}}{4}$$

Taking into consideration the respective refractive index values of the gold and SiO₂ layers at the Raman wavelength (632.8 nm), we obtain an $\delta_{ppd}' = 35.25$ nm. The obtained value presents a satisfying agreement with the experimentally deduced decay constant ($\delta_{ppd}'^{exp} = 23$ nm), verifying the interaction between the localized surface plasmon of the NPs and the delocalized surface plasmon polariton of the metal film.^{21,22}

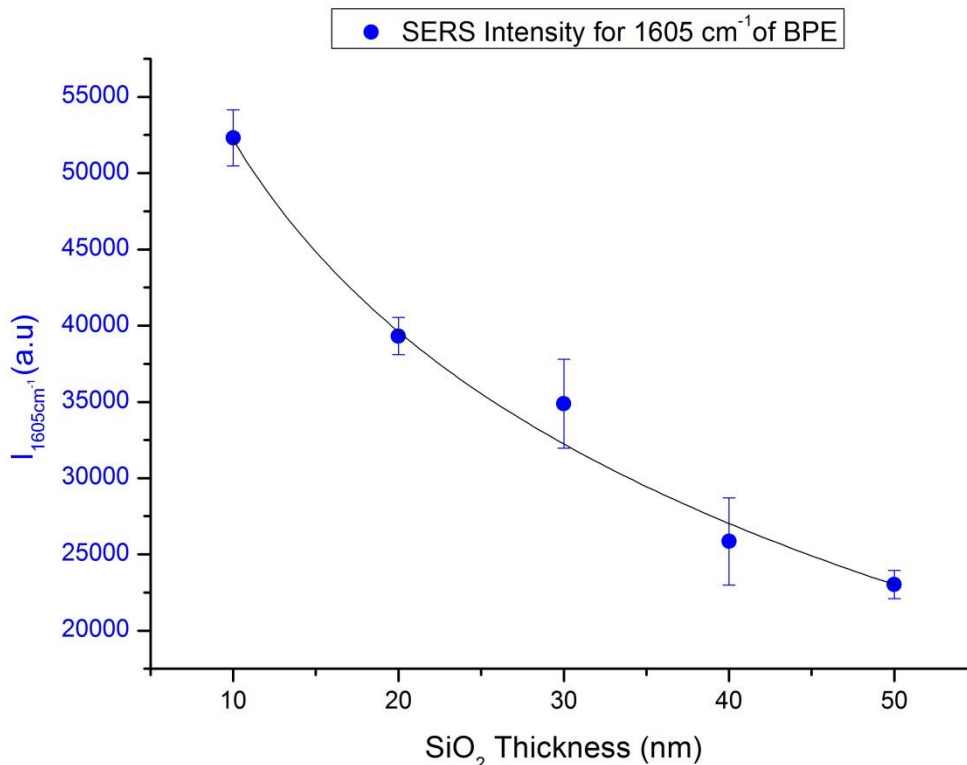


Figure IV.27 SERS intensities of the benzene ring stretching (1605 cm^{-1}) versus the SiO_2 thickness

Our fabricated Au-Ag/Au core/shell NPs have already efficient “hot-spots” providing high enhancement in SERS intensity. These hot-spots result from the interparticle coupling effect between adjacent nanoparticles. In order to follow the effect of the interaction between the nanoparticles and the Au film with changing SiO_2 thickness, we have calculated the relative enhancement factor for the Au-Ag/Au NPs caused by the coupling with the Au film. The relative enhancement factor is represented by the ratio of the SERS signal intensity obtained using the Au film-x SiO_2 -Au-Ag/Au NPs substrate $\left(I_{\text{SERS}_{1605\text{cm}^{-1}}}^{\text{Au film}-x\text{SiO}_2-(\text{Au-Ag/Au NPs})} \right)$ to that obtained over the pure Au-Ag/Au NPs $\left(I_{\text{SERS}_{1605\text{cm}^{-1}}}^{\text{Au-Ag/Au NPs}} \right)$ of value 23073 a.u. *Table IV.9* shows the relative enhancement factor calculated using the following equation:

$$EF_R = \frac{I_{\text{SERS}_{1605\text{cm}^{-1}}}^{\text{Au film}-x\text{SiO}_2-(\text{Au-Ag/Au NPs})}}{I_{\text{SERS}_{1605\text{cm}^{-1}}}^{\text{Au-Ag/Au NPs}}}$$

Table IV.9 The SERS intensity of the benzene ring stretching (1605 cm^{-1}) and the relative enhancement factor for different SiO_2 thicknesses in the Au film-x SiO_2 -(Au-Ag/Au NPs) substrates

SiO_2 thickness (nm)	$I_{\text{SERS}_{1605\text{cm}^{-1}}}^{\text{Au film-xSiO}_2-(\text{Au-Ag/Au NPs})}$ (a.u)	$EF_R = \frac{I_{\text{SERS}_{1605\text{cm}^{-1}}}^{\text{Au film-xSiO}_2-(\text{Au-Ag/Au NPs})}}{I_{\text{SERS}_{1605\text{cm}^{-1}}}^{\text{Au-Ag/Au NPs}}}$
10	52311	2.26
20	39318	1.70
30	34874	1.51
40	25849	1.12
50	23017	0.99

Figure IV.28 shows the relative enhancement factor of the benzene ring stretching peak (1605 cm^{-1}) versus the SiO_2 thickness.

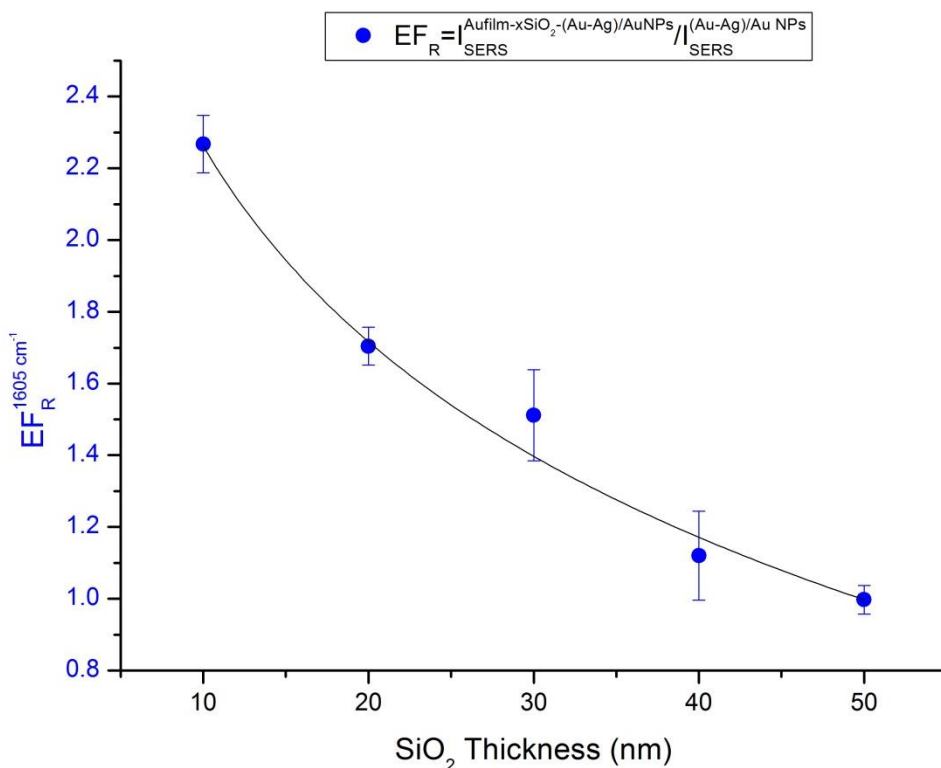


Figure IV.28 The relative enhancement factor of the benzene ring stretching peak (1605 cm^{-1}) versus the SiO_2 thickness

The relative enhancement factor rapidly decreases from its maximum at 2.3 for a 10 nm separation thickness reaching 1 for the 50 nm SiO_2 thickness. The interaction between the

Au-Ag/Au NPs and the Au film separated by 10 nm SiO₂ spacer provides an increase of more than two orders of magnitude in BPE SERS intensity than the Au-Ag/Au substrate. The improvements in SERS enhancement can be viewed as originating from the following two contributions: i) the hot-spots generated from neighboring nanoparticles and ii) the enhanced electric field confined in the gap between the nanoparticles and the film. Hence, the zone consisting of two adjacent nanoparticles over the gold film serve as an antenna concentrating radiant energy in the gap where the molecules reside.

References

1. Egerton, R. *Physical Principles of Electron Microscopy: An Introduction to TEM, SEM, and AEM.* (Springer, 2006). at <http://books.google.fr/books?id=8Z1a1IF2_OQC>
2. Bansal, A., Sekhon, J. & Verma, S. S. Scattering Efficiency and LSPR Tunability of Bimetallic Ag, Au, and Cu Nanoparticles. *Plasmonics* **9**, 143–150 (2014).
3. Link, S. & El-Sayed, M. A. Shape and size dependence of radiative, non-radiative and photothermal properties of gold nanocrystals. *Int. Rev. Phys. Chem.* **19**, 409–453 (2000).
4. Pustovalov, V. K., Astafyeva, L. G. & Fritzsche, W. Optical Properties of Core–Shell Gold–Silver and Silver–Gold Nanoparticles for Near UV and Visible Radiation Wavelengths. *Plasmonics* **7**, 469–474 (2012).
5. Bruzzone, S., Arrighini, G. P. & Guidotti, C. Theoretical study of the optical absorption behavior of Au/Ag core–shell nanoparticles. *Mater. Sci. Eng. C* **23**, 965–970 (2003).
6. Jiang, R., Chen, H., Shao, L., Li, Q. & Wang, J. Unraveling the Evolution and Nature of the Plasmons in (Au Core)-(Ag Shell) Nanorods. *Adv. Mater.* **24**, OP200–OP207 (2012).
7. Chen, Y. *et al.* The Study of Surface Plasmon in Au/Ag Core/Shell Compound Nanoparticles. *Plasmonics* **7**, 509–513 (2012).
8. Gaspar, D. *et al.* Influence of the layer thickness in plasmonic gold nanoparticles produced by thermal evaporation. *Sci. Rep.* **3**, (2013).
9. Cheng, P., Li, D. & Yang, D. Effect of rapid thermal processing on surface plasmon resonance of Ag island films. *Optoelectron. Adv. Mater. Commun.* **5**, 455–458 (2011).
10. Romanyuk, V. R., Kondratenko, O. S., Kondratenko, S. V., Kotko, A. V & Dmitruk, N. L. Transformation of thin gold films morphology and tuning of surface plasmon resonance by post-growth thermal processing. *Eur. Phys. J. - Appl. Phys.* **56**, null–null (2011).
11. Yan, C. *et al.* Molecule oxygen-driven shaping of gold islands under thermal annealing. *Appl. Surf. Sci.* **258**, 377–381 (2011).
12. Zhang, X. *et al.* Thermal-induced surface plasmon band shift of gold nanoparticle monolayer: morphology and refractive index sensitivity. *Nanotechnology* **21**, 465702 (2010).
13. Shen, H., Guillot, N., Rouxel, J., de la Chapelle, M. L. & Toury, T. Optimized plasmonic nanostructures for improved sensing activities. *Opt. Express* **20**, 21278–21290 (2012).

14. Tan, T. *et al.* LSPR-dependent SERS performance of silver nanoplates with highly stable and broad tunable LSPRs prepared through an improved seed-mediated strategy. *Phys. Chem. Chem. Phys.* **15**, 21034–21042 (2013).
15. Dragoman, M. & Dragoman, D. Plasmonics: Applications to nanoscale terahertz and optical devices. *Prog. Quantum Electron.* **32**, 1–41 (2008).
16. Maier, S. A. *Plasmonics: Fundamentals and Applications*. 224 (Springer, 2007).
17. Barnes, W. L., Dereux, A. & Ebbesen, T. W. Surface plasmon subwavelength optics. *Nature* **424**, 824–830 (2003).
18. Camden, J. P. *et al.* Probing the Structure of Single-Molecule Surface-Enhanced Raman Scattering Hot Spots. *J. Am. Chem. Soc.* **130**, 12616–12617 (2008).
19. Chen, T. *et al.* Hotspot-Induced Transformation of Surface-Enhanced Raman Scattering Fingerprints. *ACS Nano* **4**, 3087–3094 (2010).
20. Wells, S. M., Retterer, S. D., Oran, J. M. & Sepaniak, M. J. Controllable Nanofabrication of Aggregate-like Nanoparticle Substrates and Evaluation for Surface-Enhanced Raman Spectroscopy. *ACS Nano* **3**, 3845–3853 (2009).
21. Yoon, I. *et al.* Single Nanowire on a Film as an Efficient SERS-Active Platform. *J. Am. Chem. Soc.* **131**, 758–762 (2008).
22. Gehan, H. *et al.* Thermo-induced Electromagnetic Coupling in Gold/Polymer Hybrid Plasmonic Structures Probed by Surface-Enhanced Raman Scattering. *ACS Nano* **4**, 6491–6500 (2010).
23. Mubeen, S. *et al.* Plasmonic Properties of Gold Nanoparticles Separated from a Gold Mirror by an Ultrathin Oxide. *Nano Lett.* **12**, 2088–2094 (2012).
24. Aravind, P. K., Rendell, R. W. & Metiu, H. A new geometry for field enhancement in surface-enhanced spectroscopy. *Chem. Phys. Lett.* **85**, 396–403 (1982).
25. Aravind, P. K. & Metiu, H. Use of a perfectly conducting sphere to excite the plasmon of a flat surface. 1. Calculation of the local field with applications to surface-enhanced spectroscopy. *J. Phys. Chem.* **86**, 5076–5084 (1982).
26. He, L., Smith, E. A., Natan, M. J. & Keating, C. D. The Distance-Dependence of Colloidal Au-Amplified Surface Plasmon Resonance. *J. Phys. Chem. B* **108**, 10973–10980 (2004).
27. Tokareva, I., Minko, S., Fendler, J. H. & Hutter, E. Nanosensors Based on Responsive Polymer Brushes and Gold Nanoparticle Enhanced Transmission Surface Plasmon Resonance Spectroscopy. *J. Am. Chem. Soc.* **126**, 15950–15951 (2004).
28. Garrell, R. L. & Beer, K. D. Surface-enhanced Raman scattering from 4-ethylpyridine and poly(4-vinylpyridine) on gold and silver electrodes. *Langmuir* **5**, 452–458 (1989).

29. Kim, K. & Yoon, J. K. Raman Scattering of 4-Aminobenzenethiol Sandwiched between Ag/Au Nanoparticle and Macroscopically Smooth Au Substrate. *J. Phys. Chem. B* **109**, 20731–20736 (2005).
30. Anderson, D. J. & Moskovits, M. A SERS-Active System Based on Silver Nanoparticles Tethered to a Deposited Silver Film. *J. Phys. Chem. B* **110**, 13722–13727 (2006).
31. Kinnan, M. K. & Chumanov, G. Surface Enhanced Raman Scattering from Silver Nanoparticle Arrays on Silver Mirror Films: Plasmon-Induced Electronic Coupling as the Enhancement Mechanism. *J. Phys. Chem. C* **111**, 18010–18017 (2007).
32. Mock, J. J. *et al.* Distance-Dependent Plasmon Resonant Coupling between a Gold Nanoparticle and Gold Film. *Nano Lett.* **8**, 2245–2252 (2008).
33. Rodríguez-Lorenzo, L. *et al.* Zeptomol Detection Through Controlled Ultrasensitive Surface-Enhanced Raman Scattering. *J. Am. Chem. Soc.* **131**, 4616–4618 (2009).
34. Wang, K., Schonbrun, E. & Crozier, K. B. Propulsion of Gold Nanoparticles with Surface Plasmon Polaritons: Evidence of Enhanced Optical Force from Near-Field Coupling between Gold Particle and Gold Film. *Nano Lett.* **9**, 2623–2629 (2009).
35. Chen, S.-Y. *et al.* Gold Nanoparticles on Polarizable Surfaces as Raman Scattering Antennas. *ACS Nano* **4**, 6535–6546 (2010).
36. Hill, R. T. *et al.* Leveraging Nanoscale Plasmonic Modes to Achieve Reproducible Enhancement of Light. *Nano Lett.* **10**, 4150–4154 (2010).
37. Liu, B., Blaszczyk, A., Mayor, M. & Wandlowski, T. Redox-Switching in a Viologen-type Adlayer: An Electrochemical Shell-Isolated Nanoparticle Enhanced Raman Spectroscopy Study on Au(111)-(1×1) Single Crystal Electrodes. *ACS Nano* **5**, 5662–5672 (2011).
38. Yamamoto, N., Ohtani, S. & García de Abajo, F. J. Gap and Mie Plasmons in Individual Silver Nanospheres near a Silver Surface. *Nano Lett.* **11**, 91–95 (2010).
39. Daniels, J. K. & Chumanov, G. Nanoparticle–Mirror Sandwich Substrates for Surface-Enhanced Raman Scattering. *J. Phys. Chem. B* **109**, 17936–17942 (2005).
40. Ye, J. *et al.* Tuning plasmonic interaction between gold nanorings and a gold film for surface enhanced Raman scattering. *Appl. Phys. Lett.* **97**, 163106 (2010).

Chapter V

Shape-controlled Ag/Au Monometallic and Bimetallic Nanoparticles

V.1 Introduction

Following the fabrication and the characterization of the bimetallic nanoparticles carried out in the previous chapters, we are more interested in this chapter by a systematic study of their interesting features to improve our understanding of their plasmonic and SERS enhancing properties. Meanwhile thermal annealing of thin metallic films fabrication method has been employed in the previous two chapters, Electron Beam Lithography (EBL) technique is adopted in this chapter. It enables the production of nanoparticles arranged in a periodic array with well-defined parameters (shape, size, thickness, and lattice constant).¹ The advantage of the EBL technique resides in seeking the effect of each morphological parameter independently.

Therefore in this chapter we aim to study the plasmonic properties of Ag/Au bimetallic nanoparticles in comparison to Au and Ag monometallic NPs. Firstly, we investigate the size and periodicity effects of monometallic and bimetallic nanoparticles on the LSPR and SERS enhancement ability, where only Au and Ag monometallic nanoparticles have been widely investigated in the literature during the last decade.²⁻⁵ Additionally, different metallic types of nanoparticles having exactly the same morphological parameters are fabricated in order to follow the effect of nanoparticle metallic nature on the LSPR and SERS properties.

In order to study the nanoparticles type effect on the LSPR and SERS activity, five different substrates of monometallic and bimetallic nanoparticles were fabricated. Each of the fabricated substrate contains eight different patterns with variable diameter size and lattice constants. By comparison between the different patterns, we can study the size and periodicity effects on the LSPR and SERS enhancement within the same type of nanoparticles.

V.2 Monometallic and bimetallic nanocylinders arrays

The nanoparticles investigated in the following chapter are fabricated using Electron Beam Lithography (EBL) technique. The fabrication started by spin casting of polymethyl methacrylate (PMMA) solution on clean glass substrate producing a ca. 150 nm positive resist layer. The resist is then patterned by exposing it to electron beam at designed positions using a Hitachi S-2500 N Scanning Electron Microscope (SEM) guided by Nano-Pattern Generation System (NPGS) (acceleration voltage of 30 KV, electron dose range from 300 to

$450\mu\text{C}/\text{cm}^2$ and electron current of 10 pA). After exposure, the substrate is chemically developed (using water, MIBK:IPA / 1:3, IPA) causing dissociation of the exposed areas thus leaving a patterned mask for the subsequent thermal vacuum deposition of metals. Then, the substrate is immersed in acetone for 2 hours in order to remove the remaining PMMA and the metal at the non-exposed areas. Consequently, patterned metallic nanoparticles are only obtained on the substrate.

Five different substrates have been prepared exhibiting square pattern arrays of metallic nanocylinders (NCs) (area of $50\mu\text{m} \times 50\mu\text{m}$) with variable diameter sizes and lattice constants. Where two sets of different diameter sizes of 110, 140, 170 and 200 nm for each substrate, having 300 nm lattice constant for the first set and 450 nm for the second were fabricated. Therefore, this results in eight different patterns for each substrate. For better adhesion of the metallic nanocylinders (NCs), 3 nm of chromium was pre-evaporated forming an adhesion layer between the glass substrate and the desired metallic evaporation. Two monometallic substrates have been prepared, the first by evaporating 50 nm gold and the second by evaporating 50 nm silver. Additionally, three bimetallic substrates have been fabricated, the first by evaporating 25 nm gold followed by 25 nm silver, the second by successive evaporation of 25 nm silver and 25 nm gold and the third by three successive evaporation of 17 nm of gold, silver and gold. As a result, five substrates have been obtained having variable NCs types and of 50 nm height, *Figure V.1*.

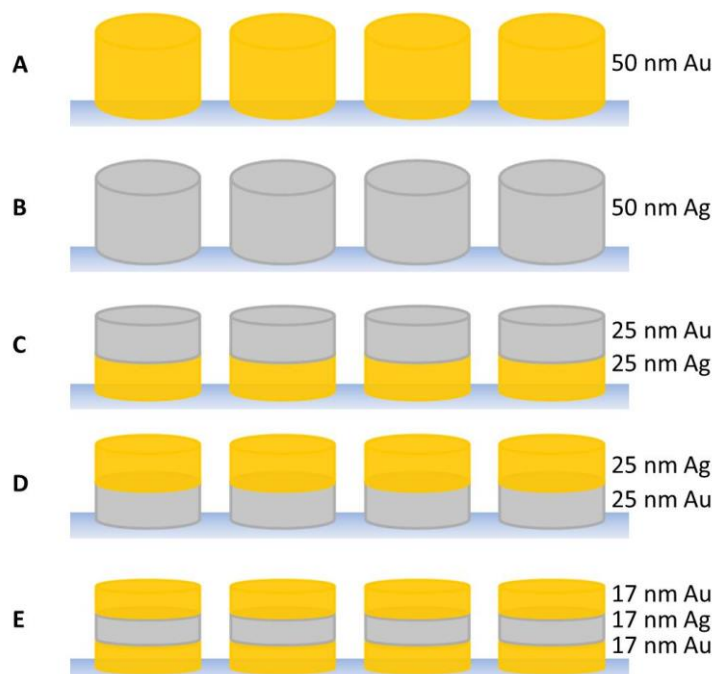


Figure V.1 Schematic presentation of the five different fabricated NCs types

The SEM images shown in *Figure V.2*, illustrate the eight different patterns of Au NCs. The careful check of the particle size and the lattice constant by applying size distribution study using ImageJ⁶ on the SEM images shows that the error in diameter between the designed parameters and the real obtained ones are in the range of 1 nm to 10 nm, while the error in lattice constant is less than 2 nm. Consequently, for better accuracy the actual parameters obtained by the SEM images are used in discussing further studies.

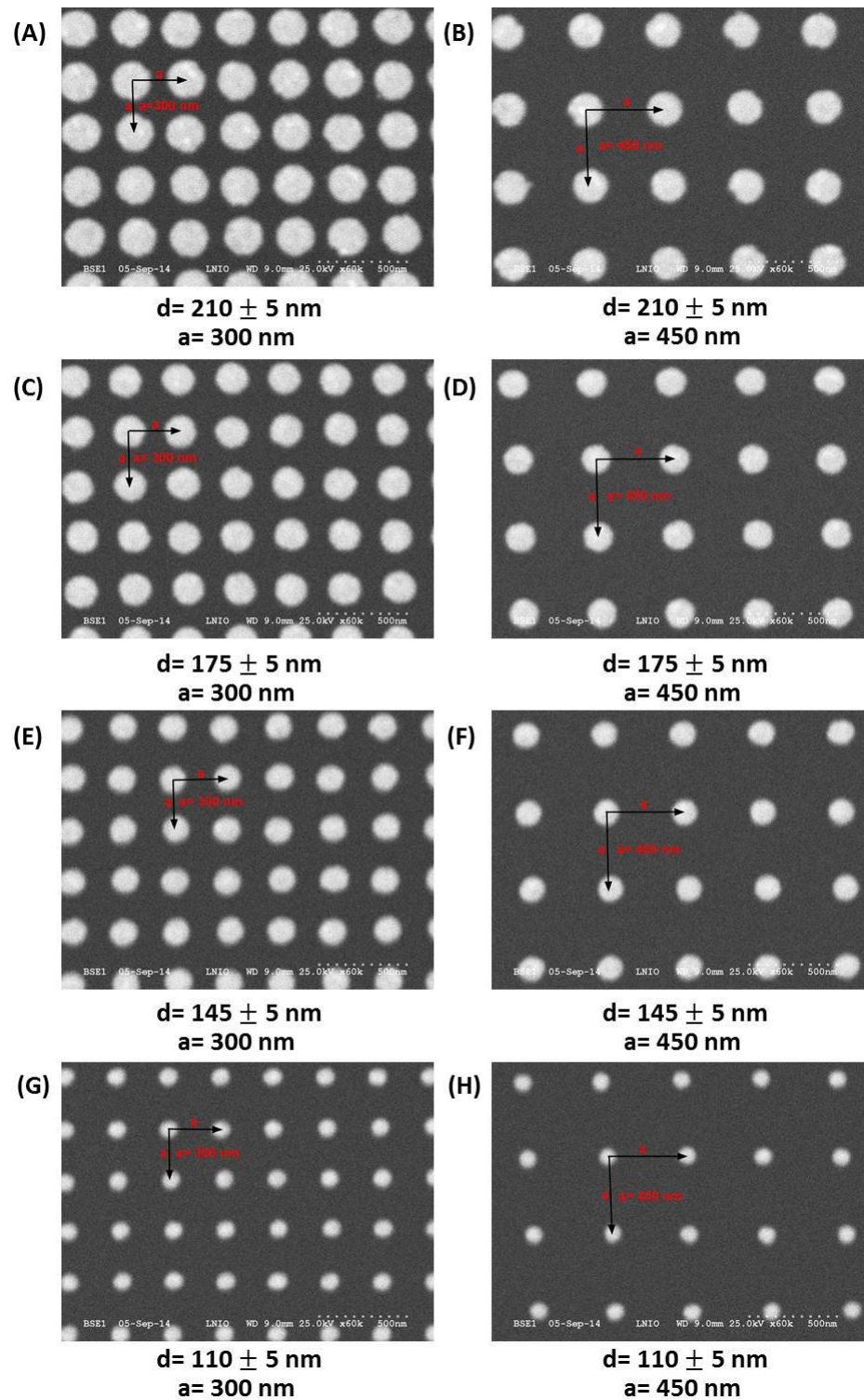


Figure V.2 SEM images for the eight different Au NCs patterns where “ d ” represents the diameter size and “ a ” the lattice constant

V.3 Extinction measurements

Extinction measurements were performed using a modified Jobin-Yvon micro Raman spectrometer (LABRAM). The samples were illuminated in normal incidence with collimated white light. The spectra were recorded in transmission configuration using an objective lens (50x, NA=0.8) by removing the edge filters. The investigated area is of approximate 10 μm in diameter, which is smaller than the array dimensions (50 μm x 50 μm).

V.3.1 The LSPR dependence on NCs size

It is well known that the increase in Ag and Au nanoparticle size results in a red-shift and broadening of the LSPR peak.^{4,7-9} Accordingly, we have tested the validity of this behavior for the Ag/Au bimetallic NCs having different composition ratios and order. *Figure V.3 A, B, C, D and E* show respectively the LSPR spectra for the Au, Ag, Au-Ag, Ag-Au and Au-Ag-Au NCs with patterns having increasing diameter size with 300 nm as a lattice constant. All figures show a red-shift and broadening behavior with increased NCs size regardless of their type and the composition. *Figure V.4 F and G* respectively illustrate the spectral position (λ_{LSPR}) and the FWHM of the LSPR peak as a function of the diameter size for the five different substrates. Both graphs show a quasi-linear relation for λ_{LSPR} and FWHM with respect to the diameter size. The increasing in Au NCs size from 110 to 210 nm in diameter exhibit a red-shift of 58 nm and an increase in FWHM of 115 nm. For Ag NCs, we obtained a red-shift of 97 nm and a peak broadening of 81 nm for the same size increase. As for the bimetallic NCs, the plasmonic resonance of the Au-Ag, Ag-Au and Au-Ag-Au NCs, red-shifts by 73, 80 and 63 nm and broadening of 144, 102 and 140 nm are observed respectively.

Thus, Au/Ag bimetallic NCs follow the same behavior regime as monometallic NCs with respect to the size effect on the LSPR position and shape, where an increase in NCs size has resulted in the red-shifting and broadening of the LSPR peak. However, the degree of this red-shift and broadening is different for each NCs type. The size increase shows high influence on the LSPR spectral position for Ag NCs and low influence for Au NCs. Meanwhile, the changing in size moderately affects the LSPR position for the bimetallic NCs. On the other hand, the peak width of the LSPR is affected by the NCs size in this decreasing order: bimetallic, Au and Ag NCs.

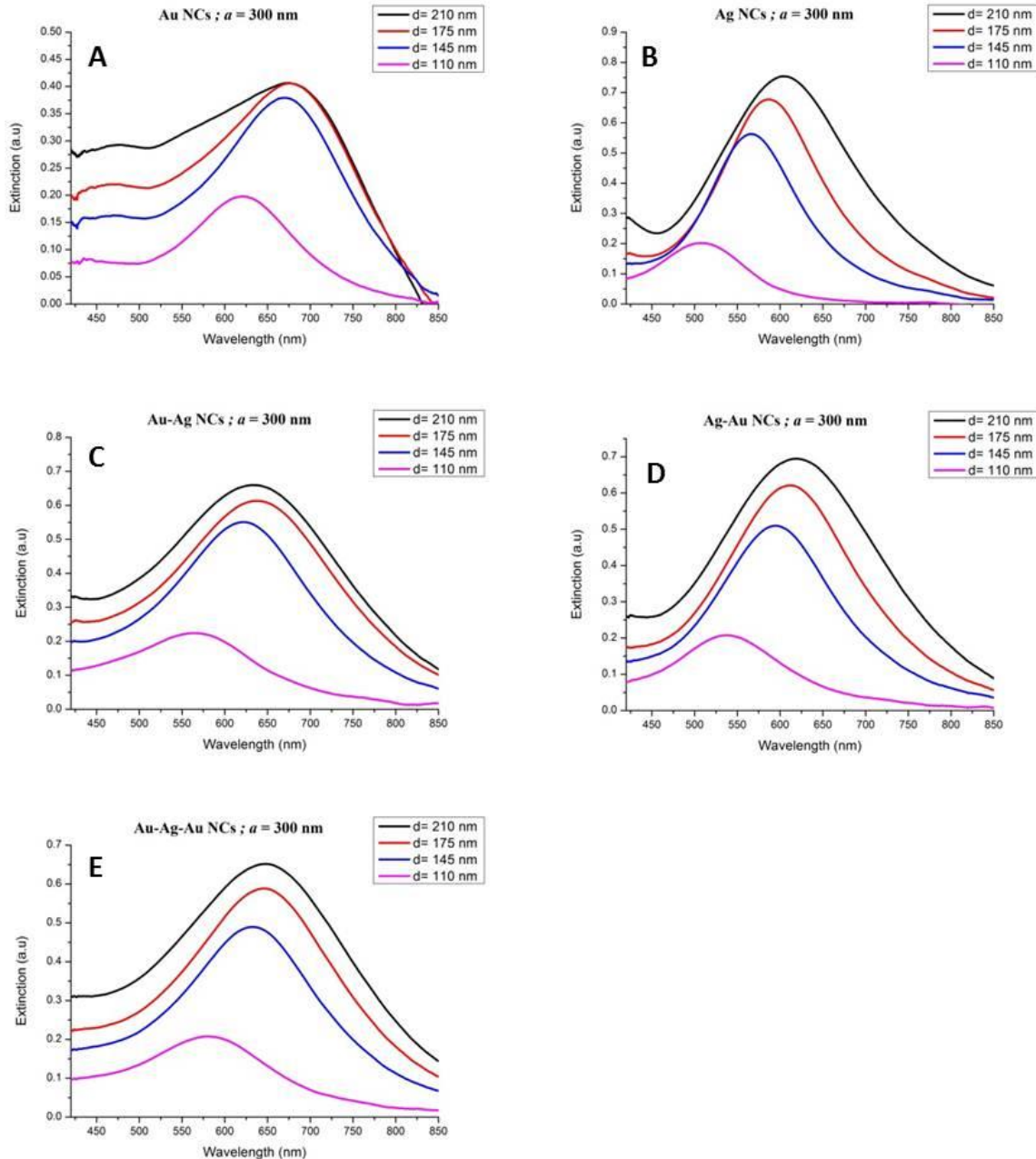


Figure V.3 The extinction spectra of (A) Au, (B) Ag, (C) Au-Ag, (D) Ag-Au and (E) Au-Ag-Au NCs patterns having different diameter sizes 110, 145, 175 and 210 nm with 300 nm as lattice constant.

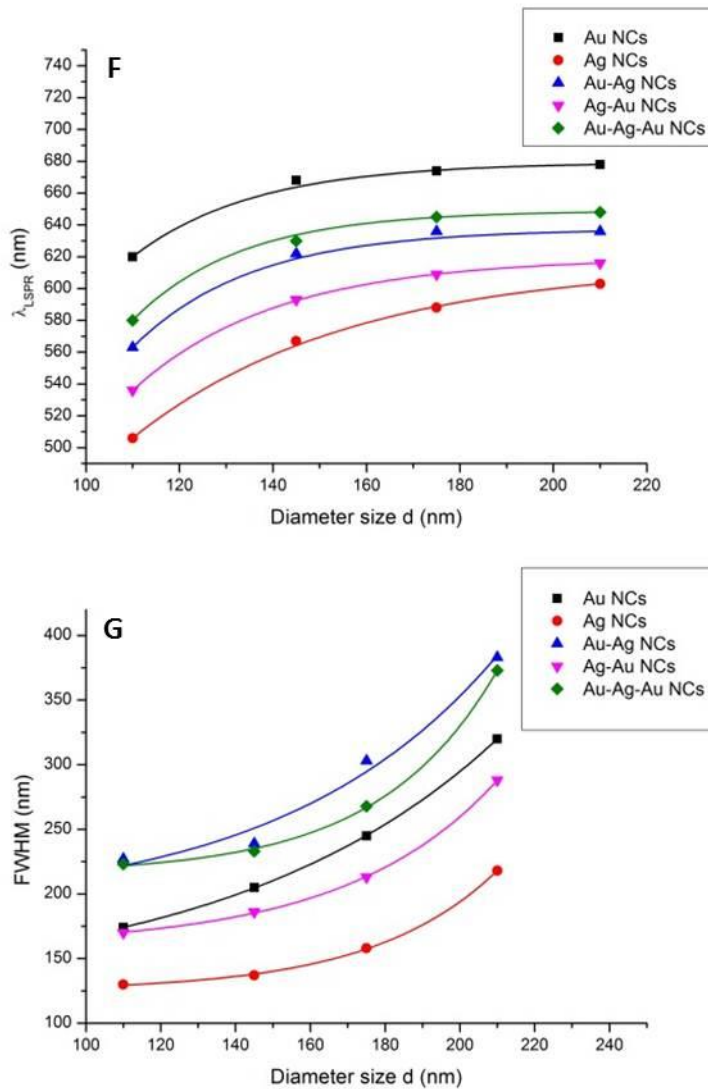


Figure V.4 The maxima wavelength λ_{LSPR} (F) and the FWHM (G) of the LSPR peak as a function of the diameter size for the Au, Ag, Au-Ag, Ag-Au and Au-Ag-Au NCs.

V.3.2 Effect of interparticle spacing on the LSPR

In addition to the size effect on the LSPR position, the inter-particle distances also influence the LSPR properties.^{8,10} In order to monitor the inter-particle separation distance effect on the LSPR, we compare the monometallic and bimetallic arrays having two different lattice constants for a fixed diameter size. *Figure V.5 A, B, C and D* show the extinction spectra for the square arrays of Au NCs with 300 and 450 nm lattice constants for diameter sizes of 110, 145, 175 and 210 nm, respectively. The spectra show red-shift as the NCs separation distance increases for all diameter sizes, which is attributed to the inter-particle coupling among neighboring particles. In earlier studies, electromagnetic interactions among

neighboring metallic nanostructures were shown to have different components, the electrostatic and electrodynamic terms. The electrostatic term, which is proportional to $1/a^3$, is dominant for relatively small inter-particle separations and it was found to cause red-shift in the LSPR peak as the lattice constant decreases. On the other hand, the electrodynamic term, being proportional to $1/a$, was shown to dominate when the lattice constant of the array is comparable to the wavelength of light. Electrodynamic interactions cause red-shifts and FWHM decrease in the resonance peak as the inter-particle separation increases.^{4,11} The lattice constants discussed in our study are comparable to the wavelength of the incident light, and the obtained red-shift behavior and FWHM decrease with particles separation increase are in good agreement with literature experimental, and modeling studies.⁴ This red-shift increases in value with increasing the diameter size, having 42, 55, 71 and 84 nm shift for 110, 145, 175 and 210 nm diameter size of Au NCs, respectively. *Figure V.5 E* shows the red-shift value $|\lambda_{LSPR}^{a=300nm} - \lambda_{LSPR}^{a=450nm}|$ as a function of the diameter size for the five different substrates Au, Ag, Au-Ag, Ag-Au and Au-Ag-Au NCs. It reveals that all types of NCs exhibit an increase in the red-shift value with the increasing in diameter size.

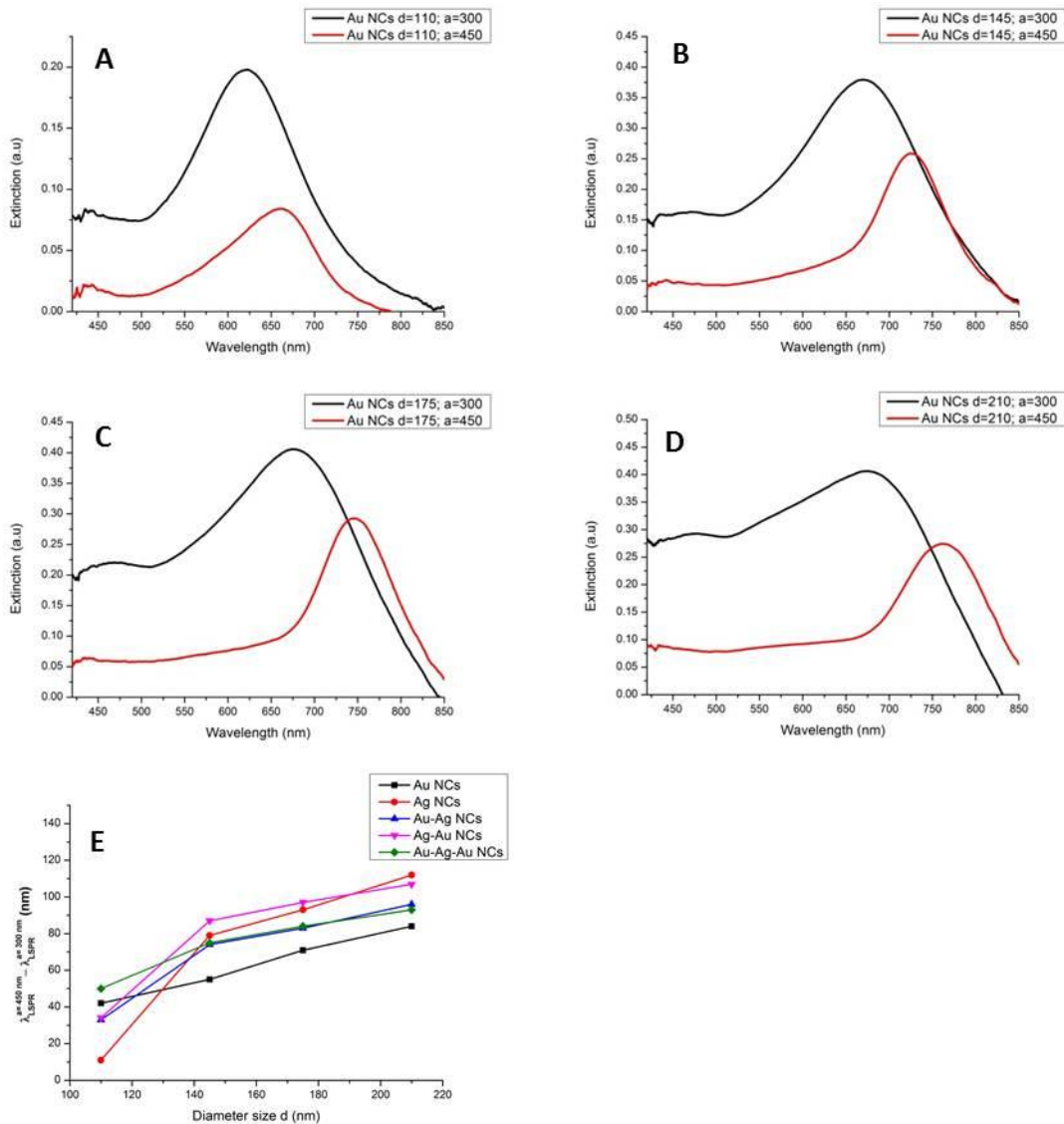


Figure V.5 The extinction spectra of Au NCs patterns of diameter sizes (A) 110, (B) 145, (C) 175 and (D) 210 nm with 300 and 450 nm lattice constant; (E) the red-shift value $|\lambda_{LSPR}^{a=300\text{nm}} - \lambda_{LSPR}^{a=450\text{nm}}|$ as a function of the diameter size for the five different substrates Au, Ag, Au-Ag, Ag-Au and Au-Ag-Au NCs.

V.3.3 Composition distribution and NCs nature effect on the LSPR

After discussing the size and periodicity effect, we focus now on the metallic composition and the evaporation metallic order effects on the LSPR properties. *Figure V.6 A, B, C and D* show the LSPR spectra for Au, Ag, Au-Ag, Ag-Au and Au-Ag-Au arrays having lattice constants of 300 nm for the 110, 145, 175 and 210 nm diameter sizes, respectively. We can notice that all figures show that the Au/Ag bimetallic NCs have LSPR spectral position lying in-between that of Ag and Au NCs. The LSPR corresponding to Au-Ag NCs is red-

shifted in comparison to the Ag-Au NCs, knowing that both NCs have equal metallic ratios of silver and gold. We interpret this difference in LSPR by the different interfaces found in the two systems, where Au-substrate and Ag-air are the two interfaces present in the Au-Ag NCs while Ag-substrate and Au-air interfaces exist in the Ag-Au NCs. Thus, the metal-substrate interface appears to overcome the metal-air interface, causing a red-shift in LSPR for the Au-Ag NCs.

Remarkably, the Ag NCs present the sharpest LSPR peak among the five different substrates for all the diameter sizes. This could be explained by the fact that Ag nanoparticles are less influenced by the inter-band transitions and conduction electrons than Au nanoparticles.¹² Additionally, we can observe a broadening in the LSPR peak of Au-Ag NCs in comparison to that of Ag-Au NCs. This can be also related to the Au-substrate interface present in Au-Ag NCs leading to LSPR with FWHM greater than that of Ag-Au NCs where the Ag-substrate interface exists, *Figure V.6*.

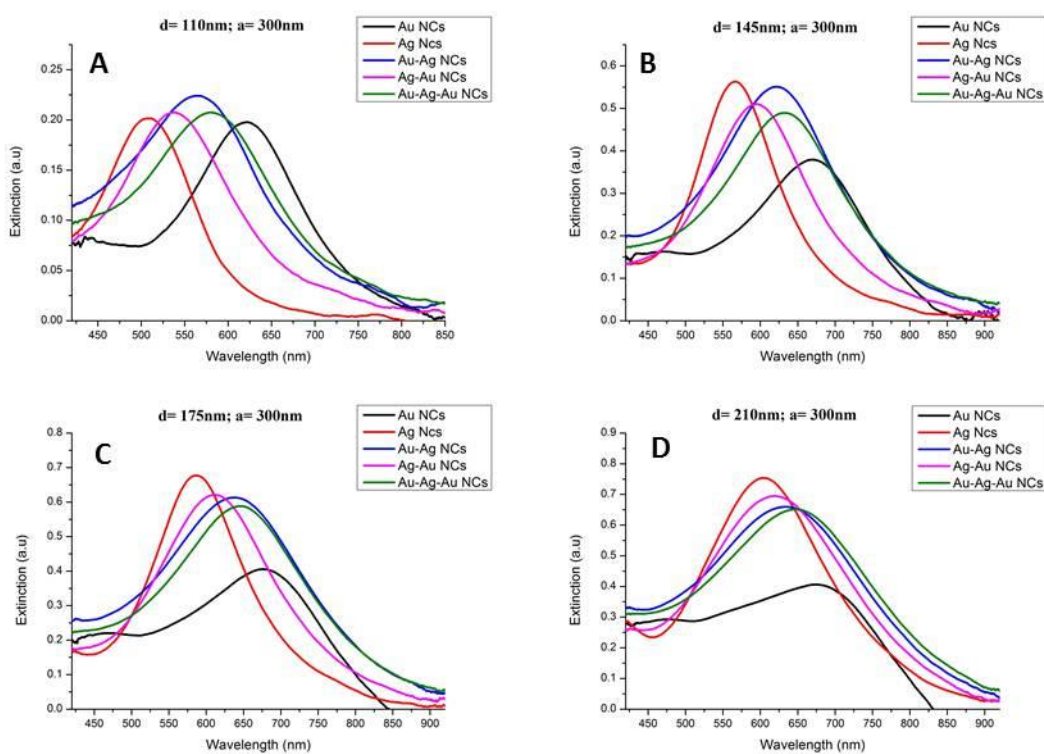


Figure V.6 The LSPR spectra for Au, Ag, Au-Ag, Ag-Au and Au-Ag-Au arrays having lattice constants of 300 nm for the (A) 110, (B) 145, (C) 175 and (D) 210 nm diameter sizes.

The Au-Ag-Au NCs exhibit LSPR position red-shifted from that of the Ag-Au and Au-Ag NCs. This red-shift can be explained by the increase in the gold metallic ratio, from ($\frac{1}{2}$ Ag, $\frac{1}{2}$ Au) for both Au-Ag and Ag-Au NCs to ($\frac{1}{3}$ Ag, $\frac{2}{3}$ Au) for the Au-Ag-Au NCs. Au-Ag-Au NCs have LSPR with FWHM value in-between that of Au-Ag and Ag-Au due to the presence of Au-substrate interface but with less Au thickness (17 nm in Au-Ag-Au and 25 nm in Au-Ag).

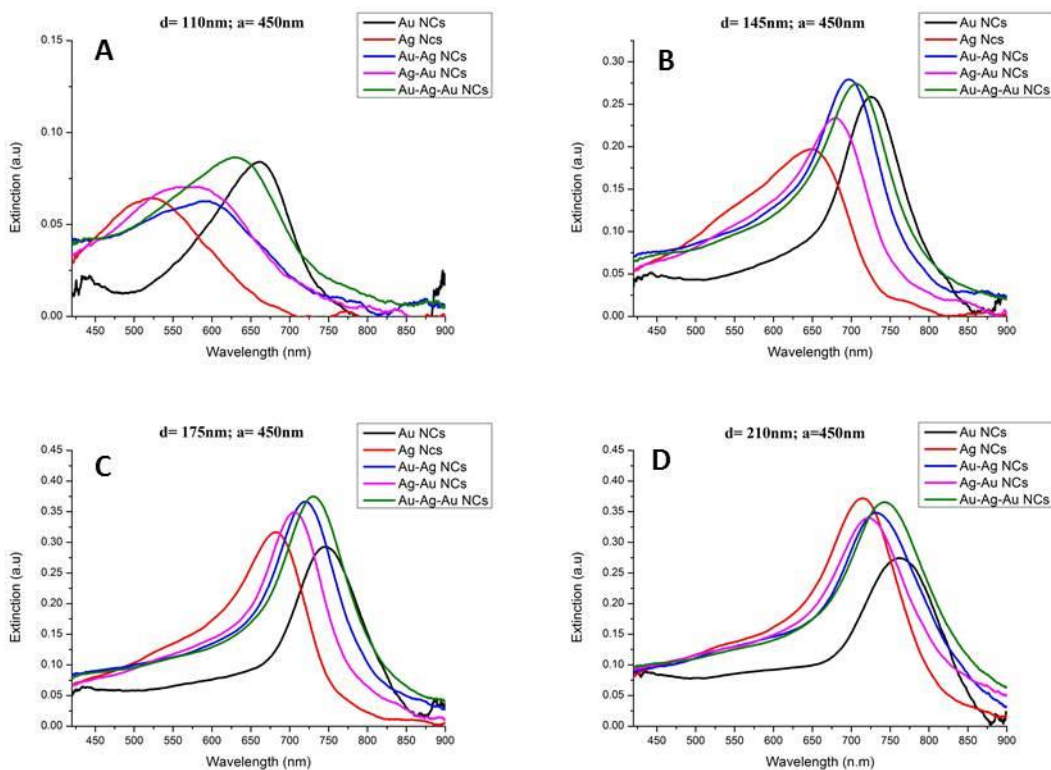


Figure V.7 The LSPR spectra for Au, Ag, Au-Ag, Ag-Au and Au-Ag-Au arrays having lattice constants of 450 nm for the (A) 110, (B) 145, (C) 175 and (D) 210 nm diameter sizes.

Figure V.7 A, B, C and D show the LSPR spectra for Au, Ag, Au-Ag, Ag-Au and Au-Ag-Au arrays having lattice constants of 450 nm for the 110, 145, 175 and 210 nm diameter sizes, respectively. As mentioned before, the increase in lattice constant do affect the LSPR peak spectral position and shape. Similarly, increasing the lattice constant from 300 nm to 450 nm affects the LSPR spectral properties in the same manner (peak position and broadening).

Even though the nanoparticles fabricated using EBL have different dimensions to those prepared using thermal annealing of thin metallic film technique, we can still compare

the composition and evaporation order effects on the general behavior of the LSPR peak. Thus, EBL samples can be employed for further understanding the LSPR behavior of the substrates discussed in the previous two chapters. Ag NPs have been further confirmed as having the sharpest LSPR peak in comparison to Au and Au/Ag bimetallic NPs. Secondly, the broader LSPR peaks obtained in the double layered system in chapter 3 for the Au-T-Ag and Ag-T-Au NPs in comparison to pure Au and Ag NPs are in good agreement with the LSPR FWHM obtained for the bimetallic NCs obtained in EBL in comparison to pure Au and Ag NCs.

Moreover, in the previous chapter it has been shown that Au-T-Ag-T-Au NPs exhibit an LSPR wavelength (599 nm) lying within that of pure monometallic nanoparticles; Au-T-Au-T-Au (605 nm) and Ag-T-Ag-T-Ag NPs(509 nm), with this value being more shifted toward that of Au-T-Au-T-Au NPs. These results are in good agreement with those obtained using EBL fabrication method, where Au-Ag-Au NCs are found to have an LSPR position (648 nm for $d= 210$ nm and $a= 300$ nm) also lying within that of pure gold (678 nm for $d= 210$ nm and $a= 300$ nm) and silver (603 nm for $d= 210$ nm and $a= 300$ nm) NCs for all the studied diameter sizes and lattice constants. Similarly to thermal annealing of thin metallic film technique, the LSPR position of Au-Ag-Au NCs is also more shifted toward that of pure Au NCs obtained using EBL fabrication method.

V.4 SERS measurements over monometallic and bimetallic NCs

Surface enhanced Raman spectroscopy measurements were realized using the high resolution Jobin Yvon-Horiba LABRAM, using a 10x objective and a helium-neon laser to excite the particle arrays at a wavelength of 632.8 nm. BPE of concentration 10^{-5} M was used as a non-resonant probe molecule with acquisition time of 10 seconds for a good S/N ratio for all SERS measurements in this chapter. NCs patterns for all types of the five substrates with 450 nm lattice constant gave very weak or no SERS signals, thus we focused our discussion on the SERS signals obtained over the arrays with lattice constant 300nm with variable diameter sizes of 110, 145, 175 and 210 nm.

The SERS signals of BPE obtained over the Au, Ag, Au-Ag, Ag-Au and Au-Ag-Au NCs arrays with the four different diameter sizes are presented in *Figure V.8 A, B, C, D and E* respectively. *Figure V.8 A* shows that for Au NCs, the SERS intensity decreases with the increasing of the diameter size. However, for Ag, Ag-Au and Au-Ag-Au NCs exhibit an

increase in SERS intensity with the increase in the diameter size (*Figure V.8 B, D and E* respectively). While for the Au-Ag NCs, the SERS signal nearly remains constant with the size increase (*Figure V.8 C*).

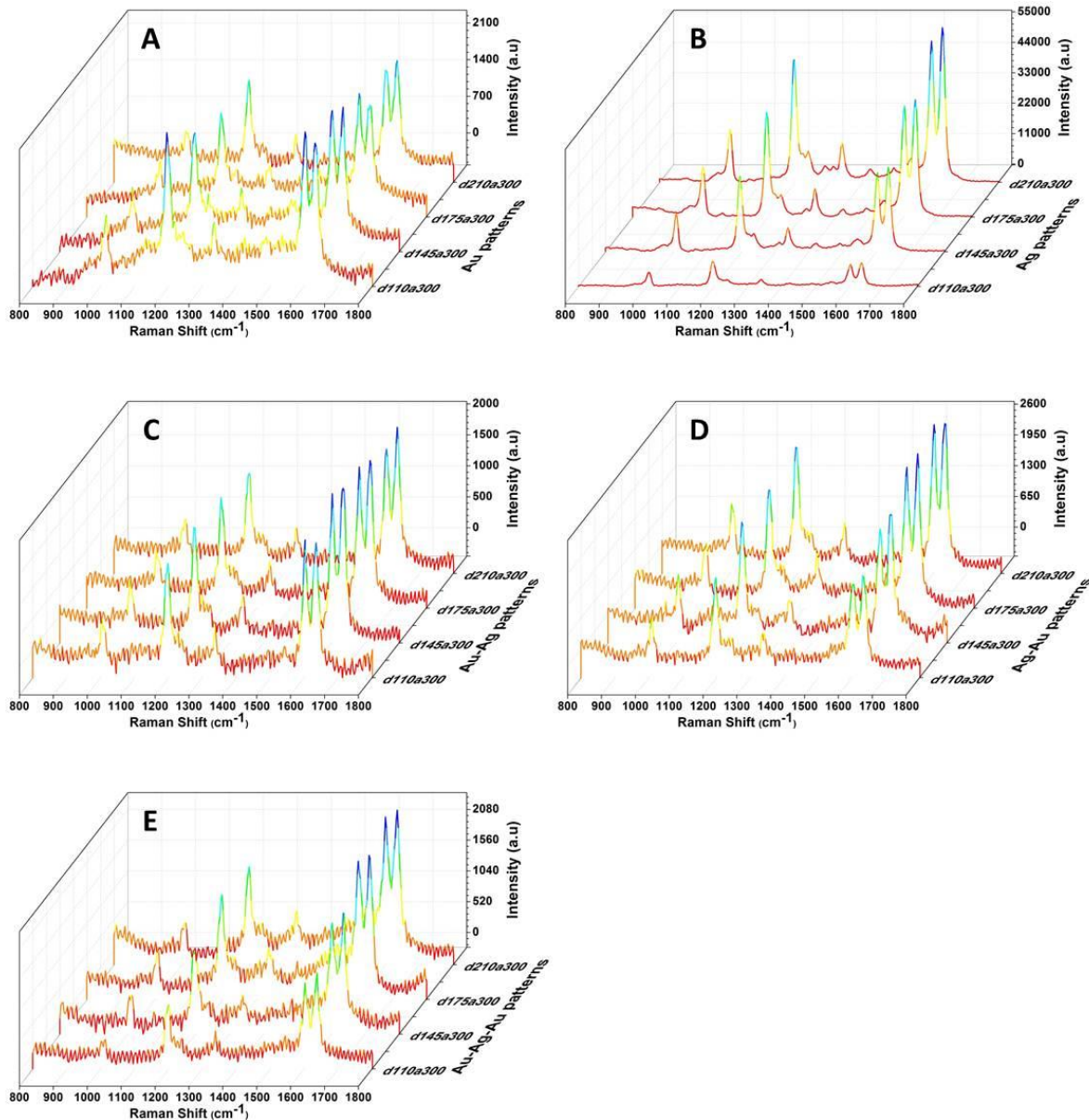


Figure V.8 SERS spectra of BPE (10^5 M) over the four different diameter sizes arrays (110, 145, 175 and 210 nm) with 300nm lattice constant for the (A) Au, (B) Ag, (C) Au-Ag, (D) Ag-Au and (E) Au-Ag-Au NCS.

A plot of the SERS intensity of the benzene ring stretching (1605 cm^{-1}) versus the diameter size of the NCs arrays for each substrate (*Figure V.9*) clearly shows the existence of

linear relationships between the two. Where for Au NCs arrays, a linear decreasing of the SERS intensity with the increasing of diameter size is observed (black line *Figure V.9*). On the other hand, a linear increasing relation of the SERS signals by increasing the size is obtained for Ag, Ag-Au and Au-Ag-Au NCs arrays (red, pink and green lines respectively) and finally the Au-Ag NCs arrays show nearly-constant SERS intensities with variation in diameter sizes (blue line). The Ag NCs provide the highest SERS signals in comparison to other types of NCs regardless the diameter size, verifying the highest SERS enhancement over Ag NPs when it's LSPR close to the excitation wavelength.

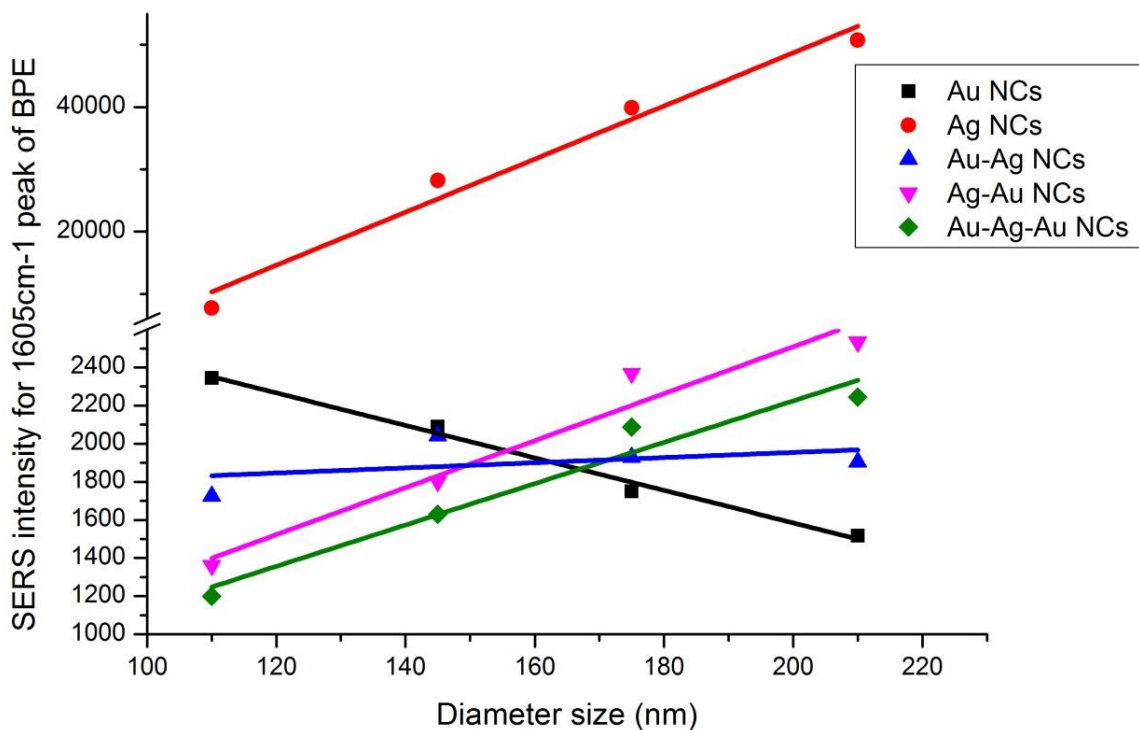


Figure V.9 Plot of the SERS intensity of the benzene ring stretching (1605 cm^{-1}) versus the diameter size of the NCs arrays (Au, Ag, Au-Ag, Ag-Au and Au-Ag-Au NCs)

In order to follow the plasmonic effect on the obtained relation between the diameter size and the SERS enhancement ability for each substrate, the SERS intensity of the benzene ring stretching (1605 cm^{-1}) is plotted versus $\Delta\lambda$ (the absolute value of the difference between the Raman excitation wavelength and the LSPR resonance wavelength) for each of the four different arrays ($d=110, 145, 175$ and 210 nm) related to the Au, Ag and Ag-Au NCs

substrates (*Figure V.10 A, B and C respectively*). Based on figure A, B and C, we observe an inversely proportional relation between the SERS intensity and $\Delta\lambda$ for the Au, Ag and Ag-Au substrates, respectively. The array exhibiting the closest LSPR spectral position to the excitation wavelength provides the highest enhancement in Raman intensities. Thus, the linear relation obtained from the SERS intensity as a function of the diameter size is explained by the increase in the degree of proximity of the array's LSPR to the extinction wavelength (632.8 nm). This is achieved by decreasing or increasing the diameter size depending on the NCs type.

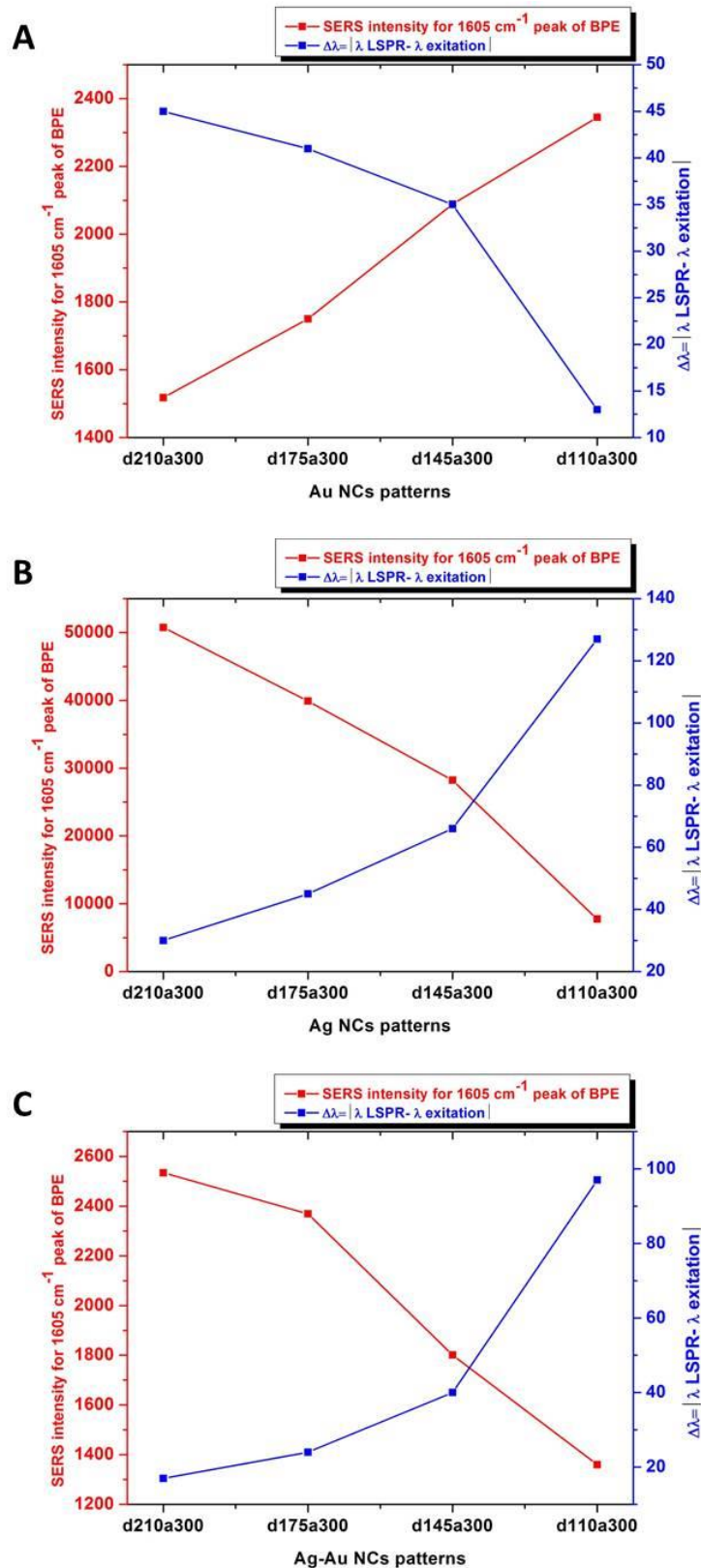


Figure V.10 The inversely proportional relation between SERS intensities of the benzene ring stretching (1605 cm^{-1}) and $\Delta\lambda$ (the absolute value for the difference between the Raman excitation wavelength, 632.8 nm , and the LSPR resonance) as a function of diameter sizes for the (A) Au, (B) Ag and (C) Ag-Au NCs patterns.

Figure V.11 shows the SERS intensities of the 1605 cm^{-1} peak plot versus $\Delta\lambda$ for the Au-Ag NCs substrate with four different diameter sizes. No specific relation appears to exist between the SERS intensity and $\Delta\lambda$. Noticeably, the diameter sizes of 145, 175 and 210 nm give nearly the same SERS intensity which is higher than that obtained over the 110 nm diameter size. This behavior could be explained by the nearly constant and closer LSPR positions of the 145 ($\Delta\lambda\sim11\text{nm}$), 175 ($\Delta\lambda\sim3\text{nm}$) and 210 nm ($\Delta\lambda\sim3\text{nm}$) diameter sized NCs to the λ_{ext} in comparison to that of the 110 nm sized NCs ($\Delta\lambda\sim70\text{nm}$).

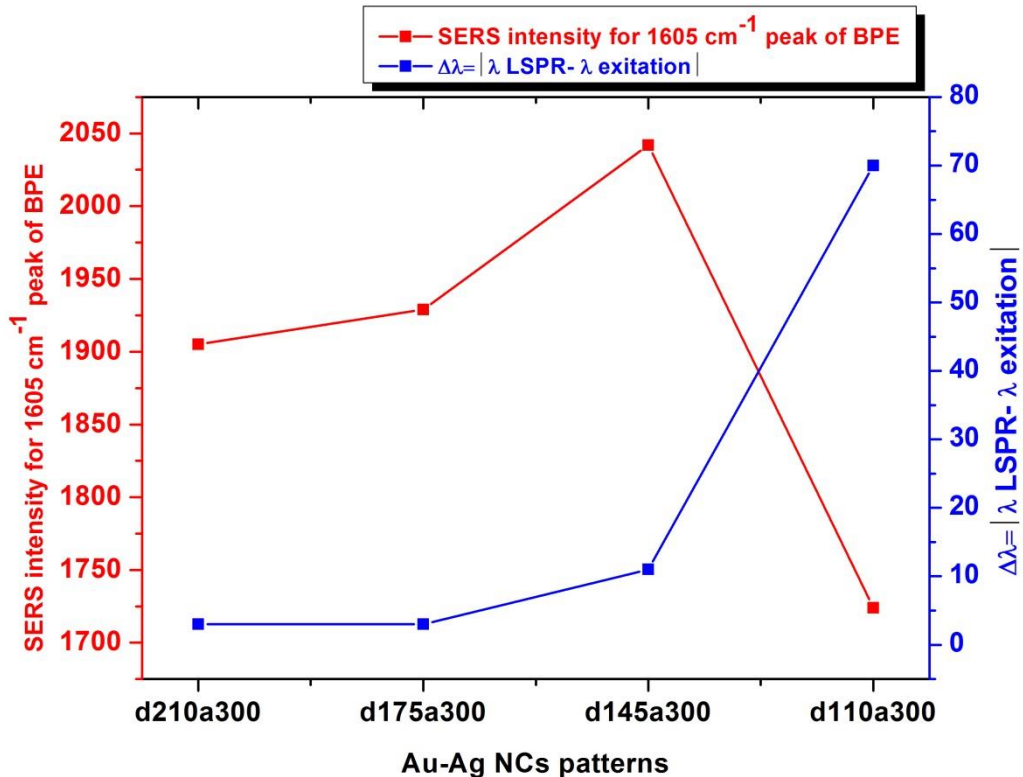


Figure V.11 The SERS intensities of the benzene ring stretching (1605 cm^{-1}) and $\Delta\lambda$ (the absolute value for the difference between the Raman excitation wavelength, 632.8 nm , and the LSPR resonance) as a function of diameter sizes for the Au-Ag NCs patterns.

As for the Au-Ag-Au NCs, also no specific relation between the SERS intensity and $\Delta\lambda$ is obtained (*Figure V.12 A*), however we do have an increase in SERS signals with the increasing of the diameter size. The arrays of diameter sizes 145, 175 and 210 nm have very close LSPR position and in close proximity to the excitation wavelength ($\Delta\lambda=3, 12$ and 15 nm respectively). On the other hand, the 110 nm diameter NCs array provides the lowest SERS enhancement which could be explained by its LSPR position far from the excitation wavelength by $\sim 53\text{ nm}$. In fact, some studies have shown that the best Raman signal

enhancement is obtained over arrays having LSPR spectral position located exactly between the excitation wavelength λ_{ext} and the Raman wavelength λ_R (related to the band of interest of the probe molecule observed)^{5,13–15} more precisely, some assumptions proposed that it should correspond to LSPR wavelength $\lambda_L = (\lambda_{\text{ext}} + \lambda_R)/2$ ¹⁴. Then, for excitation at $\lambda_{\text{ext}} = 632.8$ nm and a Raman wavelength $\lambda_R = 704$ nm (BPE band at 1605 cm^{-1}), the best LSPR position should be located at 668 nm. *Figure V.12 B* represents the SERS intensities of the benzene ring stretching (1605 cm^{-1}) plotted versus $\Delta\lambda_{L-\text{LSPR}}$ (the absolute value of the difference between the $\lambda_L = (\lambda_{\text{ext}} + \lambda_R)/2$ and the LSPR resonance) for each of the four different arrays ($d=110, 145, 175$ and 210 nm) related to the Au-Ag-Au NCs. The figure shows an inversely proportional relation between the SERS enhancement and $\Delta\lambda_{L-\text{LSPR}}$ where the Au-Ag-Au array having the LSPR wavelength closest to 668 nm has the highest SERS enhancement signal.

The SERS signals obtained over the Au, Au-Ag, Ag-Au and Au-Ag-Au NCs have comparable intensities while Ag NCs provide the highest SERS enhancement. The superiority of the Ag NCs in SERS enhancing over the other NCs can be related to the lower FWHM of the Ag NCs LSPR. This can be explained by the inversely proportional relationship between the near-field enhancement factor f and the LSPR width, where a narrower LSPR indicates a higher local field enhancement.^{16,17} Moreover, the LSPR peaks of all Ag NCs have spectral overlap with the Raman excitation wavelength. This overlap increases with increasing the Ag NCs diameter size, also explain the SERS signal increase with the Ag NCs size.

In summary, the systematic study of the Au/Ag bimetallic nanoparticles fabricated by Electron Beam Lithography (EBL) technique has showed that these bimetallic nanoparticles follow similar behavior regime as monometallic particles, where increasing the NCs size results in red shifting and broadening to the LSPR peak. Moreover, a good agreement in LSPR broadening is obtained between the double layered system in Chapter III and bimetallic NCs obtained by EBL, where LSPR of bimetallic systems are broader than those of monometallic systems. The studied monometallic and bimetallic NCs exhibit an inversely proportional relationship between the SERS intensity and $\Delta\lambda$, knowing that the array having the closest LSPR spectral position to the Raman excitation wavelength provides the highest SERS enhancement.

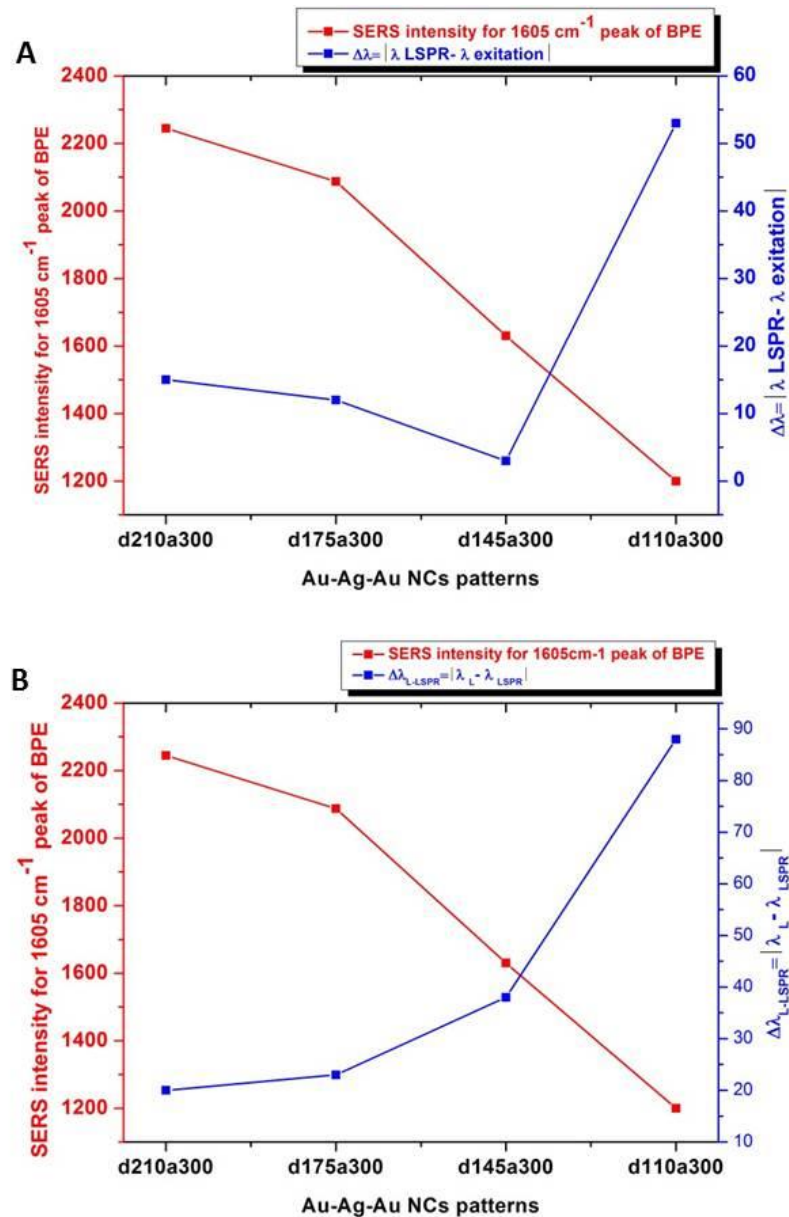


Figure V.12 The relation between SERS intensities of the benzene ring stretching (1605 cm^{-1}) and (A) $\Delta\lambda$ (the absolute value for the difference between the Raman excitation wavelength, 632.8 nm , and the LSPR resonance); (B) $\Delta\lambda_{L-LSPR}$ (the absolute value of the difference between the $\lambda_L = (\lambda_{\text{ext}} + \lambda_R)/2$ and the LSPR resonance) as a function of diameter sizes for the Au-Ag-Au NCs patterns.

References

1. Vieu, C. *et al.* Electron beam lithography: resolution limits and applications. *Appl. Surf. Sci.* **164**, 111–117 (2000).
2. Guler, U. & Turan, R. Effect of particle properties and light polarization on the plasmonic resonances in metallic nanoparticles. *Opt. Express* **18**, 17322–17338 (2010).
3. Kelly, K. L., Coronado, E., Zhao, L. L. & Schatz, G. C. The Optical Properties of Metal Nanoparticles: The Influence of Size, Shape, and Dielectric Environment. *J. Phys. Chem. B* **107**, 668–677 (2002).
4. Haynes, C. L. *et al.* Nanoparticle Optics: The Importance of Radiative Dipole Coupling in Two-Dimensional Nanoparticle Arrays†. *J. Phys. Chem. B* **107**, 7337–7342 (2003).
5. Grand, J. *et al.* Optimization of SERS-active substrates for near-field Raman spectroscopy. *Synth. Met.* **139**, 621–624 (2003).
6. ImageJ.. at <<http://imagej.nih.gov/ij/>>
7. Barchiesi, D., Kessentini, S., Guillot, N., de la Chapelle, M. L. & Grosges, T. Localized surface plasmon resonance in arrays of nano-gold cylinders: inverse problem and propagation of uncertainties. *Opt. Express* **21**, 2245–2262 (2013).
8. Lamprecht, B. *et al.* Metal Nanoparticle Gratings: Influence of Dipolar Particle Interaction on the Plasmon Resonance. *Phys. Rev. Lett.* **84**, 4721–4724 (2000).
9. Mortazavi, D., Kouzani, A. Z., Kaynak, A. & Duan, W. No Title. *Prog. Electromagn. Res.* **126**, 203–235 (2012).
10. Félidj, N. *et al.* Controlling the optical response of regular arrays of gold particles for surface-enhanced Raman scattering. *Phys. Rev. B* **65**, 75419 (2002).
11. Zhao, L., Kelly, K. L. & Schatz, G. C. The Extinction Spectra of Silver Nanoparticle Arrays: Influence of Array Structure on Plasmon Resonance Wavelength and Width†. *J. Phys. Chem. B* **107**, 7343–7350 (2003).
12. Quinten, M. *Optical Properties of Nanoparticle Systems Mie and Beyond.* (Wiley-VCH Verlag & Co. KGaA, 2011).
13. Grand, J. *et al.* Role of localized surface plasmons in surface-enhanced Raman scattering of shape-controlled metallic particles in regular arrays. *Phys. Rev. B* **72**, 33407 (2005).
14. Félidj, N. *et al.* Optimized surface-enhanced Raman scattering on gold nanoparticle arrays. *Appl. Phys. Lett.* **82**, (2003).

15. Guillot, N. *et al.* Surface enhanced Raman scattering optimization of gold nanocylinder arrays: Influence of the localized surface plasmon resonance and excitation wavelength. *Appl. Phys. Lett.* **97**, (2010).
16. Shen, H., Guillot, N., Rouxel, J., de la Chapelle, M. L. & Toury, T. Optimized plasmonic nanostructures for improved sensing activities. *Opt. Express* **20**, 21278–21290 (2012).
17. Tan, T. *et al.* LSPR-dependent SERS performance of silver nanoplates with highly stable and broad tunable LSPRs prepared through an improved seed-mediated strategy. *Phys. Chem. Chem. Phys.* **15**, 21034–21042 (2013).

General Conclusion and Perspectives

The main aim of this work was to develop reliable, highly enhancing SERS substrates which can meet the commercial standards. Based on the high enhancing ability of silver nanoparticles and the inert nature of gold nanoparticles, makes the idea of combining the two metals in a bimetallic nanostructure as an interesting approach in order to sum up the merits of both silver optical enhancing properties and gold surface properties.

The fabrication of several Au/Ag bimetallic (double-layered or triple-layered) nanoparticles SERS-active substrates have been carried out by the thermal annealing of thin metallic film strategy. Concerning the double- and triple-layered bimetallic nanoparticles, an inversely proportional relationship between the SERS intensity and $\Delta\lambda$ (the difference between the Raman excitation wavelength (632.8 nm), and the LSPR spectral position) have been observed. Notably, it was found that the substrate Au-T-Ag-T-Au exhibiting the nearest LSPR spectral position to the excitation wavelength provides the best enhancement in Raman intensities among the studied substrates. The enhancing superiority of the triple-layered nanoparticles (which exhibit lower inter-particle separation) over the double layered bimetallic nanoparticles originates from the increase in the inter-particle coupling effect. Accordingly, the substrates of the triple layered nanoparticles have more efficient hot-spots than those of the double-layered nanoparticles.

The Au-T-Ag-T-Au substrates have resulted in the highest SERS enhancing ability within the investigated bimetallic nanoparticles. The morphological and compositional studies using HRTEM imaging have showed a core/shell structure with Au-Ag mixed core and Au shell. We have also showed that the highest SERS enhancement observed over the Au-Ag/Au core/shell nanoparticles could be explained by the presence of silver in a bimetallic structure, having LSPR spectral position in resonance with the Raman excitation wavelength. The fabricated Au-Ag/Au core/shell SERS substrates exhibit high spot-to-spot homogeneity, having 2% as percentage relative standard deviation (%RSD) in the SERS signal. Moreover, the sample-to-sample reproducibility has been measured to have 8% as %RSD in the SERS signal. These core/shell nanoparticles exhibit very go long-term stability of approximately one year under ambient conditions. This high stability has been attributed to the presence of the Au protective shell. The optimization studies carried out on the Au-Ag/Au core/shell nanoparticles have shown the following i) 3nm Au -T- 3nm Ag -T- 3nm Au substrates represents the best evaporation thickness, ii) increasing the thermal annealing temperature results in an increase in the SERS enhancing ability and iii) coupling of Au-Ag/Au core/shell nanoparticles to Au film also results in improving the SERS enhancement.

The systematic study of the Au/Ag bimetallic nanoparticles using Electron Beam Lithography (EBL) technique has showed that these bimetallic nanoparticles follow the same behavior regime as monometallic particles, with respect to the size effect on the LSPR position and shape. It has been shown that, increasing the nanoparticles size results in red-shifting and peak broadening of the LSPR. Moreover, a good agreement in LSPR broadening is obtained between the double layered system in Chapter III and bimetallic nanocylinders obtained by EBL, where LSPR of bimetallic systems are broader than those of monometallic. The majority of the studied monometallic and bimetallic nanocylinders exhibit an inversely proportional relationship between the SERS intensity and $\Delta\lambda$, knowing that the array with the closest LSPR spectral position to the Raman excitation wavelength provides the highest enhancement in Raman intensities. The higher enhancement obtained over the thermally annealed nanoparticles in comparison to the EBL NCs is related the interparticle coupling effect in the thermally annealed nanoparticles, where the EBL NCs are well separated. The coupling between closely packed nanoparticles generates hotspot regions, providing higher SERS enhancement.

Recently we have started to employ metallic electroplating technique for the growth of metallic thin films. A home-made electroplating setup with rotating electrode (for better homogeneity) has been used for the fabrication of bimetallic nanoparticles. This technique is expected to provide an even more practical way for the fabrication due to its cost effectiveness and time saving. Additionally, a study of the validation of the inversely proportional relationship between SERS enhancement and $\Delta\lambda$ can be undertaken.

Additionally, aluminum (Al) and copper (Cu) can be introduced to the Ag-Au bimetallic nanoparticles forming trimetallic system. The Au-Ag-Al nanoparticles can provide further LSPR tunability towards the ultraviolet (UV) spectral region, producing potential high SERS enhancement in the UV spectral domain. The LSPR tunability towards the near-infrared (NIR) spectral domain can be achieved by the Au-Ag-Cu nanoparticles, these nanoparticles can provide high enhancements in the near-infrared surface enhanced Raman spectroscopy (NIR-SERS).

Furthermore, we can take advantage of the tunability and enhancing ability of our fabricated substrates in order to study the signal enhancing behavior in other spectroscopic techniques; fluorescence for example. We can investigate the effects of tuning the LSPR of bimetallic nanoparticles on the fluorescence intensities and the fluorescence life time.

General Conclusion and Perspectives

Minutely, we can understand the fluorescence behavior by studying the relation between the LSPR spectral properties and the fluorescence's excitation and emission wavelengths. The fluorescence enhancing beside the high SERS enhancement will impose these mentioned bimetallic substrates as universal sensing-devices. We can also investigate the use of Ag/Au bimetallic nanoparticles for increasing the photovoltaic devices efficiency. Where employing the nanoparticles in the photovoltaic device can enhance the short circuit photocurrent and improve the power conversion efficiency.

Résumé de la Thèse en Français

I. Introduction Générale

La nanotechnologie est l'art et la science de manipuler la matière à l'échelle nanométrique, présentant ainsi possibilités de créer de nouveaux matériaux avec des propriétés intéressantes et uniques. En raison des changements substantiels dans la physico-chimie des matériaux à l'échelle nanométrique par rapport à leur volume ou des atomes individuels, le domaine de la recherche sur les nanoparticules a considérablement augmenté au cours de ces trois dernières décennies.

L'intérêt de l'étude des nanoparticules est dû à leurs propriétés optiques, électroniques, magnétiques et catalytiques distinctes. En particulier, l'adoption de semi-conductrices nanostructures dans le domaine électroniques se traduit par la diminution de la taille du navire de l'ordinateur, ce qui augmente la densité de courant dans les batteries au lithium-ion et la conversion de la lumière en électricité par des cellules solaires. En plus, les points quantiques, des particules d'oxyde de fer et d'autres nanoparticules se sont révélés être des agents très efficaces pour l'imagerie, la détection et l'intervention raupeutic dans le domaine biomédical. En outre, les matériaux à l'échelle nanométrique ont prouvé leur potentiel pour améliorer l'environnement, à la fois par l'application directe de ces matériaux afin de détecter, prévenir et éliminer les polluants, et indirectement grâce à la nanotechnologie pour concevoir propre processus industriel et de créer des produits écologiques.

La capacité d'empreinte moléculaire de la spectroscopie Raman en fait un outil intéressant dans des applications de détection. Cependant, deux inconvénients empêche Raman d'être une technique de détection de premier plan; la faible section (moins de 10^{-29} $\text{cm}^2.\text{sr}^{-1}$) où une sur $10^6\text{-}10^8$ photons incidents est en fait diffusée Raman et les phénomènes concurrents ; fluorescence; qui est 13 fois de la magnitude en section plus élevés que diffusion Raman typique. Pour les trois dernières décennies, les techniques de Raman ont connu une application croissante dans de nombreux domaines. L'intérêt dans la spectroscopie Raman est réapparu en raison de la forte exaltation des signaux Raman observées pour les molécules dans une proximité de surfaces métalliques spéciaux. Cette exaltations du signal Raman, dite Raman exaltée de surface (SERS) ouvre une large gamme d'application de la technique Raman pour l'analyse des traces, analyse chimique, la surveillance environnementale et les traitements biomédicaux.

SERS provient de réponses optiques couplés de nanostructures métalliques tels que l'or, l'argent ou le cuivre, et des molécules qui se trouvent sur leurs surfaces. Ce type de

nanoparticules diffère fortement de leur correspondant massif dans leur réponse optique pour qu'ils puissent présenter une résonance plasmons de surface localisés (LSPR). Ces oscillations collectives des électrons lors de l'excitation par le plomb lumière à une bande d'extinction forte dans le domaine spectral visible ou le proche infrarouge. Les propriétés spectrales de ce comportement de résonance dépendent fortement de la taille, de la forme du métal et diélectrique entourant des particules.

Poussé par la recherche de fiables substrats SERS pour les applications de détection, le but de notre étude est de concevoir SERS-actives substrats susceptibles de répondre aux exigences suivantes : facteur important d'exaltation, une bonne stabilité, reproductibilité, homogénéité, fabrication facile et à grande échelle. Recuit thermique de couches métalliques minces procédé de nano-fabrication répond à la plupart des exigences. Parallèlement, les nanoparticules d'argent présentent significativement plus exaltée mise en valeur du champ électrique par rapport à des nanoparticules d'or, d'imposer l'argent comme matériau idéal pour les substrats SERS caractérisées par des facteurs élevés de exaltation. Toutefois, les nanoparticules d'argent fabriquées par la stratégie susmentionnée précédente ont LSPR en baisse dans la gamme spectrale 400-470 nm, limitant ainsi les hautes exaltations pour Raman longueurs d'onde d'excitation situées dans ou à proximité de ce domaine spectral, alors que la majorité des spectromètres Raman ont d'onde d'excitation de 633 nm. Cependant, nanoparticules d'argent sont instables en raison de sulfuration et l'oxydation de surface. Au contraire, les nanoparticules d'or montrer une grande stabilité dans des conditions physiologiques et avoir la position LSPR dans la gamme spectrale de 550 à 650 nm suivant la même stratégie de fabrication. Combinant ainsi les deux métaux dans une nanostructure bimétallique semble être une approche prometteuse pour résumer les mérites de deux, les propriétés optiques d'exaltation de l'argent et les propriétés surfacique d'or.

Ce manuscrit est divisé en cinq chapitres.

Dans le premier chapitre, nous décrivons les caractéristiques optiques de nanostructures nobles. Une accentuation particulière est mise sur le caractère soutenable de ces biens par le changement dans la taille, la forme et la séparation entre des nanoparticules. Un fond de diffusion Raman, SERS, les mécanismes d'exaltation largement rapporté et les récentes réalisations dans le domaine de la SERS sont racontés.

Tout au long du chapitre II, nous présentons la mise en place expérimentale utilisée pour la fabrication des nanoparticules (de recuit thermique de couches métalliques minces et

lithographie par faisceau d'électrons). En outre, nous présentons les différentes techniques de caractérisation utilisés dans cette étude qui a aidé de manière complémentaire dans la compréhension de la composition de nanoparticules, leur morphologie et propriétés optiques. Il s'agit notamment de spectroscopie photoélectronique aux rayons X (XPS), la microscopie électronique (microscopie électronique à balayage (MEB) et microscopie électronique à transmission (MET)), la spectroscopie infrarouge proche UV-Vis, et la spectroscopie Raman.

Dans le chapitre III, la fabrication de substrats bimétalliques de Au / Ag nanoparticules réalisé par recuit thermique de couches minces métalliques est présentée. La composition chimique des substrats de SERS préparé est vérifiée à l'aide de XPS. Ensuite, les caractérisations morphologiques et optiques des nanoparticules obtenues sont étudiées par MEB et spectroscopie UV-Vis proche IR. En outre, la capacité de exaltation SERS des nanoparticules en couche doubles est comparée à celle des nanoparticules Au / Ag en couche triples.

Dans le chapitre IV, nous étudions d'abord l'homogénéité, la reproductibilité et la stabilité de la SERS substrat Au / Ag nanoparticules bimétalliques qui présentent le signal le plus intense d'amélioration de Raman. Ensuite, nous présentons la possibilité d'optimisation sur ce substrat pour une exaltation de la SERS plus efficace. L'épaisseur de la couche évaporée, les effets de la température de recuit et le couplage des nanoparticules bimétalliques Au / Ag avec le film Au sont morphologiquement et optiquement étudiés afin de mieux comprendre leur effet sur l'activité de la SERS.

Dans le dernier chapitre de ce manuscrit, une étude systématique des caractéristiques des Au / Ag bimétalliques en utilisant un faisceau d'électrons Lithographie (EBL) stratégie de fabrication est pris en compte afin d'améliorer notre compréhension de leurs propriétés plasmoniques et exaltation SERS. Tout d'abord, la taille et la périodicité des effets des nanoparticules bimétalliques sur la LSPR et la SERS capacité d'exaltation sont étudiés en détail. D'autre part, les types de compositions métalliques différentes et ayant des paramètres morphologiques nanocylindres unifiés sont fabriqués de manière à suivre l'effet de leur nature métallique et de la composition sur les propriétés de LSPR et SERS.

A la fin, nous présentons une conclusion générale de ce travail en fonction des résultats obtenus. Nous présentons également nos perspectives concernant ce sujet.

II. Méthodes et techniques expérimentales

Dans cette partie, nous présentons les différentes techniques expérimentales utilisées dans le cadre de nos travaux.

II.1 Fabrication de nanostructures métalliques

II.1.1 Recuit thermique de couches métalliques

Le dépôt physique par phase vapeur (PVD) est un ensemble collectif des procédés utilisés pour déposer des couches minces de matériau, typiquement de l'ordre de quelques nanomètres à plusieurs micromètres. Le processus commence par la fourniture d'énergie thermique à la matière d'origine, soit par courant électrique ou faisceau d'électrons directe. Comme le matériau se rapproche de sa température de fusion, des atomes individuels commencent à s'évaporer de manière uniforme et isotrope à partir de la source. Le procédé est effectué dans un environnement sous vide, ce qui permet les atomes évaporés pour atteindre le substrat sans risque de collision avec les gaz atmosphériques. La pression résiduelle dans le système, la température de la source, la distance substrat-source et la durée de dépôt sont des paramètres clés de PVD.

II.1.2 Lithographie par faisceau d'électrons (EBL)

Lithographie par faisceau d'électrons est une technique spécialisée pour la fabrication de modèles extrêmement fines jusqu'à l'échelle du nanomètre. Dérivé de microscopes électroniques à balayage, cette technique est basée sur le balayage d'un faisceau d'électrons focalisé à travers le substrat recouvert d'électrons couche de résist sensible. L'exposition résister à faisceau d'électrons avec des paramètres spécifiques conduit à motifs bien définis. Les principales caractéristiques de la technique EBL sont: i) la haute résolution et la homogène, ii) la flexibilité de technique permettant large gamme de matériaux et nombre presque infini de modèles et iii) lent, coûteux et compliqué.

La Figure 1 montre les étapes de fabrication de nanoparticules métalliques à l'utilisation de EBL.

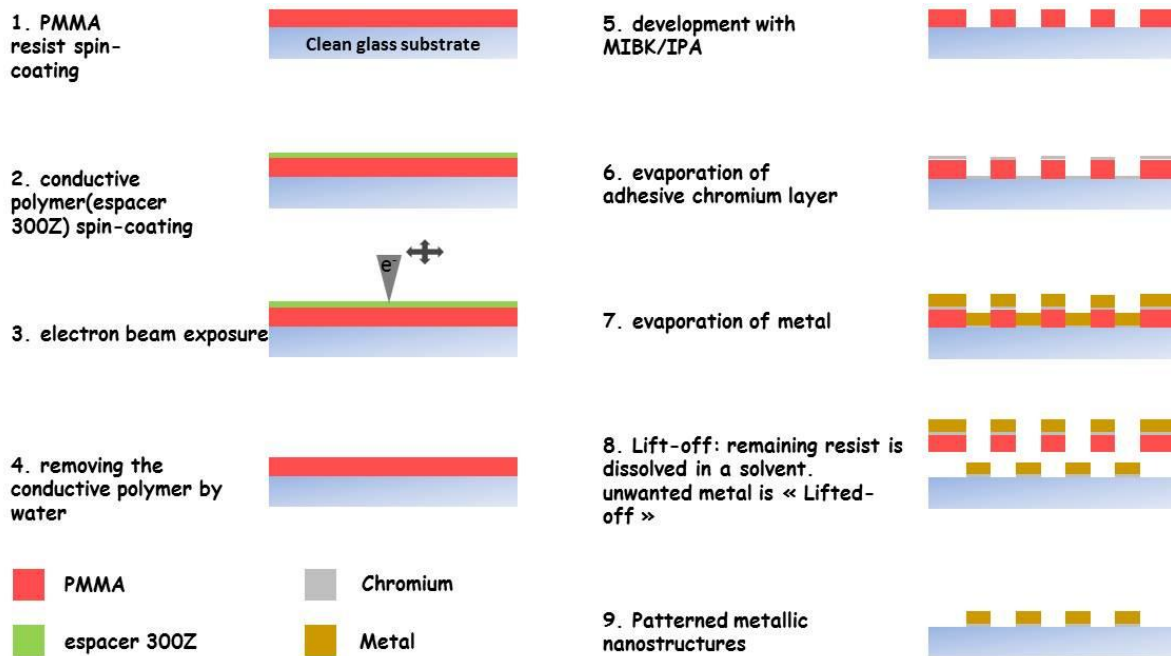


Figure 1. Le schéma du procédé de lithographie par faisceau d'électrons

Les mesures ont été mises au point par les ingénieurs et les chercheurs du laboratoire LNIO, l'UTT et ont été adaptées de manière compatible pour la préparation des nanostructures. Ces étapes sont les suivantes: 1) dépôt de résist positive par faisceau d'électrons, 2) dépôt d'une couche conductrice, 3) l'exposition au faisceau d'électrons, 4) le développement de produits chimiques, 5) la métallisation et 6) "lift-off".

II.2 Spectroscopie UV-Vis-NIR

Dans le présent travail, un UV-Vis-NIR spectromètre fait maison avait été utilisé pour étudier les propriétés optiques des nanoparticules préparées. Ces propriétés optiques des nanoparticules sont très dépendants de leur taille, la forme et d'autres caractéristiques, et qu'ils interagissent avec des longueurs d'onde spécifiques de la lumière qui se compose à la base pour le domaine de la plasmonique. Cela rend la spectroscopie UV-Vis-NIR comme une technique d'instruction utile pour leur identification et leur caractérisation.

II.3 Spectrométrie photoélectronique X (XPS)

Dans notre étude, XPS est utilisé pour confirmer la composition des nanoparticules bimétalliques Au / Ag fabriqués. Les données de XPS obtenues ont été analysées afin d'assurer le pourcentage de métal évaporé de chaque substrat par calcul de l'aire sous les pics Ag3d et Au4f.

II.4 Microscopie électronique à balayage (MEB)

La microscopie électronique à balayage est utilisé pour obtenir des informations sur la morphologie de la surface de l'échantillon, l'homogénéité chimique, la composition chimique qualitative et quantitative à l'échelle micrométrique ou nanométrique. Dans ce manuscrit, MEB est principalement utilisé pour visualiser les propriétés morphologiques des nanoparticules monométalliques et bimétalliques fabriqué.

II.5 Microscopie électronique en transmission (MET)

La microscopie électronique en transmission à travers trois modes de fonctionnement différents, donne des informations sur la structure cristalline et la composition chimique du matériau étudié. Le mode d'imagerie utilisé dans ce manuscrit est le mode d'imagerie à champ claire. Dans ce mode, les zones épaisses de l'échantillon ou régions avec un nombre atomique (Z) plus élevé donnent une contraste sombre.

II.6 Système Raman

Tous les spectres Raman et SERS présenté dans ce manuscrit ont été recueillies à l'aide du microscope Raman à haute résolution Jobin-Yvon Horiba (LABRAM). Elle est équipé d'un microscope optique Olympus des objectifs différents (10x NA 0,25, 50x NA 0,8, 100X NA 0,9), un laser d'excitation hélium néon de 632,8 nm de longueur d'onde, un dispersion de réseau de 600 lignes / mm, un chemin monochromateur de 800 mm et un détecteur à effet Peltier de CD (1024x256 pixels) de 16 bits dynamique.

III. Études morphologiques et optiques sur les nanoparticules bimétalliques de Au/Ag

Tout au long de ce chapitre, nous étudier la combinaison de les métaux d'argent et d'or dans des nanoparticules bimétalliques en double-couches et triples- couches pour avoir des substrat SERS accordable et comment cette accordabilité peut affecter la capacité de l'exaltation de la SERS des substrats. En particulier, nous allons étudier l'effet de la composition et l'effet morphologique de la position sur la résonance de plasmons de surface localisés en et la relation entre ce dernière et la capacité d'exaltation de la SERS.

III.2 Nanoparticules bimétalliques en couche double

III.2.1 La fabrication et le recuit des nanoparticules

Les nanoparticules étudiées dans cette partie ont été fabriqués par recuit thermique de couches métallique mince. Quatre nanoparticules différentes en double-couches ont été produites et qui sont représentés par: Au-T-Au, Ag-T-Ag, Au-T-Ag et Ag-T-Au. Tous les détails expérimentaux du procédé de fabrication sont résumés dans le Table 1.

Table 1. Détails expérimentaux de fabrication de nanoparticules bimétalliques en double couches

	1 ^{ère} évaporation		Recuit thermique		2 ^{eme} évaporation	
	Métal	Épaisseur (nm)	Temperature (°C)	Temps (s)	Métal	Épaisseur (nm)
Au-T-Au	Au	2	250	20	Au	2
Ag-T-Ag	Ag	2	250	20	Ag	2
Au-T-Ag	Au	2	250	20	Ag	2
Ag-T-Au	Ag	2	250	20	Au	2

La spectrométrie photoélectronique X (XPS) a été utilisée pour vérifier la composition des doubles couches de nanoparticules bimétalliques Table 2.

Table 2. Les positions de pics Ag 3d et Au 4f, FWHM, area et le pourcentage de Ag et Au dans les substrats Ag-T-Au et Au-T-Ag.

	Nom	Position	FWHM ^{a)}	Area	At% ^{b)}
Au-T-Ag	Ag 3d	368.2	2.435	58248.0	57.8
	Au4f	84.2	2.556	44299.6	42.2
Ag-T-Au	Ag 3d	368.2	2.492	85011.2	43.9
	Au 4f	84.2	2.584	113470.0	56.1

a) FWHM is the Full width at half maximum; b) At% is the metal percentage of Au and Ag

III.2.3 Accordabilité de LSPR de nanoparticules bimétalliques en double couche

Les images MEB des nanoparticules Au-T-Ag et Ag-T-Au présentés dans la Figure 2 (a) et la Figure 2 (b), respectivement, ont montré que la taille moyenne des Au-Ag-T IP et Ag-T IP -AU sont 14 nm et 16 nm Figure 2 (c) et (d).

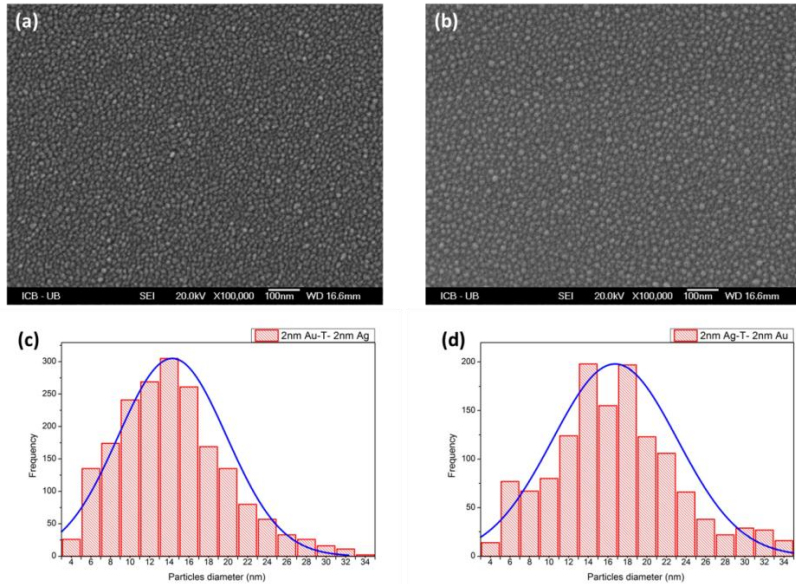


Figure 2. Images MEB de la (a) Au-Ag-T et (b) Ag-T-Au nanoparticules; distribution granulométrique correspondant aux images MEB pour la (c) Au-Ag-T et (d) Ag-T-Au nanoparticules

Les mesures LSPR pour tous les substrats ont été réalisées en utilisant la spectroscopie UV-Vis-NIR ($200 \leq \lambda \leq 1100$ nm). La position spectrale LSPR du substrat Au-Ag-T se situe

entre la LSPR de substrat d'argent pur (Ag-T-Ag) et celle du substrat d'or pur (Au-T-Au) Figure 3. Cela révèle l'effet plasmonique de l'métal de cœur qui est de l'or. Pour les nanoparticules d'Ag-T-Au, la position LSPR obtenue est décalé vers le rouge par rapport aux Au-Ag-T, ce qui peut s'expliquer par l'influence prédominante de la plasmonique Au sur le cœur d'Ag. En outre, on peut remarquer que les deux pics de substrats bimétalliques sont plus larges que celles de monométallique.

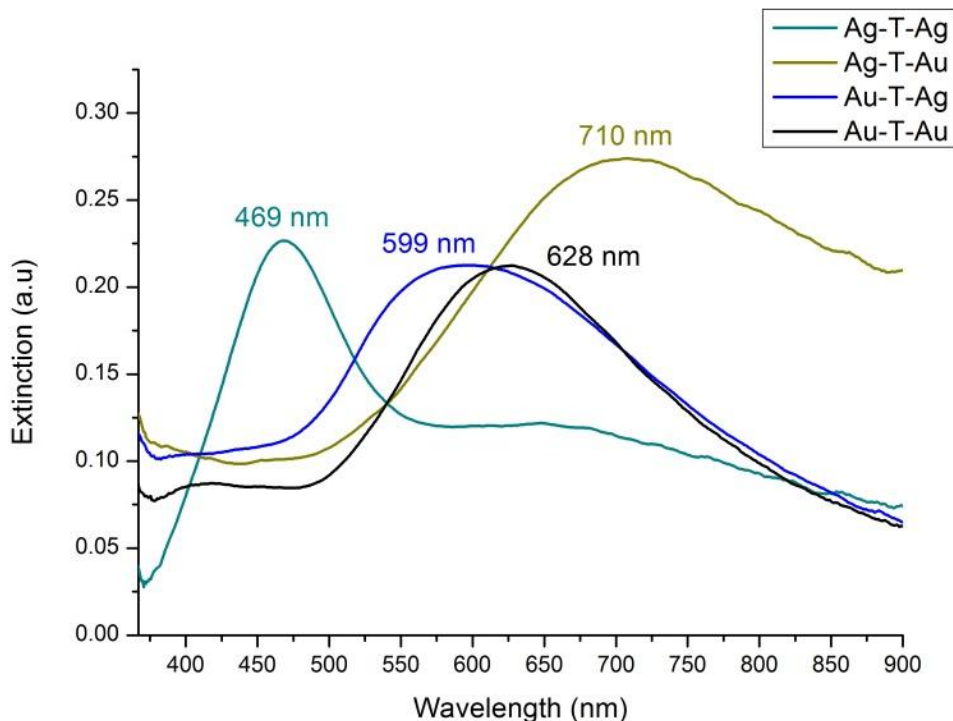


Figure 3. Spectres LSPR pour les nanoparticules en doubles couches: Ag-T-Ag, Ag-T-Au, Au-T-Ag, et Au-T-Au.

III.2.4 LSPR effet sur la diffusion Raman exaltée de Surface

Afin d'évaluer l'effet de la position de plasmons de surface localisés sur l'exaltation Raman, les intensités SERS de benzène ring stretching (1605 cm^{-1}) sont tracées vers $\Delta\lambda$ (la valeur absolue de la différence entre le longueur d'onde d'excitation Raman (632,8 nm) et la résonance LSPR) pour chacun des quatre substrats (Figure 4).

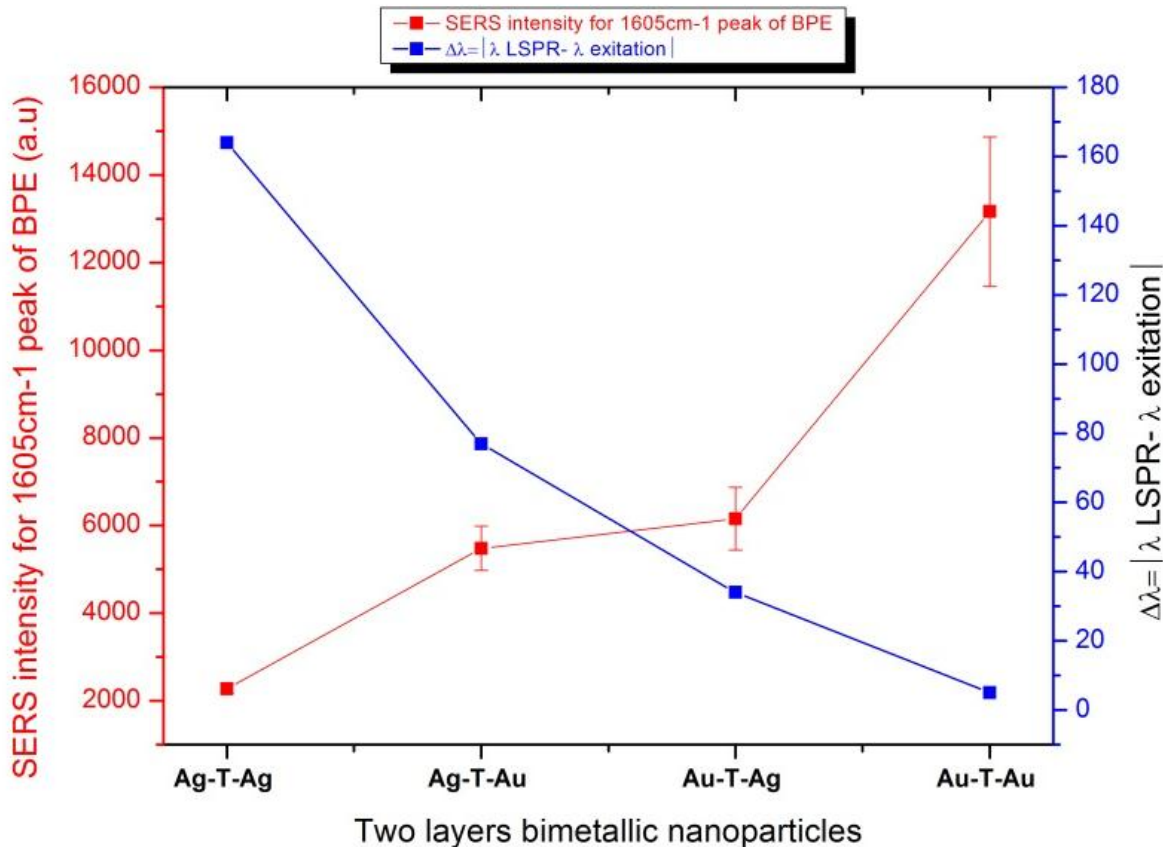


Figure 4. La relation inversement proportionnelle entre les intensités SERS de benzène ring stretching (1605 cm^{-1}) et $\Delta\lambda$ pour Ag-T-Ag, Ag-T-Au, Au-T-Ag, et Au-T-Au substrats.

Il est clair d'après la figure, on observe une relation inversement proportionnelle entre l'intensité de la SERS et $\Delta\lambda$. Le substrat présentant la position spectrale de LSPR plus proche de la longueur d'onde d'excitation fournit le plus haut dans la mise en valeur des intensités Raman qui est le cas pour le substrat au-T-Au.

III.3 Nanoparticules bimétalliques Au / Ag en trois couches

III.3.1 La fabrication et le recuit des nanoparticules

Quatre types nanoparticules trois couches ont été fabriqués, qui sont représentés comme suit: Ag-T-Au-T-Au, Ag-Au-T-T-Ag, Au-T-Ag-T-Ag et Au-T-Ag-T-Au. Tous les détails expérimentaux du procédé de fabrication sont résumés dans le Table 3.

Table 3. Les détails expérimentaux pour la fabrication des nanoparticules bimétalliques trois couches

		Ag-T-Au-T-	Ag-T-Au-T-	Au-T-Ag-T-	Au-T-Ag-T-
		Au	Ag	Ag	Au
1^{ere} évaporation	Métal	Ag	Ag	Au	Au
	Epaisseur (nm)	2	2	2	2
1^{ere} recuit thermique	Température (°C)	250	250	250	250
	Temps (s)	20	20	20	20
2^{eme} évaporation	Métal	Au	Au	Ag	Ag
	Epaisseur (nm)	2	2	2	2
2^{eme} recuit thermique	Température (°C)	250	250	250	250
	Temps (s)	20	20	20	20
3^{eme} évaporation	Métal	Au	Ag	Ag	Au
	Epaisseur (nm)	2	2	2	2

De même pour les nanoparticules bimétalliques en doubles couches de, la technique XPS a été utilisé pour assurer la composition métallique des nanoparticules (Table 4).

Table 4. Les positions de pics Ag 3d et Au 4f, FWHM, area et le pourcentage de Ag et Au dans les quatre substrats.

	Name	Position	FWHM ^{a)}	Area	At% ^{b)}
Au-T-Ag-T- Ag	Ag 3d	368.8	2.522	168614	91.7
	Au4f	84.2	2.640	15797	8.3
Ag-T-Au-T- Ag	Ag 3d	368.2	2.606	134050	74.5
	Au4f	84.2	3.013	47851	25.5
Ag-T-Au-T- Au	Ag 3d	368.2	2.674	2820	11.8
	Au4f	84.2	2.673	21090	88.2
Au-T-Ag-T- Au	Ag 3d	368.2	2.522	27754	23.8
	Au4f	84.2	2.687	92522	76.2

a) FWHM is the Full width at half maximum; b) At% is the metal percentage of Au and Ag

III.3.3 Accordabilité de LSPR de nanoparticules bimétalliques en triple couche

Toutes les mesures LSPR pour les substrats bimétalliques en couches triple ont été réalisées en utilisant la spectroscopie UV-Vis-NIR. La Figure 5 représente les positions spectrales LSPR pour chacun des quatre substrats. L'étude de l'effet du pourcentage de chaque métal évaporé sur les positions LSPR montre que, avec l'augmentation de pourcentage de l'or à l'intérieur de la nanoparticule à un décalage vers le rouge est obtenue.

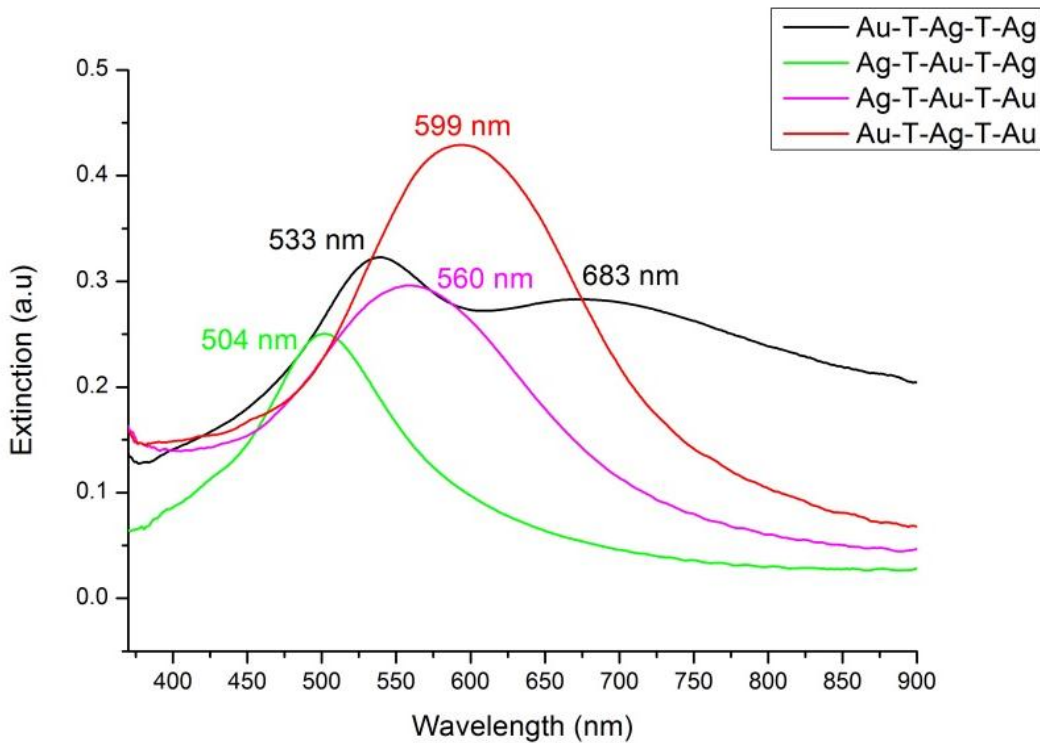


Figure 5. Spectres LSPR pour les nanoparticules bimétalliques en couches triples Au-T-Ag-T-Ag, Ag-T-Au-T-Ag, Ag-T-Au-T-Au, et Au-T-Ag-T-Au substrats.

Suivi de l'effet de l'ordre de l'évaporation de métal sur la position LSPR révèle un effet plasmonique supérieur de la première couche à la deuxième couche. En d'autres termes, la présence d'or dans la première couche aura une incidence sur la résonance plasmonique de plus que sa présence dans la deuxième couche. Le plus important, la troisième couche a un effet plus fort sur LSPR des deux premières couches.

III.3.4 LSPR effet sur la diffusion Raman exaltée de Surface

Afin de trouver la relation entre la capacité d'exaltation des substrats par rapport à leurs positions de LSPR, l'intensité de SERS de benzene ring stretching (1605 cm^{-1}) est tracées en fonction de $\Delta\lambda$ Figure 6.

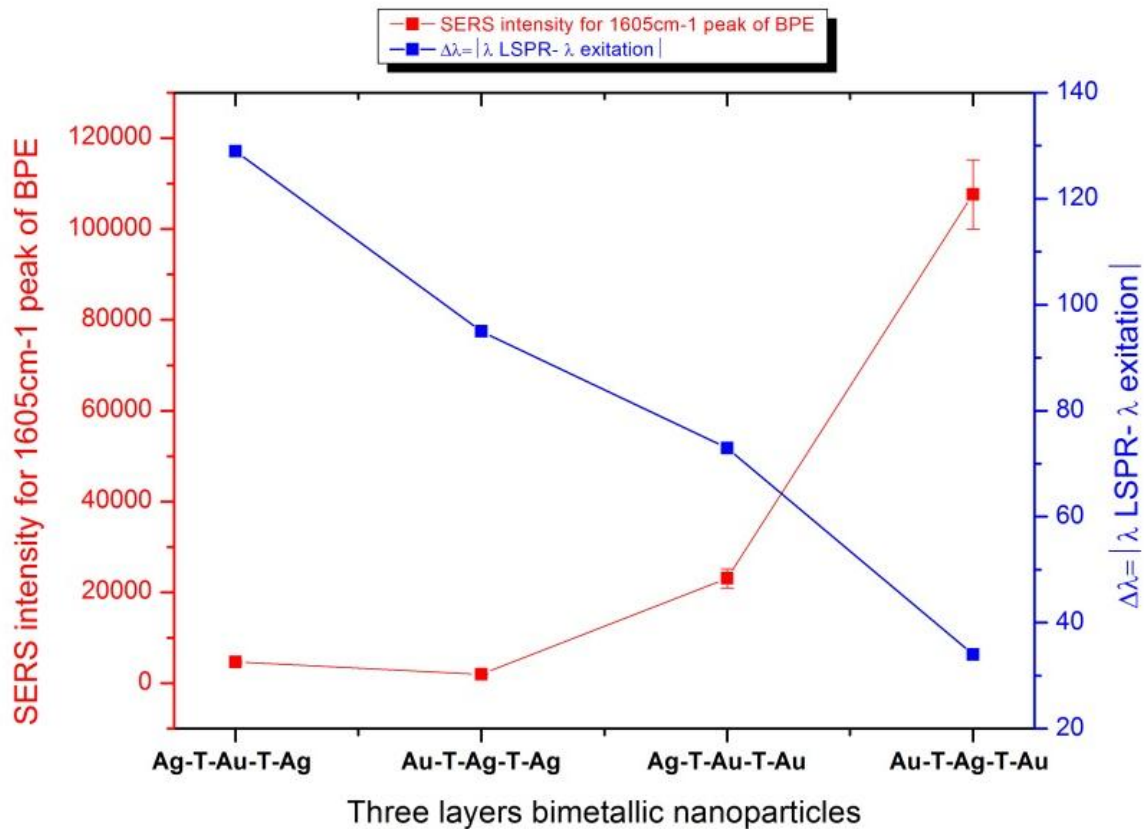


Figure 6. La relation inversement proportionnelle entre les intensités SERS de benzène ring stretching (1605 cm^{-1}) et $\Delta\lambda$ pour les substrats Au-T-Ag-T-Ag, Ag-T-Au-T-Ag, Ag-T-Au-T-Au, and Au-T-Ag-T-Au

De même pour système de couches doubler, une relation inversement proportionnelle entre l'intensité de la SERS et $\Delta\lambda$ est obtenue aussi pour le système à trois couches. L'Au-T-Ag-T-Au système, qui présente la plus petite $\Delta\lambda$ avec une position spectrale LSPR à 599 nm et une densité optique de 0,47 fournit le signal SERS plus intense. En outre, la supériorité dans l'exaltation de la SERS du système à trois couches sur le système à deux couches provient de la diminution de l'espacement inter-particules pour le système à trois couches. Par conséquent, les substrats en triple couche ont plus efficaces "points chauds" que les substrats à double couche.

IV. Amélioration de les nanoparticules bimétalliques de Au / Ag substrats pour des applications de SERS

Suite à l'étude réalisés dans le chapitre précédent et sachant que l'exaltation de la SERS élevé a été obtenu sur le substrat Au-T-Ag-T-Au, nous avons cherché dans ce chapitre à étudier ce substrat dans plus de détails, désireux de comprendre la raison de cette exaltation, en plus d'étudier les possibilités d'optimisation.

Tout d'abord, nous allons étudier l'effet de chaque étape de la fabrication sur l'exaltation de la SERS en utilisant la caractérisation morphologique et l'effet plasmonique. Ensuite, nous allons suivre l'effet de l'épaisseur évaporée, la température de recuit thermique et le couplage avec un film métallique à améliorer le substrat Au-T-Ag-T-Au.

IV.2 Au-Ag/Au cœur/coquille nanoparticules bimétalliques

IV.2.1 Etude morphologique

L'image MET à haute résolution d'une seule nanoparticule de Au-T-Ag-T-Au (Figure 7) montre une structure cœur /coquille de 15,6 nm /2,3 nm. Le noyau est un mélange de les deux métals d'or et d'argent et la coque est constituée de Au pur.

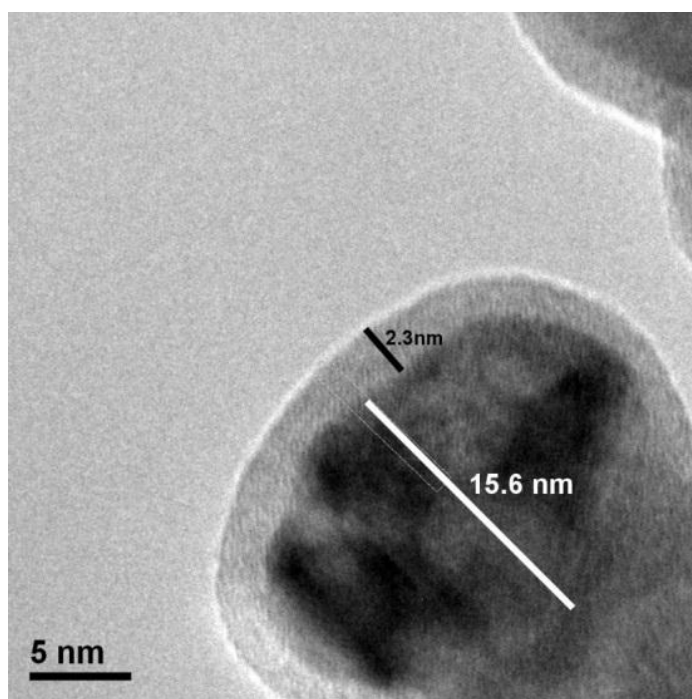


Figure 7. Image MET à haute résolution d'une seule NP de Au-T-Ag-T-Au

IV.2.2 Effet de présence d'Argent en Au-Ag/Au nanoparticules sur le comportement optique et l'exaltation

Afin de suivre l'effet de la présence de l'argent dans Au-Ag / Au nanoparticules, nous l'avons comparé avec des NP d'argent pures en couches-triple, Ag-T-Ag-T-Ag et trois nanoparticules d'or pur aussi en couches-triples Au-T-Au-T-Au. La *Figure 8* montre les positions LSPR pour les trois substrats correspondants.

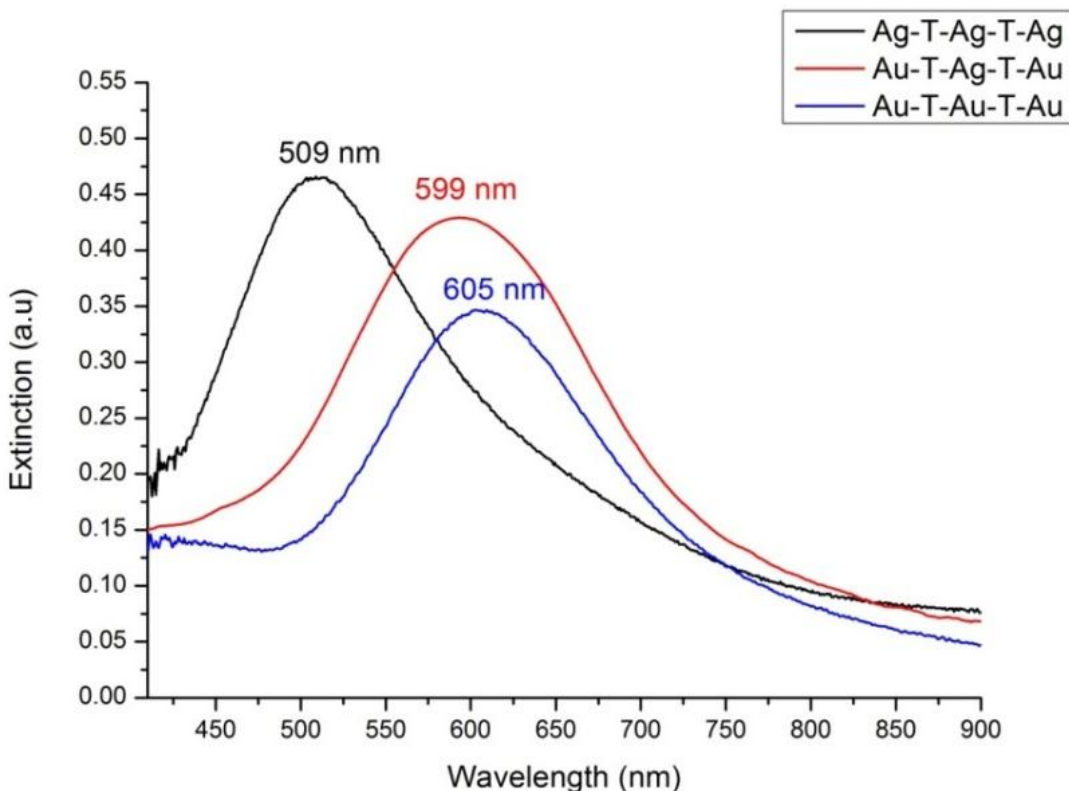


Figure 8. Spectres d'extinction pour les NPs Ag-T-Ag-T-Ag (noir), Au-T-Ag-T-Au (rouge), et Au-T-Au-T-Au (bleu).

La substitution du second métal évaporé à Au-T-Au -T-Au en argent n'a pas largement affecter la position LSPR. Cependant, d'exaltation supérieure est obtenue au cours de l'Au-T-T-Ag-Au en comparaison avec le substrat au-T-T-Au-Au, Figure 9. Cette amélioration ultérieure peut être attribuée à la présence d'argent dans un système comportant LSPR position spectrale en résonance avec l'onde d'excitation Raman.

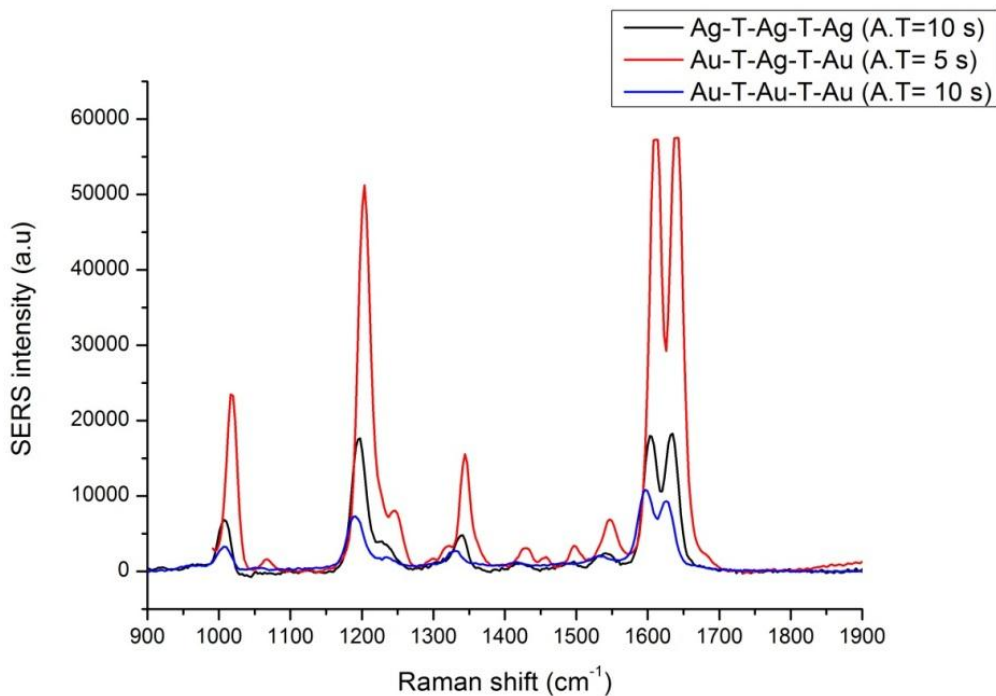


Figure 9. SERS signals for BPE solution ($10^{-5} M$) over Ag-T-Ag-T-Ag, Au-T-Ag-T-Au, and the Au-T-Au-T-Au NPs

IV.2.3 L'homogénéité, la stabilité et la reproductibilité

Comme indiqué précédemment, l'objectif de notre travail est de fabriquer des substrats SERS caractérisés par une haute capacité d'exaltation associée à l'homogénéité, la reproductibilité et une grande stabilité dans des conditions physiologiques. Ainsi, nous avons testé les propriétés mentionnées pour le substrat ayant l'exaltation de SERS le plus élevé; Au-Ag/Au cœur/coquille nanoparticules.

En ce qui concerne l'homogénéité des signaux SERS à travers le substrat, des mesures SERS ont été faites pour 10 gouttes de solution BPE placés sur 10 positions différentes. L'écart type relatif des mesures SERS obtenus soit 2% pour les NPs de Au-Ag/Au cœur/coquille, prouver l'homogénéité du substrat.

En ce qui concerne la reproductibilité, nous avons comparé cinq substrats fabriqués séparément. L'écart type relatif calculé de l'intensité de la SERS a été obtenu à 8%, ce qui prouve également la reproductibilité du substrat.

Afin d'évaluer le rôle de la coque d'Au pour assurer la stabilité des Au-Ag /Au NPs, une étude de SERS a été réalisé sur fraîchement préparés Au-T-Ag-T-Au et Au-T-Ag NPs.

Après un an, à peu près le même signal de SERS a été obtenu au cours des Au-Ag /Au NPs alors que sur Au-T-Ag semble s'estomper presque totalement. La raison de ces résultats peut être attribuée à la sulfuration ou de l'oxydation de l'argent dans les NPs d'Au-T-Ag, quant à ce problème est évité dans le cas de Au-Ag /Au depuis l'argent est encapsulé et protégé par la coque en or.

IV.3 Optimisation

IV.3.1 Variations d'épaisseur de métal évaporés

Sachant que la taille des nanoparticules ont un effet direct sur la position spectrale de la résonance de plasmon de surface localisée, où l'augmentation de la taille va conduire à un décalage vers le rouge dans la position LSPR. Par conséquent, en augmentant l'épaisseur de métal évaporé, on s'attend à ce que la taille des nanoparticules augmente tout en maintenant les paramètres de recuit thermique fixes (température et temps). La relation inversement proportionnelle entre l'intensité de la SERS et $\Delta\lambda$ est soutenue dans cette étude, nous permettant d'optimiser les Au-Ag/Au nanoparticules bimétalliques pour une meilleure capacité d'exaltation en utilisant la structure de le substrat 3nmAu-T-3nmAg-T-2nmAu.

Figure 10.

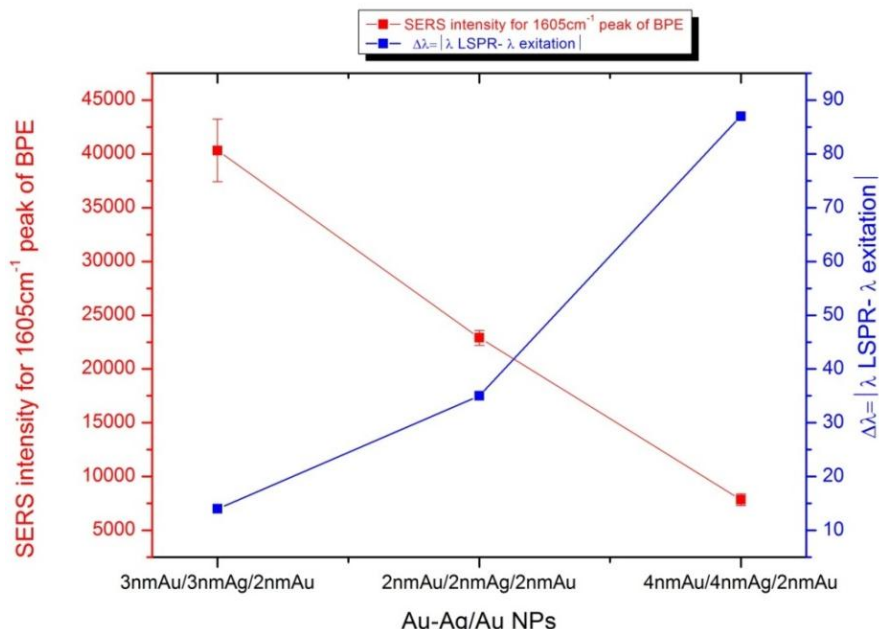


Figure 10. La relation inversement proportionnelle entre les intensités SERS de benzène ring stretching (1605 cm^{-1}) et $\Delta\lambda$ pour les substrats $2\text{nmAu-T-2nmAg-T-2nmAu}$, $3\text{nmAu-T-3nmAg-T-2nmAu}$, and $4\text{nmAu-T-4nmAg-T-2nmAu}$

IV.3.2 Effet de recuit thermique

En plus d'étudier l'effet de l'épaisseur de l'évaporation sur la position spectrale LSPR et son influence sur l'aptitude à l'amélioration de la diffusion Raman, le paramètre de température de recuit thermique est également étudié. Au-Ag / Au bimétallique nanoparticules cœur / coquille ont été fabriqués suivant la même stratégie avec différentes températures de recuit thermique allant de 150 ° C à 350 ° C (50 ° C Les intervalles). La Figure 11 représente la relation entre l'amélioration de la capacité des substrats par rapport à mi-hauteur, où une relation de proportionnalité inverse est observé. Cette étude a optimisé le PN noyau / enveloppe SERS amélioration Au-Ag / Au en augmentant la température de traitement thermique de recuit, avec 350 ° C apparaissant comme la température optimale.

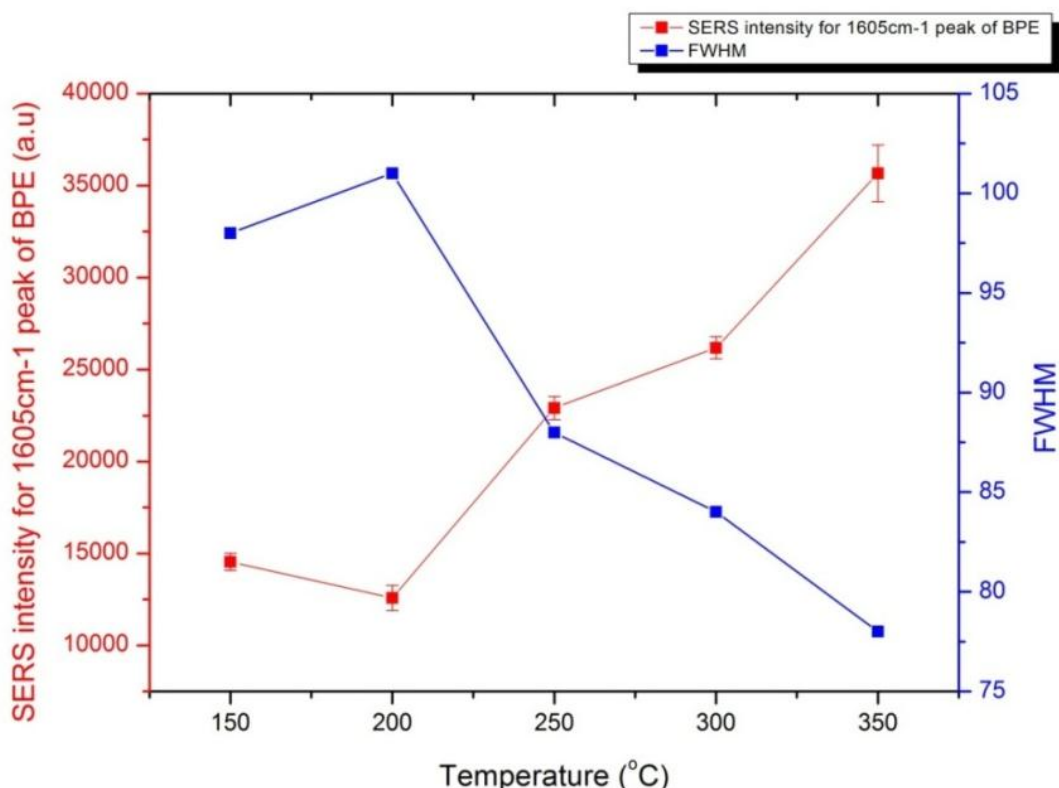


Figure 11. La relation inversement proportionnelle entre les intensités SERS de benzène ring stretching (1605 cm^{-1}) et FWHM pour les substrats Au-Ag/Au avec de recuit thermique a températures différentes

IV.3.3 Couplage entre les nanoparticules de Au-Ag/Au cœur / coquille et couche d'Au

Il a été démontré que le couplage entre les plasmons de surface localisés de nanoparticules serrées forment les blocs de construction pour des substrats SERS efficaces.

En outre, les nanoparticules résidant au-dessus de couche métallique montrent également des effets d'exaltation prometteuses dans les signaux Raman.

Pour cette étude, cinq substrats représentés par la notation suivante 30 nm couche d'Au-xSiO₂-Au-Ag/Au NPs, où x = 10, 20, 30, 40 et 50 nm ont été fabriquées (Tableau 5). En plus du substrat de Au-Ag /Au qui servent de référence pour notre étude a été préparé également.

Tableau 5. Les détails expérimentaux pour la fabrication des cinq substrats : 30 nm Au - xSiO₂-Au-Ag/Au (x = 10, 20, 30, 40 et 50 nm) et le substrat de référence Au-Ag/Au.

	Couche d'Au (nm)	Couche d'SiO ₂ (nm)	Au-Ag/Au NPs Epaisseur = 2nm Temperature = 250°C
Au-10nmSiO₂-(Au-Ag/Au NPs)	30	10	Au-T-Ag-T-Au
Au-20nmSiO₂-(Au-Ag/Au NPs)	30	20	Au-T-Ag-T-Au
Au-30nmSiO₂-(Au-Ag/Au NPs)	30	30	Au-T-Ag-T-Au
Au-40nmSiO₂-(Au-Ag/Au NPs)	30	40	Au-T-Ag-T-Au
Au-50nmSiO₂-(Au-Ag/Au NPs)	30	50	Au-T-Ag-T-Au
Au-Ag/Au NPs	-	-	Au-T-Ag-T-Au

Afin d'étudier la relation entre la capacité d'exaltation de la structure de couche d'Au-xSiO₂-Au-Ag/Au NPs et l'épaisseur de l'entretoise, l'intensité de SERS de benzene ring stretching (1605 cm^{-1}) sont tracées en fonction de l'épaisseur de SiO₂, Figure 12. On pouvait s'y attendre, l'intensité de la SERS chute de manière significative sur l'augmentation de

l'épaisseur de couche de silice de 10 à 50 nm. La tendance observée à l'exaltation du signal par rapport à l'épaisseur de la couche d'oxyde peut être attribuée à la nature évanescante à décroissance exponentielle pour les plasmons de surface polariton dans le couche d'or. L'augmentation dans l'exaltation est liée à l'interaction entre le plasmon de surface localisé de les nanoparticules et le plasmon polariton de surface délocalisée du la couche métallique.

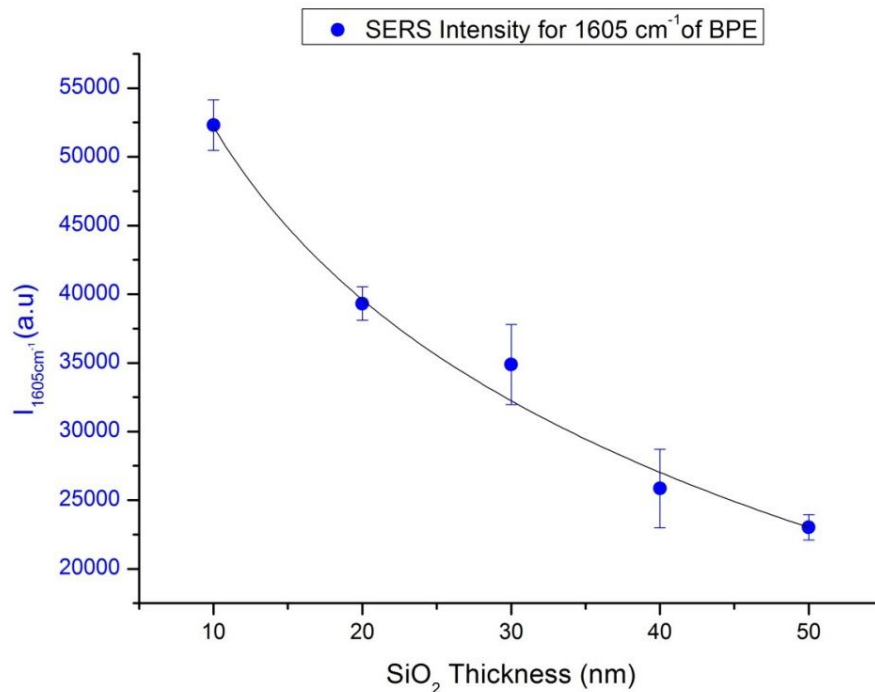


Figure 12. L'intensité de la SERS benzene ring stretching (1605 cm^{-1}) par rapport à l'épaisseur de SiO_2

Les améliorations dans l'exaltations de SERS peuvent être considérés comme provenant des deux contributions suivantes: i) les points chauds générés à partir de nanoparticules voisins et ii) le champ électrique amélioré confinés dans l'écart entre les nanoparticules et le couche d'or. Par conséquent, la zone constituée de deux nanoparticules adjacentes sur le couche d'or servir d'antenne concentrer l'énergie rayonnante dans l'espace où se trouvent les molécules.

V. Contrôle de forme des nanoparticules monométalliques et bimétalliques

Afin d'améliorer les propriétés plasmoniques et l'exaltation raman (SERS) des nanoparticules bimétalliques faites précédemment nous avons réalisé une étude systématique de leurs caractéristiques.

V.1 Motifs des nanocylindres mono métalliques et bimétalliques

Les cinq substrats préparés différemment sont constituées de zones de 50 µm X 50 µm de nanocylindres métalliques (CN) avec des diamètres et des constantes de maille variables. Ces substrats sont formées de monocouches ou bicouches métalliques de la manière suivante : Au, Ag, Au-Ag, Ag-Au et Au-Ag-Au avec une épaisseur constante de 50nm. Sur chaque substrat, deux séries de réseaux ont été fabriquées de diamètres différents de 110, 140, 170 et 200 nm avec deux constantes de mailles différentes : 300 nm et 450 nm.

V.1.1 La dépendance de la LSPR sur la taille de nano cylindre

Il est bien connu que l'augmentation de la taille des nanoparticules de Ag et Au provoque un décalage vers le rouge et un élargissement du pic de LSPR. En conséquence, nous avons testé la validité de ce comportement pour les NC bimétalliques (Ag/Au) ayant des différents rapports de compositions métalliques. Les Figure 13 A, B, C, D et E représentent respectivement les spectres LSPR pour les NC de l'Au, Ag, Au-Ag, Ag-Au et Au-Ag-Au ayant des motifs de diamètres différents et de constante de maille de 300 nm. Il a été montré que les NC bimétalliques ont le même comportement que les NC monométalliques. La taille des NC influe la position et la forme LSPR : une augmentation de la taille des NC entraîne un décalage vers le rouge et élargissement du pic LSPR (Figure 14).

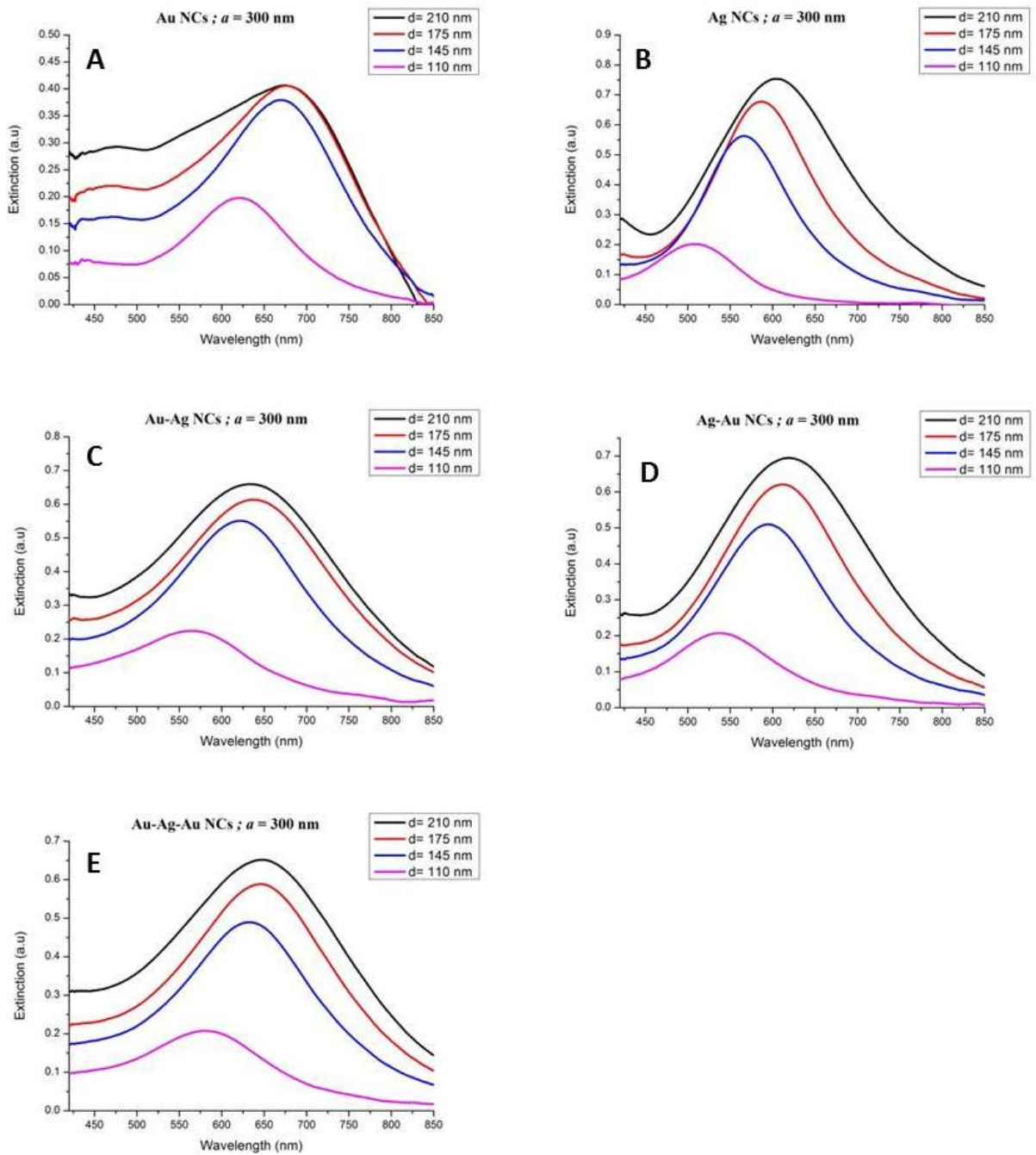


Figure 13 Les spectres d'extinction pour les (A) Au, (B) Ag, (C) Au-Ag, (D) Ag-Au et (E) Au-Ag-Au NC ayant des diamètres différentes 110, 145, 175 et 210 nm et 300 nm comme constante de maille

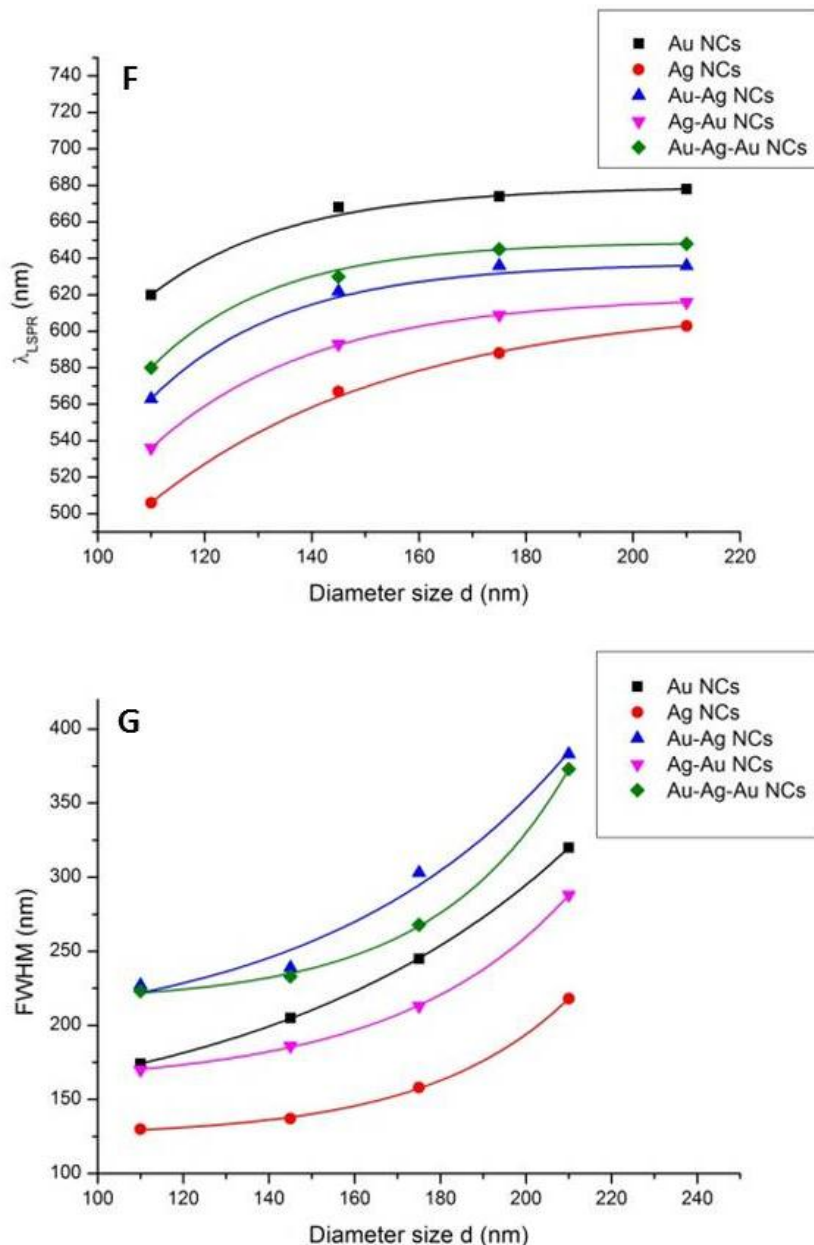


Figure 14 La longueur d'onde maximale λ_{max} (F) et la FWHM (G) du pic LSPR en fonction de diamètre des NC de l'Au, Ag, Au, Ag, Au et Ag-Au-Ag-Au.

V.1.2 Effet de la distribution des couches métalliques et la nature des NC sur la LSPR

Après avoir discuté l'effet de taille, nous nous concentrons maintenant sur les effets de composition métallique et l'ordre de ces couches métalliques sur les propriétés de LSPR. Les Figure 15A, B, C et D montrent les spectres LSPR pour les motifs de Au, Ag, Au-Ag, Ag-Au et Au-Ag-Au avec 110, 145, 175 et 210 nm comme diamètres respectivement. Les NC composé d'Ag présentent le pic LSPR le plus intense parmi les cinq substrats différents peu importe le diamètre. Cela pourrait s'expliquer par le fait que les nanoparticules des Au sont

plus influencées par les transitions inter-bandes et les électrons de conduction que les nanoparticules d'Ag. En outre, nous observons un élargissement du pic LSPR de Au-Ag par rapport à celle de Ag-Au. Cela peut également être lié à l'interface Au-substrat présent dans les NC Au-Ag. Cette interface mène à des pics LSPR avec FWHM supérieure à celle de NC Ag-Au (interface Ag-substrat), voir Figure 15. En outre, pour les NC d'Au-Ag-Au les pics de LSPR représente un décalage vers le rouge en comparaison avec les NC de l'Ag-Au-Ag et Au. Ce décalage vers le rouge peut être expliqué par l'augmentation de la proportion de l'or.

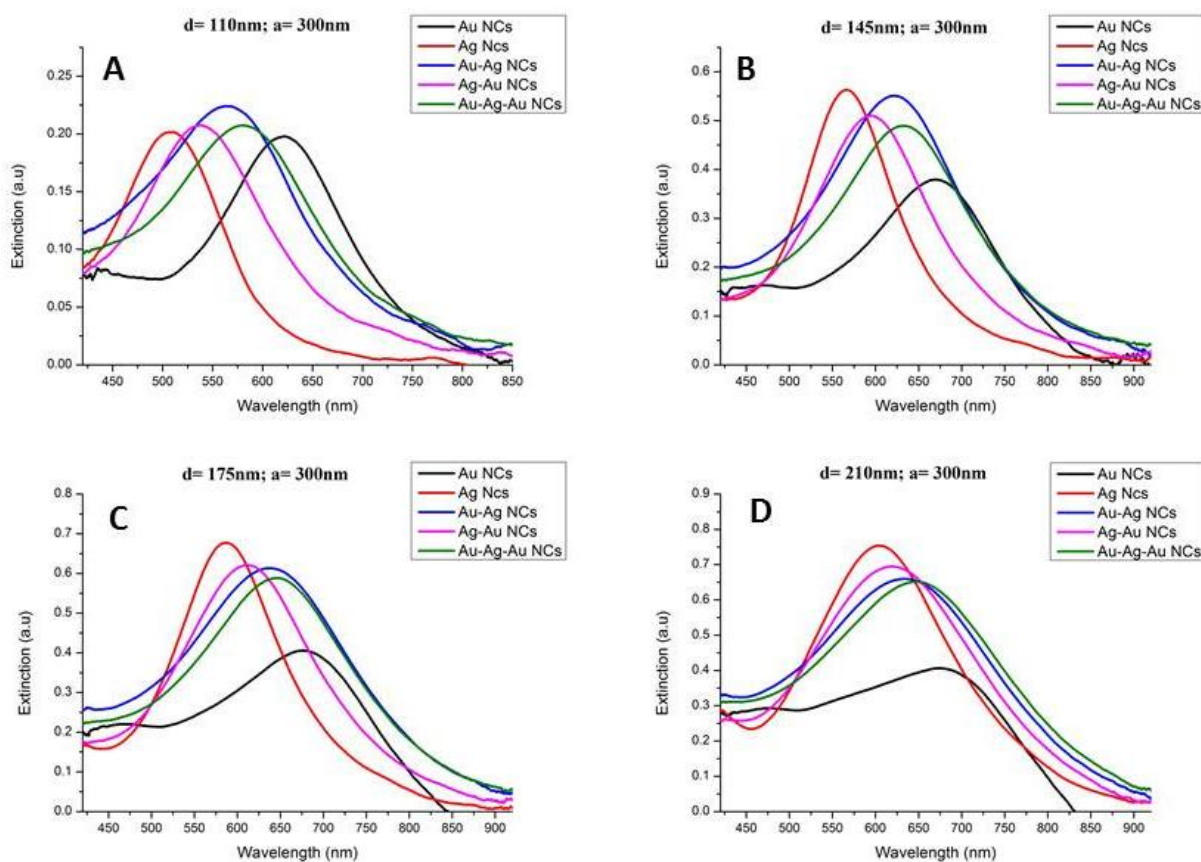


Figure 15 Les spectres LSPR pour les motifs d'Au, Ag, Au-Ag, Ag-Au et Au-Ag-Au ayant des constantes de maille de 300 nm pour le (A) 110, (B) 145, (C) 175 et (D) 210 nm diamètres.

V.2 Mesures SERS sur les NC monométallique et bimétalliques

L'exaltation SERS des motifs Au, Ag, Au-Ag, Ag-Au et Au-Ag-Au NCS avec les quatre diamètres différents ont été étudiés. En conséquence, l'intensité de SERS de cycle benzène (1605 cm^{-1}) en fonction du diamètre du chaque substrat (Figure 16) montre l'existence d'une relation linéaire entre les deux.

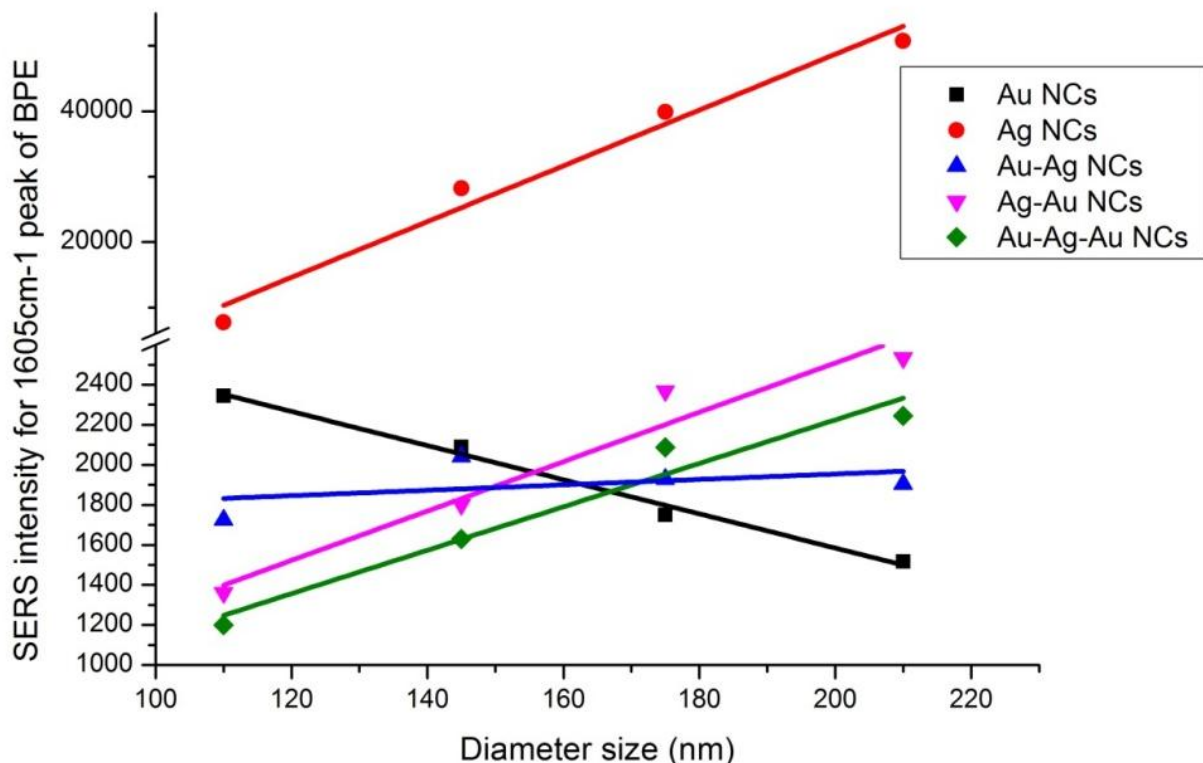


Figure 16. Courbe de l'intensité SERS du cycle benzène (1605 cm^{-1}) en fonction de la taille des NC (Au, Ag, Au-Ag, Ag-Au and Au-Ag-Au NC)

Pour étudier l'effet plasmonique sur la relation obtenue entre la diamètre et l'exaltation de SERS de chaque substrat, l'intensité de la SERS (1605 cm^{-1}) sont tracées en fonction de $\Delta\lambda$ (la valeur absolue de la différence entre la longueur d'onde Raman d'excitation et la longueur d'onde de résonance LSPR) pour chacune des quatre matrices différentes ($d = 110, 145, 175$ et 210 nm) pour les substrats d'Au, Ag et Ag-Au (Figure 17 A, B et C respectivement). L'intensité des pics SERS est inversement proportionnelle à $\Delta\lambda$ pour les substrats Au, Ag et Ag-Au, respectivement. Les structures ayant une position spectrale de LSPR plus proche à la longueur d'onde d'excitation fournissent la plus haute exaltation de l'intensité Raman. Ainsi, la relation linéaire obtenue à partir de l'intensité de SERS en fonction du diamètre est expliquée par l'augmentation du degré de proximité de LSPR à la longueur d'onde d'extinction ($632,8\text{ nm}$).

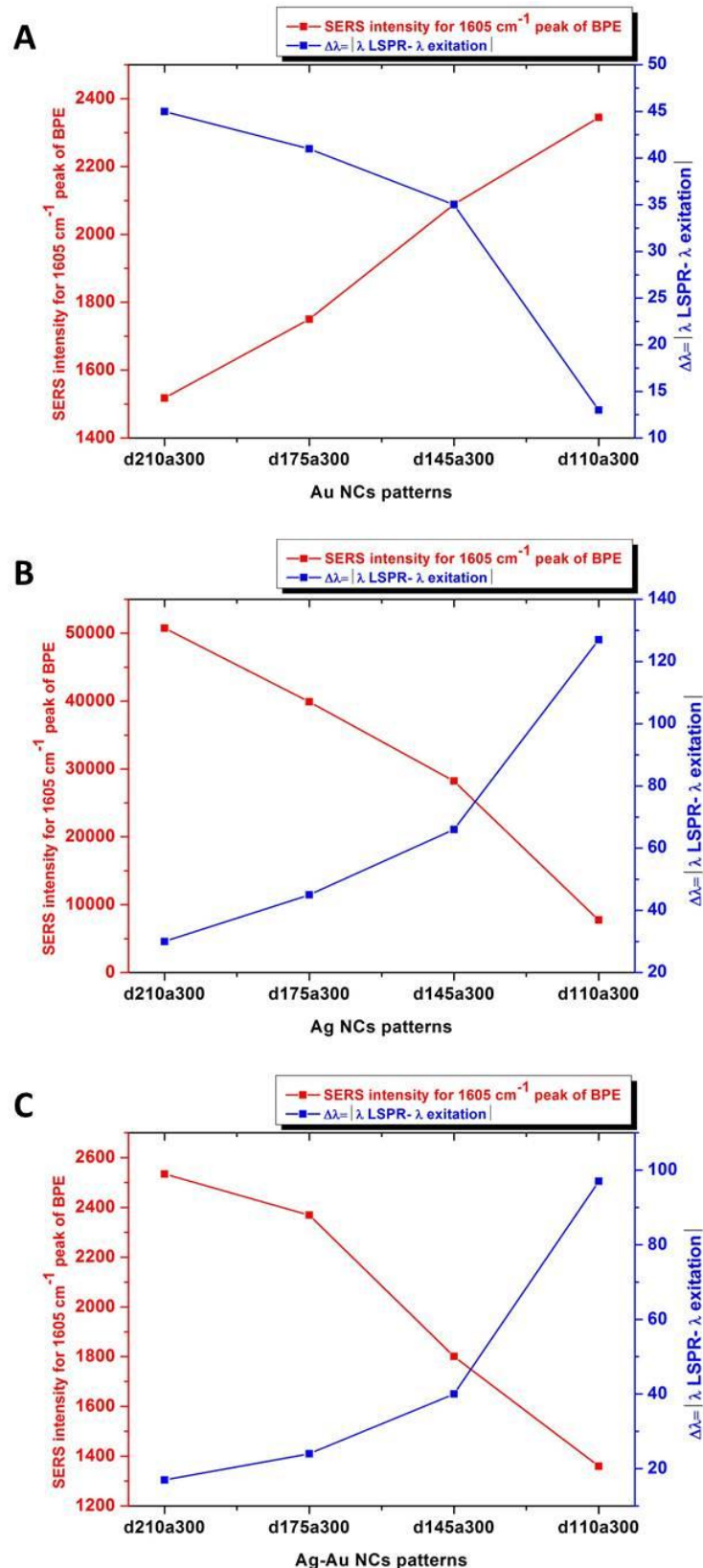


Figure 17. Relation entre l'intensité SERS des cycles benzène (1605 cm^{-1}) et $\Delta\lambda$ (la valeur absolue de la différence entre la longueur d'onde d'excitation, 632.8 nm et la resonance LSPR) en fonction des diamètres des NC (A) Au, (B) Ag et (C) Ag-Au.

VI. Conclusion Générale et Perspectives

L'objectif principal de ce travail était de développer fiables et très améliorant SERS substrats qui peuvent répondre aux normes commerciales. Sur la base de la capacité de haut exaltation de nanoparticules d'argent et la nature inerte de nanoparticules d'or, rend l'idée de combiner les deux métaux dans une nanostructure bimétallique comme une approche intéressante pour résumer les mérites des propriétés d'exaltation d'argent et les propriétés surfacique d'or.

La fabrication de plusieurs SERS-actives substrats bimétalliques de Au / Ag nanoparticules (double-couches ou trois couches) ont été menées par la stratégie recuit thermique de couche métallique mince. En ce qui concerne les nanoparticules bimétalliques double et triple-couches, une relation inversement proportionnelle entre l'intensité de la SERS et $\Delta\lambda$ (la différence entre la longueur d'onde d'excitation Raman (632,8 nm), et la position spectrale LSPR) ont été observés. Notamment, il a été constaté que le substrat Au-T-Ag-T-Au présentant la position spectrale de LSPR le plus proche à la longueur d'onde d'excitation fournit la meilleure exaltation des intensités Raman entre les substrats étudiés. La supériorité d'exaltation des nanoparticules en triples couches (qui présentent une séparation entre les particules plus faible) sur les nanoparticules bimétalliques en doubles couches provient de l'augmentation de l'effet de couplage entre les particules. En conséquence, les substrats des nanoparticules en couches triples ont des points chauds plus efficaces que celles des nanoparticules en doubles couche.

Les substrats Au-T-Ag-T-Au ont la capacité d'exaltation SERS le plus entraîné les nanoparticules bimétalliques étudiés. Les études morphologiques et de composition à l'aide de l'imagerie HRTEM ont montré une structure cœur / coquille avec un cœur mixte de Au-Ag et un coquille en Au. Nous avons également montré que la plus grande exaltation de la SERS observée au cours des nanoparticules Au-Ag / Au cœur / coquille pourrait s'expliquer par la présence de l'argent dans une structure bimétallique, ayant LSPR position spectrale en résonance avec la longueur d'onde d'excitation Raman. Les substrats SERS de Au-Ag / Au cœur/coquille présentent une grande homogénéité place à place, ayant de 2% en pourcentage écart type relatif (% RSD) dans le signal SERS. De plus, la reproductibilité de l'échantillon à l'échantillon a été mesurée à avoir 8% en % RSD dans le signal SERS. Ces nanoparticules présentent une très forte stabilité à long terme d'environ un an dans des conditions ambiantes. Cette stabilité élevée a été attribuée à la présence de la coque de protection ; Au. Les études d'optimisation réalisées sur les nanoparticules de Au-Ag / Au cœur/coquille ont montré la

suite : i) 3 nm Au -T- 3nm Ag -T- 3 nm Au substrats représente la meilleure épaisseur de l'évaporation, ii) l'augmentation de la température de recuit thermiques résultats dans une augmentation de la capacité de exaltation de la SERS et iii) le couplage de nanoparticules d'Au-Ag / Au de film d'Au entraîne également l'amélioration de la exaltation de la SERS.

L'étude systématique des nanoparticules bimétalliques Au / Ag en utilisant un faisceau d'électrons Lithographie (EBL) technique a montré que ces nanoparticules bimétalliques suivent le même régime de comportement des particules monométalliques, par rapport à l'effet de taille sur la position et la forme de LSPR. Il a été montré que l'augmentation de taille des nanoparticules en résultats en décalage vers le rouge en résonance et l'élargissement des pics de la LSPR. En outre, une bonne d'accord dans LSPR élargissement est obtenu entre le système à double couche dans le chapitre III et nanocylindres bimétalliques obtenues par EBL, où LSPR des systèmes bimétalliques sont plus larges que celles de monométallique. La majorité de les nanocylindres monométallique et bimétalliques présentent une relation inversement proportionnelle entre l'intensité de la SERS et $\Delta\lambda$, sachant que la matrice avec la position LSPR spectrale la plus proche à la longueur d'onde d'excitation Raman fournit la plus haute exaltation des intensités Raman.

Récemment, nous avons commencé à employer la technique de galvanoplastie métallique pour la croissance de couches métalliques minces. Une installation de galvanoplastie fait maison avec électrode rotative (pour une meilleure homogénéité) a été utilisé pour la fabrication de nanoparticules bi-métalliques. Cette technique devrait fournir un moyen encore plus pratique pour la fabrication en raison de sa rentabilité et de gain de temps. En outre, une étude de la validation de la relation inversement proportionnelle entre l'exaltation de la SERS et $\Delta\lambda$ peut être entrepris.

En outre, nous pouvons profiter de l'accordabilité et la capacité d'exaltation de nos substrats fabriqués afin d'étudier la possibilité d'exaltation dans d'autres techniques spectroscopiques; fluorescence par exemple. En outre, nous pouvons étudier les effets d'accorder la LSPR de nanoparticules bimétalliques sur les intensités de fluorescence et la durée de vie. La exaltation fluorescence à côté de la exaltation de la SERS imposera ces substrats bimétalliques mentionnés comme des dispositifs de détection universels.

Mohammad Yehia KHAYWAH

Doctorat : Optique et Nanotechnologies

Année 2014

Nouveaux substrats bimétalliques ultrasensibles pour la diffusion Raman exaltée de surface

Afin de développer des capteurs ultrasensibles des substrats fiables pour la diffusion Raman exaltée de surface (SERS) ont été fabriqués. Les deux meilleurs candidats de matériaux constituant les nanoparticules pour des substrats SERS sont l'argent et l'or. L'argent présente un meilleur facteur d'exaltation de l'intensité Raman et l'or est stable dans les milieux biologiques. C'est pourquoi la combinaison de ces deux métaux dans des nanostructures bimétalliques semble être une approche prometteuse qui combine les propriétés de surface de l'or et d'exaltation de l'argent. Le recuit thermique des couches métalliques minces est utilisé comme une technique simple et peu coûteuse. Cette dernière permet d'élaborer des substrats homogènes et reproductibles de nanoparticules bimétalliques or-argent ayant un facteur d'exaltation importante. Ces nanoparticules gardent leurs propriétés d'exaltation même après une année de fabrication. En jouant sur la composition de nanoparticules bimétalliques il est possible d'avoir une résonance de plasmons de surface localisés (LSPR) sur tout le spectre visible. Ces substrats sont caractérisés par une exaltation SERS supérieure lorsque la résonance plasmon est plus proche de la longueur d'onde d'excitation Raman. En outre, les nanoparticules bimétalliques de différentes tailles, compositions ont été réalisés par lithographie électronique. L'étude systématique de leurs propriétés plasmoniques et de leur exaltation SERS a révélé une conservation du lien entre résonance plasmon et signal SERS.

Mots clés : Raman, effet augmenté en surface - nanoparticules - résonance plasmonique de surface - or - argent - lithographie par faisceau d'électrons.

New Ultrasensitive Bimetallic Substrates for Surface Enhanced Raman Scattering

Driven by the interest in finding ultrasensitive sensors devices, reliable surface enhanced Raman scattering (SERS) based substrates are fabricated. Silver and gold nanoparticles are two of the best candidates for SERS substrates where Ag nanoparticles exhibit large enhancing ability in Raman intensity while Au nanostructures are stable in biological systems. Hence, combining the two metals in bimetallic nanostructures appeared to be a promising approach in order to sum the merits of Au surface properties and Ag enhancing ability. Thermal annealing of thin metallic films is used as a simple and relatively inexpensive technique to elaborate homogeneous and reproducible Ag/Au bimetallic nanoparticles SERS substrates with high enhancing ability. The fabricated nanoparticles proved their enhancing stability even after one year of fabrication. Manipulating the composition of Ag/Au bimetallic NPs resulted in tuning the Localized Surface Plasmon Resonance (LSPR) over the whole visible spectrum, where the substrates are characterized with higher SERS enhancement when they exhibit LSPR closer to the Raman excitation wavelength. Additionally, bimetallic nanoparticles patterns with different size, composition and lattice constants have been conducted by electron beam lithography. The systematic study of their interesting plasmonic and SERS enhancing properties revealed maintenance in the LSPR-SERS relation by changing the nanoparticle size.

Keywords: Raman effect, surface enhanced – nanoparticles - surface plasmon resonance – gold – silver - lithography, electron beam.

Thèse réalisée en partenariat entre :



Ecole Doctorale "Sciences et Technologies"